

A Thesis Submitted for the Degree of PhD at the University of Warwick

Permanent WRAP URL:

<http://wrap.warwick.ac.uk/142667>

Copyright and reuse:

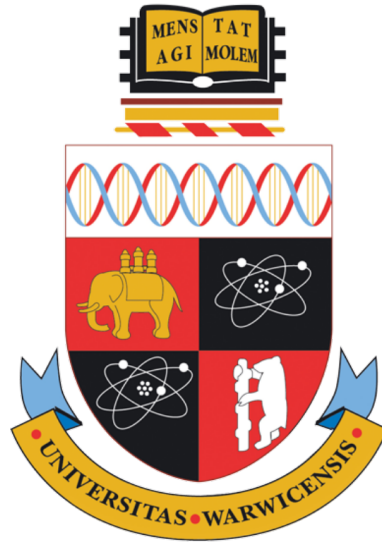
This thesis is made available online and is protected by original copyright.

Please scroll down to view the document itself.

Please refer to the repository record for this item for information to help you to cite it.

Our policy information is available from the repository home page.

For more information, please contact the WRAP Team at: wrap@warwick.ac.uk



Applications of Transit Surveys to Red Dwarfs

by

Emma Alexandra Foxell

Thesis

Submitted to the University of Warwick

for the degree of

Doctor of Philosophy

Astronomy and Astrophysics

March 2020

Contents

List of Tables	vi
List of Figures	x
Acknowledgments	xviii
Declarations	xix
Abstract	xx
Abbreviations	xxi
Chapter 1 Introduction	1
1.1 An overview of exoplanet discovery	1
1.2 Exoplanet Detection Techniques	3
1.2.1 Transit Photometry	3
1.2.2 Radial Velocity	7
1.2.3 Direct Imaging	10
1.2.4 Transit timing variations	11
1.2.5 Microlensing	11
1.2.6 Astrometry	12
1.3 Wide field transit surveys	12
1.4 Targeted Surveys	16
1.5 Confirmation of Transiting Exoplanets	17
1.5.1 False positives	18
1.5.2 Follow up observations	21
1.6 M dwarfs	22
1.7 Key questions to address	23

Chapter 2	Methods	24
2.0.1	CCD cameras and saturation	24
2.1	Image processing	26
2.1.1	Bias	26
2.1.2	Dark	28
2.1.3	Flat	28
2.1.4	Data Reduction	28
2.2	Aperture Photometry	29
2.3	Observing tools	30
2.3.1	Predicting future phase coverage	30
2.3.2	Autoguiding	31
2.4	Algorithms	31
2.4.1	Bayesian Statistics and MCMC	31
2.4.2	Lomb Scargle	33
2.4.3	Box Least Squares (BLS)	34
2.5	Transit fitting	35
2.5.1	Estimating orbital period from a single transit	35
2.6	Transit Injection	35
2.6.1	Limb darkening toolkit	35
2.6.2	PyTransit	36
2.7	Summary	36
Chapter 3	Investigation into Saturated Stars in the Next Generation	
	Transit Survey	37
3.1	Introduction	37
3.1.1	The Next Generation Transit Survey	37
3.1.2	Motivation for Studying Saturated Stars	38
3.1.3	Saturated star studies in <i>Kepler</i> data	40
3.1.4	NGTS CCDs	41
3.1.5	Standard NGTS data reduction	41
3.1.6	The data	42
3.2	Saturated Stars in the Standard Pipeline	43
3.2.1	Identifying Saturated Stars	43
3.2.2	The standard pipeline aperture	43
3.3	Larger Circular Apertures	45
3.3.1	Why test larger circular apertures	45
3.3.2	Lightcurves and Thumbnails for Larger Circular Apertures	47

3.3.3	Comparison of apertures 4 and 5 to the standard aperture 3 .	51
3.3.4	Conclusion	55
3.4	Rectangular apertures	55
3.4.1	Motivation	55
3.4.2	Determining aperture length	56
3.4.3	Finding relationship between length and star magnitude . .	59
3.4.4	Determining aperture width	60
3.4.5	Rectangular aperture photometry	60
3.4.6	Comparison of rectangular to circular pipeline apertures . . .	66
3.4.7	Investigation of light curve precision using rectangular apertures	67
3.5	Charge Conservation	71
3.5.1	The camera settings	71
3.5.2	Method to test charge conservation	72
3.5.3	Data Analysis	73
3.5.4	Results	74
3.5.5	Conclusion	78
3.6	Gain calculation	78
3.7	Conclusions	80
3.7.1	Investigation of saturated stars' nature	80
3.7.2	Summary	82
3.7.3	End state	83

Chapter 4 A Transiting Exoplanet Survey in the Habitable Zones of six mid-to-late M dwarfs with NITES 85

4.1	Introduction	85
4.2	Observations	89
4.2.1	Survey strategy	89
4.2.2	Observations	90
4.2.3	Data Reduction	92
4.3	Results	93
4.3.1	Transit-like features	93
4.3.2	Flares	96
4.3.3	Phase coverage and the Habitable Zone	99
4.4	Analysis	102
4.4.1	BLS search	102
4.4.2	BLS results	103
4.4.3	Transit injection	104

4.4.4	Lomb Scargle	108
4.5	Discussion	109
4.5.1	MEarth data	109
4.5.2	TESS data	110
4.5.3	Habitability	111
4.5.4	Comparison to expected number of detections	112
4.6	Conclusions	114
4.7	Tables of individual events	116

Chapter 5 Characterisation of Two Low Mass Eclipsing Binaries (EBLMs) from *SuperWASP* **118**

5.1	Introduction	118
5.1.1	Low mass stars	118
5.1.2	Low mass stars in binaries	119
5.1.3	Identification of EBLMs from SuperWASP	120
5.1.4	Contributions	120
5.2	Initial Observations	121
5.3	Spectral follow up observations	123
5.3.1	Spectral follow up of WASPJ02+40	123
5.3.2	FIES Spectroscopy of WASPJ23+29	124
5.4	Follow up photometry	126
5.5	Analysis and results	128
5.5.1	Stellar parameters	128
5.5.2	Global modelling with ELLC	130
5.6	Results	134
5.6.1	WASPJ23+29	134
5.6.2	WASPJ02+40	142
5.7	Discussion	148
5.7.1	EBLMs in context	148
5.8	Conclusions and Future work	151

Chapter 6 Conclusions and Prospects **153**

6.1	Conclusions	153
6.1.1	Investigation into Saturated Stars in the Next Generation Transit Survey	153
6.1.2	A Transiting Exoplanet Survey in the Habitable Zones of six mid-to-late M dwarfs with NITES	155

6.1.3	Characterisation of Two Low Mass Eclipsing Binaries (EBLMs) from <i>SuperWASP</i>	156
6.2	Future outlook	158

List of Tables

3.1	The range of mean fluxes and fractional RMSs of flux for saturated and bright unsaturated stars using different rectangular apertures. .	69
3.2	The range of mean fluxes and RMS values of flux for saturated and bright unsaturated stars using pipeline apertures.	69
3.3	Table shows measured gain values from both PAG settings for all cameras.	80
4.1	Stellar parameters of targeted Mdwarfs, where T shows the effective temperatures and L the luminosity. Source: ^a : Gaia DR2, ^b : 2MASS, ^c : Simbad, ^d : TESS Candidate Target List (<i>CTL</i>) v8.0. All magnitudes are Vega magnitudes apart from I magnitudes for MD20+58 and MD22+40, which are AB magnitudes.	93
4.2	Flare information on targeted Mdwarfs. Hours observed includes all data, including flares and noisy data. Targets were observed for an average of 3.4 hours per night, with the mean hours of observation varying from 2.8 to 4.9 hours, depending on the object. Average flare frequencies are given per night of observation (rather than 24 hours) and per hour of observation.	99
4.3	Number of observed hours, phase coverage and calculated habitable zone limits of targeted Mdwarfs. Filtered nights excludes nights with nightly RMS above the values specified in the max RMS column. The habitable zone limits are calculated from TESS <i>CTL</i> v8.0 and are indicated by Runaway GH (runaway greenhouse) and Max GH (maximum greenhouse). 50 % phase coverage period includes flares, but excludes filtered RMS.	101

4.4	Parameters used in injection and for BLS search. The frequency factor controls the frequency spacing, defining the coarseness of the BLS search. Limb darkening constants for transit injection were calculated using the limb darkening toolkit (LDTk) (Parviainen and Aigrain, 2015) with TESS <i>CTL</i> temperature and $\log g$ values and zero metallicity.	102
4.5	BLS results. Nightly RMS values greater than the max RMS were not included in the BLS analysis. Other parameters are obtained from the BLS. Results from the highest peak for each object are shown. .	104
4.6	Results from injection tests at the inner edge of the habitable zone (runaway greenhouse limit) for all target stars. For each target, the runaway greenhouse period, minimum radius ratio recovered at any injected phase, and corresponding minimum radius (calculated using TESS <i>CTL</i> v8.0 parameters) are given. The probability of transit at the inner edge is calculated for the given minimum radius using equation 4.5, as described in Section 4.5.4.	107
4.7	Results from multi-period injection tests. All but the last column give results from injection at a random phase to find maximum period and minimum radius sensitivity for each target. Columns 2–4 give the minimum radius ratio recovered in the injection tests, its SNR, and the corresponding minimum radius (calculated using TESS <i>CTL</i> v8.0 parameters). Columns 5–8 give the maximum period where at least two transits are correctly detected for each radius ratio (RR) at the random injected phase. The rightmost column shows the results from the multi-period, multiple phase test, and gives the maximum period where transits of radius ratio 0.2 were recovered at all five phases. This required all shorter tested periods to be recovered.	109
4.8	Filtered table of interesting events, listing transit-like features, including their depth and periods estimated from the single transit where available.	116
4.9	All flares identified in the survey. None were observed for MD20+58. Flare peak fluxes are given, where fluxes outside the flare are normalised to 1. Calculated energies are in erg.	116
5.1	Stellar properties. ^a : Gaia DR2. ^b : Simbad	122
5.2	Summary of 13 new spectral radial velocities for WASPJ02+40. . . .	123
5.3	Summary of 19 new <i>FIES</i> radial velocities (RVs) for WASPJ23+29.	124

5.4	Summary of <i>NITES</i> follow-up photometry of WASPJ23+29. The exposure time, out of transit RMS values and aperture radius are given for each night.	126
5.5	Stellar parameters of WASPJ23+29 from spectroscopic analysis. . .	129
5.6	Stellar parameters of WASPJ02+40 from spectral analysis. Parameters ‘Spectra’ were determined in iSpec with abundances relative to solar values in Grevesse et al. (2007). Resulting stellar parameters of WASPJ02+40 output by the isochrones package (Morton, 2015) are given under ‘Isochrones’, see text for details. *Note: Mass and radius in this column are calculated using the Torres et al. (2010) relation.	130
5.7	Initial parameters used for WASPJ02+40. SuperWASP = determined from SuperWASP photometry. RVs = radial velocities. Spectra = from spectral analysis. v_{sys} = systematic velocity. Ldc = limb darkening constant.	132
5.8	Initial parameters used for WASPJ23+29. RVs = radial velocities. Spectra = from spectral analysis. v_{sys} = systematic velocity. Ldc = limb darkening constant.	133
5.9	Output parameters derived from ELLC for WASPJ23+29, using primary star parameters from the Torres et al. (2010) relation.	135
5.10	Derived parameters comparison for WASPJ23+29. All parameters for Chaturvedi et al. (2016) come from joint modelling with EXOFAST apart from T_{eff} , $\log g$, $[Fe/H]$ and primary stellar mass and radius which are reported to come from spectral analysis using PARAS data. ‘ELLC Torres’ shows ELLC results using primary star mass and radius calculated from spectra using the Torres et al. (2010) relation.	139
5.11	Stellar parameters of WASPJ23+29 from Chaturvedi et al. (2016). Parameters within the PARAS column were calculated by Chaturvedi et al. (2016) using PARAS spectra. Parameters within the SOPHIE column were calculated using archival SOPHIE spectra. They estimate mass and radius using the Torres et al. (2010) calibration.	140
5.12	Stellar parameters of WASPJ23+29 calculated using the isochrones package (Morton, 2015), see text for details.	142

5.13	Derived parameters comparison for WASPJ23+29. The second column (Chat. 2016) gives parameters as reported in Chaturvedi et al. (2016) come from joint modelling with EXOFAST apart from T_{eff} , $\log g$, $[Fe/H]$ and primary stellar mass and radius reported from spectral analysis using PARAS data. Where there is a second row of data, these record our calculation of errors based on their spectral parameters, and marked by ‘this work’. The third column (ELLC Torres) shows ELLC results using mass and radius derived from Torres et al. (2010) as external parameters. The fourth column shows ELLC results using mass and radius derived from isochrones.	143
5.14	Output parameters derived from ELLC for WASPJ02+40. ‘Isochrone R’ gives results using the radius derived from isochrones as an external parameter, ‘Torres RM’ gives results using the parameters derived using the Torres et al. (2010) relationship and ‘Gaia R’ gives results using the Gaia DR2 radius. Primary star mass and radius parameters used in ELLC are also given for reference.	146

List of Figures

1.1	Cumulative frequency of exoplanet discovery by year, colour coded by detection method. Figure from the NASA Exoplanet Archive, accessed 09/03/2020.	2
1.2	Figure illustrating the geometry of orbital inclination. After: https://www.paulanthonywilson.com , accessed 09/03/2020.	4
1.3	Top: Phase folded lightcurve of NGTS 2b, adapted from Raynard et al. (2018). Bottom: Relative positions of planet and stellar disks, showing the four contacts and location of mid-transit. Parameters b , $R_* + R_p$ yield l via trigonometry, giving the transit duration, T_{dur}	5
1.4	Radial velocity curve of 51 Peg phase folded on the period of its planet, 51 Peg b. From Mayor and Queloz (1995).	8
1.5	Geometry of an elliptical orbit. Note periastron is the pericentre specifically for stars. After Perryman (2018).	9
1.6	Lens magnification of the background star in OGLE-2005-BLG- 390L (Beaulieu et al., 2006). Detail of the distortion due to the lens star's $5.5 M_{\oplus}$ planet at 2.1 AU is shown in the inset.	12
1.7	Example eclipsing binary light curve from Kepler showing a deep primary eclipse and clear secondary eclipses. From Prsa et al. (2011).	19
1.8	Comparison of the spectral energy distribution of different spectral types as indicated in the figure. After: http://www.astronomy.ohio-state.edu , accessed 01/06/2020.	22
2.1	The rain bucket analogy for how CCDs work where the rain represents photons and the buckets the pixels. From Janesick and Blouke (1987).	25

2.2	The linearity response of a typical CCD. This example has ADC (or A/D) saturation at 32767 ADU (a 15-bit ADC). The full well capacity is 150,000 electrons. A gain of $4.5 \text{ e}^-/\text{ADU}$ means ADC saturation occurs at $32767 \times 4.5 = 147451$ photons and pixel saturation at $150,000/4.5 = 33,333$ ADU. From Howell (2006).	27
2.3	Increase in phase coverage for observing the night of 15th January 2019 for two targets: MD07+16 (top) and MD11+06 (bottom). For each, the top subplot compares already observed phase coverage (blue) and phase coverage if the additional night of observations takes place (red), while the bottom subplot shows the increase in phase coverage between the two at each test period.	32
3.1	Thumbnail images: the left plot shows a bright star that is below saturation, which is contained within the standard 3 pixel aperture indicated by the red circle. The right plot shows a saturated star whose light extends beyond the same standard 3 pixel aperture. . . .	40
3.2	Top: Fractional RMS vs mean flux for stars in field NG0304-1115. Objects identified as saturated have mean fluxes greater than the saturation level indicated by the red vertical line at 38000 ADU/second. Bottom: fractional RMS noise as a function of stellar brightness for data points binned to one hour exposure, from Wheatley et al. (2018).	44
3.3	RMS vs mean flux for stars in field NG0304-1115 using different sized circular apertures. Aperture 3 is in blue, aperture 4 is in green and aperture 5 is in red. The saturation limit of 38000 ADU/second for aperture 3 is indicated by the red vertical line, which corresponds to a magnitude of 9.0 in R.	46
3.4	Light curves for saturated objects in field NG0304-1115. Flux (in ADU/s) is plotted against time index to reduce white space, with red vertical lines separating the different nights. Flux values flagged by the pipeline were not plotted. Each subplot shows a different object, with the object number indicated on the right. Flux as measured within aperture 3 is shown in blue, aperture 4 in brown and aperture 5 in cyan.	48
3.5	Light curves of more saturated objects, as per Figure 3.4. Airmass is also plotted in green.	49

3.6	Light curves for bright unsaturated objects in field NG0304-1115. Flux (in ADU/s) is plotted against time index to reduce white space, with red vertical lines separating the different nights. Flux values which were flagged by the pipeline were not plotted. Each subplot shows a different object, with the object number indicated on the right. Flux as measured within aperture 3 is shown in blue, aperture 4 in brown and aperture 5 in cyan.	50
3.7	Thumbnails of saturated stars in field NG0304-1115 from the autoguider reference image, where colour scales with flux value. The star's catalogue number is given above each subfigure. Apertures 3, 4 and 5 are plotted over the star, with their mean flux (in ADU/s) given in the same colour. The saturation level for this field is 38000 ADU/s.	52
3.8	Thumbnail plots as per Figure 3.7 but for bright unsaturated stars.	53
3.9	Comparison of mean fluxes between apertures 3, 4 and 5 for saturated (red crosses) and bright unsaturated (blue circles) stars. Top: mean flux ratio between apertures 5 and 3. Bottom: comparison of the additional flux captured using the larger apertures 4 and 5 by plotting the ratio of their mean flux with that of aperture 3. The 1:1 line is plotted in blue.	54
3.10	The measured vertical extents of the blooming pattern from the catalogue x position in individual frames is shown for each saturated star. This is used to help identify what size rectangular aperture to use for producing lightcurves. Each coloured block of points plotted against the time index shows a different night in the first 21 nights that vertical extents were measured for. Each row is labelled by the object id and its corresponding R magnitude. For reference, the airmass is also plotted.	57
3.11	R magnitudes vs maximum measured vertical extent. For each object, both the maximum vertical extent measured on any night and the maximum of the nightly 99th percentile lengths are shown. Both saturated and bright unsaturated objects are plotted, separated by the vertical line. Overall maximum lengths (plotted as circles) vary greatly for both saturated and bright unsaturated objects whereas the 99th percentile shows a stronger trend with increasing magnitude. This suggests that the 99th percentile is a more reliable measurement of suitable aperture length because it is less affected by spurious detections.	58

3.12	Vertical extent vs magnitude for R, NGTS I, NGTS G and Gaia magnitudes. Lengths are the maximum of nightly 99th percentiles found in Section 3.4.2. Saturated stars and bright unsaturated stars are both plotted, separated by a vertical line. A linear trend is fitted to the saturated stars for each magnitude set. In the NGTS I and G bands (the two leftmost panels), object 1536 with length 24 pixels is a clear outlier, so is excluded from the linear fit. The two rightmost panels show two linear fits, one including and one excluding the magnitude for object 1536 for comparison.	60
3.13	Example thumbnails illustrating outlying fluxes, where each column shows stars from the same frame. The position of the pipeline aperture is shown by the red circle, and purple and green rectangles represent rectangular apertures of widths 6 and 12 respectively. The left plot shows thumbnails from the fifth night, where in the middle column, apertures are not centred on the stars due to increased autoguider error, causing outlying fluxes. Its adjacent columns show thumbnails from images two minutes before and after the central column, where apertures are centred on the stars as the autoguider error is less than one pixel. The righthand plot shows thumbnails from the first two frames of the third night (plotted in green in Figure 3.14), showing apertures in the first image are not placed on the stars. . .	62
3.14	Lightcurves showing outlying fluxes for rectangular aperture with width 6. Dotted lines indicate the frames where the autoguider error is greater than three times the RMS, which correlates with the dropout fluxes. The bottom two panels of each figure indicate the autoguider position error for x and y axes. Top: saturated stars, bottom: bright below saturation stars.	63
3.15	Lightcurves of bright unsaturated stars using rectangular apertures with width 6 after removal of outlying flux associated with autoguider error and the first frame of the night. A couple of nights have flux values off the scale.	64
3.16	Lightcurves of saturated stars using rectangular apertures with lengths tailored to the star and widths as specified. These show lightcurves after removal of frames with outlying flux in width 6 lightcurves that were associated with autoguider error and the first frame of the night. A couple of nights have flux values off the scale. The top panel of subplot (b) shows the airmass during observations.	65

3.17	Ratio of median measured fluxes using circular apertures 3, 4 and 5 and rectangular apertures with width 6 pixels against median rectangular flux. Values for the same star have the same x value. The red dashed line separates bright unsaturated and saturated stars. . . .	66
3.18	Relative flux lightcurves for stars as labelled using a rectangular aperture of width 6. The lightcurve for each star is measured as a fraction of the standard star (the sum of bright unsaturated star fluxes) measured using a rectangular aperture of the same width. The top figure shows saturated stars and the bottom bright unsaturated stars. . . .	68
3.19	Fractional RMS vs the mean flux. Bright unsaturated stars are plotted as red crosses and saturated stars as blue crosses. The different panels show results from rectangular widths of 6 (left) and 12 pixels (right).	70
3.20	Flux vs expected flux values using standard NGTS settings, voltage VI227 and gain PAG2. The top figure shows results for camera 809 and the bottom camera 805. The top panel of each figure shows the ratio of mean measured flux/ expected flux, while the bottom shows peak pixel values. The black horizontal line shows the theoretical maximum pixel value in electron units.	76
3.21	Flux vs expected flux values using standard NGTS voltage VI227 but changing the gain to PAG1. The top figure shows results for camera 809 and the bottom camera 805. The top panel of each figure shows the ratio of mean measured flux/ expected flux, while the bottom shows peak pixel values. The black horizontal line shows the theoretical maximum pixel value in electron units.	77
3.22	Flux vs expected flux values using gain setting PAG1 and other voltages for camera 809. The top figure shows VI190 and the bottom shows VI168. The top panel of each figure shows the ratio of mean measured flux/ expected flux, while the bottom shows peak pixel values. The black horizontal line shows the theoretical maximum pixel value in electron units.	79
3.23	Plots of mean flux against variance used to calculate the gain for VI227, PAG 1 (both in units of ADU). Each subplot shows a different camera.	81

4.1	Calculated throughput (transmission vs wavelength) for the NITES I and R filters. The blackbody spectrum for stars with temperatures 2700 and 3000 K are also plotted.	91
4.2	Plots of example individual nightly light curves displaying initial candidates identified with transit-like features. The raw data with 30 second exposures is in the top row, the middle row shows data fitted to the linear trend in the top row. The bottom row shows the fitted data binned to a factor of 4. The residual RMS compared to a linear fit is given for the out of transit data for both the unbinned and binned data. The caption for each gives the target and the night of observation.	94
4.3	As per Figure 4.2. Plot of initial candidate transit for MD07+16, 20171222.	95
4.4	Single night lightcurves with fitted transit models and their residuals. Top: MD18+29, night 20190606. Middle: MD22+40, night 20180827. Bottom: MD07+16 on night 20171222.	97
4.5	As per Figure 4.2, with RMS values given for out of flare data. Plots of example individual nightly light curves showing flares.	98
4.6	Phase coverage of the targeted Mdwarfs. Each subplot shows the phase coverage of one of the six Mdwarfs. The shaded region shows the extent of the habitable zone, calculated using runaway greenhouse and maximum greenhouse boundaries, with parameters from the TESS <i>CTL</i> . The first period with phase coverage below 50 % (excluding 1 day aliases) is indicated by the vertical red dotted line. Phase coverage includes flare data but excludes data with higher RMS values.	101
4.7	BLS results. (a) MD02+22: a clear significant peak is seen at 1 day, most likely due to the day-night cycle. (b) MD07+16: no significant peak is seen in the BLS spectrum.	103
4.8	Transit model fit to the individual transit identified by BLS for MD07+16, which was observed on the night of 20190128.	105
4.9	BLS results for MD07+16 without filtering the data. Two transits of similar depth are identified by BLS in the data but the phase folded light curve shows their durations are very different.	105

4.10	Examples of BLS injection recovery results (a) Injected transits are recognisable for MD11+06 for an injected planet with radius ratio 0.075 and period 8.09 days, although BLS recovers a period of 5.93 days. (b) The correct period of 17.73 days is recovered by BLS for MD07+16 with injected planet radius ratio of 0.15.	107
5.1	Phase folded light curve of all <i>SuperWASP</i> data for WASPJ02+40. Primary transit can be clearly seen around phase 0.3 and no secondary is visible.	121
5.2	Individual <i>SuperWASP</i> light curves for WASPJ23+29. Produced by James McCormac.	122
5.3	RV measurements of WASPJ23+29. The top panel shows the phased RV measurements from the <i>FIES</i> , <i>SOPHIE</i> and <i>PARAS</i> spectrographs in black, green and blue points respectively. The <i>SOPHIE</i> and <i>PARAS</i> data are taken from Chaturvedi et al. (2016) and have been included in the global modelling in Section 5.5.2. The bottom panel shows the residuals after subtracting the best fitting model. Note that error bars are plotted on the upper plot but are smaller than the point size used in the figure. Relative scales of the error bars are more clearly seen in the lower panel. Produced by James McCormac.	125
5.4	<i>NITES</i> eclipse photometry of WASPJ23+29. Black points are the photometric data. Red lines show the best fitting model from Section 5.5.2. Four individual transits observed by <i>NITES</i> are shown offset from a flux ratio of 1, labelled by the date of observation. The residuals to the best fitting model are shown in the lower section of the figure, again labelled by date of observation. The grey points on night 20120829 were affected by a jump in the telescope position at the time of the second dip during the eclipse. Grey points were excluded from the global model in Section 5.5.2. Produced by James McCormac.	127
5.5	WASPJ23+29 fitted light curve and radial velocity model using spectral parameters derived from Torres et al. (2010).	136
5.6	WASPJ23+29 corner plot for the fitted model shown in Figure 5.5. Parameters from left to right: r_1/a , r_2/r_1 , K , inclination, eccentricity, ω , q , v_{sys} <i>PARAS</i> , v_{sys} <i>SOPHIE</i> , v_{sys} <i>FIES</i> , t_0	137
5.7	WASPJ02+40 fitted light curve and RV model output from <i>ELLIC</i> using external parameters from isochrones.	144

- 5.8 WASPJ02+40 corner plot for model parameters output from ELLC using external parameters from isochrones. Parameters from left to right: r_1/a , r_2/r_1 , K , inclination, q , v_{sys} SOPHIE, v_{sys} IDS, t_0 145
- 5.9 Mass radius plot for low mass stars (less than $0.4 M_\odot$) split by orbital period. Plotted lines are isochrones from Baraffe et al. (2015) with ages in Gyr as indicated. The inset plots show a zoomed-in region comparing the modelled EBLMs to the isochrone lines, see text for details. Top: orbital periods less than 10 days. WASPJ02+40 values from ELLC are in red. Bottom: orbital periods more than 10 days. WASPJ23+29 values from ELLC are in red, and Chaturvedi et al. (2016)'s value is in brown. Note: Chaturvedi et al. (2016)'s value nearly entirely overlaps with our calculated value using isochrones. . . . 152

Acknowledgments

Firstly, I would like to say a big thank you to my supervisors Don Pollacco and Richard West for their guidance over these years and for the opportunity to work in such an exciting field. My thanks also to James McCormac for managing the NITES telescope and for his patience and assistance in evening and night-time telescope issues. I would also like to thank the NITES observing team for their work observing the NITES M dwarf survey.

To the University of Warwick Astronomy group, thank you for making it an enjoyable place to work and for your help in answering questions about data reduction and coding.

Finally thank you to friends and family for always being willing to listen to how the research was going along the way.

Declarations

This thesis is submitted to the University of Warwick in support of my application for the degree of Doctor of Philosophy. It has been composed by myself and has not been submitted in any previous application for any degree. Work within Chapter 3 was presented as a poster at the Transiting Exoplanets conference at Keele University in July 2017. Work within Chapter 4 was presented as a poster at the UK Exoplanet Meeting at the University of Oxford in April 2019 and as a talk at the European Week of Astronomy and Space Science (EWASS) in Lyon in June 2019. It is currently under review for publication. Work within the Chapter 5 on EBLMs was also presented as a talk at EWASS 2019.

Work presented is my own work except where stated otherwise. Observations for the NITES M dwarf survey presented in Chapter 4 were carried out by a team of observers at the University of Warwick: David Armstrong, James Blake, David Brown, Paul Chote, Benjamin Cooke, John Dolan, George King, Kristine Lam, James McCormac, Hugh Osborn, Don Pollacco and Simon Walker. The NITES photometric pipeline was created by James McCormac. NITES observing scripts and software were written by James McCormac and Paul Chote. I selected targets, performed the data reductions and analysis, and inspected and interpreted the data.

The EBLM data in Chapter 5 come from a list of *SuperWASP* EBLMs compiled by James McCormac. Guillaume Hébrard obtained spectra and the radial velocities from them. James McCormac adapted ELLC for modelling *SuperWASP* EBLMs. Amanda Doyle ran spectral fitting for WASPJ23+29. James McCormac ran initial fitting for WASPJ23+29, fitting the NITES photometry, as presented in Figure 5.4, and radial velocity data as presented in Figure 5.3.

Abstract

Many hot Jupiters have been discovered from the ground and *Kepler* discovered many exoplanets around fainter stars, but searches push for more smaller planets around bright stars. Transit photometry also relies on knowledge of host star properties, less certain for later spectral types. This thesis aimed to investigate detecting planets smaller than Jupiter around bright, later spectral types and to help better understand M dwarf properties.

NGTS aims to discover Neptune-sized exoplanets around K and M dwarfs. In Chapter 3, I investigated the brightest stars, saturated in the standard pipeline. While relatively few, these targets are highly valuable. I investigated whether saturated star fluxes could be recovered by using custom apertures, finding tailored rectangular apertures captured them well. I show the difference in noise between bright unsaturated stars and saturated stars is reduced using rectangular apertures rather than the standard pipeline, and is the same for a number of cases. However, to perform saturated star photometry, NGTS needs to change its operational gain setting, to allow charge to be conserved.

Earth-sized habitable zone exoplanets are easier to detect around later spectral types as smaller, cooler stars are more favourable for transit photometry. However, their exoplanets are difficult to find in wide-field transit surveys due to their inherent comparative faintness. For this reason, I conducted a targeted survey of mid-late M dwarfs, presented in Chapter 4. Six relatively bright M dwarfs with spectral types M5–M8 were intensely observed, aiming for 50% phase coverage into their habitable zones. Some late M dwarfs also exhibit high flaring frequencies, so for the highest flaring rate target, I investigated the habitability for any habitable zone planets, finding them likely uninhabitable.

Stellar properties are a large source of potential uncertainty in determining exoplanet properties, especially for mid-to-late M dwarfs, where stellar evolutionary models show inconsistency with observed data. Testing these models requires independently determined parameters, which is possible using EBLMs from transit surveys. In Chapter 5, I fit two EBLMs from *SuperWASP*. I find both secondary stars sit close to the bottom of the main sequence, where there are few other measured stars. However, properties of the higher mass (primary) star can still have large uncertainties, affecting uncertainties for the secondary star, and values vary depending on how primary star mass and radius are determined.

Overall, this thesis shows some ongoing areas of interest within transit surveys. I determined how saturated star fluxes in NGTS could be used to search for valuable transiting exoplanets around bright stars. I conducted a survey of relatively bright mid-to-late M dwarfs specifically searching for Earth-sized exoplanets within their habitable zone. While no exoplanets were found, transit injections showed that we were sensitive to these planet sizes around at least some of our targets. I also fitted two low mass eclipsing binaries with the aim of better informing low mass stellar evolutionary models. I find that both secondary stars have potential but increased precision on their primary star properties is still needed.

Abbreviations

MCMC	Markov chain Monte Carlo	BLS	Box Least Squares
RV	radial velocity	SDE	signal detection efficiency
ADU	Analogue-to-Digital Unit	RMS	root mean square
ADC	Analogue-to-Digital Converter	R_{\oplus}	Earth Radius, 6378 km
CCD	Charge-Coupled Device	M_{\oplus}	Earth Mass, 5.972×10^{24} kg
EBLM	low mass eclipsing binary	M_J	Jupiter Mass, 1.898×10^{27} kg
CTL	Candidate Target List	R_J	Jupiter Radius, 71492 km
TIC	TESS Input Catalogue	M_{\odot}	Solar Mass, 1.988×10^{30} kg
ldc	limb darkening constant	R_{\odot}	Solar Radius, 695700 km
CME	coronal mass ejection		
NGTS	Next Generation Transit Survey		
TESS	Transiting Exoplanet Survey Satellite		
NITES	The Near-Infrared Transiting Exoplanet Survey		

Chapter 1

Introduction

1.1 An overview of exoplanet discovery

First exoplanet discoveries

Ancient astronomers noticed how the paths of some ‘stars’ in the sky moved drastically compared to the backdrop of stars. These were named ‘planetes asteres’ by the ancient Greeks or ‘wandering stars’. For thousands of years, the only other planets known in the universe were those visible by eye in our own solar system: Mercury, Venus, Mars, Jupiter and Saturn.

The invention of the telescope allowed Galileo to study the detail of Jupiter and observe its moons. The telescope later enabled the discovery of the outer planets: Uranus in 1781 by William Herschel and Neptune by Johann Gottfried Galle in 1846.

It was not until 1992 when the first planet orbiting another star, known as an exoplanet, was discovered. Wolszczan and Frail (1992) found two exoplanets orbiting the millisecond pulsar PSR 1257+12. Differences in the arrival time of pulses from the pulsar could be fit by Keplerian orbits of planetary mass objects, indicating the first known exoplanets. The first exoplanet orbiting a Sun-like star was found by Mayor and Queloz in 1995 using the radial velocity technique (see Section 1.2.2). The discovery of 51 Peg b had a large impact on the field as this half Jupiter mass planet orbited in just 4 days where theory stated forming such large planets was not possible.

The discovery of such close in planets paved the way for exoplanet detection using the transit method (see Section 1.2.1). The first observation of a transiting exoplanet was of HD 209458 b in 1999 (Charbonneau et al., 2000; Henry et al., 2000), where transit times were predicted from the radial velocity curve. Transit

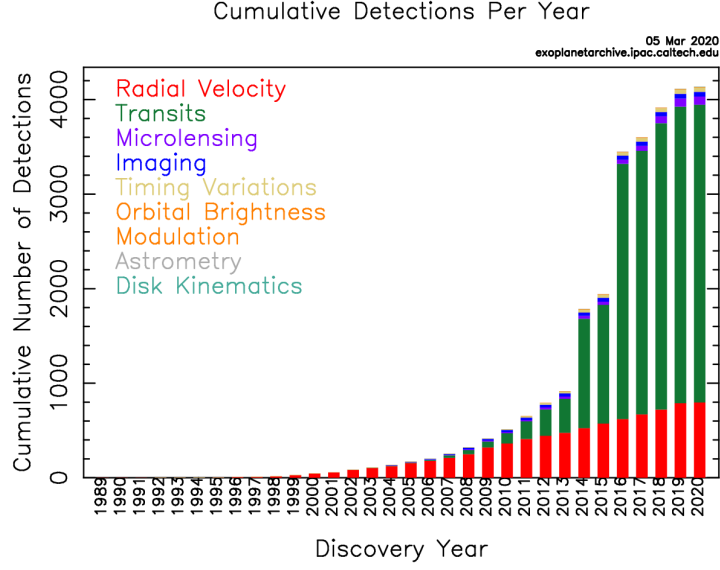


Figure 1.1: Cumulative frequency of exoplanet discovery by year, colour coded by detection method. Figure from the NASA Exoplanet Archive, accessed 09/03/2020.

observations work best for close in planets as they are much likely to pass in front of their star from our view point on Earth. Transit surveys allow telescopes to monitor hundreds or even thousands of stars at the same time, and have dominated the discovery of exoplanets in recent years, see Figure 1.1.

Exoplanet discovery until now

Figure 1.1 shows the number of known exoplanets by year and detection method. To date, 4135 exoplanets have been confirmed or validated (NASA Exoplanet Archive ¹, accessed 09/03/2020). From 1995 to 2013, the radial velocity technique dominated in the discovery of exoplanets. Since the detection of the transit of HD 209458 b, dedicated transit surveys, such as SuperWASP (Pollacco et al., 2006), HAT (Bakos et al., 2004) and Kepler (Borucki et al., 2010) have been very successful, with transit detections accounting for the majority of known exoplanets since 2014. However it should be noted that many Kepler exoplanets have not been confirmed by radial velocity observations due to the faintness of their stars and instead have been validated using statistical techniques to rule out false positives (Morton, 2015). To give a sense of the numbers, only 820 transiting exoplanets out of 2972 have a measured planetary mass (exoplanet.eu, 10th March 2020).

In the following section, the different techniques used to detect exoplanets

¹<https://exoplanetarchive.ipac.caltech.edu/index.html>

are described. For the rest of the introduction, we predominately focus on transit photometry as this forms the basis of this thesis.

1.2 Exoplanet Detection Techniques

A number of techniques have been used for exoplanet discovery. Each are suited to different parameter spaces in terms of distance from their star and exoplanet size, and provide different information on the exoplanet. In terms of exoplanet discovery, the transit and radial velocity techniques have really dominated the field, with 2972 confirmed or validated transiting exoplanets and 812 discovered by radial velocity (exoplanet.eu, 10th March 2020).

1.2.1 Transit Photometry

What is a transit?

If a planet crosses the disk of its host star from the observer’s point of view then this planet is said to transit. The planet blocks out a small fraction of the star’s light every orbit, resulting in a periodic dip in observed flux. If the entirety of the planet’s disk is observed to pass in front of the star’s disk, the drop in flux is given by:

$$\frac{\Delta F}{F} = \frac{R_P^2}{R_*^2} \quad (1.1)$$

Here F is the flux measured from the star out of transit, ΔF is the observed change in flux during transit and the right-hand side is the ratio of the areas of the planet and stellar disks. Hence observing the depth of a transit gives an estimate of the relative radii of the planet and its host star.

System Geometry

We can only observe planets transit when our line of sight closely aligns with the planet’s orbital plane, which occurs for inclinations, $i > i_c$ where:

$$\cos i_c \leq \frac{R_p + R_*}{a} \quad (1.2)$$

as given in Haswell (2010). Figure 1.2 shows the system geometry, with inclination defined as the angle between the orthogonal of the line of sight and the line from the stellar centre to the planet. Typically transiting exoplanets have an orbital inclination very close to 90° , which gives an impact parameter b (as shown

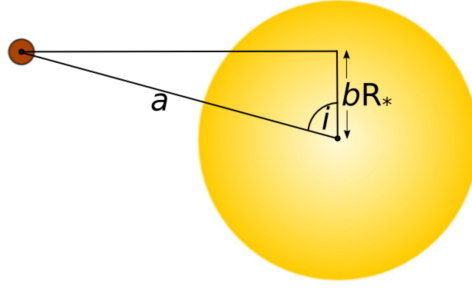


Figure 1.2: Figure illustrating the geometry of orbital inclination. After: <https://www.paulanthonywilson.com>, accessed 09/03/2020.

in Figure 1.2) of 0. Planets at orbital distances very closer to their star, can be observed to transit on a wider range of inclinations.

Light Curve Shape

Figure 1.3 shows an ideal transit light curve observed in a ground-based survey and a model of the transit geometry. The out of transit flux has been normalised to 1. The flux level begins dropping when the planet's disk starts to pass in front of the star (labelled contact 1). The flux level continues to decrease during ingress as the planet crosses the star's limb, until the entirety of the planet's disk overlaps with the stellar disk at contact point 2. In the simple model, the flux level stays constant at its minimum level as the planet moves across the star. In reality, this does not happen due to limb darkening, as discussed below. The difference in flux between the out of transit value and this minimum value gives the transit depth, ΔF . Between contact points 3 and 4, flux increases again during egress as the planet crosses the stellar limb. Halfway between contact points 2 and 3 is the mid-transit time, t_0 .

Limb darkening

In reality, flux does not stay constant between contact points 2 and 3 due to the limb darkening effect. From the observer's point of view, the stellar disk centre is brighter than its edges. Photons emitted in the observer's direction travel radially outwards at the centre of the stellar disk whereas at the limb light has to travel obliquely. This means for the same optical depth and therefore pathlength, light from the centre is emitted from a deeper, hotter layer than at the limb. Hence, the observer sees a greater intensity of light at the centre than the limb. A transiting planet blocks brighter stellar light at the stellar centre than the limb, so observed

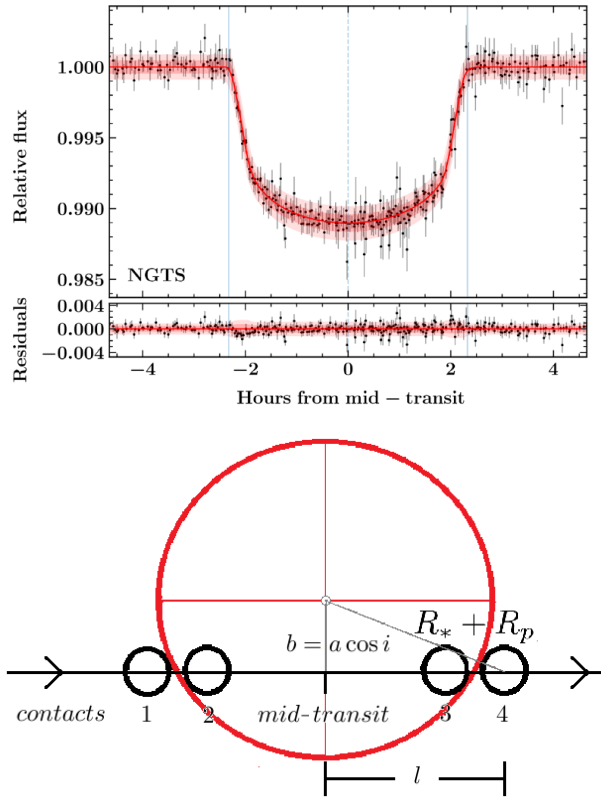


Figure 1.3: Top: Phase folded lightcurve of NGTS 2b, adapted from Raynard et al. (2018). Bottom: Relative positions of planet and stellar disks, showing the four contacts and location of mid-transit. Parameters b , $R_* + R_p$ yield l via trigonometry, giving the transit duration, T_{dur} .

flux continues to decrease until the mid-transit point before slowly increasing again, producing a smooth curved bottom to the lightcurve.

The amount of limb darkening varies by wavelength, structure of the star and detailed stellar composition. The limb darkening effect can only be directly measured for the Sun so models are needed to extrapolate for other stars. The four common limb darkening laws adapted are the linear law, the logarithmic law, the quadratic law and the cubic law.

Transit Duration

For a circular orbit, trigonometry gives the length of transit, l , in terms of b , R_p and R_* , from which the total duration of transit between contacts 1 and 4 is:

$$T_{dur} = \frac{P}{\pi} \sin^{-1} \left(\frac{\sqrt{(R_* + R_p)^2 - a^2 \cos^2 i}}{a} \right) \quad (1.3)$$

Where only one transit is observed, the transit duration can be used to estimate the planet's orbital period, as discussed in Section 2.5.1.

Fitting Light Curves

Based purely on the principal features of the observed light curve: transit depth, total duration of transit and duration of full transit (between contacts 2 and 3), the absolute sizes in the system are unknown. However the principle light curve features are used to define first order estimates which form the seeds of a χ^2 search for unknowns in parameter space. The three dimensionless quantities which describe the system are:

1. Planet-star radius ratio: $\frac{R_p}{R_*} = \sqrt{\frac{\Delta F}{F}}$,
2. Impact parameter $b = a \cos i$, the projected distance between the planet and star at mid-transit,
3. Planet semi-major axis to stellar radius ratio $\frac{a}{R_*}$.

Transits occur periodically, once per planet's orbit. From observing multiple transits we can calculate the orbital period as the time difference between them. The semi-major axis, a , can be found by substituting the period, P , into Kepler's third law and assuming $M_* \gg M_p$:

$$a \approx \left(GM_* \left(\frac{P^2}{2\pi} \right) \right)^{\frac{1}{3}} \quad (1.4)$$

Finding system dimensions

To convert the dimensionless quantities into planet and stellar parameters requires estimating stellar parameters from its spectrum. Spectra are fitted to estimate surface gravity ($\log g$), effective temperature and metallicity. These values are input into stellar evolution models to fit for stellar radius and mass. Stellar radius can then be substituted into Equation 1.1 to find the planet radius. Estimates of physical parameters are found alongside limb darkening coefficients of the adopted limb darkening law. Iterative minimisation of the reduced χ^2 fit must balance fitting to the light curve with the resulting stellar radius agreeing with theoretical models.

Types of planet sensitive to

Transit surveys are most sensitive to close-in planets as inclination arguments mean there is a higher probability they will transit. Planets on short periods transit more often, meaning a transit is more likely to be detected within a given observing season. Planets with relatively large radius ratios compared to their stars produce larger transit depths and the larger reductions in flux are easier to detect. However, this is strongly dependent on the signal to noise ratio, so it is easier to spot smaller transits around brighter stars than faint ones.

1.2.2 Radial Velocity

Planets and their stars orbit the centre of mass in the system, so stellar motion can indicate an orbiting planet. However, whether we can observe the stellar motion depends on the system orientation and the relative masses of planet and star.

The radial velocity technique measures the amount a star's spectrum shifts due to the Doppler effect. Spectra are red shifted as the planet tugs its star away from us and blue shifted as the star is tugged towards us over one orbit of the planet. The semi-amplitude of radial velocity shift (K_*) is related to the relative masses of the planet (m_p) and star (M_*) by (e.g. Perryman, 2018):

$$K_* = \left(\frac{2\pi G}{P} \right)^{1/3} \frac{m_p \sin i}{(M_* + m_p)^{2/3}} \frac{1}{\sqrt{1 - e^2}} \quad (1.5)$$

where P is the planet's orbital period, i is the inclination (as defined in Section 1.2.1) and e is the orbital eccentricity. A circular orbit with zero eccentricity produces a sinusoidal radial velocity shape, with eccentric orbits modulating the shape. The first exoplanet around a sun-like star was discovered using the radial velocity technique. Figure 1.4 shows the radial velocity plot which clearly shows the

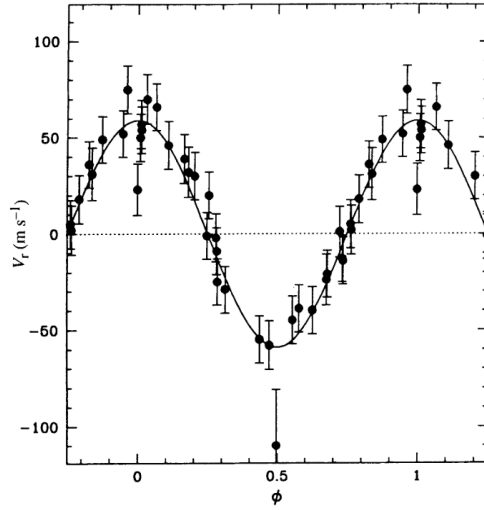


Figure 1.4: Radial velocity curve of 51 Peg phase folded on the period of its planet, 51 Peg b. From Mayor and Queloz (1995).

sinusoidal shape indicating a circular orbit.

In practice, a number of spectra are taken at different orbital phases of a planet's orbit (separations of hours to days for close in planets) and cross correlated against a template spectrum at rest wavelength. The wavelength shift, $\Delta\lambda$, from the template or emitted wavelength, λ_{em} , gives the radial velocity shift, v_r , at different times (as shown in Equation 1.6, e.g. Perryman (2018)).

$$v_r = \frac{\Delta\lambda}{\lambda_{em}} c \quad (1.6)$$

For a single planet, radial velocity measurements alone can estimate five parameters related to the star's Keplerian orbit: eccentricity, planet orbital period, semi-amplitude of radial velocity, the time of periastron passage (i.e. when the planet is closest to the star) and the argument of periastron, ω , the angle between the longitude of ascending node and periastron, as shown in Figure 1.5 (Perryman, 2018). Additionally, two other components are often included: the systemic velocity, the constant radial velocity of the system's centre of mass compared to the solar system, which can also include the radial velocity offset of the instrument, and a linear trend parameter to account for instrumental drift and potentially unidentified massive long period companions.

The radial velocity semi-major amplitudes along with the stellar mass derived from spectroscopy (as detailed in Section 1.2.1), give the minimum planet mass $m \sin i$. As inclination cannot be determined from radial velocity data, the true

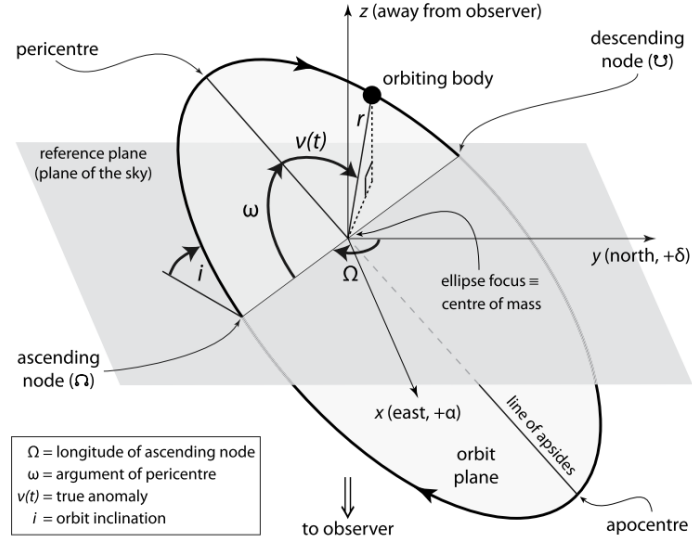


Figure 1.5: Geometry of an elliptical orbit. Note periastron is the pericentre specifically for stars. After Perryman (2018).

planet mass is unknown.

Equation 1.5 shows that the radial velocity semi-amplitude increases for higher planet to star mass ratios and planet inclinations where $\sin i$ is closer to 1. This technique is most sensitive to planets with relatively high masses compared to their stars which orbit at inclinations closer to edge on. Radial velocity measurements are sensitive to a wider range of inclinations than transits. The ability to take radial velocity measurements throughout a planet's orbit, rather than waiting for a transit, which may not occur, means high mass planets have been found at longer periods, on the order of years. Due to these advantages, radial velocity surveys were the most prolific at discovering exoplanets until the Kepler mission (Borucki et al., 2010).

Radial velocity surveys observe one target at a time and have typically targeted bright stars to maximise signal for high precision spectroscopy. In comparison, wide field transit surveys monitor large numbers of stars at once encompassing a range of magnitudes and the brightest stars may not be usable due to saturation. Chapter 3 investigates whether specialised apertures can recover star brightness for one type of saturation. Transits can be detected around fainter stars than radial velocity measurements can be made. As a result, not all transiting planets have radial velocity confirmation, despite favourable orientation, as fainter stellar magnitudes mean the signal to noise in the spectra is too low for high precision spectroscopy.

1.2.3 Direct Imaging

Transit and radial velocity detections infer the existence of a planet from observations of its star. However another method of exoplanet detection is direct imaging, which involves detecting light from an exoplanet independently of its star. The challenges of direct imaging are clear: trying to image a very faint source that is very close to a much brighter one. There are two limiting factors here: the angular separation between the planet and star on the sky and their relative brightnesses.

In principle, planets can either be imaged using light reflected from the star or in their thermal emission. Planets have much lower temperatures, T , than stars and Wien’s displacement law shows that the peak emission for a blackbody is at longer wavelengths, λ , for cooler objects:

$$\lambda_{max}T = 2.897 \times 10^{-3}mK \quad (1.7)$$

This means the planet to star flux ratio is of order 10^{-10} in visible light but increases to 10^{-6} in the mid-infrared (Beichman et al., 1999), meaning a higher proportion of photons come from the planet at infrared wavelengths. However, even at optimum wavelengths, still only 1 in 10^6 photons are emitted by the planet so often a coronagraph is used to block out as much of the star’s light as possible and increase the contrast ratio.

Increased thermal emission from the planet increases the contrast ratio, making planets easier to detect. This makes direct imaging best suited to young giant planets that are still producing thermal emission due to gravitational contraction. As planets can only be detected at large angular separations from their star due to the star’s glare, direct imaging is best suited to planets distant from their stars, on the order of 10s to 100s AU (Perryman, 2018). Angular separation on the sky between star and planet increases when the systems are closer to us, so direct imaging targets nearby stars.

To date, 40 planets with masses less than 13 Jupiter masses (M_J), the approximate mass divide between planets and brown dwarfs (Burrows et al., 1997), have been detected by direct imaging (exoplanet.eu, 10th March 2020). These include the four planet system, HR 8799 (Marois et al., 2008), and planets in debris disk systems such as Fomalhaut (Kalas et al., 2008). Direct imaging surveys are restricted to observing target one star at a time and require large telescope apertures to increase angular resolution and adaptive optics to correct for atmospheric motion. Direct imaging also needs multiple epoch images to confirm a planet changes position over its orbit and that it is not a background object.

1.2.4 Transit timing variations

Transit timing variations (TTVs) are a technique for discovering additional, potentially non-transiting companions in a system hosting a transiting exoplanet. This technique relies on measuring changes in the observed mid-transit time of the transiting exoplanet compared to a fixed orbital period (Agol et al., 2005).

The presence of sufficiently close and massive planets will gravitationally perturb the system, causing the mid-transit time of the transiting exoplanet to appear early or late. The effect is amplified for planets in resonant orbits where one planet completes exactly x orbits in the time another planet completes exactly y orbits, causing TTVs of up to several minutes, which vary in a sinusoidal trend over a number of orbits.

Currently there are 13 exoplanets in 12 systems discovered using TTVs (exoplanet.eu, 10th March 2020), the first in 2016 by Mancini et al..

1.2.5 Microlensing

Gravitational microlensing is an effect of general relativity. Light rays from a source are deflected by the gravitational potential of a foreground star (the lens), causing magnification and distortion of the background star. This occurs due to extremely precise alignment (~ 1 milliarcseconds, mas) between the observer, source and lens. During this chance alignment, the lens star magnifies the background star over the period of hours, days or weeks, as shown in Figure 1.6. If the lens star has a planet, this introduces additional magnification, distorting the smooth magnification profile. The distortion shape depends on the planet's orbit and relative masses of the lens star and planet.

As the chance of a microlensing event occurring for a given star is so small, microlensing campaigns such as OGLE (Optical Gravitational Lens Experiment, Udalski, 2003)) monitor large numbers of stars at a time. The lensing probability increases for densely packed regions of stars, so they monitor the galactic bulge. There are 99 confirmed microlensing exoplanets with masses less than $13 M_J$ (exoplanet.eu, 10th March 2020).

Microlensing has the advantage of sensitivity to low mass exoplanets at several AU, filling a complementary part of the exoplanet mass and radius diagram. It is also sensitive to more distant stellar systems. One of the main disadvantages of microlensing is that the chance alignment occurs only once, so confirmation and follow up observations after the event are limited. The other limitation is the degeneracy between the lensing and lensed mass meaning multiple solutions are found for

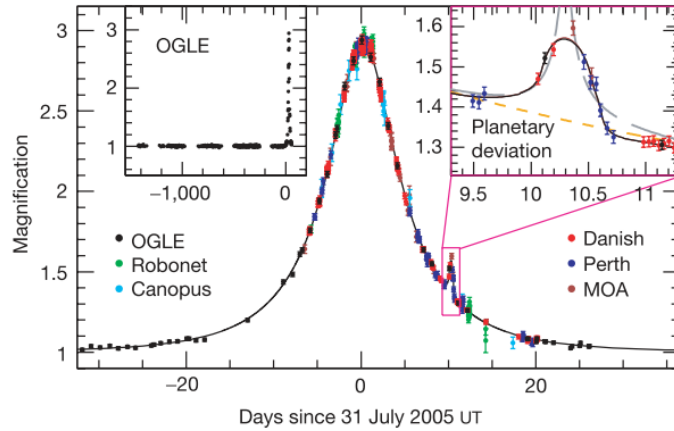


Figure 1.6: Lens magnification of the background star in OGLE-2005-BLG- 390L (Beaulieu et al., 2006). Detail of the distortion due to the lens star’s $5.5 M_{\oplus}$ planet at 2.1 AU is shown in the inset.

the relative masses in the lensed system which can affect whether we are observing a planet or not.

1.2.6 Astrometry

Astrometry measures the change in stellar position on the sky due to reflex motion from its orbiting planet. While radial velocity is sensitive to the motion towards and away from us, astrometry is sensitive to exoplanets which orbit face on. The positional changes are of order $1 \mu\text{as}$ to 1 mas (Perryman, 2011). There are two planets with masses less than $13 M_J$ discovered using astrometry (exoplanet.eu, 10th March 2020). The discovery of exoplanets using astrometry is expected to come into its own with future data releases from The Gaia space mission Gaia Collaboration et al. (2016). Gaia is expected to find 21,000 high mass, long period exoplanets in its nominal 5 year mission, including 25-50 with periods of 2-3 years (Perryman et al., 2014).

1.3 Wide field transit surveys

The first exoplanets observed to transit were planets discovered by radial velocity. These exoplanets were hot Jupiters, approximately Jupiter mass planets with orbital periods of a few days to weeks. Characterising an exoplanet by radial velocity measurements will constrain when a transit will occur, and approximately 10 % of

randomly inclined hot Jupiters will transit, as transit probability on a circular orbit is stellar radius as a function of planet semi-major axis (Borucki and Summers, 1984). While radial velocity instruments are limited to observing one target at a time, photometric surveys can observe many targets, with the number limited by the field of view and the ability to obtain enough signal for sufficient photometric precision. Photometric surveys can also use commercially available equipment, making instrumentation cheaper.

Transit searches

When searching for transiting planets, we do not know if and when around a given star they will transit. To maximise the number of planets, wide angle surveys, such as WASP (Pollacco et al., 2006), simultaneously survey tens of thousands of relatively bright stars for months. After observing, data is processed: an astrometric solution is found, and magnitudes and errors calculated. When the season ends, implementations of Sysrem (Tamuz et al., 2005) remove correlated systematic errors, and other trends can be removed using the Trend Filtering Algorithm (TFA) (Kovács et al., 2005). After processing, possible transits are identified using the Box Least Squares algorithm (BLS, Kovács et al., 2002), as discussed in Section 2.4.3. False positives, including stellar binaries, are then eliminated as discussed in Section 1.5.1. Light curve models and a description of limb darkening are used to estimate candidate parameters. Only the most promising candidates are confirmed using radial velocity measurements, with one observation ruling out double-lined binaries and fast rotators, and a second to reject narrow single lined binaries. Host star parameters are then found using radial velocity diagnostic spectral lines and evolutionary models, as discussed in Sections 1.2.1 and 5.5.1 and planetary parameters from a χ^2 combined fit to photometric and radial velocity data.

The main noise limitation from space is stellar surface structure, e.g. star spots, the extent of which is greatly affected by spectral type. Ground observations are most limited by changing atmospheric transparency, which reduces photometric precision. This can be partially corrected in real time using adaptive optics.

WASP

The Wide Angle Search for Planets (WASP) is a transiting exoplanet survey which achieved first light in 2003. It consisted of two observatories: SuperWASP-N at La Roques Observatory in La Palma and SuperWASP-S at SAAO. Together these sites cover a large fraction of the sky, with declinations from -90 degrees to 60 degrees.

Each SuperWASP observatory has 8 wide angle cameras on a single mount, with a combined field of view of 482 deg^2 (Pollacco et al., 2006), with a pixel scale of 13.7 seconds. The instrument uses 200mm f/1.8 telephoto lenses and exposure times are 30 seconds. The wide angle cameras enable SuperWASP to monitor many stars at once, increasing the likelihood of observing a transit. SuperWASP was designed to survey the sky and identify transit amplitudes with $\delta V \sim 0.01$, i.e. hot Jupiters around main sequence FGK dwarfs. The instruments have a wide spectral response over visible light (400-700 nm), making it suitable for solar-like stars.

Initially, the cameras cycled between several fields on a given night to maximise the number observed. However, the observing strategy was later changed to sit on a given field throughout a night’s observations to improve the data precision.

The confirmed exoplanets orbit bright stars ($9 \leq V \leq 13$) which are amenable to radial velocity confirmation. Bright stars are also amenable to further follow up observations, such as transmission spectroscopy (see Section 1.5.2), increasing our understanding of these systems. 181 WASP exoplanets have been published² making it the most successful ground-based transiting exoplanet survey.

NGTS

The Next Generation Transit Survey (NGTS) is a transiting exoplanet survey based at the ESO Paranal observatory in Chile (Wheatley et al., 2018). It has twelve 20cm aperture telescopes, each with a field of view of 8 deg^2 , giving a combined field of view of 96 deg^2 . The pixel scale is 5 arcseconds, allowing higher spatial resolution than wide-field transit surveys including SuperWASP and TESS with larger pixel scales, meaning reduced contamination within a pixel by additional stellar sources.

The NGTS survey strategy involves manually selected survey fields for all telescopes, typically with up to 15,000 stars brighter than I band magnitude of 16, of which at least 70% are dwarf stars (Wheatley et al., 2018). Selected fields are usually more than 20 degrees from the Galactic plane to avoid crowding. A given telescope observes the selected field for the season, every night while the field is 30 degrees above the horizon. Pre-assigned fields are spaced so two fields are observed on a given night. The telescopes may observe a contiguous area, with typical 3% overlap between fields but this is not necessarily the case. 10 second exposures give a detection limit close to I magnitude of 16. Many stars have fractional RMS noise values below 1 mmag (in one hour binned exposures), with stars fainter than the scintillation limit at $I \sim 12.5$, achieving comparable photometric precision to TESS (Wheatley et al., 2018; Ricker et al., 2015).

²<https://wasp-planets.net/wasp-planets/>

High photometric precision is achieved by each telescope being on its own mount, precise autoguiding and high quality CCD cameras. The high photometric precision of NGTS means it is sensitive to smaller planets than SuperWASP, e.g. NGTS-4 b is Neptune-sized (West et al., 2019), and can detect planets around fainter stars.

NGTS uses red-sensitive cameras, making it more sensitive to late K and early M dwarfs (Wheatley et al., 2018). Indeed, the first exoplanet announced by NGTS, NGTS-1b, is a hot Jupiter around an early M dwarf (Bayliss et al., 2018), and challenged planet formation mechanisms as the most massive planet found around an M dwarf.

As of 10th March 2020, 9 exoplanets have been published and one brown dwarf, alongside studies of eclipsing binaries, stellar flares and open clusters.

TESS

The Transiting Exoplanet Survey Satellite (TESS) was launched in April 2018, before beginning science operations in July. In its primary mission, TESS will survey most of the sky, observing 13 strips in each hemisphere for 27 days each (Ricker et al., 2015). The four cameras each monitor a field of 24x24 degrees, have lenses with diameter 10.5cm and pixel scales of 21 arcseconds. Continuous 2 second exposures are produced, which are summed to give 2 minute exposures. Preselected stars are downloaded to give exposures with 2 minute cadence, whereas full frame images have 30 minute cadence.

The mission’s main aim to discover 50 small exoplanets (less than 4 Earth radii) with measurable mass (Stassun et al., 2019). Compared to NASA’s previous space exoplanet mission, Kepler, TESS has red sensitive cameras, with a spectral response function corresponding to 600-1000nm (Ricker et al., 2015). This makes TESS more sensitive to red dwarf stars, which are brighter at redder wavelengths. Focusing on smaller red dwarf stars makes rocky planets easier to detect as they produce a deeper transit signal.

TESS is also focusing on the brighter stars, specifically on a preselected catalogue of stars: the Candidate Target List (CTL). Brighter stars are more amenable to radial velocity follow up, allowing determination of planet masses and helping TESS fulfill its primary aim. Data for targets in the CTL are downloaded at 2 minute cadence, with the full image downloaded at 30 minute cadence. The CTL includes all stars in the TESS Input Catalogue (TIC) which are brighter than TESS magnitude of 13 and with radii of less than $5 R_{\odot}$ (Stassun et al., 2018). The most recent version is TICv8 (Stassun et al., 2019), used in this work.

TICv8 also includes version 2 of the Cool Dwarf Catalogue (Muirhead et al., 2018; Stassun et al., 2019), which incorporates Gaia DR2 astrometric parallax and photometric measurements. The Cool Dwarf Catalogue 2 includes stars with $V - J$ colour greater than 2.7 and *Gaia* G_{RP} band magnitude of less than 18 (Stassun et al., 2019). The Cool Dwarf Catalogue corresponds to stars with effective temperatures of less than 4000 K, i.e. late K and M dwarfs.

As of 10th March 2020, TESS has discovered 41 confirmed exoplanets ³. These exoplanets have radii ranging from 0.7-17 R_{\oplus} orbiting stars with radii 0.17-2.9 R_{\odot} (Kostov et al., 2019; Huber et al., 2019). Of these, 3 exoplanets orbit 2 stars with radii less than 0.2 R_{\odot} (Crossfield et al., 2019; Vanderspek et al., 2019), corresponding to mid-to-late M dwarfs. Most exoplanets found by TESS orbit stars with earlier spectral types: early M- late F dwarfs.

1.4 Targeted Surveys

While wide-field surveys have the advantage of monitoring large numbers of stars at a time, targeted surveys can be complementary to them, targeting specific types of stars. A number of surveys have targeted M dwarfs as these targets are of great interest (see Chapter 4) and sufficiently bright M dwarfs are distributed across the sky.

MEarth

The MEarth project’s aim is to discover transiting exoplanets around close mid M dwarfs (Irwin et al., 2009b). Specifically they survey 2000 nearby ($d \leq 40pc$) M dwarfs with $R_* \leq 0.33R_{\odot}$ with the goal of detecting rocky planets transiting in the habitable zone. MEarth has two observing sites, one in each hemisphere: Fred Lawrence Whipple Observatory on Mount Hopkins in the north, and Cerro Tololo Inter-American Observatory in Chile in the south. Each observatory has eight independent robotic telescopes of 40cm diameter. The field of view is 25x25 arcminutes and the pixel scale is 0.75 arcseconds. MEarth increases its sensitivity to M dwarfs using red sensitive CCDs with a custom filter determining the lower limit of 700 nm and a red limit determined by the quantum efficiency of the CCD (~ 1050 nm) (Nutzman and Charbonneau, 2008), giving a similar passband to the Cousins I filter (Irwin et al., 2009b). The survey design allows different exposure times for different targets.

³<https://tess.mit.edu/publications/>

To maximise the number of observed targets on a given night, MEarth cycles between a list of targets, taking photometric measurements every 20–30 minutes (Irwin et al., 2009b, 2014). High cadence observations are triggered in real time if a reduction in flux is recorded, to determine if it is a transit event or a false alarm.

MEarth has discovered three exoplanets to date, including the highly studied super Earth GJ1214 b orbiting a $0.2 R_{\odot}$ star (Charbonneau et al., 2009). MEarth has also been used for the confirmation of exoplanets discovered by other telescopes and for measuring stellar rotation periods.

TRAPPIST

TRAPPIST is another targeted survey of M dwarfs which uses two robotic 60cm telescopes, TRAPPIST-South at La Silla Observatory in Chile (Gillon et al., 2011) and TRAPPIST-North at Oukaïmeden Observatory in the Atlas Mountains in Morocco. The telescopes have a field of view of 22×22 arcminutes and a camera pixel scale of 0.64 arcseconds. The survey targets 50 of the brightest ultracool dwarfs ($T_{eff} \leq 2700$ K). Each target is observed continuously over the course of a night and at least 100 hours of observations are obtained, with around 40 targets observed by TRAPPIST-South between 2011 and 2017. The TRAPPIST-South telescope was designed as a prototype for SPECULOOS (Delrez et al., 2018)

This survey detected transits around the M8 dwarf Trappist-1 (Gillon et al., 2016) mostly using an I+z filter (with $> 90\%$ transmittance between 750–1100 nm). Follow up observations revealed a compact system of seven transiting Earth-sized planets orbiting within 19 days, with three planets in the habitable zone (Gillon et al., 2017). The discovery of this system has spurred many papers and allowed investigation into the dynamics and evolution of exoplanets around a late M dwarf star.

1.5 Confirmation of Transiting Exoplanets

The rest of this paper focuses on exoplanets discovered using transit photometry. This and the following sections discuss why transit candidates from transit surveys need confirmation and some of the false positives that can resemble transiting exoplanets.

Transiting signals detected in transit surveys are considered candidate exoplanets until a measurement of their mass can be obtained. In most cases, these candidates are confirmed using radial velocity measurements. Spectra are taken at several points over the planet’s orbital period from transit observations and the

amplitude of the radial velocity shift is measured to find relative masses of the two objects. The radial velocity method can confirm whether transits are caused by a planet or one of the false positive scenarios discussed in the next section.

Where a star is too faint for radial velocity measurements but contains multiple exoplanet candidate planets, these can sometimes be confirmed by measuring transit timing variations (TTVs). Deriving mass constraints from TTVs is less precise than using radial velocity measurements but can still be useful. Trappist-1 is one case where the star is too faint for radial velocity measurements but planet confirmation and constraints on their masses were achieved using TTVs in this seven planet system (Grimm et al., 2018).

1.5.1 False positives

A number of objects cause false positives in transit surveys: these signals look like transiting exoplanets but are caused by other objects. These false positives include eclipsing binaries, giant stars, blended signals and low mass eclipsing binaries (EBLMs). I discuss how they can be mistaken for transiting exoplanets and how they can be distinguished.

Eclipsing binary

Most astrophysical false positives in a transit survey are due to eclipsing binaries. In a binary star system, if the orbital plane is aligned with our line of sight, we can see the stars eclipsing. For example consider a binary system where star A is larger than star B. If star B passes in front of star A from our point of view, then it will block out a portion of star A's light, causing a reduction in light. Eclipsing stars can be identified from their much deeper eclipses, as the relative sizes of the stars are more similar. Another telltale sign is the observation of a secondary eclipse, where star B passes behind star A, leading to another reduction in flux. If the stars have similar sizes and brightness, then the eclipses can be a similar depth, which can be mistaken as an eclipsing object on half the true period, and therefore for a planet if the inclination is sufficiently low. Eclipsing binaries produce V-shaped eclipses without a flat bottomed lightcurve, and may produce phase dependent ellipsoidal variation which can be identified in higher resolution photometry. If none of these measures are sufficient to determine whether the eclipsing object is a star, one spectrum will identify double lined eclipsing binaries and fast rotators and spectra observed at both quadratures (phases 0.25 and 0.75) will identify large radial velocity shifts.

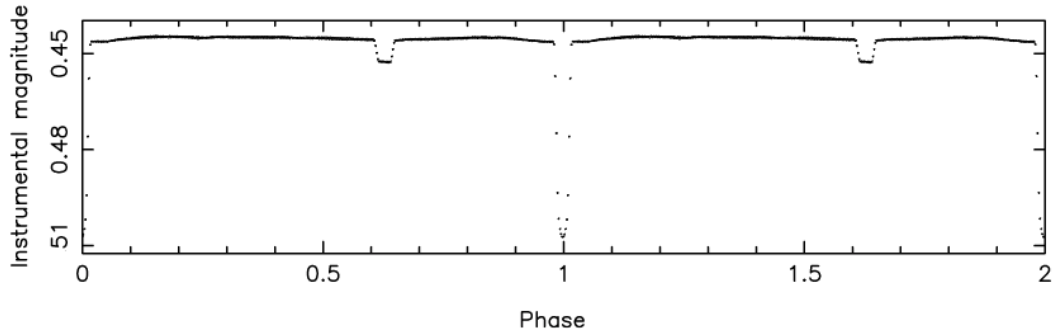


Figure 1.7: Example eclipsing binary light curve from Kepler showing a deep primary eclipse and clear secondary eclipses. From Prsa et al. (2011).

Giant star

Transit lightcurves give only the radius ratio between the transiting object and its star. If the star is a giant, then a 1 % transit depth is too deep to be caused by transiting exoplanet. Therefore, external information is required to determine the approximate radius of the star and therefore the type of object transiting it.

A star's nature can be estimated by examining external catalogues: photometric catalogues provide the magnitudes in different passbands and astrometric catalogues can estimate its proper motion. Closer stars have higher proper motion (relative motion of a star against the background of stars). Plotting proper motion against colour enable possible giant stars to be identified by their redder colours and lower proper motion. The spectral type can be estimated by comparing the best SED fits, one assuming the star is on the main sequence and another that it is a giant. If catalogue data is insufficient, then observing the star's spectrum will confirm if it is a giant. However this requires spectroscopic data which is a particularly limited resource for transit survey projects.

The Gaia space mission (Gaia Collaboration et al., 2016) has been performing the most detailed astrometric mapping of 100 billion stars across the sky since 2014. Since the release of Gaia DR2 data (Gaia Collaboration et al., 2018), identification of likely giant stars is significantly more straightforward. Stars brighter than G magnitude = 17 and temperatures 3000–10000 K have calculated radii in Gaia DR2 (Gaia Collaboration et al., 2018), which encompasses most stars targeted in transit surveys. For fainter stars or where this information is missing, a Hertzsprung-Russell diagram can be plotted to indicate whether the star is likely a giant.

Blended eclipsing binary

Transit surveys tend to have large fields of view, so there may be more than one star on a pixel, or very close by on the sky. If an eclipsing binary system produces eclipses near to a bright single star, these eclipses are blended and appear shallower, and may be mistaken for transits around the brighter star. These are called blended eclipsing binaries. Blended eclipsing binaries have been identified with follow up photometric observations at higher resolution, where individual pixels cover a smaller sky area. At the expected transit time, the transit is not observed on the target star, but may be on a fainter nearby star. Alternatively, spectroscopic follow up does not detect the radial velocity signal of a planet on the target star.

To help identify these false positives before follow up observations, centroiding analysis has been developed. Thanks to its very precise autoguiding, (McCormac et al., 2013), NGTS can use centroiding to identify blended eclipsing binaries before follow up observations. Centroiding analysis measures the x, y pixel coordinates of the centre of light (Günther et al., 2017). If a transit occurs on the target star, the flux level will drop during transit but the centroid will not shift. However, if the apparent transit is caused by a blended eclipsing binary, the centroid will shift coinciding with the apparent transit. This is because less light comes from eclipsing binary during transit so the centre of light shifts in the opposite direction to the eclipsing binary, towards the target star. Günther et al. (2017) detect centroid shifts with average precision of 0.75 milli-pixel for an NGTS pixel size of 4.97 arcsec.

Low mass eclipsing binaries (EBLMs)

The largest exoplanets have radii 1.5–2 times that of Jupiter. However, late M dwarf stars have similar radii, so the transit of a large exoplanet and a small star will produce similar depths. Whether the eclipsing object is a small star or a large exoplanet is distinguished by determining its mass using radial velocity measurements. Low mass eclipsing binaries (EBLMs) are binary systems consisting of a low mass star eclipsing a solar type star. The much larger mass of an EBLM eclipse will produce radial velocity shifts of order km/s, compared to 100s m/s for a hot Jupiter. While identified as a false positive in transit searches, EBLMs are valuable systems for determining the properties of late type stars. EBLMs are discussed further in Chapter 5.

1.5.2 Follow up observations

Transmission and emission spectroscopy

Transit photometry and radial velocity measurements used in discovery and confirmation of an exoplanet provide bulk properties of the planet including its radius, mass, density, period and effective temperature. Additional information can be found by looking at the exoplanet’s atmospheric composition, which can give insight into how planets formed and have evolved.

Transmission spectroscopy is an observational technique to infer information about the atmospheres of known transiting exoplanets. During transit, the star’s light passes through the exoplanet’s nightside atmosphere where some wavelengths are absorbed more than others, leading to wavelength dependent transit depths. This signal increases for larger atmospheres, where the annular region of the atmosphere observed during transit, is often given as $5H$, where H is the scale height (Perryman, 2011). Scale height can be calculated using Equation 1.8, where k is the Boltzmann constant, T_{atm} is the planet’s atmosphere temperature, μ_{mol} the mean molecular weight and g_p the planet’s surface gravity. Therefore the greatest signal occurs for hot Jupiters, being gas planets with hot, low mass atmospheres inflated by high irradiation from their close star. However this signal is still small. The first detection of an exoplanet atmosphere, that of $V = 7.6$ mag HD 209 458 b, found the additional dimming by sodium was deeper by just $2.32 \pm 0.57 \times 10^{-4}$ compared to adjacent bands (Charbonneau et al., 2002). Transmission spectroscopy is limited to brighter stars where sufficient photons can be captured for a signal to noise high enough to distinguish the change in absorption between adjacent wavelengths.

$$H = \frac{kT_{atm}}{\mu_{mol}g_p} \quad (1.8)$$

Emission spectroscopy is used to observe an exoplanet during secondary eclipse. It is complementary to transmission spectroscopy, as it observes the dayside atmosphere of an exoplanet. Emission spectroscopy can be used to indicate the temperature profile of the exoplanet with height and measure the dayside temperature. The temperature difference between the dayside and nightside of an exoplanet can also indicate atmospheric dynamics as large differences indicate low heat redistribution, e.g. in WASP 19 b (Gibson et al., 2010) and low differences indicate efficient heat distribution, e.g. in HD 189733 b (Grillmair et al., 2007).

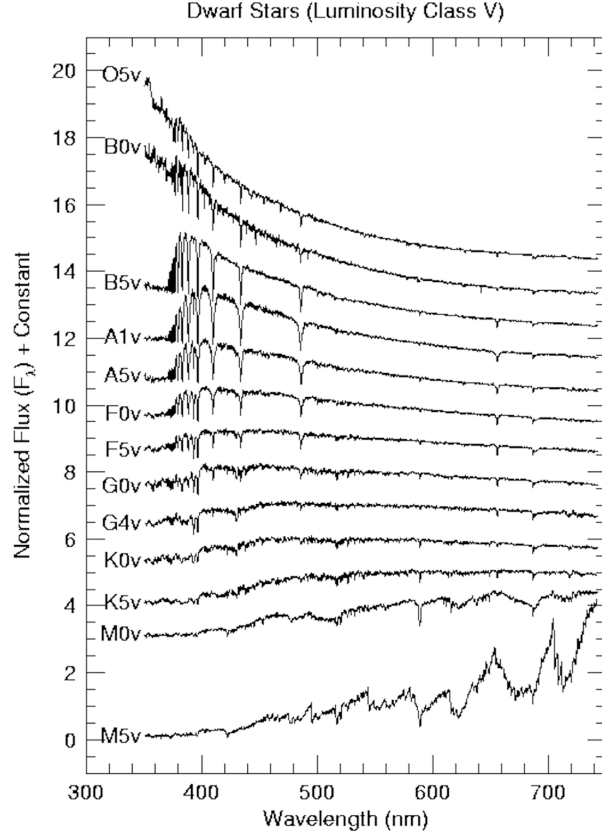


Figure 1.8: Comparison of the spectral energy distribution of different spectral types as indicated in the figure. After: <http://www.astronomy.ohio-state.edu>, accessed 01/06/2020.

1.6 M dwarfs

M dwarf stars sit at the bottom of the main sequence, with masses ranging from approximately 0.08 to $0.55 M_{\odot}$ (Pecaut and Mamajek, 2013). Figure 1.8 shows example spectral energy distributions for different spectral types throughout the main sequence. Stars broadly emit as blackbodies according to Planck’s law. For later spectral types, Wien’s law shows that as the effective temperature decreases, the peak wavelength of emission increases. While the Sun (5800 K) peaks at 500 nm, an early M dwarf (M0) with temperature 3800 K peaks at 750 nm and a late M dwarf (M8) with temperature 2700 K, peaks at 1050 nm. This motivates the use of red sensitive cameras when observing M dwarfs to maximise the observed signal. In Chapter 4, the M dwarfs studied have spectral types M5–M8, covering effective temperatures 2722 – 3025 K, masses 0.10 – $0.17 M_{\odot}$ and luminosities 0.001 – $0.003 L_{\odot}$.

1.7 Key questions to address

A theme in this thesis is what can transit surveys tell us about M dwarfs, as both companions to more massive stars and their planetary systems? This is accompanied by a study of saturated stars in a survey designed to detect transits around K and M dwarfs. Key questions addressed by this thesis are:

- Can saturated stars be included in transit searches? Specifically, can we recover photometry of stars which are saturated in transit surveys so we are sensitive to transiting exoplanets around them? This is a challenge in wide-field surveys optimised to observe a maximum number of useful targets but where the brightest stars, which make the most valuable targets for more detailed follow up observations, are saturated. Chapter 3 investigates saturated stars in the Next Generation Transit Survey to see if sufficiently precise photometry can be recovered by using custom apertures, which includes investigation into whether charge is conserved.
- Can we find transiting exoplanets in the habitable zones of mid-to-late M dwarfs in a dedicated survey with a red sensitive camera? What planet sizes and orbital periods are we sensitive to? How might the habitability of these exoplanets be impacted by flares from their close stars? Mid-to-late M dwarfs are currently the best opportunity for detecting terrestrial planets in the habitable zone, making any planets around them of great interest. However, few have been found due to their inherent faintness, which requires dedicated surveys to discover more. Chapter 4 presents the results from a dedicated survey of a small group of mid-to-late M dwarfs using the Near-Infrared Transiting ExoplanetS (NITES) telescope, which has a red sensitive camera. From this, we can place some constraints on our sensitivity to Earth and Neptune-sized planets around them. The chapter also investigates the effect of the observed flaring rate on exoplanets which may exist around these stars.
- What are the properties of M dwarf stars in low mass eclipsing binaries (EBLMs)? How do the properties of these stars vary between short and long period systems? There has long been an inconsistency between the observed and theoretical properties of M dwarf stars. Observing these stars in EBLM systems can help constrain the observed properties of M dwarfs but more data points are needed to allow comparison with models. In Chapter 5, two EBLM systems from *SuperWASP* are characterised, one short and the other long period, and compared to theoretical models to determine their consistency.

Chapter 2

Methods

2.0.1 CCD cameras and saturation

How CCDs work

Many astronomical cameras use charge coupled devices (CCDs) as their detectors. All three science chapters in this thesis make use of photometric data taken using CCDs. Each pixel in a CCD array captures photons and the light received is converted into a digital signal that can be read by a computer. The rain bucket analogy for how CCDs work is shown in Figure 2.1. The falling rain is analogous to the incoming photons from a star, while the rows and columns of buckets filling up with rain represent the pixels receiving photons during an exposure. Once the exposure is finished, the water from each bucket is transferred to the bucket on their right, with the rightmost buckets in each row transferring their water to the readout array/ serial register. Each bucket on the readout array in turn transfers its water to the measuring cylinder so the amount of water in each bucket, representing the amount of photons in each pixel, can be measured. The readout process continues with the newly rightmost bucket in each row transferring their water to the readout array to be measured, until all buckets have been measured. The final result is a 2D array of amount of rainfall across the field.

Real CCDs are made of silicon. Incoming photons within the right energy range hit the silicon, producing a charge within a pixel due to the photoelectric effect. The band gap energy of silicon corresponds to the photon energy or wavelength that the CCD can absorb and therefore detect. Photon absorption excites a lower energy valence band electron into the conduction band so it is ‘free’. Subpixel electrodes called gates are supplied with a positive voltage to hold the freed electrons in place during the exposure as neighbouring gates with a less positive charge creates a

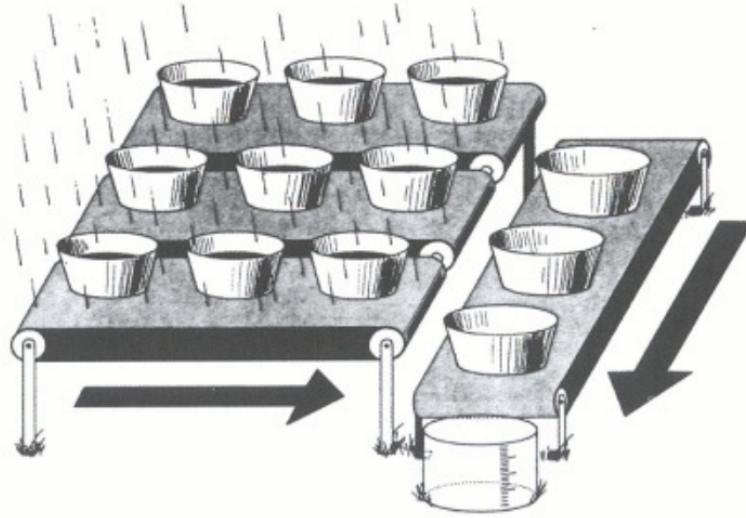


Figure 2.1: The rain bucket analogy for how CCDs work where the rain represents photons and the buckets the pixels. From Janesick and Blouke (1987).

potential well and prevents electrons moving into neighbouring pixels. Once the exposure is complete, clock voltages are cycled to transfer the charge in each pixel to the readout array in turn, to be read.

The charge collected in each pixel is measured as the difference in voltage from a set value before being amplified and converted to a digital number in ADUs (analogue-to-digital units) by an analogue-to-digital converter (ADC). The amount of voltage or electrons needed to produce 1 ADU is the device's gain (given in electrons/ADU). This means for example that if 1876 electrons were detected and the gain was $10\text{ }e^-/\text{ADU}$ then the output would be 188 ADU (note only integer ADU values can be recorded so these are rounded).

CCDs have revolutionised astronomy, as the incoming flux is linear to the output signal over a wide range of photon intensities. Previously the use of photographic plates was common place which are non-linear and have much lower sensitivity requiring long exposure times. CCDs have much higher quantum efficiencies (QE), the ratio of incoming photons to photons detected in the device, with quantum efficiencies peaking at $>90\%$ (Howell, 2006), much higher than even hypersensitised photographic plates ($<10\%$). CCDs also are much more able to observe at redder wavelengths ($>700\text{ }\mu\text{m}$) with higher quantum efficiencies due to silicon's energy sensitivity range.

Linearity and Saturation

CCDs respond linearly over a large range of values so the input is directly proportional to the output signal. However, beyond a certain value the CCD will suffer from non-linearity and in some cases saturation. This is particularly relevant in the investigation of the NGTS camera saturation limits in Chapter 3. The maximum output value that a CCD can produce is set by the number of bits in the ADC: NGTS has a 16-bit ADC meaning it can handle flux values up to 2^{16} or 65535 ADU. This is shown as the A/D saturation level in Figure 2.2. Another type of saturation occurs beyond a certain input as the pixel well becomes full. This means that the potential well already contains so many electrons that it can no longer provide a strong enough attraction for more incoming electrons, so these can ‘bleed’ into neighbouring pixels, creating bright streaks away from the saturated pixel(s) in opposite directions. In Figure 2.2, non-linearity begins at 1.17×10^5 photons or 26000 ADU, still within possible output ADU values. Most professional CCDs reach saturation before the non-linear regime begins (Howell, 2006).

2.1 Image processing

Before scientific photometric measurements can be made using CCD data, frames need to be processed. In Chapter 4, I correct for the bias, dark current and interpixel sensitivity variations in the CCD, and in Chapters 3 and 5, these steps are accounted for in the pipelines the data I use have been processed through.

2.1.1 Bias

Bias frames are a 0 second frame taken without exposure to light, to measure the zero noise level of a CCD. Measuring all pixels in a bias frame will give a mean flux value of 0 with a small gaussian distribution due to readout noise. In practice, negative values are undesirable as it requires using a bit number in the Analogue-to-Digital Converter to represent the negative sign, reducing the overall dynamic range, i.e. the ability to differentiate between input photoelectrons (Howell, 2006). Negative values are avoided by applying a positive bias voltage across the CCD, shifting all measured fluxes to positive values. As the bias is affected by the read noise (faster readout causes higher readout noise), the same readout speed should be used for bias and science images.

For photometric survey observations, multiple bias frames are taken every night, and combined to produce the master bias frame. This master bias is the

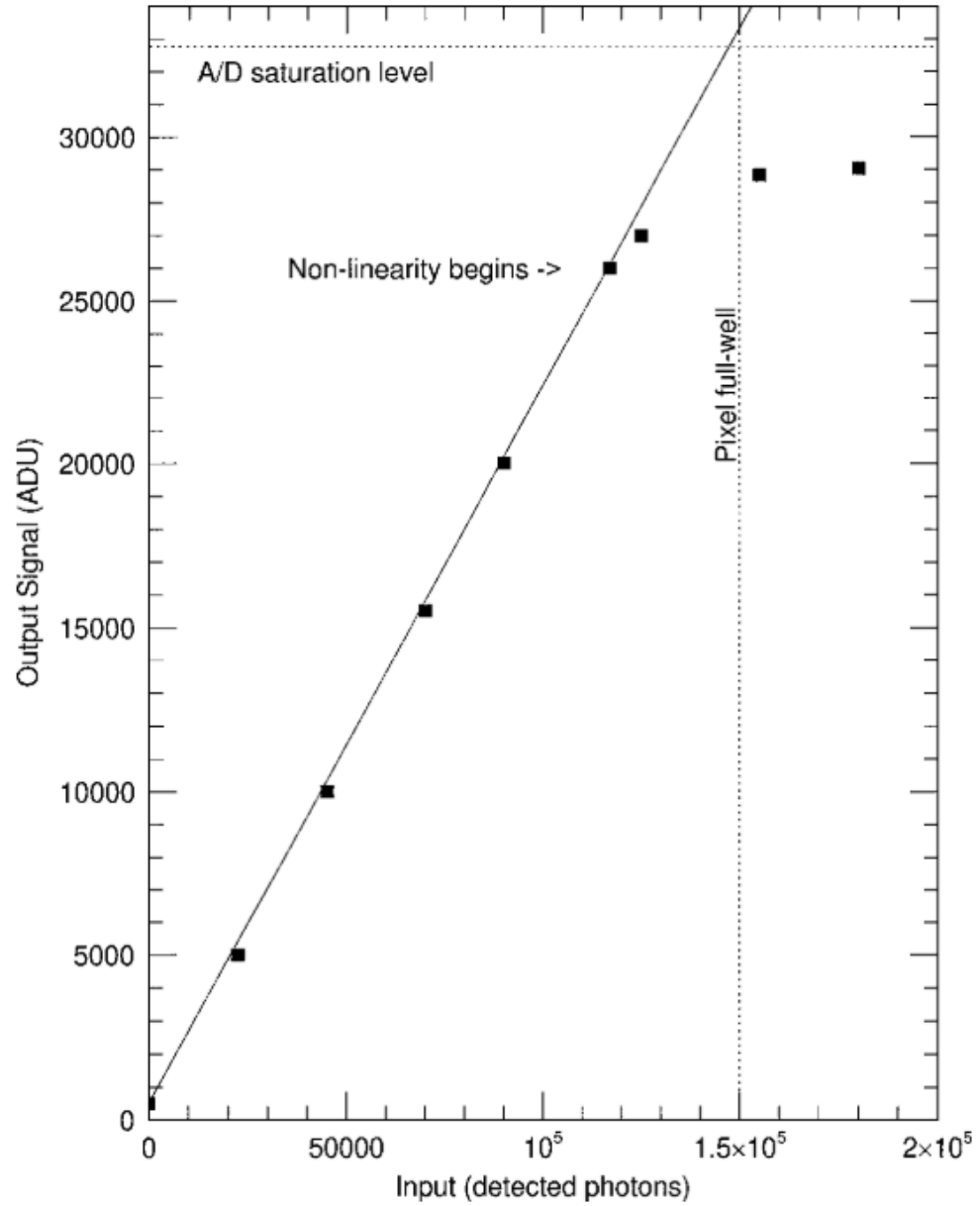


Figure 2.2: The linearity response of a typical CCD. This example has ADC (or A/D) saturation at 32767 ADU (a 15-bit ADC). The full well capacity is 150,000 electrons. A gain of $4.5 \text{ e}^-/\text{s}/\text{ADU}$ means ADC saturation occurs at $32767 \times 4.5 = 147451$ photons and pixel saturation at $150,000/4.5 = 33,333$ ADU. From Howell (2006).

average or median of all frames and eliminates cosmic rays, read noise and random fluctuations found in individual frames.

2.1.2 Dark

Dark frames are similar to bias frames with a closed shutter but have non-zero integration times. These record the dark current caused by electrons freed from the CCD silicon valence bands due to thermal agitation, as opposed to electrons induced by photons from the target. The amount of dark current is strongly dependent of the CCD temperature, which is why astronomical CCDs are often cooled (e.g. NITES operates at -40°C and NGTS at -70°C). The dark frames include the bias as well as the thermal image so are bias-subtracted before combination. Dark frames should be taken using the same exposure time as the science frames to measure the dark current accumulated during that time. If dark frames have a different exposure time they can be scaled to the exposure time of the flats and science images.

Master darks are the median of individual bias-subtracted dark frames. They allow identification of any bad or ‘hot’ pixels to avoid locating targets of interest on.

2.1.3 Flat

Flat fields measure the pixel-to-pixel sensitivity variations (due to varying gain or quantum efficiency) of the detector and location of any dust in the optical path. As the effect of dust and quantum efficiency are wavelength dependent, flats should be taken using the same filter as for observation (Howell, 2006). Quantum efficiency also decreases at lower temperatures, so flat field exposures should be taken at the same temperature as science observations. Flat fields should be exposed to a uniform light source, typically a dome screen (dome flats) or the twilight sky (sky flats). Vignetting, the reduction in light around the frame edges, can also be corrected using flat fielding. A master flat is made by taking the median of individual bias-subtracted flat fields.

2.1.4 Data Reduction

The master bias and dark frames are subtracted from the science frames. Dark current is negligible for NGTS due to its low operating temperature and high quality electronics, so the master dark is not subtracted in this case. The science frames are then divided by the master flat field, ready for photometric measurements. More information about image processing can be found in the Handbook of CCD Astronomy (Howell, 2006).

2.2 Aperture Photometry

Photometry is the measurement of the number of photons received within a certain region of the instrument. In transit surveys, aperture photometry is typically used, where pixel counts within a fixed size region are summed to give the measured flux of the target. This method is used in all three science chapters, and in Chapter 3, I discuss using specialised apertures suited to the saturated stars. SuperWASP, NGTS and NITES all use circular apertures in their standard pipeline, whereas TESS uses rectangular apertures. When using circular apertures, the measured flux of a pixel is multiplied by the fraction of that pixel within the aperture.

The placement of apertures can be determined using astrometry or using centroiding. When using astrometry, apertures are placed at the coordinates of known stars. The full World Coordinate System (WCS) astrometric solution of a frame is found to identify locations of sources within a field of view and apertures are placed on targets of interest. In NGTS, apertures are placed for all targets brighter than I magnitude of 16 at the astrometrically solved positions. While NGTS has very precise autoguiding to maintain stars on the same pixel, astrometric solutions are used for each image to account for field stretching due to differential atmospheric refraction and any field rotation due to imperfect polar alignment (Wheatley et al., 2018).

NITES however has a much smaller field of view, so is less susceptible to these field effects. Additionally its pipeline is designed to perform photometry on one target star relative to a number of comparison stars. Apertures are manually placed in the autoguider reference frame using the SAOImage ds9 application and its centroid function (Joye and Mandel, 2003). In the pipeline, apertures in the reference frame are re-centroided using SEP (source extractor in python, Barbary (2016)), before being repositioned according to the autoguider x and y pixel shifts measured by DONUTS (McCormac et al., 2013).

In the NITES photometric pipeline written by James McCormac, there are two stages. The first stage processes the data to measure the flux in each aperture using SEP’s ‘sum_circle’ function Barbary (2016). The reference image is astrometrically solved and apertures positioned as described above. The x and y positions, flux and fluxerr, including and excluding the sky flux and the maximum pixel value are recorded for each aperture in each frame.

In the second stage, the relative photometry light curve is produced. In each frame, the relative target flux is calculated as target flux divided by the sum of the comparison stars’ flux, with errors calculated using the quotient rule. A linear fit

to the out of transit or whole night of data is used to produce a normalised light curve. The light curve noise is quantified by calculating the standard deviation. Correlations with airmass, x and y position and sky level are also plotted to help identify trends. Aperture flux and maximum pixel values are plotted for all stars to check for brightness and saturation. Each comparison star light curve is plotted against the others to identify noisy targets and those with trends. I extended the pipeline to exclude any comparison stars which were identified as unsuitable without having to reprocess the data.

2.3 Observing tools

2.3.1 Predicting future phase coverage

Estimating the phase coverage that can be obtained in a given night’s observation is a useful parameter when aiming to maximise phase coverage at different periods. I wrote a tool to predict the increase in phase coverage, which uses the autoplan code written by James McCormac, to help plan observations for the NITES survey in Chapter 4.

The user specifies a target of interest from the targetlist and the intended date of observation. The autoplan script was written by James McCormac for automatically generating NITES observation plans for a given target and night. Autoplan makes use of the PyEphem module (Rhodes, 2011) to find the rising and setting times of a stellar target at a specified location, find the sky distance between the target and Moon and find times of dusk and dawn twilights. Autoplan then has the start and end time of observations for a given target.

The phase coverage predictor queries autoplan for the start and end times of observation. It uses these start and end times to predict the timings of observations, assuming 30 second exposure and a 5 second interval between exposures. The tool then adds these predicted timings to any already observed observation times and calculates the phase coverage.

Phase coverage is calculated for all test periods. The user can define the minimum and maximum test periods, the defaults are 0.8 to 35 days with test periods at 0.2 day intervals. Observed and predicted times are phase folded onto the test period (i.e. divided by the test period and the fractional value taken) to give the orbital phase. The tool then compares phases where data is present to every 1 % of phase: if there is a data point within this one percent of phase then this phase is covered. Plots of phase coverage against test periods are compared for observed and predicted times and observed data only to indicate the increase

in phase coverage from one or more nights of observation. On a given night, phase coverage for different targets can be compared to optimise the target chosen. An example for the night of 15th January 2019 in Figure 2.3 shows MD11+06 (bottom) has much greater increase in phase coverage than MD07+16 (top). This is taken into consideration along with moon distance and how long the target is observable for.

2.3.2 Autoguiding

Both NGTS and NITES (in Chapters 3 and 4 respectively) use the DONUTS autoguiding software (McCormac et al., 2013) designed to maintain the target on the same CCD pixels over the course of the observations. DONUTS measures the pixel shift between a given science frame and a reference image to recentre telescope pointing between each frame. Maintaining targets on the same CCD pixels over the observations helps reduce flux variability due to differing pixel sensitivity.

During the reduction of NITES data in Chapter 4, the measured pixel shifts between frames is used to recentre the apertures for photometry, helping increase the accuracy of flux measurements.

2.4 Algorithms

2.4.1 Bayesian Statistics and MCMC

Bayesian statistics describes the probability of an event given prior information. This is relevant to Chapter 5, in determining the uncertainties of the best fitting models. Bayes' theorem is used to find the posterior probability distribution $P(M|D)$, i.e. the probability the model, M , is produced, given a set of data, D . It is found as:

$$P(M|D) = \frac{P(D|M)P(M)}{P(D)} \quad (2.1)$$

The posterior probability distribution is determined by: the likelihood, $P(D|M)$, i.e. the probability of observing the data given the model, the prior probability, $P(M)$, i.e. the probability of the model before the data is considered, and the bayesian evidence, $P(D)$, which is the probability of the data given the model type without assuming any specific model parameters.

Priors are used to capture information already known about the system from external data, such as the temperature of a star from spectroscopic analysis or

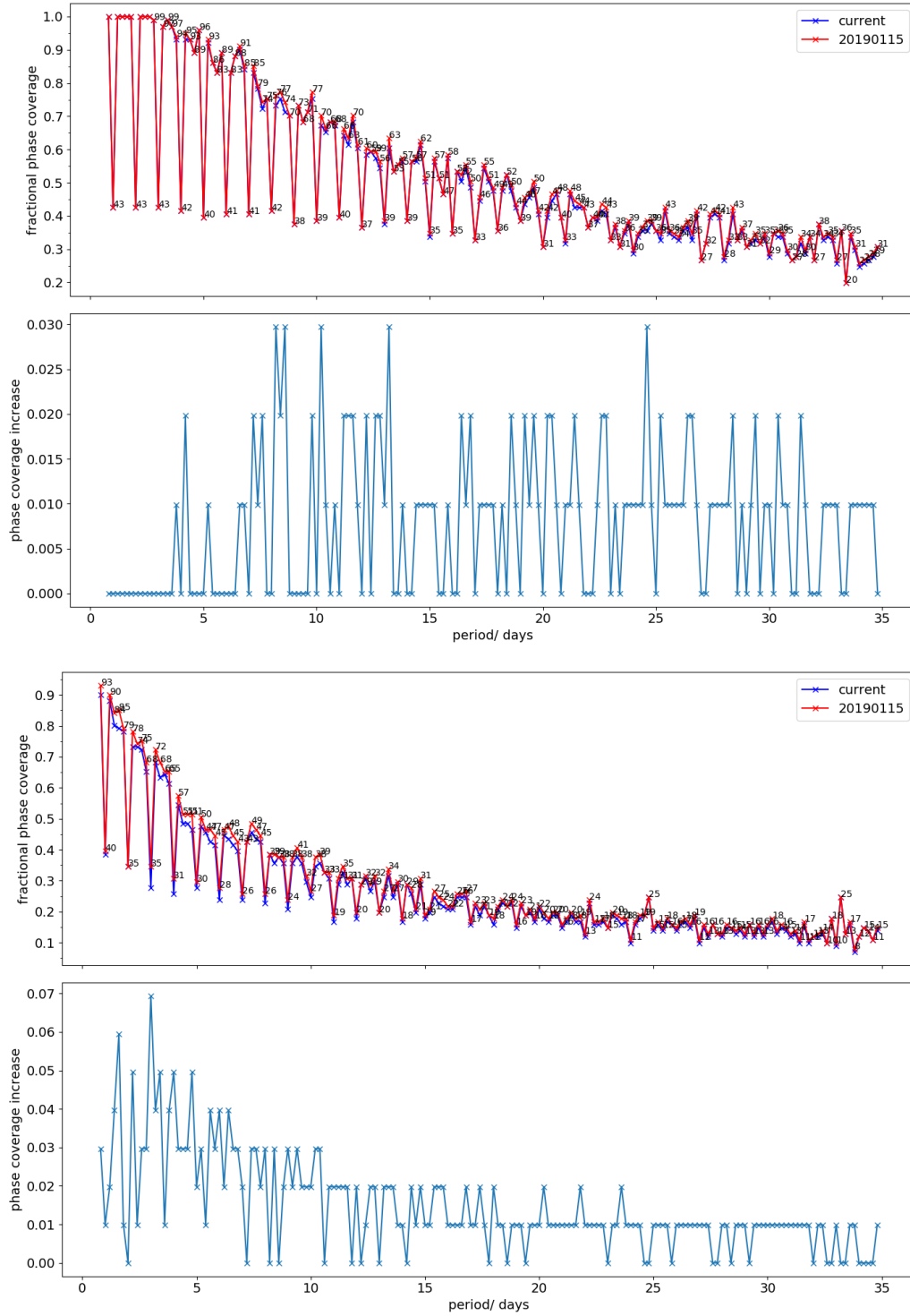


Figure 2.3: Increase in phase coverage for observing the night of 15th January 2019 for two targets: MD07+16 (top) and MD11+06 (bottom). For each, the top subplot compares already observed phase coverage (blue) and phase coverage if the additional night of observations takes place (red), while the bottom subplot shows the increase in phase coverage between the two at each test period.

to exclude values which are unphysical. It is important that the priors do not overconstrain the model and instead the data itself drives the posterior distribution.

Markov chain Monte Carlo (MCMC) algorithms are designed to sample the posterior probability distribution efficiently. The Metropolis-Hastings method (Metropolis et al., 1953; Hastings, 1970) is commonly used for implementing MCMCs. At each step in the chain, the algorithm calculates the relative posterior probability distribution of the next proposed step $P(M_{n+1}|D)$ compared to that of the current position $P(M_n|D)$. If model $n + 1$ has a higher posterior probability distribution, then it is likely a better fit to the data and the probability ratio will be higher. If this probability ratio is greater than a randomly generated number between 0 and 1, the chain moves to this proposed step $n + 1$. If not, the chain remains at position n . Hence, better fitting models are more likely to be accepted and the algorithm should converge over time to a stationary set of model parameters. For efficient sampling, the $n + 1$ step should be accepted in 20 to 50 % of cases (Gelman and Rubin, 1996). The advantage of calculating the probability ratio is that it cancels out calculation of the bayesian evidence, which is computationally expensive.

EMCEE (Foreman-Mackey et al., 2013) is a python package for MCMC. EMCEE simultaneously evolves an ensemble of n walkers, which allows sampling of n parameter space positions at each time step. The proposed next step of each walker considers the current position of other walkers, allowing the algorithm to converge much faster than when using a single chain. A thinning factor, f , may also be used, as in Chapter 5. In this case, only every f th step is accepted. Walkers explore the parameter space and over time, the chains should converge to the optimal model parameters, with high posterior probability, with the number of steps required increasing if the initial parameters are far away. The initial region before the chains converge are discarded as the ‘burn in’ phase before the posterior probability distribution is calculated to identify model parameters (typically the mean/median of chain values) and their uncertainties (the distribution of chain values).

2.4.2 Lomb Scargle

The Lomb-Scargle periodogram (after Lomb (1976) and Scargle (1982)) is a common tool for detecting periodic signals in unevenly spaced observations. It fits a sinusoidal model to the data at each frequency tested, with a larger power reflecting a better fit. It then returns a periodogram in frequency space to display the powers at different frequencies, and identifies the frequency with the largest power, which can then be converted to a period. Peak significance is found by comparing power peaks to the false alarm probability level, the probability of measuring a peak of a given

height assuming the data has no periodic component, only gaussian noise. The Lomb Scargle algorithm is used in Chapter 4 to investigate sinusoidal signals in the NITES data.

2.4.3 Box Least Squares (BLS)

Box-fitting least squares (BLS) is a commonly used algorithm for identifying periodic transits introduced by Kovács et al. (2002). BLS is the basis for identifying exoplanet candidates in SuperWASP, NGTS and other transit surveys today, and initially identified the EBLMs as transit candidates in Chapter 5. BLS is a key method in Chapter 4 to search for periodic transiting exoplanet signals. The technique uses least squares fits of step functions on the folded signal for a range of trial periods.

The algorithm simplifies the U-shape of transit into a ‘box’ function with two fitted flux values: H for out of transit points and L for in transit data. Alongside the period P_0 , the epoch of transit, t_0 , and the fractional transit length, q , are parameters of the best fit model.

For a set of i data points, a trial period is tested by fitting a box function to the folded time series. For this test period, different transit start and end times (i_1, i_2) are tested to try minimise the average squared deviation of the fit, D , by least squares minimisation and find the signal residue (SR) of the time series at that trial period. SR_{max} is the maximum signal residue at a given period, found by optimising trial values of H , L , i_1 and i_2 . Repeating for a range of trial periods and plotting SR_{max} vs frequency, the highest peak of SR (SR_{peak}) should give the transit period.

The relative strength of a given peak can be calculated using the Signal Detection Efficiency (SDE):

$$SDE = \frac{SR_{peak} - \langle SR \rangle}{sd(SR)} \quad (2.2)$$

where $\langle SR \rangle$ is the average peak and $sd(SR)$ is the standard deviation of SR over the frequency band tested. Higher values of SDE indicate that this period is more strongly preferred, making it more likely a real detection. Transit surveys often cut on a minimum SDE value of 5 or 6 (e.g. 5 in NGTS (Wheatley et al., 2018)) to reduce the number of marginal detections that are likely false positives.

BLS results can also be characterised by the effective SNR given by:

$$\alpha = \frac{\delta}{\sigma} \sqrt{nq} \quad (2.3)$$

where δ is the transit depth, $H - L$, and σ/\sqrt{nq} is the standard deviation of the average of all measurements within transit. An effective SNR , $\alpha = 6$, indicates that in and out of transit levels can be distinguished at 3σ significance, giving confidence to a transit event.

2.5 Transit fitting

2.5.1 Estimating orbital period from a single transit

The orbital period can be estimated from a single transit using parameters derived from the shape of the lightcurve and assuming a circular orbit. This method is used in Chapter 4 to estimate periods from single transit events. Kepler’s third law states:

$$P^2 = \frac{4\pi^2 a^3}{G(M_s + M_p)} \quad (2.4)$$

Kepler’s third law is arranged in terms of stellar mass and substituted into the stellar density equation: $\rho = M_s/R_s^3$. The ratio a/R_* is given in terms of the transit depth ΔF , impact parameter b , total and full transit durations (T_T , T_F) and the period P , which assuming $a \gg R_*$, simplifies to:

$$P = \frac{G\pi}{32} \frac{M_s}{R_s^3} \frac{(T_T^2 - T_F^2)^{3/2}}{\Delta F^{3/4}} \quad (2.5)$$

(e.g. Perryman, 2011). The period can be estimated from the stellar mass and radius (M_s , R_s) from the parameters derived from the shape of the lightcurve, assuming $b = 0$.

2.6 Transit Injection

2.6.1 Limb darkening toolkit

As discussed in Section 1.2.1, limb darkening affects the transit shape, so must be accounted for when simulating and modelling transit shapes. It is used in simulating transits in Chapter 4 and in modelling properties of the EBLMs in Chapter 5. The limb darkening toolkit (LDTk) (Parviainen and Aigrain, 2015) calculates model specific limb darkening coefficients using a library of PHOENIX-generated specific intensity spectra. The user specifies the filter wavelength range and stellar parameters with uncertainties (temperature, log g and metallicity), which the toolkit uses to

generate limb darkening profiles with uncertainties from the modelled stellar spectra. Limb darkening coefficients and their associated uncertainties for the specified limb darkening law are then generated from the limb darkening profiles.

Two limb darkening coefficients: C_u and C_v , are determined for the limb darkening quadratic law:

$$1 - C_u(1 - \mu) - C_v(1 - \mu)^2 \quad (2.6)$$

where $\mu = \sqrt{1 - z^2}$, and z is the normalised distance from the centre of the stellar disk.

2.6.2 PyTransit

PyTransit (Parviainen, 2015) is an exoplanet light curve modelling package which I use in Chapter 4 to model transits for injection and recovery tests. It implements the Mandel and Agol (2002) analytical transit light curve models for uniform and quadratic limb darkening. Flux, f , is calculated over the course of a transit as a function of radius ratio, k , and projected distance, z . Flux using the quadratic limb darkening law is calculated as:

$$f(k, z) = 1 - \frac{(1 - c)\lambda_e(k, z) + c\lambda_d(k, z) + b\eta_d(k, z)}{1 - a/3 - b/6} \quad (2.7)$$

where $c = a + 2b$, a and b are the limb darkening coefficients, λ_e is the disc fraction obscured in the absence of limb darkening and together with λ_d and η_d are parameters depending on k and z as given in Mandel and Agol (2002).

Transit light curve models are generated for supplied limb darkening coefficients using the quadratic limb darkening model for specified data times, radius ratio, transit ephemeris, period, semi-major axis in terms of stellar radii, inclination, eccentricity and argument of periastron. For transit injections in Chapter 4, I assume inclination and argument of periastron are 90° and eccentricity is 0 for a circular, edge on transit.

2.7 Summary

These photometric processing techniques, observing tools and algorithms have been key for obtaining the scientific results in this thesis. The next chapter is devoted to the investigation of saturated stars within the NGTS survey.

Chapter 3

Investigation into Saturated Stars in the Next Generation Transit Survey

3.1 Introduction

This project has been focused on investigating bright stars which appear saturated in the NGTS pipeline. I introduce the Next Generation Transit Survey, our motivation for studying saturated stars and why these stars need to be treated differently considering how CCDs respond to saturation. In the next sections, I explain how I identified saturated stars and show how aperture photometry using the standard pipeline does not capture the fluxes of these stars well.

3.1.1 The Next Generation Transit Survey

I have been investigating saturated stars in data collected by the Next Generation Transit Survey (NGTS). NGTS (Wheatley et al., 2018) is a wide-field ground-based photometric survey. The survey facility is based at Cerro Paranal, Chile, the same site as the European Southern Observatory, and consists of an array of twelve 20cm telescopes with a combined field of view of 100 square degrees. It uses red sensitive CCDs to maximise sensitivity to late K and early M dwarf stars to achieve the high precision of 0.1 % in one hour for stars brighter than $I = 13$ (Wheatley et al., 2018). The motivation of NGTS is to find transiting Neptune-sized exoplanets around bright K and early M dwarf stars suitable for characterisation by telescopes such as the VLT, ELT and JWST.

Exposure times of 10 seconds are used in the survey, leading to saturation

at approximately R magnitude of 10, brighter than all but the very brightest M dwarfs. Chazelas et al. (2012) found in one NGTS field, NGTS would achieve 3 mmag photometry or better for 843 stars of K or M spectral type. Using a typical early M dwarf radius of $0.5 M_{\odot}$ (M1, Pecaut and Mamajek (2013)), a transiting planet with Neptune’s radius produces a 0.5% transit. Wheatley et al. (2018) found from injection tests into NGTS data that most transits of 0.5% or deeper were detected at periods out to at least 10 days. All sky catalogues of bright M dwarfs (e.g. Lepine and Gaidos, 2011; Lepine et al., 2013) typically cut at a J magnitude of 9 or 10. Taking a J magnitude of 10, and using an I–J colour of 1.9 for M2 stars (Hawley et al., 2002), bright early M dwarfs are I magnitude of about 12 or brighter. Therefore NGTS is sensitive to hot Neptune-sized planets around early M dwarfs.

The NGTS telescopes follow a given field each night for the observing season, which typically lasts six months. Data are then processed using the NGTS pipeline to correct for systematic trends common across stars in the field, such as the effects of changing airmass. Once the data are processed, transits are searched for in the data using the Box Least Squares algorithm (BLS; Kovács et al. (2002); Collier Cameron et al. (2006)) which searches for periodic dips with lower levels of flux present for a given star. The outputs of BLS are then ‘eyeballed’ by members of the NGTS collaboration to vet high quality candidates. Candidates are confirmed by spectroscopic follow up, with spectral analysis providing the host star parameters and radial velocity measurements giving the relative mass of its orbiting exoplanet.

3.1.2 Motivation for Studying Saturated Stars

Stars appearing saturated are brightest.

Currently saturated stars are not used. However by definition these saturated stars are very bright and would make very suitable follow up targets. Around 3000 transiting exoplanets have been detected (exoplanet.eu, Roques and Schneider (2015)), and while transit photometry reveals a planet’s radius and distance from its star, the planet’s characteristics, including its composition and whether it has an atmosphere are particularly interesting. Usually radial velocities are measured to find the planet mass, which can be used to find the mean density and give a first indication of the composition. Radial velocity measurements requires bright host stars to obtain high spectral resolution at sufficient signal to noise for planet detection. Brighter stars allow more precise measurements of radial velocities, and fainter than a certain magnitude, they are not possible.

Significantly, much of the motivation for finding planets which transit bright

stars is the opportunity to uncover more about the planet’s formation, evolution and properties through studying the planet’s atmosphere. Atmospheric observations use transmission and emission spectroscopy which are limited to bright stars. As a guideline, host stars brighter than V magnitude of 12 can be considered for transmission spectroscopy (Kirk, 2018), although stars with V magnitudes brighter than 10 are favoured (Perryman, 2018). High photometric precision is required to regularly make exoplanet atmosphere detections using transmission spectroscopy. For example Charbonneau et al. (2002) found observing the transit of HD 209458 b ($V = 7.6$ mag) using sodium lines was just 232 parts per million (ppm) deeper, requiring 57 ppm precision for a 4σ detection. The signal to noise ratio at resolution R is diminished by a factor of $0.8R^{0.5}$ compared to the summed spectrum (Haswell, 2010) so high signal to noise ratios and therefore large numbers of photons are required.

This is why most atmospheric characterisation has focused on planets around a small number of bright stars. Therefore saturated stars could make very suitable spectroscopic targets. Additionally, this is why the Transiting Exoplanet Survey Satellite (TESS; Ricker et al., 2015) launched December 2017, is conducting a whole sky survey from space targeting focusing on the brighter stars. The first half of the TESS primary mission has spent 30 days on each of 13 fields in the southern hemisphere, which overlaps with NGTS survey fields, allowing NGTS follow up of TESS candidates with higher image resolution (as the pixels are smaller) and for longer periods of time.

Why saturated stars need to be treated differently

The exposure time of wide field surveys for exoplanets is set to extract useful photometry of the maximum number of stars, producing a number of saturated stars in observed wide field surveys. Saturated stars are currently discarded and considered a nuisance, contaminating observations of nearby stars. This is due to blooming: observations of a very bright star causes the charge in a pixel to exceed the saturation level making the charge bleed into adjacent pixels. The flux from the star is not contained within the standard 3 pixel radius aperture, as shown in Figure 3.1, so some of the flux would not be recorded for the star using the standard aperture. As this flux is lost, the extra systematics in the light curve makes finding transits impossible.

In their current state, saturated stars cannot be used as within the standard aperture size of 3 pixels, flux level is not proportional to the actual brightness of the star. I am investigating whether the actual brightness of the star can be recovered

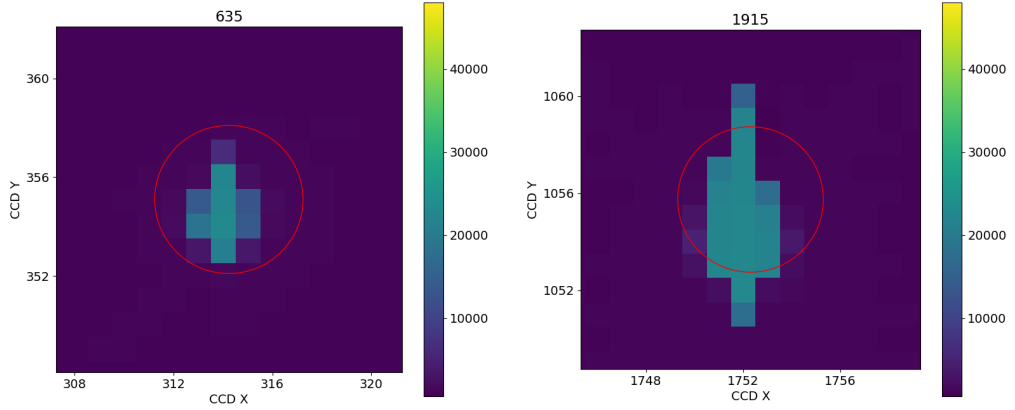


Figure 3.1: Thumbnail images: the left plot shows a bright star that is below saturation, which is contained within the standard 3 pixel aperture indicated by the red circle. The right plot shows a saturated star whose light extends beyond the same standard 3 pixel aperture.

using larger aperture sizes, to constrain what stellar magnitudes can be recovered from the data for use in the transit survey.

To achieve this, I need to identify which stars are saturated in each field and compare their light curves to those of bright stars just below the saturation limit, for both standard and larger aperture sizes.

3.1.3 Saturated star studies in *Kepler* data

Saturated stars have been studied in data from the *Kepler* Space Telescope, whose detector saturates at $K_p \sim 11.3$ (Gilliland et al., 2010). Photometry of stars brighter than this has been performed on *Kepler* and *K2* data using two different methods. Smear data, caused by light falling on the detector during readout (*Kepler* lacks a shutter), give photometric data for each CCD column. However stars captured within the same column are confused, leading to sometimes significant contamination (Pope et al., 2016, 2019). A second more precise method is halo photometry: capturing the halo of scattered light around a saturated star to recover relative photometry. This involves constructing a light curve as a linear combination of individual pixel time series and performing a weighted minimisation function. Halo photometry has been employed using *K2* data for individual targets (White et al., 2017; Farr et al., 2018) and for a larger catalogue of stars (Pope et al., 2019). This required downloading data using a larger radius: 12–20 pixels, generally requiring targets to be specifically proposed and targeted with this method. Their investigation of stars with magnitudes $11.5 < K_p < 12.5$, equivalent to the bright

unsaturated stars investigated in this chapter, showed similar 6.5 hour Combined Differential Photometric Precision using halo photometry to that of the standard pipelines.

3.1.4 NGTS CCDs

The NGTS telescopes are fitted with a 2048 x 2048 pixel CCD manufactured by e2v technologies plc. Pixels are in a 2048 x 2048 array and each pixel is 13.5 microns in size. CCDs are read at a speed of 3 MHz, so the whole image is read in 1.5 seconds. The NGTS team worked with Andor to modify the standard camera and improve photometric precision. Modifications include changing the analogue readout electronics to maximise bias and gain stability and optimising the collection phase CCD voltage to maximise charge conservation for saturated stars.

NGTS uses CCD42-40 back illuminated thinned CCD sensors, which as they are back illuminated means the photons do not pass the electrode gates so avoid subpixel sensitivities. The version used in NGTS are deep depleted, made of thicker high resistance silicon which can hold more electrons in their deeper pixel wells. The high resistivity CCD can be fully depleted, which increases the quantum efficiency in the red optical, increasing sensitivity to redder K and M dwarfs. The disadvantage of the deep depletion version is a higher dark current than the standard device because they are made of thicker silicon but this is not an issue for NGTS as the dark current is still much lower than the sky background as the CCDs are operated at -70 °C.

High resistance CCDs mean that electrons are more likely to stay in their pixels, which is an important factor when considering charge diffusion and saturated stars.

3.1.5 Standard NGTS data reduction

NGTS data are reduced using a custom pipeline. A catalogue of target stars is generated for each observational field by carrying out source detection on a stacked averaged and dithered master image of the field in NGTS data. This was done in the pre-*Gaia DR2* era to reduce the risk of source apertures being misplaced due to the proper motion of stars, which would disproportionally affect M dwarfs, which are of great interest in the survey. Detected sources are cross-matched with other catalogues including the AAVSO Photometric All-Sky Survey (APASS; Henden and Munari (2014)), *Gaia* (*Gaia* Collaboration et al., 2016) and 2MASS (Skrutskie et al., 2006), where limits on colour and separation are used to avoid spurious matches.

The catalogue has a cut-off at an I-band magnitude of 16, close to the detection limit for a 10 second exposure, where the I-band zero point of the field is computed from the APASS matches.

Science images are bias subtracted and flat-fielded for each field using master frames generated using the full observing season. For each field, a full World Coordinate System (WCS) astrometric solution is found per image, enabling apertures to be placed precisely. Aperture photometry using CASUTools IMCORE.LIST (Irwin et al., 2004), is performed at the positions identified in the astrometry for all stars identified in the target catalogue. The standard pipeline uses a circular aperture with a radius of 3 pixels (15 arcsec). Pipeline fluxes are given in ADU/second, measured by summing fluxes from all pixels in the aperture and dividing by the exposure length. Lightcurves for the whole observing season are created from the photometry of each object, which are then detrended.

NGTS lightcurves are detrended using an implementation of SysRem (Tamuz et al., 2005), an updated version from WASP (Collier Cameron et al., 2006). SysRem removes signals common to multiple stars, including those with varying amplitudes. The first step in this is to calculate a mean light curve, which is used as an artificial standard star to correct for first order effects common to all light curves.

Additional systematic signals which are not completely removed by SysRem correlate with Moon phase and sidereal time. The instrumental flux is correlated with sidereal time, airmass and sub-pixel movements of stars due to differential atmospheric refraction, so these trends may be caused by differential extinction, imperfect flat fielding or sub-pixel sensitivity variations. Periodic systematics and periodic stellar signals are identified by analysing the signal variance. These signals are removed after checking the signal is not transit-shaped. After detrending, lightcurves are searched for exoplanet transits using the box least squares (BLS) algorithm, see Methods.

3.1.6 The data

The data in this project were from the NGTS main survey of 30 fields observed for various dates between 21-09-2015 and 27-06-2016, with each field observed for approximately 2–3 months. Each field is observed by one telescope with a field of view of 12 deg². The version of data I used was processed in the NGTS pipeline under the TEST16A run. Much of the investigation in this project focused on one field of data, designated NG0304-1115, observed between 04-11-2015 and 01-03-2016. In this field 3691 stars were identified in the catalogue and 114663 science frames were taken.

3.2 Saturated Stars in the Standard Pipeline

3.2.1 Identifying Saturated Stars

Plotting the log fractional root mean square (RMS) flux against the log mean flux for all stars in a field allows identification of the saturated stars. In the analysis described below I selected only stars for which the number of extracted photometric data points was greater than 95% of the total number of images. This is to remove the effect of stars which had only a few spurious points.

I plotted the log RMS flux against the log mean flux from the standard aperture radius size of 3 pixels for the whole season's data of that field to compare the relative noise in the lightcurves for stars of different brightnesses. Figure 3.2 shows a general trend which starts as linearly decreasing before levelling off. This reflects the total fractional RMS noise which for brighter stars is dominated by a constant level of scintillation, as seen in the bottom plot of Figure 3.2. However beyond a certain mean flux value, stars leave this linear trend and start increasing in RMS flux, representing the flux level where saturation of the aperture photometry in that camera begins. Aperture saturation is caused by flux blooming beyond the aperture limits and is not directly comparable to the saturation point for an individual pixel, as discussed in Section 2.0.1. Examination of the log RMS flux vs mean flux plots allowed identification of the aperture saturation point for each field in ADU/second.

I identified saturated stars for further study by filtering for those with mean fluxes above the saturation limit. For NG0304-1115, I found 11 stars that are saturated for study in the rest of this chapter. In the following sections, I investigate whether these stars identified as saturated in the standard pipeline aperture can be recovered by changing the aperture used for photometry. I also identified another group of stars for comparison which were still bright but had flux levels from 80 % the saturation limit up to the saturation limit itself, which I call 'bright unsaturated' stars. The value of 80 % was chosen to give a minimum of six bright stars in nearly every field (one field had five stars). This would allow a reasonable number of bright unsaturated stars in all these fields in the case of future investigation.

3.2.2 The standard pipeline aperture

I plotted lightcurves for the objects produced using the standard pipeline aperture. These fluxes had already been detrended by the pipeline to account for observing through changing airmass and other factors. I also filtered out data points which had been flagged by the pipeline e.g. because the data was bad quality.

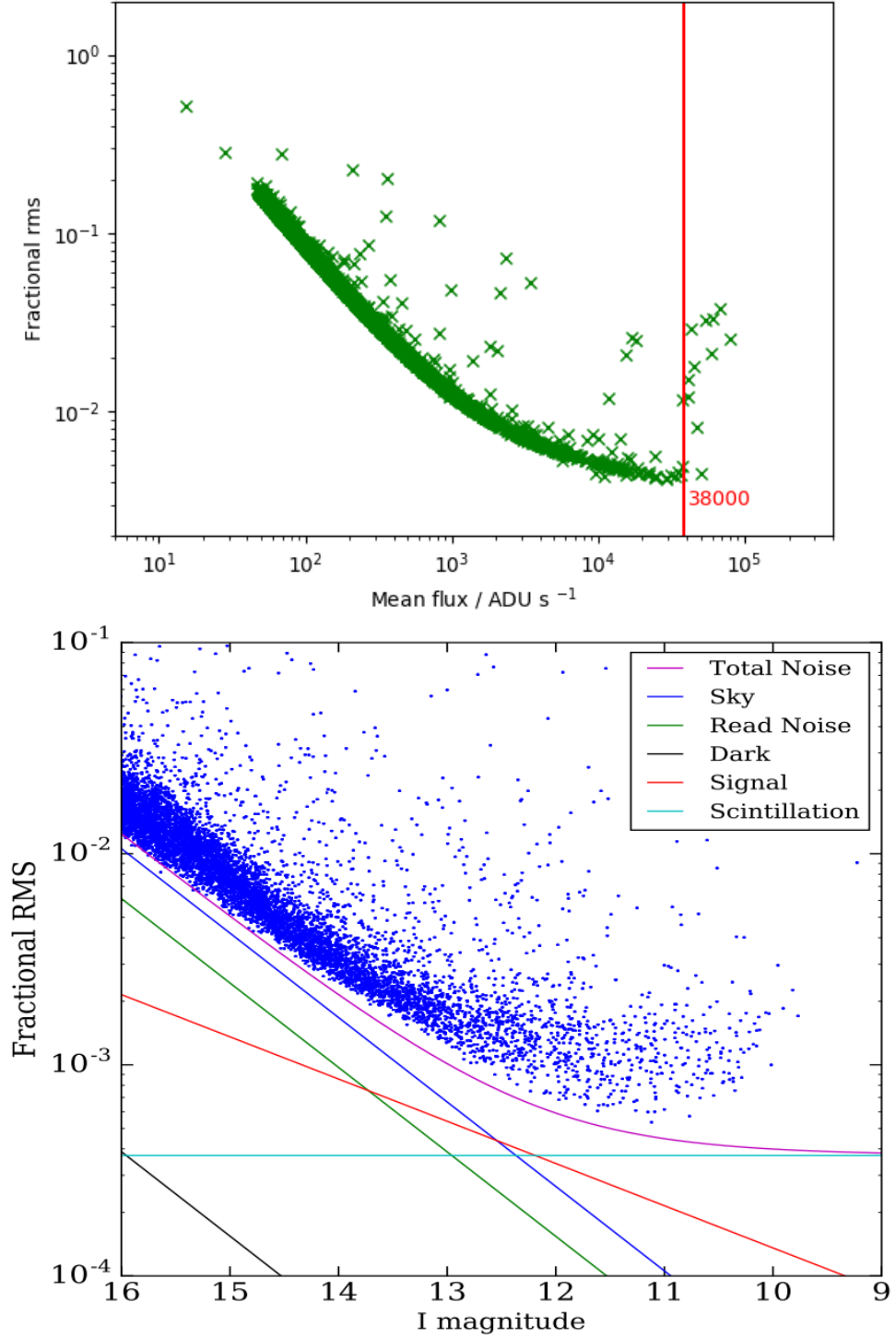


Figure 3.2: Top: Fractional RMS vs mean flux for stars in field NG0304-1115. Objects identified as saturated have mean fluxes greater than the saturation level indicated by the red vertical line at 38000 ADU/second. Bottom: fractional RMS noise as a function of stellar brightness for data points binned to one hour exposure, from Wheatley et al. (2018).

Lightcurves for the saturated objects using the standard pipeline aperture radius of 3 pixels are plotted in blue in Figures 3.4 and 3.5 with each row representing a different star. The ‘bright unsaturated’ stars can be seen in Figure 3.6. In general, the saturated stars display greater variation in the flux level across the timeseries, with more variation seen for the brighter objects. Some exceptions can be seen, notably saturated star 3615 is bright (with mean flux ~ 50000 ADU/second) but very quiet, agreeing with its much lower fractional RMS value in Figure 3.2 (0.004, in line with bright unsaturated stars).

3.3 Larger Circular Apertures

3.3.1 Why test larger circular apertures

As the flux of saturated stars is not contained within the standard pipeline aperture, larger apertures are needed to try capture the flux of these brighter stars. I investigated using larger circular apertures as this could be implemented simply in the NGTS pipeline. I tested two sizes of larger apertures, aperture 4 with radius $3\sqrt{2}$ pixels and aperture 5 with radius of 6 pixels.

Apertures 4 and 5 were chosen for testing as increasing the size of apertures means that the flux which has bled over into neighbouring pixels would hopefully be captured. This is balanced against an increase in aperture size increasing the likelihood of blending with other sources, and increasing the sky background noise. The photometric pipeline was rerun for all stars identified in the field, using apertures 4 and 5 positioned at the same coordinates.

We would expect that increasing the aperture size to increase the aperture saturation point for a given field. I plotted the fractional RMS against the mean flux for apertures 3, 4 and 5 in Figure 3.3, and this suggests that the saturation limit does increase with increasing aperture size: note the logarithmic scale for the mean flux. This suggests that if we increase the apertures sizes used in photometry, we should be able to recover more precise photometry for stars brighter than the saturation limit (R magnitude of 9.0) using the standard NGTS survey integration time. Specifically using aperture 5, R magnitudes up to approximately 8.4 should give photometry of a similar precision. However using the larger aperture 5 leads to increased photometric scatter for objects fainter than R magnitude of 12.0. Identification of catalogue magnitudes is discussed in Section 3.4.3.

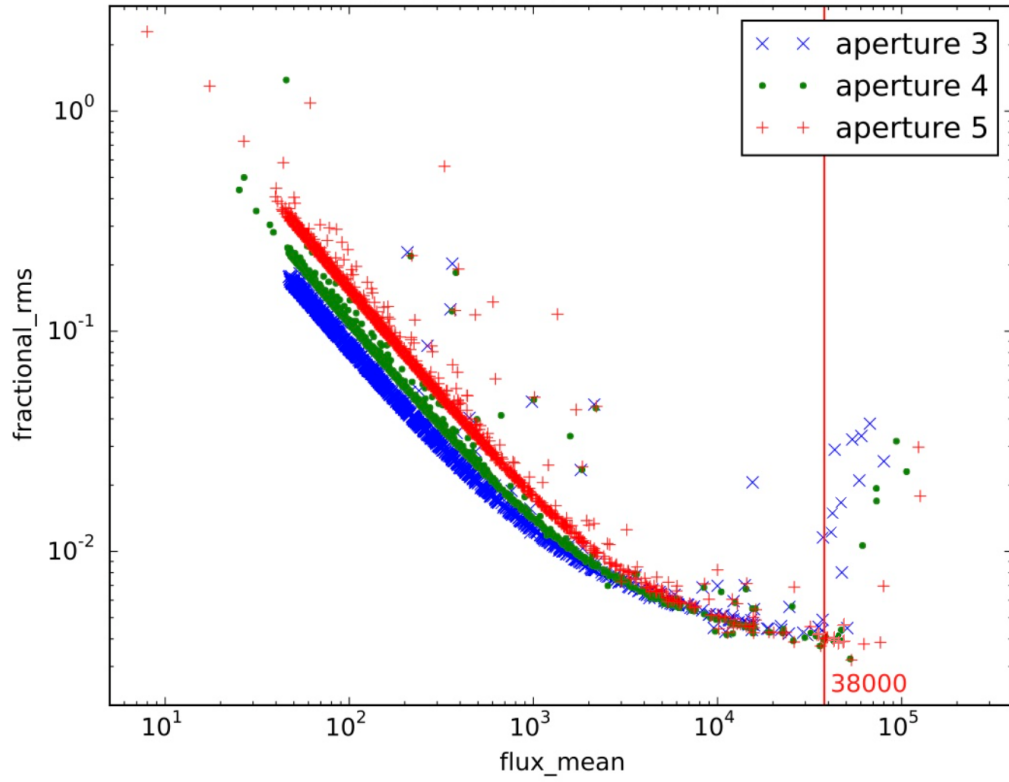


Figure 3.3: RMS vs mean flux for stars in field NG0304-1115 using different sized circular apertures. Aperture 3 is in blue, aperture 4 is in green and aperture 5 is in red. The saturation limit of 38000 ADU/second for aperture 3 is indicated by the red vertical line, which corresponds to a magnitude of 9.0 in R.

3.3.2 Lightcurves and Thumbnails for Larger Circular Apertures

I plot lightcurves for the saturated objects identified in Section 3.2.1 in Figure 3.4 and Figure 3.5, where each row shows a different object. Lightcurves are plotted for the whole season against image index, so the gaps in the data due to the night-day cycle are removed. Flux values which were flagged by the pipeline as being poor quality were not plotted. Flux values for apertures 3, 4 and 5 are shown in blue, brown and cyan respectively.

The lightcurves of saturated stars show a clear increase in the flux level between aperture 3 and aperture 4. The brighter saturated stars also show a clear increase between aperture 4 and 5. The flux levels for the fainter of the saturated stars display less variation at apertures 4 and 5 than the standard pipeline aperture of 3 pixels, indicating lower RMS values and that the stellar flux was contained at larger apertures.

For comparison, the lightcurves of the bright unsaturated stars are shown in Figure 3.6. These show less variation in the lightcurves than the saturated stars, with increases in the aperture size not displaying the same level of increased flux seen in the saturated stars. An exception is seen for object 1987 where aperture 5 shows a marked increase in flux compared to apertures 3 and 4. Examination of images revealed flux present outside aperture 3 presumably due to a close neighbour.

I also investigated the thumbnail images of these stars. Figure 3.7 shows a thumbnail image around each of the saturated stars with apertures 3, 4 and 5 overplotted using the same coordinates as for the photometry. The mean fluxes measured using each aperture are also given. For comparison the bright unsaturated stars are shown in Figure 3.8. The bright unsaturated stars are clearly contained within the standard 3 pixel aperture, with only relatively small increases in the mean flux seen when the aperture size is increased (the maximum increase in flux between apertures 3 and 4 is just under 1000 counts, for object 1386). In comparison, the saturated objects show a minimum increase in mean flux between apertures 3 and 4 of 1300 counts for object 787 and a maximum change of 27000 for object 1536. This demonstrates that while all these stars have fluxes above the saturation limit, there is great variety between them.

There is clear variation in the image size of the star between saturated stars, with some appearing to be contained within aperture 5 and others not at all. Whilst we could increase the size of circular apertures further to capture the lost flux, larger increases in aperture size will increase the noise from the sky background and run the risk of including contaminating stars.

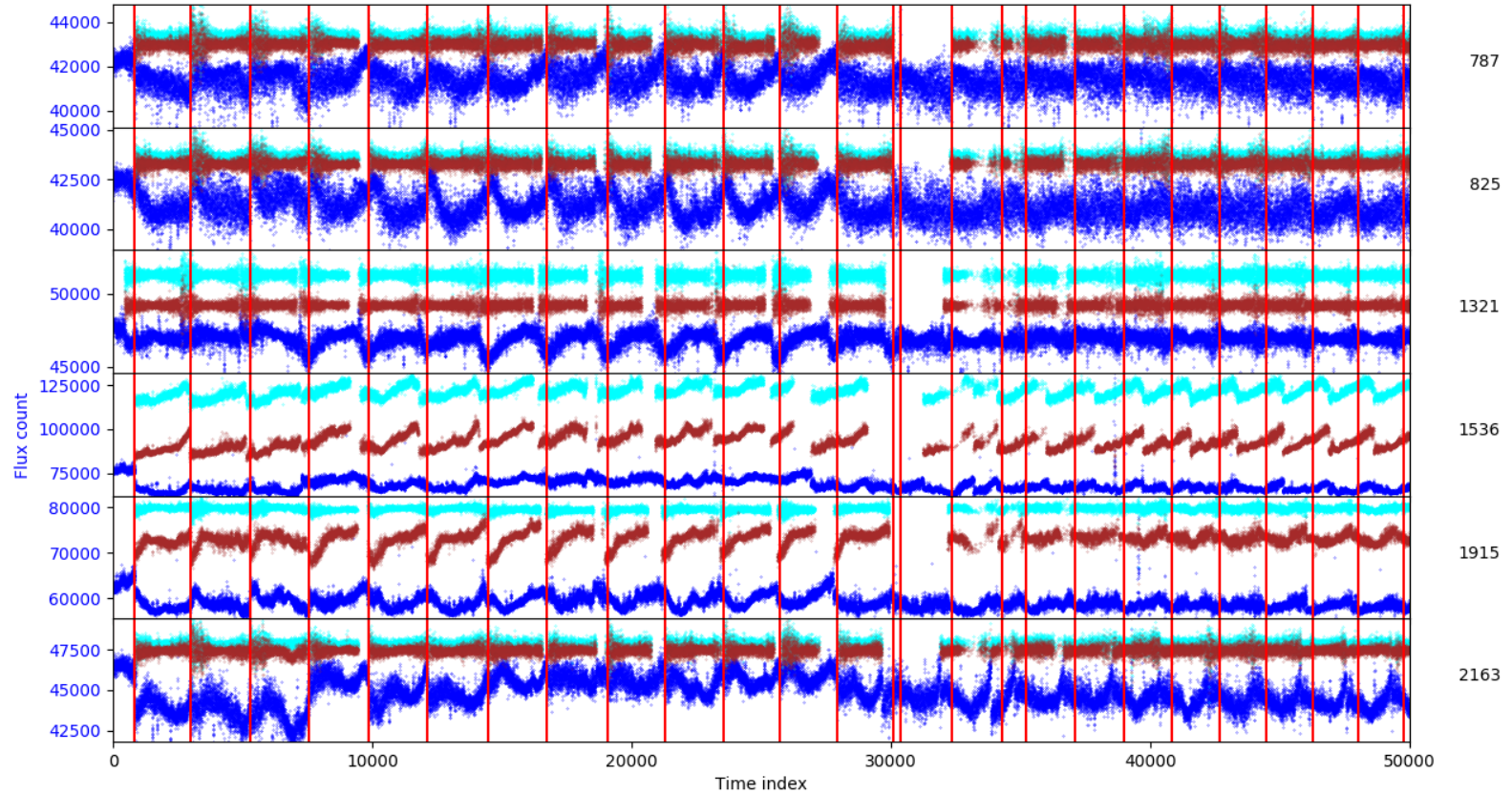


Figure 3.4: Light curves for saturated objects in field NG0304-1115. Flux (in ADU/s) is plotted against time index to reduce white space, with red vertical lines separating the different nights. Flux values flagged by the pipeline were not plotted. Each subplot shows a different object, with the object number indicated on the right. Flux as measured within aperture 3 is shown in blue, aperture 4 in brown and aperture 5 in cyan.

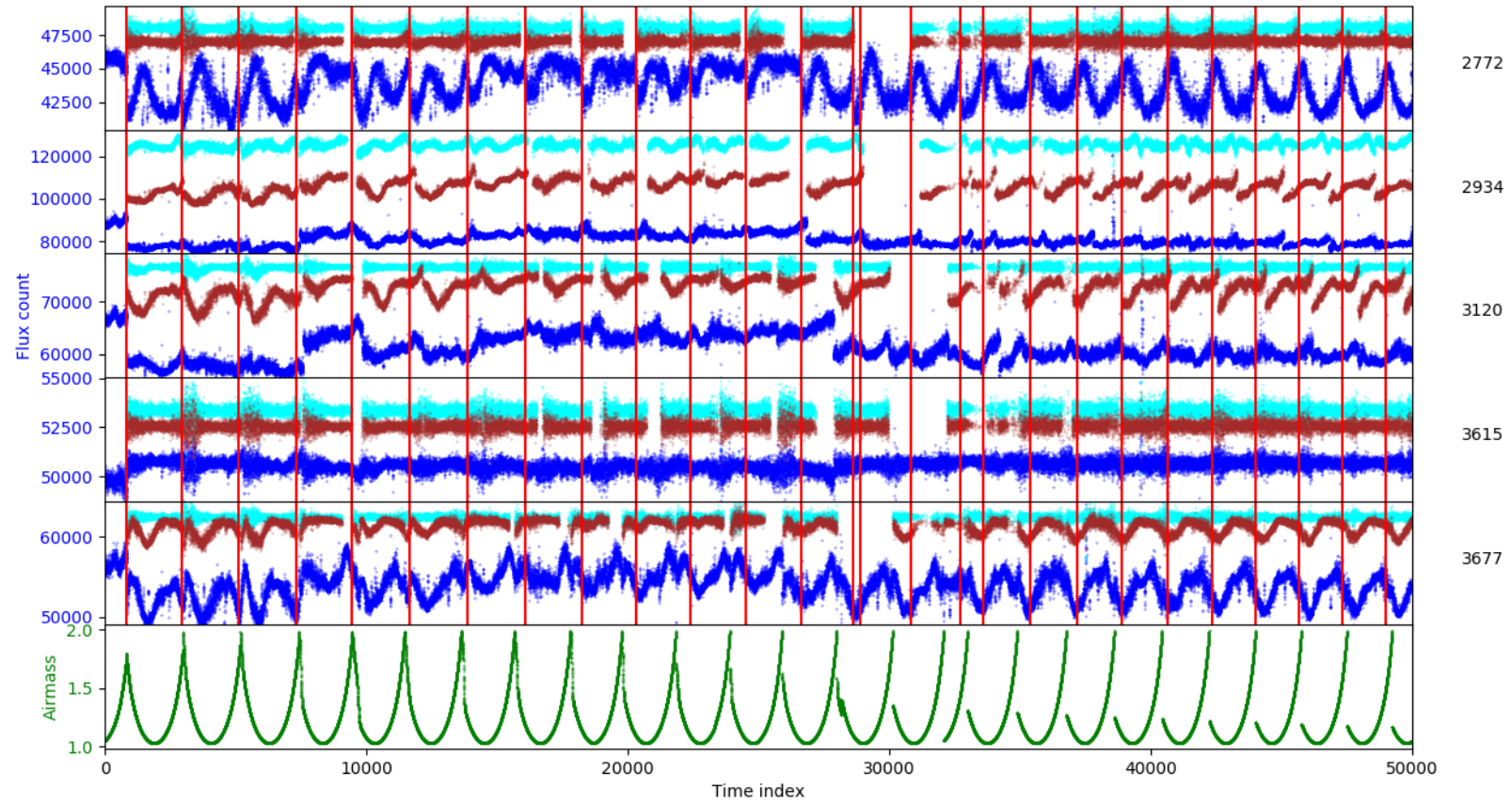


Figure 3.5: Light curves of more saturated objects, as per Figure 3.4. Airmass is also plotted in green.

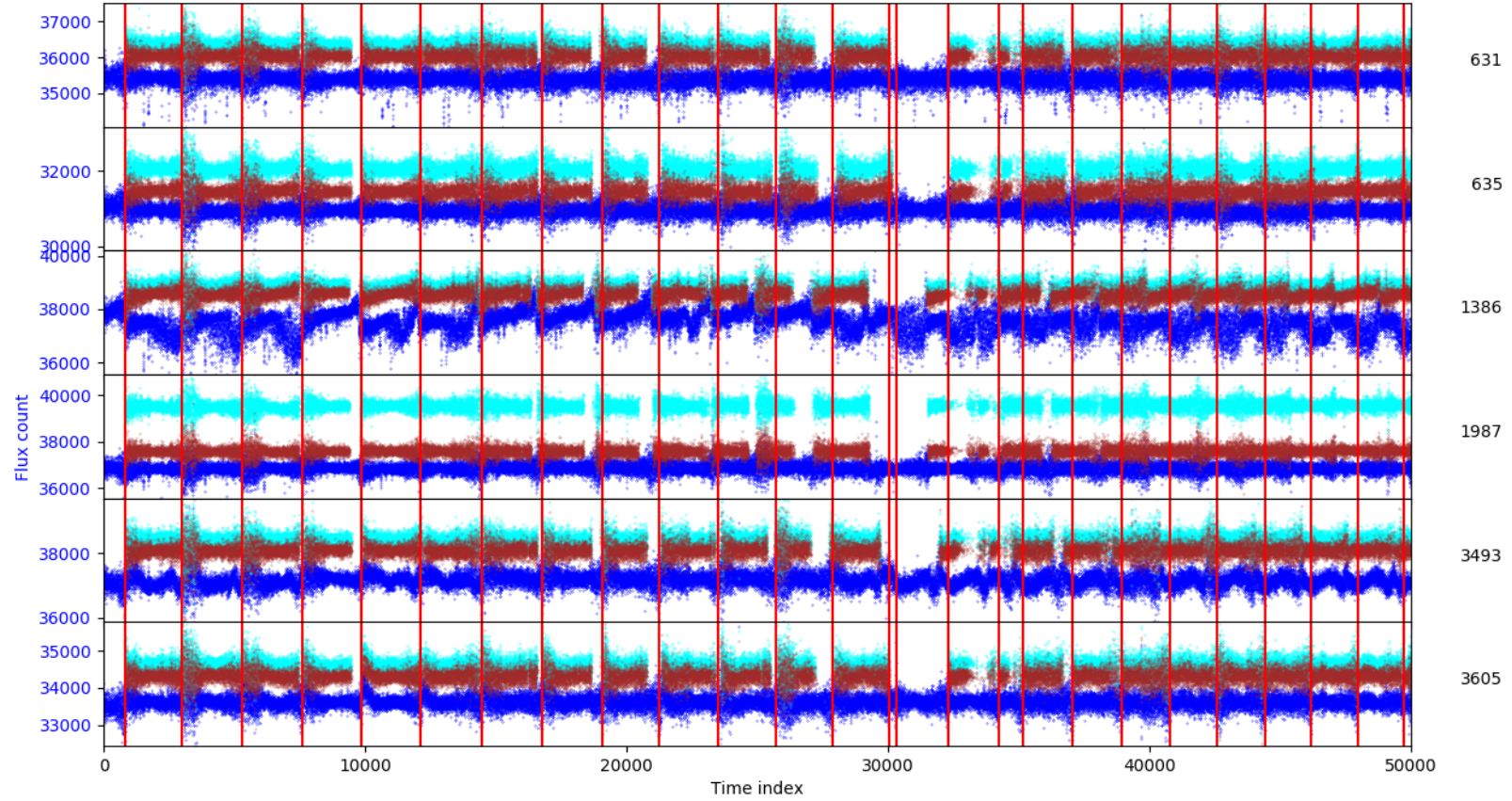


Figure 3.6: Light curves for bright unsaturated objects in field NG0304-1115. Flux (in ADU/s) is plotted against time index to reduce white space, with red vertical lines separating the different nights. Flux values which were flagged by the pipeline were not plotted. Each subplot shows a different object, with the object number indicated on the right. Flux as measured within aperture 3 is shown in blue, aperture 4 in brown and aperture 5 in cyan.

3.3.3 Comparison of apertures 4 and 5 to the standard aperture 3

To further compare the relative increases in flux levels with increased aperture size for both saturated and bright unsaturated stars, I plot the ratio of mean fluxes for circular apertures 4 and 5 compared to the standard pipeline aperture of 3 pixels in Figure 3.9. These show that the larger apertures capture more flux for the saturated stars, where one star (object 1536) shows 40% more flux using aperture 4 than aperture 3 and 80% more flux using aperture 5. Looking at the bright unsaturated stars, the mean flux does not increase as much using larger apertures, on the order of a few percent, implying that the flux for bright unsaturated stars is not bleeding into pixels outside the standard aperture. Note that using the mean flux of aperture 3 does not equate to the star brightness as some flux is outside the aperture, although some correlation will be seen.

The RMS flux plot Figure 3.3 allows us to compare the fractional RMS values between different apertures. Bright unsaturated stars (at fluxes just below the saturation point) have fractional RMS of approximately 0.0025. In comparison, saturated stars have fractional RMS values varying between 0.008–0.08 (with one additional object having exceptionally low RMS of 0.0025). Increasing the aperture size shows that saturated stars are quieter apertures 4 and 5, with fractional RMS values between 0.001–0.03 and 0.001–0.04 respectively. Figure 3.3 also illustrates why a larger aperture is not used for fainter stars, as at lower fluxes the fractional RMS using aperture 5 has higher fractional RMS values, i.e. is relatively noisy, due to the additional sky background included. Together these points show that specialised treatment of saturated stars is needed.

The bottom plot of Figure 3.9 compares the ratios of mean fluxes using apertures 4 and 5 against each other. A star at (1.0,1.0) has all its flux captured within the standard pipeline radius of 3 pixels. A star on the 1:1 line has all its flux captured in aperture 4, and a star above the line has additional flux captured using aperture 5. In general, the greater the increase in ratio of mean flux captured in aperture 4 compared to aperture 3, the more the ratio of mean flux captured in aperture 5 compared to aperture 3 also increases, above the 1:1 line.

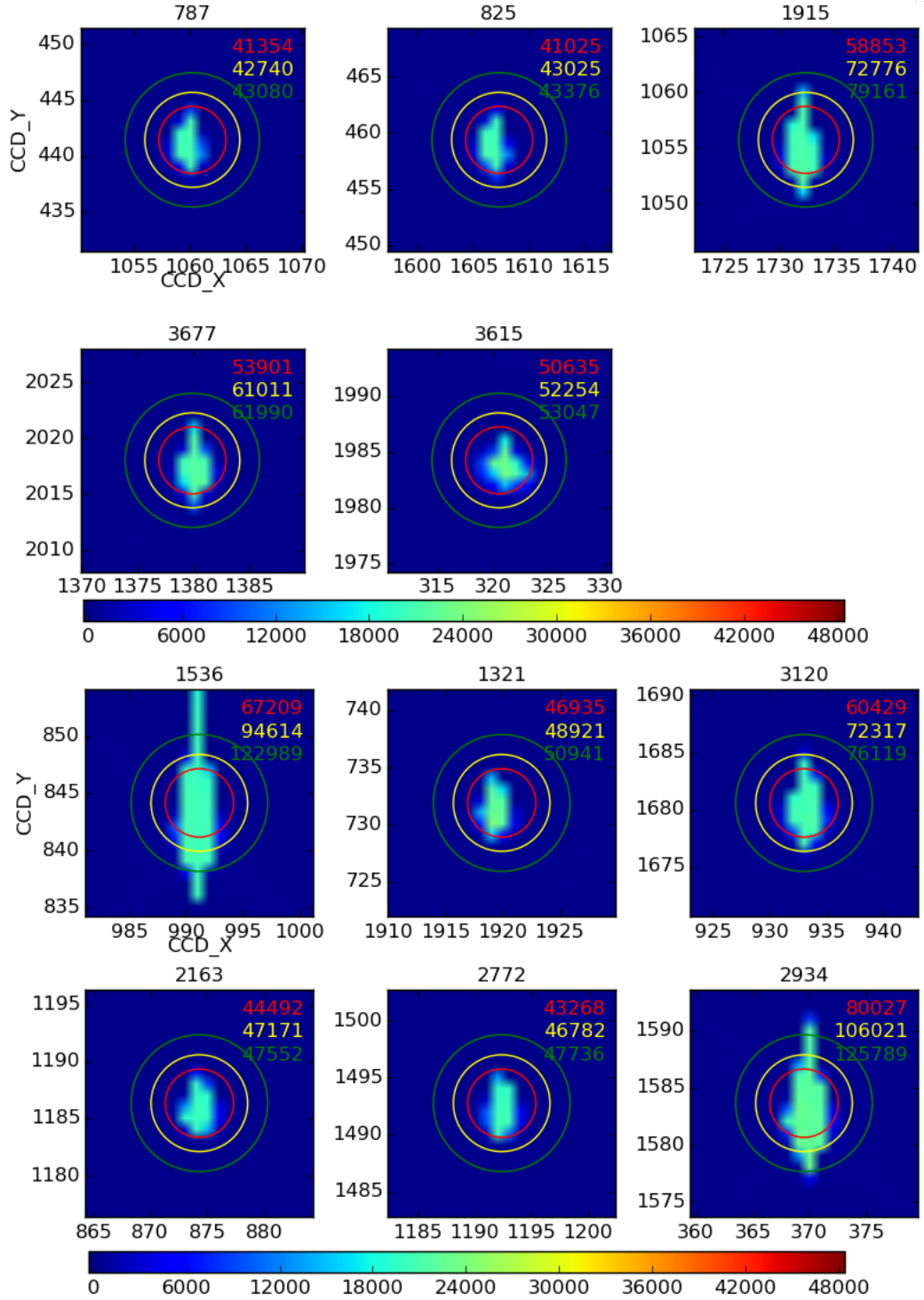


Figure 3.7: Thumbnails of saturated stars in field NG0304-1115 from the autoguider reference image, where colour scales with flux value. The star's catalogue number is given above each subfigure. Apertures 3, 4 and 5 are plotted over the star, with their mean flux (in ADU/s) given in the same colour. The saturation level for this field is 38000 ADU/s.

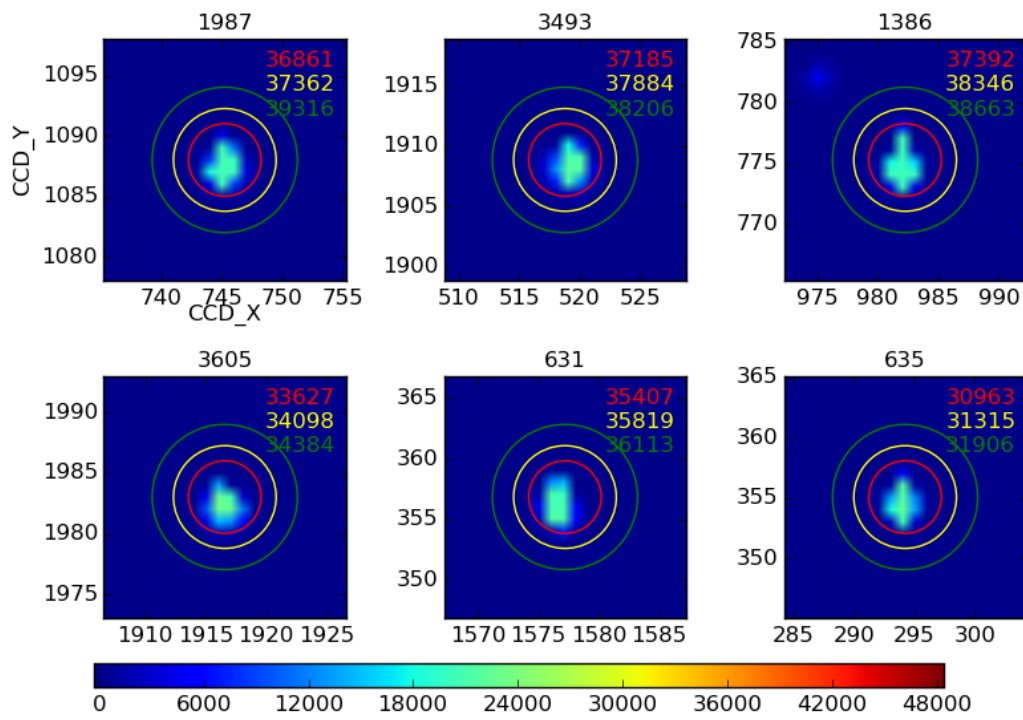


Figure 3.8: Thumbnail plots as per Figure 3.7 but for bright unsaturated stars.

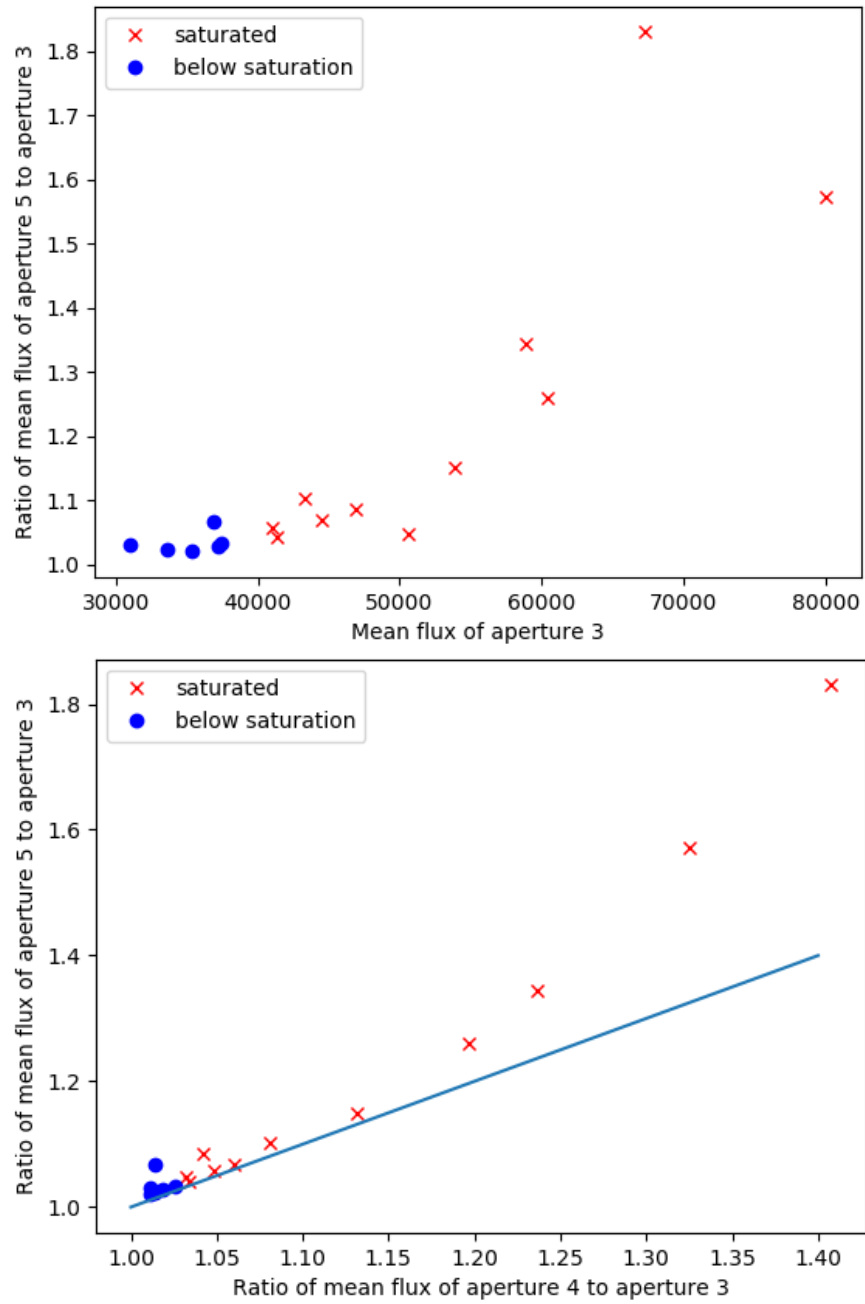


Figure 3.9: Comparison of mean fluxes between apertures 3, 4 and 5 for saturated (red crosses) and bright unsaturated (blue circles) stars. Top: mean flux ratio between apertures 5 and 3. Bottom: comparison of the additional flux captured using the larger apertures 4 and 5 by plotting the ratio of their mean flux with that of aperture 3. The 1:1 line is plotted in blue.

3.3.4 Conclusion

Often circular apertures are used for photometry of stars as this generally best fits the shapes of stars in CCD images. Point sources do not appear as point images due to diffraction within the telescope, instead an Airy disk pattern is seen. When observing from the ground, the Earth’s atmosphere smears these airy disks to an extent dependent on the seeing, giving images with a quasi-gaussian profile that are best fitted using circular apertures.

However, for the bright saturated stars studied here, examination of the thumbnails demonstrates that their shape is very different to those below saturation. Saturated stars are more elongated as the flux spills preferentially in the vertical direction (CCD Y) due to the CCD structure, specifically because this is the direction in which flux is transferred by the serial register. The elongated shape of saturated stars suggests that circular apertures are not optimal for them due to the increase in background sky pixels this includes. The degree to which saturated star flux spreads in both directions depends on the CCD structure and its voltage and gain settings, as discussed in Section 3.5.2, but often shows a preferential direction, making the general results applicable.

Using the standard pipeline circular aperture with radius 3 pixels, stars with fluxes beyond the saturation limit of 38000 ADU/s (which corresponds to an R magnitude of 9) show increased photometric scatter. Larger circular apertures reduce the amount of photometric scatter for stars up to an R magnitude 8.35 at the expense of worse photometry for stars fainter than an R magnitude of 12, and increased sky pixels included in the aperture. Circular apertures were found to be unsuited to the shape of saturated stars on the CCD. Instead, in the next section I consider using rectangular apertures.

3.4 Rectangular apertures

3.4.1 Motivation

The previous section demonstrated that circular apertures are not well suited to saturated stars, due to their elongated shape on the CCD as seen in the thumbnail images. I investigated whether rectangular apertures would be better suited to capturing the flux of saturated stars, while minimising additional background sky flux and the risk of contaminating stars.

The thumbnails also illustrated a wide variety in the extent to which the saturated star’s flux spread with star brightness. We wish to tailor the length of

the rectangular aperture to suit the star. In this section I aim to find a relationship between stellar flux (and ultimately magnitude) and the rectangular aperture length used to capture the flux. I then use these rectangular apertures to measure the stellar flux and compare them to circular apertures for the saturated and below saturated stars.

3.4.2 Determining aperture length

We wished to measure the required height of a rectangular aperture based on the star's length on the CCD. I defined the vertical extent of a star as the number of contiguous pixels containing flux values greater than 5σ above the median background level, where $1\sigma = 1.48 \times \text{median absolute deviation (MAD)}$ (Hoaglin et al., 1983).

In a given frame, I measured the vertical (y direction) extent of each saturated star from the catalogue x,y coordinates in both the y+ direction and the y- direction and combined them together. The process was repeated to measure the vertical extent from the catalogue x-3 to x+2 positions. This accounted for cases where the circular apertures were not centred on the greatest extent of blooming.

The process was repeated to measure the vertical extents in every frame for the first 21 nights in the observing season. Figure 3.10 shows the vertical extent measured over a night increases before decreasing again, which seems to correlate with the airmass. This is expected given that higher airmasses mean lower flux levels and so fewer electrons to bloom, so there is less spreading of flux. Most stars show reasonably consistent vertical extents but some, notably object 1536, show stronger trends of variation.

From the measured vertical extents, I determined the rectangular aperture lengths for each star. Using an aperture length of the maximum length measured at any position on any night would measure the stellar flux to at least the 5σ level above the background in every frame. However, I found these maximum lengths were not a good fit for the saturated or bright unsaturated stars as they can be strongly affected by outliers, as seen in Figure 3.10, perhaps caused by a satellite passing across this star on the CCD.

Instead I identify nightly maximums excluding outliers by finding the 99th percentile vertical extent measured at each x position. Hundreds or thousands of frames are collected per night observed (the first night seen in blue in Figure 3.10 is relatively short in this sample and contains 870 images) so calculation of the 99th percentile is straightforward. Each star's aperture length was then determined as the maximum of all nights' 99th percentiles.

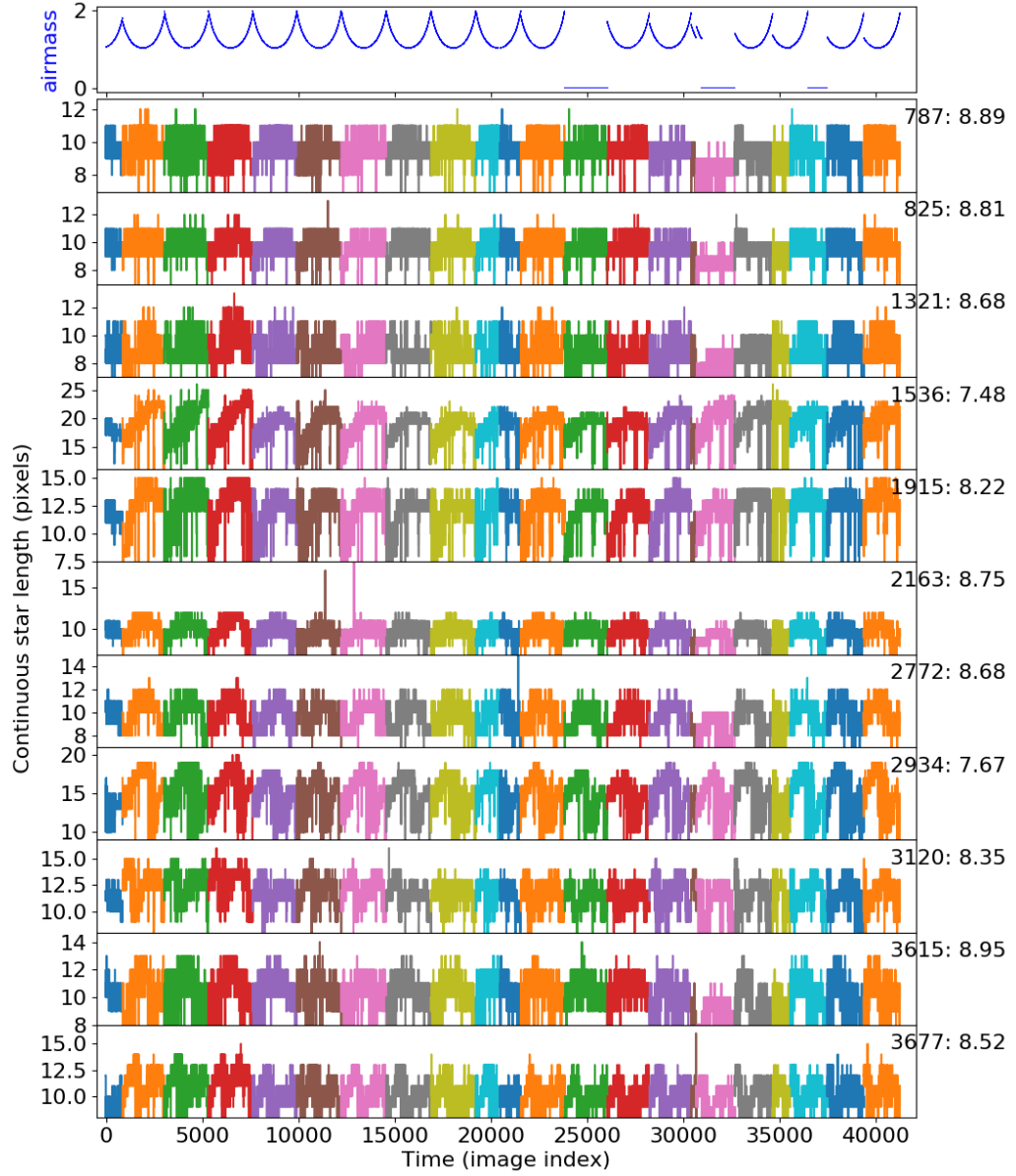


Figure 3.10: The measured vertical extents of the blooming pattern from the catalogue x position in individual frames is shown for each saturated star. This is used to help identify what size rectangular aperture to use for producing lightcurves. Each coloured block of points plotted against the time index shows a different night in the first 21 nights that vertical extents were measured for. Each row is labelled by the object id and its corresponding R magnitude. For reference, the airmass is also plotted.

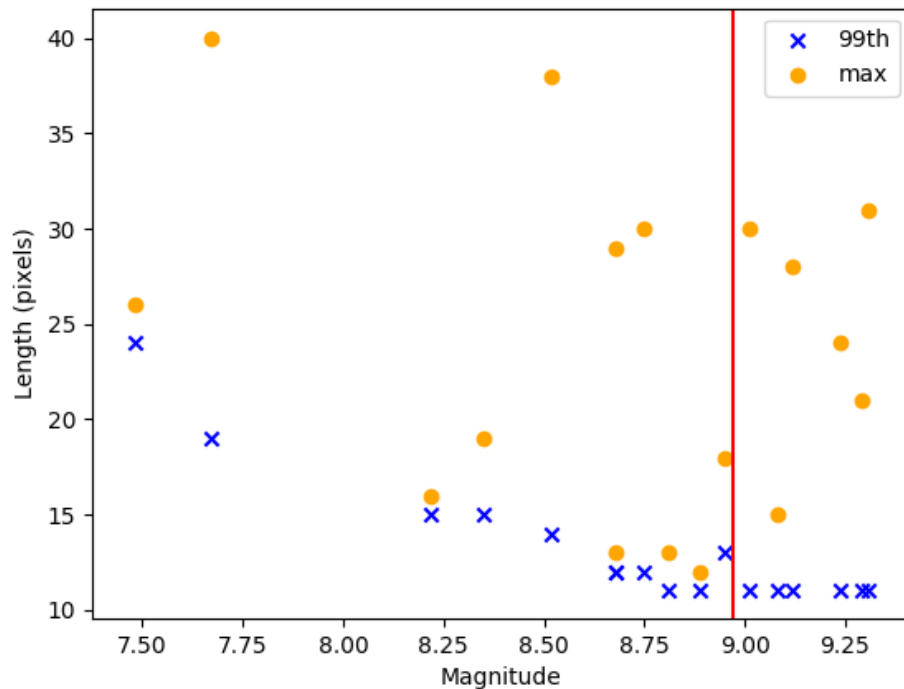


Figure 3.11: R magnitudes vs maximum measured vertical extent. For each object, both the maximum vertical extent measured on any night and the maximum of the nightly 99th percentile lengths are shown. Both saturated and bright unsaturated objects are plotted, separated by the vertical line. Overall maximum lengths (plotted as circles) vary greatly for both saturated and bright unsaturated objects whereas the 99th percentile shows a stronger trend with increasing magnitude. This suggests that the 99th percentile is a more reliable measurement of suitable aperture length because it is less affected by spurious detections.

I compare the maximum lengths and the maximum of all nights' 99th percentile lengths in Figure 3.11 for the R magnitude (magnitudes are determined in Section 3.4.3). This illustrates that the 99th percentile provides a more sensible fit for the data, where lengths are expected to increase for brighter stars. Vertical extents found using the 99th percentile ranged from 11 to 24 pixels and were found at the catalogue x and $x-1$ positions. In Section 3.4.3, I look for a relationship between these measured lengths and stellar magnitude.

3.4.3 Finding relationship between length and star magnitude

Having determined the rectangular aperture lengths to use for each of the saturated stars, we wanted to find a relationship between the length and stellar magnitude. This would allow us to look up what length to use based on a stellar magnitude for additional stars or for other fields observed with the same camera. To do this, I made use of crossmatches of NGTS' catalogue with external catalogues, where the sky positions and measured magnitudes of the stars in each field are cross correlated with external surveys to find the best match within a defined brightness and position.

Initially, stellar magnitudes were found in the NGTS crossmatched catalogue, which contained V and R magnitudes from NOMAD from UCAC2. Crossmatching with APASS i and r magnitudes was also available but did not contain matches for a significant number of the targets so I opted to use the R magnitudes from NOMAD. This provides the R magnitudes in Figure 3.12, which is available for all of the saturated and bright unsaturated stars.

A new processing of the field using a more recent version of the pipeline, named CYCLE1807, became available in late 2018. This included additional cross-matched magnitudes from Gaia DR2, APASS, 2MASS and WISE, as well as NGTS' own calculated I and G band magnitudes, within the main catalogue. I crossmatched the saturated and bright unsaturated stars in the TEST16A catalogue used in this analysis against the CYCLE1807 catalogue to identify their magnitudes in external catalogues.

The star with vertical extent of 24 pixels is a clear outlier in the NGTS I and G magnitude bands in Figure 3.12. This was a spurious detection in the CYCLE1807 crossmatched catalogue, where one blooming saturated star was identified as two sources, which was checked using the Gaia archive¹ and SDSS images using Simbad². The (one) source was correctly identified for the R and Gaia G magnitudes, so these were not affected.

In general, we might expect for the saturated stars that magnitudes from external catalogues may provide more accurate magnitudes as the NGTS derived magnitudes are determined using the standard 3 pixel aperture. Linear fits were used to find the calculated lengths for a given magnitude in the different bands. I calculated the residuals of the fits as the sum of the squares of the fit errors. Comparing the residuals between Gaia G and R magnitudes where all stars are included, I find R magnitudes have smaller residuals than Gaia G magnitudes, so use calculated lengths from the R magnitudes for the calculated lengths.

¹<https://gea.esac.esa.int/archive/>

²simbad.u-strasbg.fr/

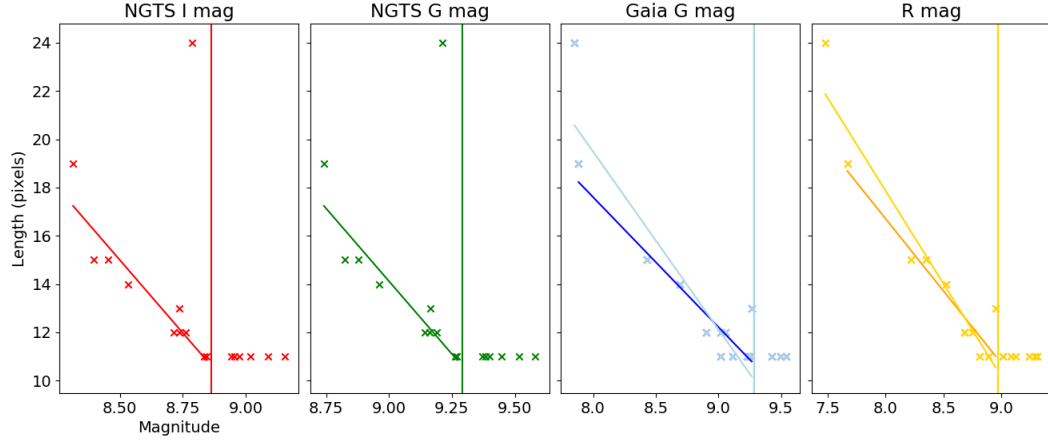


Figure 3.12: Vertical extent vs magnitude for R, NGTS I, NGTS G and Gaia magnitudes. Lengths are the maximum of nightly 99th percentiles found in Section 3.4.2. Saturated stars and bright unsaturated stars are both plotted, separated by a vertical line. A linear trend is fitted to the saturated stars for each magnitude set. In the NGTS I and G bands (the two leftmost panels), object 1536 with length 24 pixels is a clear outlier, so is excluded from the linear fit. The two rightmost panels show two linear fits, one including and one excluding the magnitude for object 1536 for comparison.

3.4.4 Determining aperture width

While the thumbnails of saturated stars showed their extent in the CCDY direction varied a lot, their widths were much more constant. To find a consistent width to use for all saturated stars, I defined apertures with widths of 3, 6 and 12 pixels (where 6 pixels is the same width as the standard pipeline aperture 3). I perform aperture photometry using these widths and the lengths determined in Section 3.4.2 and compare the fluxes obtained in Section 3.4.5.

3.4.5 Rectangular aperture photometry

Aperture photometry is run on the reduced data using rectangular apertures with the measured length determined in Section 3.4.2 and widths of 6 and 12 pixels. In each frame, apertures were centred at the astrometrically solved position of each saturated and bright unsaturated star in the catalogue and photometry performed using the `python photutils.RectangularAperture` function. Using an aperture width of 6 pixels shows some variation in flux, with a number of ‘dropout’ fluxes which are not seen with the wider aperture of 12 pixels. Here flux drops suddenly to significantly below the nightly median, often close to zero. The variation in measured

flux suggests either this width is not sufficient to capture all the stellar flux or the aperture placement may be off by a couple of pixels in these frames.

Identification and removal of outlying fluxes

I plotted the stellar aperture positions over CCD images which displayed these ‘dropout’ fluxes, a couple of examples can be seen in Figure 3.14. These revealed a systematic shift in the CCD position for all stars in the same frame compared to their aperture positions. Width 12 was less affected as the shift was generally sufficiently small to be contained within the wider aperture, but this width seemed excessive compared to the width of the star.

I investigated using source extractor in python (SEP; Barbary, 2016) to see if placing my own apertures fared better than using positions in the catalogue. SEP performs source extraction and centroiding to identify the centre of light for sources within a frame. I found that SEP centroiding was sometimes more accurate than the astrometric solution in locating star positions and sometimes it was worse. Overall, the SEP positions appeared to produce noisier lightcurves and are less consistent in the same frame between objects, so I use the catalogue positions instead.

I investigated whether the dropout fluxes could be accounted for by the autoguider error. NGTS uses autoguiding to maintain stars on the same pixels and records the image autoguider error compared to the master image. Each NGTS frame is solved astrometrically so the placement of apertures should not be affected by the error. However, Figure 3.14 shows that large autoguider errors are correlated with dropout fluxes for both saturated and bright unsaturated stars.

I filtered out frames where the autoguider error is greater than three times the RMS, i.e. 3.38 pixels in x and 1.52 pixels in y. I also found that the first frame on many nights was also outlying despite not being identified by its autoguider error, an example is shown in the right-hand plot of Figure 3.13. These frames were also removed, so overall 794 of 41113 frames were removed.

Rectangular aperture lightcurves

Lightcurves after removing outlying fluxes, associated with autoguider errors and the first exposure of the night, are shown in Figures 3.15 and 3.16. The bulk trends can now be seen in the lightcurves using rectangular aperture widths of 6 pixels, revealing some common trends remain for both saturated and bright unsaturated stars, including a correlation with airmass.

Aperture photometry was also performed using the lengths calculated in

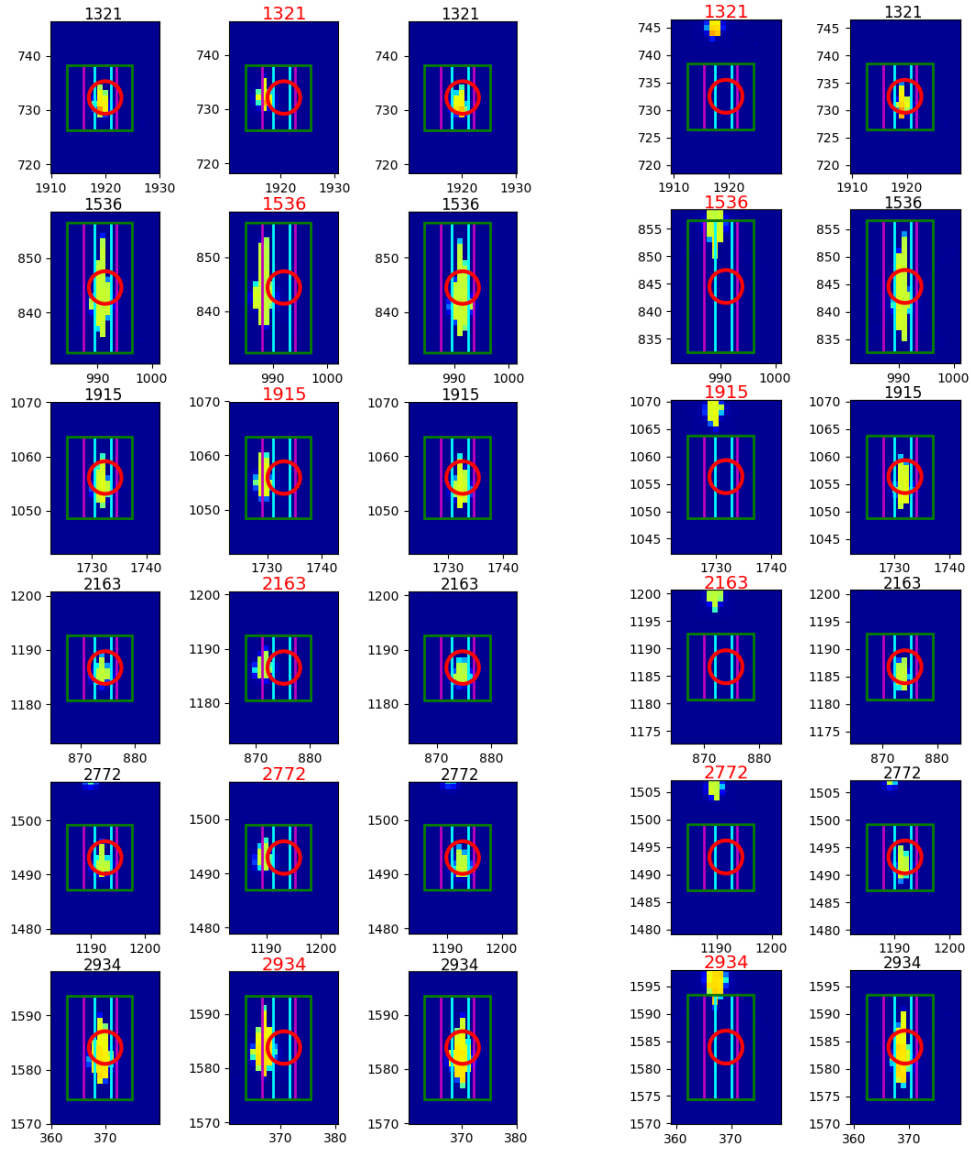


Figure 3.13: Example thumbnails illustrating outlying fluxes, where each column shows stars from the same frame. The position of the pipeline aperture is shown by the red circle, and purple and green rectangles represent rectangular apertures of widths 6 and 12 respectively. The left plot shows thumbnails from the fifth night, where in the middle column, apertures are not centred on the stars due to increased autoguider error, causing outlying fluxes. Its adjacent columns show thumbnails from images two minutes before and after the central column, where apertures are centred on the stars as the autoguider error is less than one pixel. The righthand plot shows thumbnails from the first two frames of the third night (plotted in green in Figure 3.14), showing apertures in the first image are not placed on the stars.

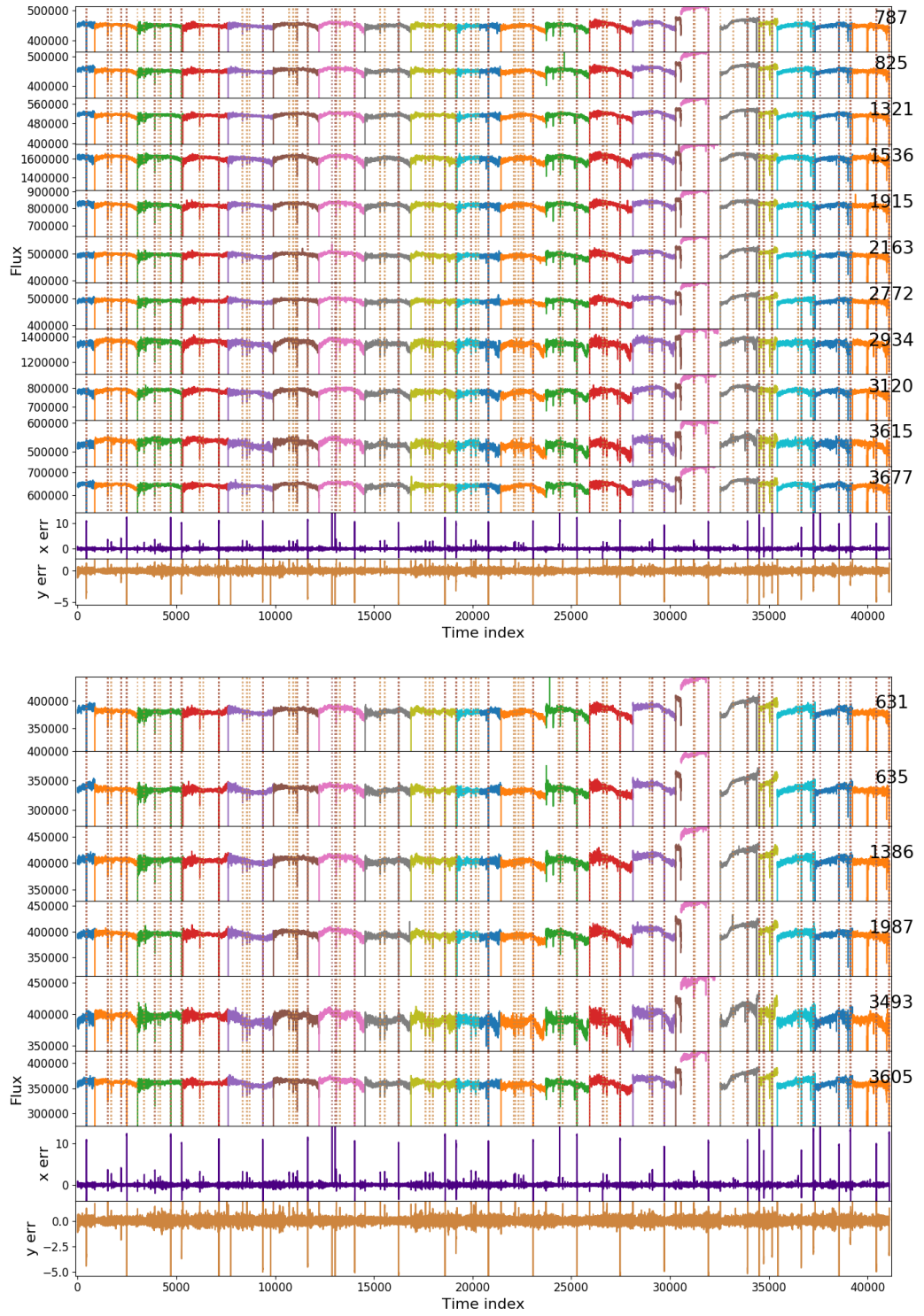


Figure 3.14: Lightcurves showing outlying fluxes for rectangular aperture with width 6. Dotted lines indicate the frames where the autoguider error is greater than three times the RMS, which correlates with the dropout fluxes. The bottom two panels of each figure indicate the autoguider position error for x and y axes. Top: saturated stars, bottom: bright below saturation stars.

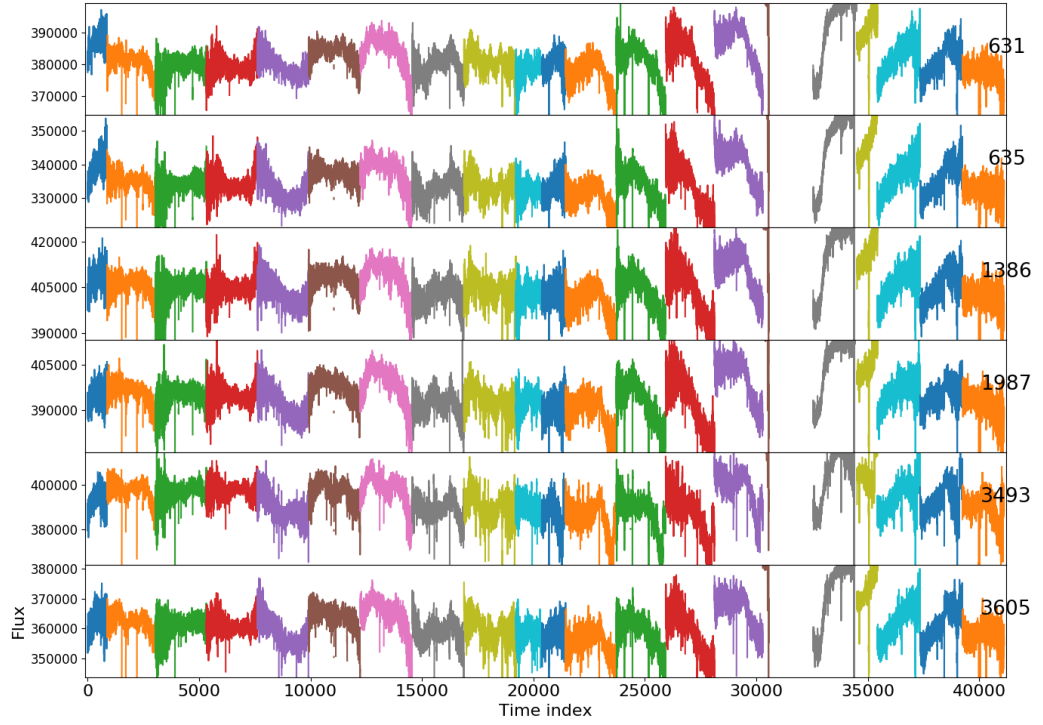
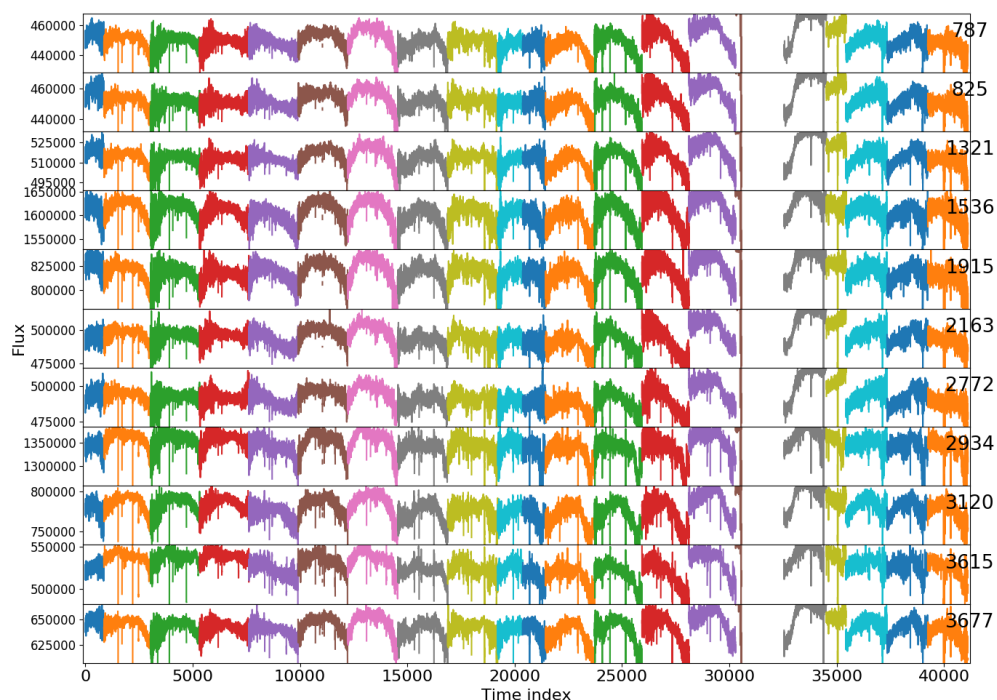
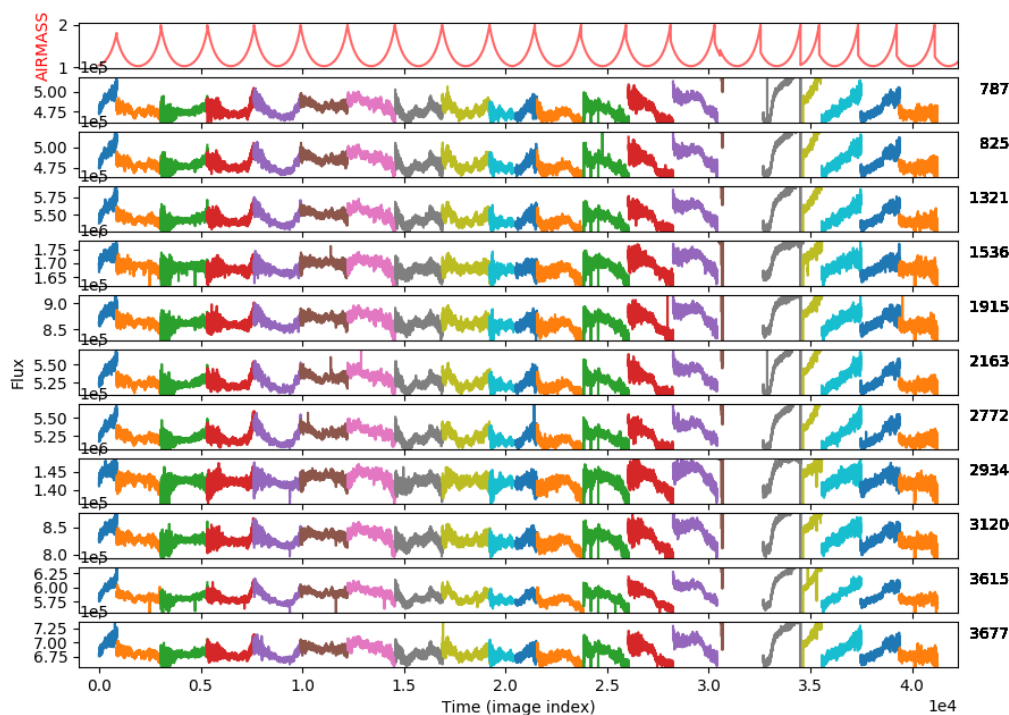


Figure 3.15: Lightcurves of bright unsaturated stars using rectangular apertures with width 6 after removal of outlying flux associated with autoguider error and the first frame of the night. A couple of nights have flux values off the scale.

Section 3.4.3 for a given star R magnitude for comparison. These lightcurves have very similar patterns and levels of flux as when using the measured apertures so are not shown. This is not too surprising as the calculated and measured lengths are similar and its possible the larger length only applies in a few frames. The rest of the chapter uses photometry from the measured lengths.



(a) Width 6



(b) Width 12

Figure 3.16: Lightcurves of saturated stars using rectangular apertures with lengths tailored to the star and widths as specified. These show lightcurves after removal of frames with outlying flux in width 6 lightcurves that were associated with autoguider error and the first frame of the night. A couple of nights have flux values off the scale. The top panel of subplot (b) shows the airmass during observations.

3.4.6 Comparison of rectangular to circular pipeline apertures

Having obtained the lightcurves and removing outlying fluxes associated with autoguider error in Section 3.4.5, I investigate how much flux pipeline apertures lose compared to rectangular apertures for both saturated and bright unsaturated stars. The median flux ratio between circular apertures 3, 4 and 5 and rectangular apertures using a width of 6 pixels are plotted against the rectangular apertures median flux in Figure 3.17. Circular apertures show a large drop off in the fraction of flux captured, which occurs at higher fluxes for apertures 4 and 5. For the brightest star, of the flux captured using the rectangular apertures, just 42%, 57% and 75% of flux is captured by apertures 3, 4 and 5 respectively. We would expect the bright unsaturated stars to contain 100 % of flux, so the 5+% difference likely stems from additional processing in the pipeline affecting the median value. Fluxes measured using circular apertures processed through the pipeline cannot be directly compared to the rectangular apertures as the pipeline detrends for observational factors such as airmass, and excludes flagged data. The pipeline median is also calculated using the full season of data, whereas the rectangular apertures are based on a month's worth. However, it is clear that rectangular apertures capture flux that is lost when using circular apertures for saturated stars.

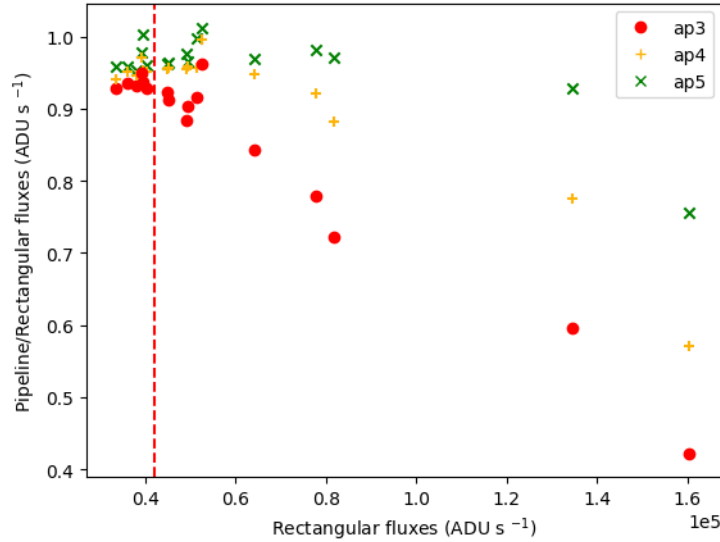


Figure 3.17: Ratio of median measured fluxes using circular apertures 3, 4 and 5 and rectangular apertures with width 6 pixels against median rectangular flux. Values for the same star have the same x value. The red dashed line separates bright unsaturated and saturated stars.

3.4.7 Investigation of light curve precision using rectangular apertures

As the lightcurves from Section 3.4.5 showed trends common to both saturated and bright unsaturated stars, I tried to account for these common trends before determining their precision. I created a standard star by summing the bright unsaturated star fluxes for all stars apart from star 635, which was identified as noisier, especially in night 16 (starting at index around 31000, in pink). For each rectangular aperture width, I divided the fluxes for each star by the standard star to give relative lightcurves. Lightcurves for each night still showed signs of airmass producing curved trends for each night. To account for this, I fitted the relative lightcurve for each night with a second order polynomial.

The resulting lightcurves are shown in Figure 3.18. From these lightcurves I calculated the flux RMS and the mean fractional flux. The mean fractional flux is multiplied by the mean standard star flux to give the mean flux for each star. In these calculations I excluded nights 15 and 16 around index 30000 as they are outlying compared to the other nights, likely due to proximity to the bright moon. Mean flux is plotted against the fractional RMS in Figure 3.19 and mean flux and RMS ranges are given in Table 3.1. We find that using a rectangular aperture width of 6 pixels gives a maximum fractional RMS of 0.015 for saturated stars compared to 0.011 for bright unsaturated stars. Saturated stars show similar maximum RMS values for rectangular width of 6 and 12 pixels.

Compared to the pipeline circular apertures shown in Table 3.2, saturated stars show significantly lower fractional RMS values based on rectangular fluxes, with maximum RMS of 0.015 for width 6 compared to 0.038 using the circular pipeline aperture 3 which has the same width. Rectangular apertures still show lower RMS values when compared to the pipeline circular aperture 5 (with diameter of 12 pixels), with width 12 having a maximum fractional RMS of 0.014 compared to 0.030. This indicates that lightcurves for these saturated stars up to R magnitude of 7.5 are much less noisy using rectangular apertures, showing up to a factor of 2.5 improvement over the standard pipeline aperture and a factor of 2 compared to the larger circular aperture 5.

Bright unsaturated stars are slightly noisier in the rectangular aperture photometry than in the pipeline. Their median fractional RMS is 0.008 using a width of 6 pixels compared to 0.004 in the standard pipeline. This is likely due to more sophisticated detrending of lightcurves in the pipeline and excluding flagged data.

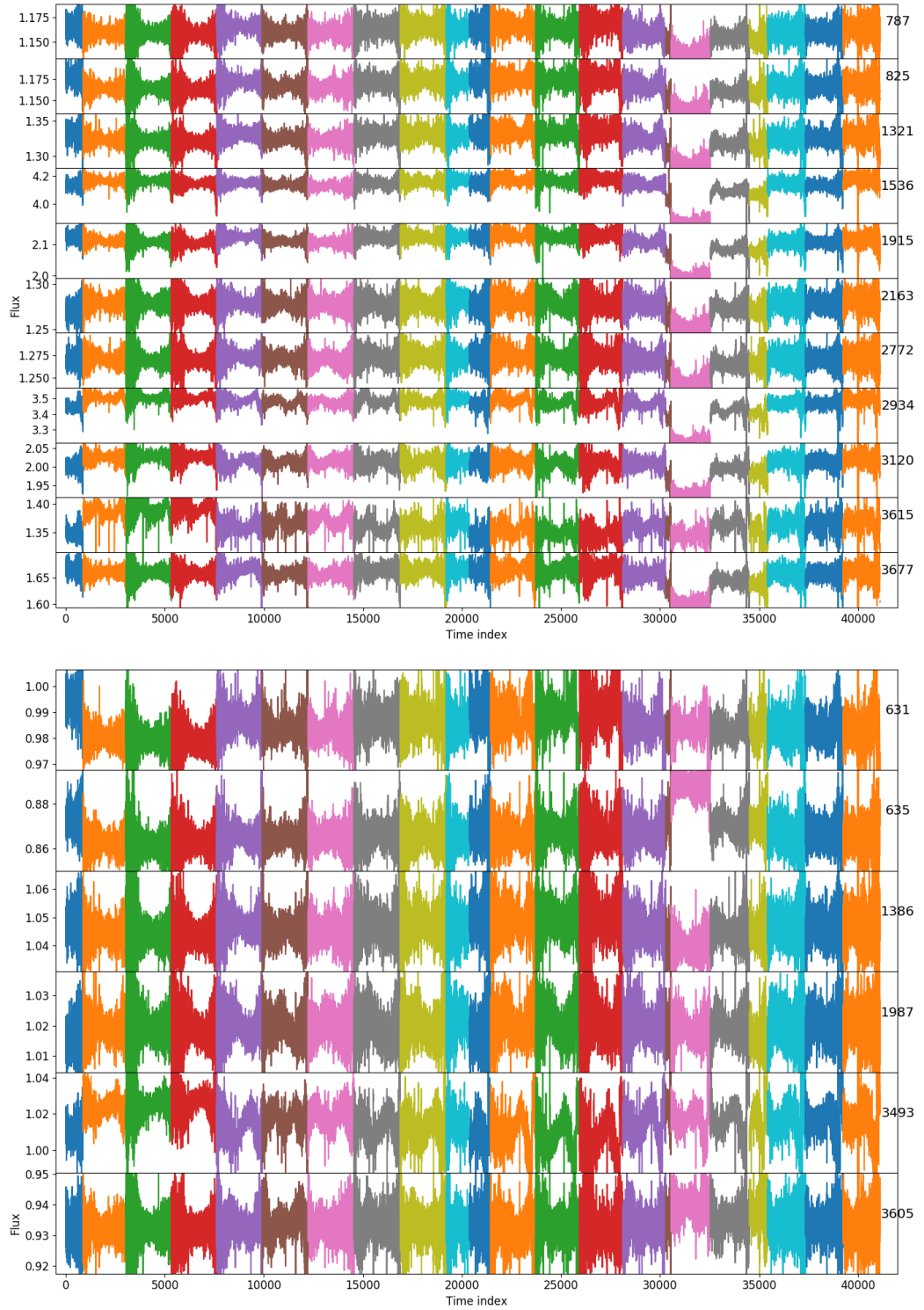


Figure 3.18: Relative flux lightcurves for stars as labelled using a rectangular aperture of width 6. The lightcurve for each star is measured as a fraction of the standard star (the sum of bright unsaturated star fluxes) measured using a rectangular aperture of the same width. The top figure shows saturated stars and the bottom bright unsaturated stars.

Table 3.1: The range of mean fluxes and fractional RMSs of flux for saturated and bright unsaturated stars using different rectangular apertures.

aperture width	star type	flux range	fractional RMS range
6	unsaturated	270174–326495	0.006–0.011
6	saturated	362413–1293896	0.007–0.015
12	unsaturated	295075–352734	0.005–0.008
12	saturated	389171–1370674	0.007–0.014

Table 3.2: The range of mean fluxes and RMS values of flux for saturated and bright unsaturated stars using pipeline apertures.

pipeline aperture	star type	flux range	fractional RMS range
3	unsaturated	30963–37392	0.004–0.011
3	saturated	41025–80027	0.004–0.038
4	unsaturated	31315–38346	0.004–0.004
4	saturated	42740–106021	0.003–0.031
5	unsaturated	31906–39316	0.004–0.004
5	saturated	43080–125789	0.003–0.030

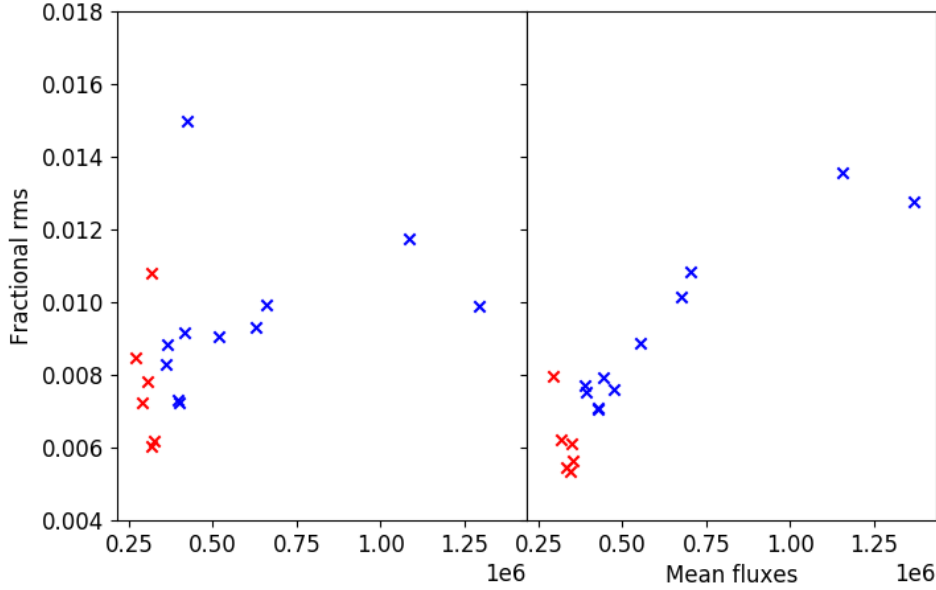


Figure 3.19: Fractional RMS vs the mean flux. Bright unsaturated stars are plotted as red crosses and saturated stars as blue crosses. The different panels show results from rectangular widths of 6 (left) and 12 pixels (right).

If the rectangular photometry of these bright unsaturated stars was processed using *sysrem*, their RMS would be expected to reduce to that of the circular apertures, an approximately 50% reduction.

Currently, the fractional RMS values indicate the lightcurves may be too noisy to recover exoplanet transits. However, the expected percentage decrease in RMS from detrending rectangular aperture photometry of bright unsaturated stars is expected to apply to saturated stars also. Therefore, once detrended, saturated stars are likely to have RMS values of approximately 0.004–0.008, with most of them having similar RMS values to the bright unsaturated stars. Therefore, the data quality of saturated stars is expected to be similar to that of bright, unsaturated stars. The sensitivity to transits should therefore be roughly similar to the rest of the NGTS survey data, so detecting planets in the sub 0.5% depth regime should be possible. Here, smaller transit depths are detectable by phase folding the data over multiple transits observed over the season and binning the data.

To automate this process within the pipeline would need some optimisation but there is no purely computational barrier to implementing it. It would require providing the saturation level of each field, which should be done on a field by field or camera by camera basis. The length-magnitude relationship should be calculated

for each camera by measuring the length of saturated stars in a field and checked in another field. This may be quite computationally expensive but is not prohibitive and should only be required for one or two fields in each camera. After this, the aperture length would be determined by looking up the magnitude in crossmatched catalogue. Detrending in the pipeline using SYSREM afterwards is unlikely to be computationally prohibitive.

3.5 Charge Conservation

The NGTS cameras have adjustable voltage and gain settings which alters how many electrons are produced per ADU and likely affects whether charge is conserved (i.e. whether flux increases linearly at high flux values). In this section I confirm whether charge is conserved in the current operating settings of NGTS and compare this to other voltage and gain settings.

What is charge conservation?

If the charge is conserved then the incoming photon signal is directly proportional to the output ADU values. For the saturated stars, the circular apertures do not contain all the stellar flux as it has bled into neighbouring pixels. However using appropriately sized apertures will capture all the output flux on the CCD image, and if charge is conserved then this output ADU will be directly proportional to the incoming photon signal from the star. If charge is conserved, when a pixel nears saturation, the photon signal is not lost but induced electrons are redirected to neighbouring pixels.

Why charge conservation is important

If charge is not conserved then the measured electrons are not directly proportional to measured flux and the number of incoming photons, therefore the measured signal is not an accurate representation of photons received at the CCD chip. NGTS relies on detecting periodic percent or subpercent decreases in starlight to fulfill its purpose of finding transiting exoplanets, so requires accurate, directly proportional photometry.

3.5.1 The camera settings

The NGTS cameras are a custom version of the Andor iKon-L 936 camera, and have three collection phase voltage settings (VI 168, VI 190 and VI 227), where a higher

value refers to a lower voltage. The collection phase voltage alters the maximum electron signal that can be held in the pixel well (O’Connor, 2015). The cameras have gain settings PAG1 and PAG2, where PAG2 has lower gain factors, indicating fewer electrons per resulting ADU. Measurements of the gain values are given in Section 3.6 below. The standard operating mode of NGTS is a voltage setting of VI227 with gain setting PAG2. This was selected previously to optimise the range of values NGTS is sensitive to.

3.5.2 Method to test charge conservation

Observations

For all 11 cameras that were on-sky in March 2016, a series of sky exposures were taken with varying exposure time to allow charge conservation to be investigated. Exposures were taken of directly overhead (i.e. with telescopes pointing at the zenith) as star fluxes are maximised when travelling through less atmosphere. Each camera imaged their own field, although there may be some overlap on sky. Exposure lengths were 2, 4, 6, 8, 10, 12, 15, 18, 22, 26, and 30 seconds. Exposures with length 4–30 seconds were interleaved with 2 second exposures to test for change between the 2 second exposures throughout the observation. This exposure cycle was repeated again immediately afterwards. For reference, the NGTS survey uses exposure lengths of 10 seconds.

Determining objects and apertures

Frames from different cameras were analysed separately. 22 objects were hand selected for each field in the 30 second frame using SAO ds9 (Joye and Mandel, 2003). The brightest stars were found to have V magnitudes of 6.3 using the astrometrically solved images to identify the stars in Simbad (Wenger et al., 2000). Circular apertures were drawn around the stars to contain their flux in the most extended direction. Frames taken using the same camera use the same objects to allow comparison of the same stars at different exposure times.

For VI227 and VI190 frames, flux blooms in the vertical direction so twice the circular aperture radius in the longest exposure was used to give the rectangular aperture’s height. After experimenting with different widths, I selected an aperture width of 14 pixels for VI227 and a width of 20 pixels for VI190 (as the flux spreads more in a horizontal direction than for VI227). VI168 frames display a more circular spread of flux, with the brightest blooming more horizontally. For VI168, I opted for circular apertures with radii determined from the 30 second frame.

Aperture photometry

I performed aperture photometry on images after background subtraction with SEP. Flux is measured at the coordinates of the 22 selected objects using the apertures determined in Section 3.5.2. For VI168, aperture photometry is performed using SEP's `sum_circle` function and for VI227 and VI190, photutils' `Rectangular Aperture` and `aperture_photometry` functions are used. We did not expect to see any significant pixel drifts during the exposures, thanks to excellent guiding in NGTS. However as apertures are not recentred between frames, I plotted the apertures over the selected stars in each frame to check that the stars are contained within the apertures in all frames.

3.5.3 Data Analysis

Peak flux

For each object, the peak flux is identified as the maximum pixel flux value within its aperture in the background subtracted flux images. Peak flux values for each object are plotted against the expected flux (calculated in Section 3.5.3 below) for figures within Section 3.5.4.

The theoretical maximum peak pixel flux is the maximum output value set by the Analogue-to-Digital Converter as discussed in Section 2.0.1. NGTS CCDs use a 16 bit converter so the maximum pixel value is 65535 ADU. I multiplied the maximum pixel value by the gain (as in Equation 3.1) to find the maximum pixel value in units of electrons. The maximum pixel value is also plotted for figures within Section 3.5.4.

$$flux(e^-s) = flux(ADU) \times gain \quad (3.1)$$

Flux values from different gain settings can be compared when in electron units. I discuss how gain values were measured in Section 3.6.

Measured flux

Aperture photometry gives the measured fluxes of stars in each frame. I plotted the selected star fluxes for frames with a two second exposure time, to confirm these remained consistent over the course of observations.

The mean measured flux is calculated for each star from exposures of the same length. The measured flux error is calculated as the root mean square value over the mean. Measured fluxes are converted from ADU to electron units by

multiplying by the gain. This conversion allows comparison of fluxes from different gain settings.

Calculating Expected Flux

I test whether charge is conserved by comparing the measured flux value to that expected for each star. Expected flux is calculated by scaling up the mean flux in the two second exposures $flux_{2secs}$ to the exposure times in seconds, t_{exp} , in the other frames.

This scaling factor is not exactly the increase in exposure time as the shutter travel time, dt , needs to be accounted for. I tested a number of shutter travel times, finding 0.035 seconds best as this centred lower flux levels of measured/expected flux at 1.

Expected flux ($flux_{exp}$) is calculated as:

$$flux_{exp} = s_f \times flux_{2secs} \times gain \quad (3.2)$$

where the scaling factor $s_f = (t_{exp} + dt)/2$.

Measured/expected flux ratio

I investigated whether measured flux is conserved at higher flux levels by plotting the measured flux/ expected flux ratio against expected flux for the selected stars. Plotting against expected flux rather than exposure time accounts for star brightness so we can easily see if measured flux drops off for brighter stars. Errors on measured/expected flux are found by combining errors on measured and expected flux using the quotient method. These plots are the top panels in figures in Section 3.5.4.

I also plot the peak pixel flux against expected aperture flux for all selected objects in Section 3.5.4. This allows us to confirm whether the pixels are saturated and judge star brightness. If measured/expected flux stays at a constant level of 1 while the peak fluxes are at their maximum value then the charge is conserved in conditions of pixel saturation.

3.5.4 Results

Investigating changing gain

In the first stage, I investigated whether charge is conserved for cameras 805 and 809 when using the standard NGTS voltage VI227. These cameras were selected as 809 represents a camera with relatively a low PAG1 gain value, while that of 805 is much

higher (see Section 3.6). Figure 3.20 shows results using standard NGTS settings with gain PAG2. For both cameras, we can see that the measured/expected flux drops significantly below 1 at higher expected flux values, indicating that flux is lost and therefore charge is not conserved. Specifically, measured/expected flux drops down to just below 0.90 for the highest expected flux values in camera 805 and to 0.80 in camera 809, indicating 10 % and 20 % flux loss respectively. Peak pixel values for higher expected flux values (greater than approximately 1×10^7 electrons) are constant for both cameras, indicating pixel saturation. Together these indicate that charge is not conserved using the standard NGTS voltage VI227 and gain setting PAG2.

I then investigated charge conservation using the same stars when the gain setting is changed to PAG1 and voltage remains the same (VI227). Figure 3.21 shows for both cameras, the level of measured/expected flux stays reasonably constant around 1 even at all expected flux values. There is no drop off at higher expected flux values, i.e. for brighter stars. Theoretical maximum pixel values in electron units are much higher in PAG1 than in PAG2, especially for camera 805 due to its higher PAG1 gain value. While for PAG2, peak pixel values are close to the theoretical maximum, they are much lower than the theoretical maximum in PAG1, indicating that a large amount of the dynamic range of the ADC is not being used. Again, peak pixel values for higher expected flux values are constant for both cameras, indicating pixel saturation. Combined, the lack of flux drop off and constant peak pixel values at high expected flux means that while an individual pixel reaches its maximum value and saturates, the additional flux is not lost, but diverted to neighbouring pixels so overall the charge is conserved to approximately the 1 % level in the aperture.

Investigating different voltages

Having established that charge is conserved using gain setting PAG1 when the voltage is VI227, I investigated higher voltages to see if charge remained conserved. In Andor cameras, VI number is anti-correlated with physical voltage and the current NGTS setting, VI227 is the lowest programmable voltage for the NGTS cameras. Higher voltages have the advantage of larger well depth, meaning less blooming, so smaller apertures can be used and the dynamical range is increased, meaning more differentiation between flux levels. Figure 3.22 shows that for both voltages, dynamical range is increased compared to voltage VI227, as peak pixel values are closer to the theoretical maximum. However, as voltage increases, more flux is lost. Hence, flux is best conserved using the standard NGTS voltage VI227 and changing

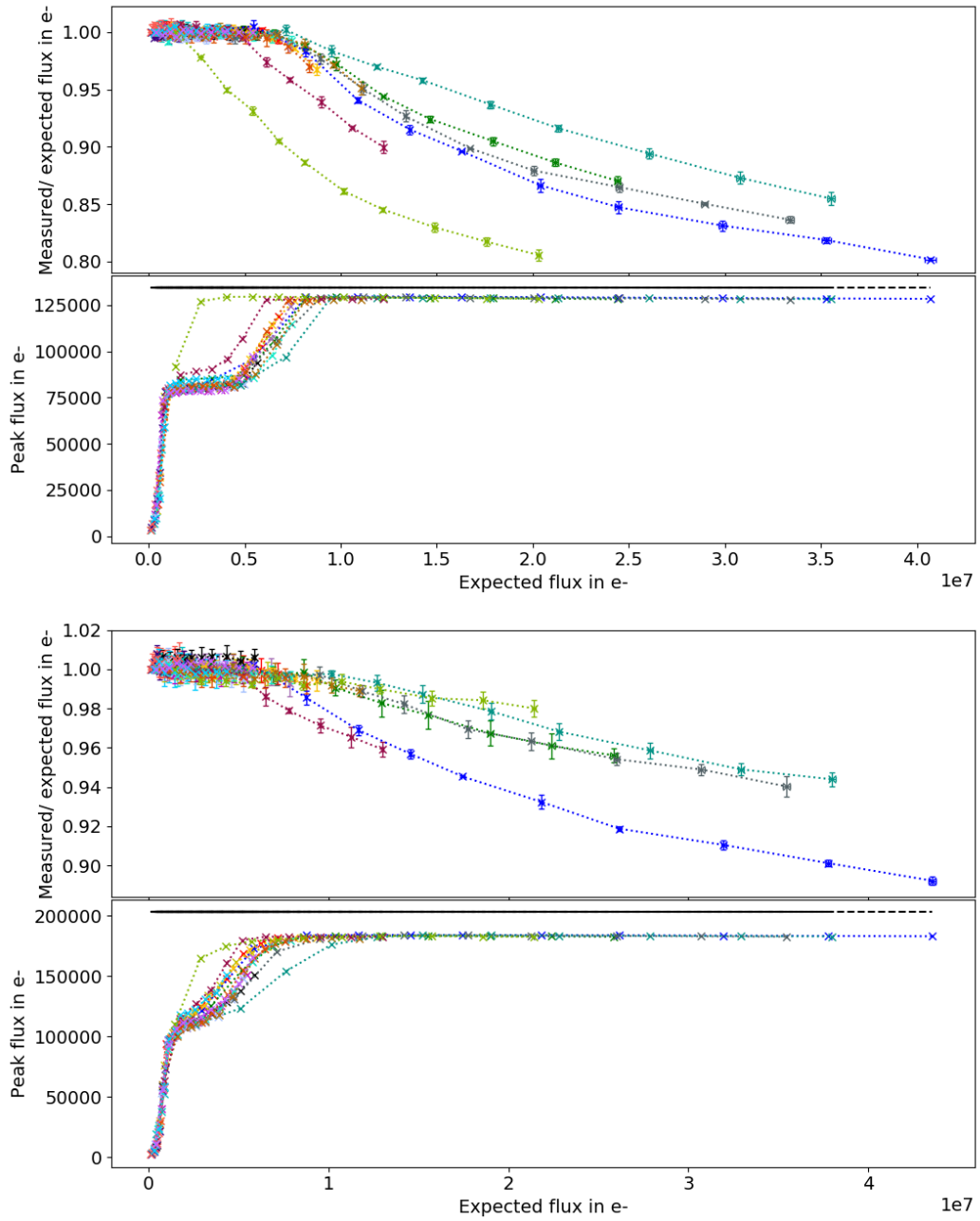


Figure 3.20: Flux vs expected flux values using standard NGTS settings, voltage VI227 and gain PAG2. The top figure shows results for camera 809 and the bottom camera 805. The top panel of each figure shows the ratio of mean measured flux/expected flux, while the bottom shows peak pixel values. The black horizontal line shows the theoretical maximum pixel value in electron units.

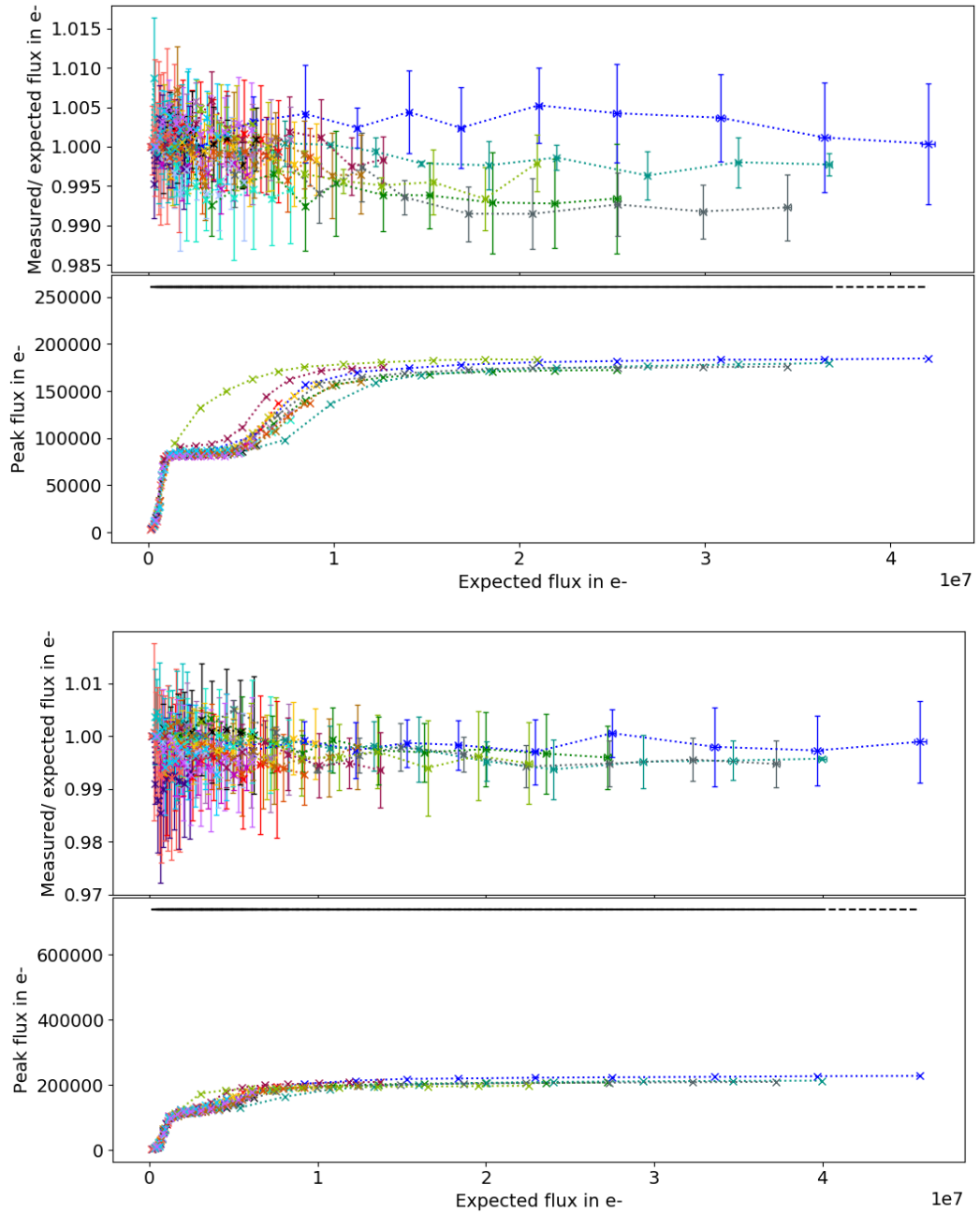


Figure 3.21: Flux vs expected flux values using standard NGTS voltage VI227 but changing the gain to PAG1. The top figure shows results for camera 809 and the bottom camera 805. The top panel of each figure shows the ratio of mean measured flux/ expected flux, while the bottom shows peak pixel values. The black horizontal line shows the theoretical maximum pixel value in electron units.

the gain setting to PAG1.

Investigating all cameras

Having established that charge is best conserved using VI227 and PAG1 for cameras 805 and 809, I checked whether charge was conserved using these settings for the other cameras. Data was also collected for cameras 801, 803, 804, 806, 808, 810, 811, 812 and 813. I found that charge was conserved to the $\sim 1\%$ level using these settings for all cameras.

3.5.5 Conclusion

Of the investigated gain and voltage combinations, only the current voltage setting VI227 and a higher gain setting (PAG1) shows charge conservation to the $\sim 1\%$ level for stars up to V magnitude 6.3. Using a higher voltage setting would be preferable due to decreased blooming but charge was not conserved at higher voltages. Peak flux plots (see Section 3.5.3) display a plateau before increasing to the maximum measured flux value at higher expected flux values.

3.6 Gain calculation

Flux is typically measured in ADU values which is calculated by the ADC from the number of free electrons and the gain value. To compare flux values from different gain settings, flux values must be converted from ADU to electron units. This requires the gain value for each camera, i.e. how many electrons are converted into 1 ADU output.

Exposures were taken for all cameras with a uniform background lighting level using a closed dome, with uncovered telescopes pointing at the zenith with all lights on inside. Zero length exposures were taken to act as bias frames. Exposures were taken with times between 1 second and the maximum exposure length at one or two second intervals. Exposures are expected to be saturated before reaching the maximum exposure length. Two exposures are taken for each exposure length, with a 1 second exposure taken in between them. These exposures were taken by James McCormac and Thomas Loudon.

For each exposure length, the pair of exposures are bias subtracted. The central 200 square pixels of both frames are used to find an average frame, from which a mean flux value is found. The difference between the two frames is found and flux variance is calculated as the average of the squared deviations in the central region.

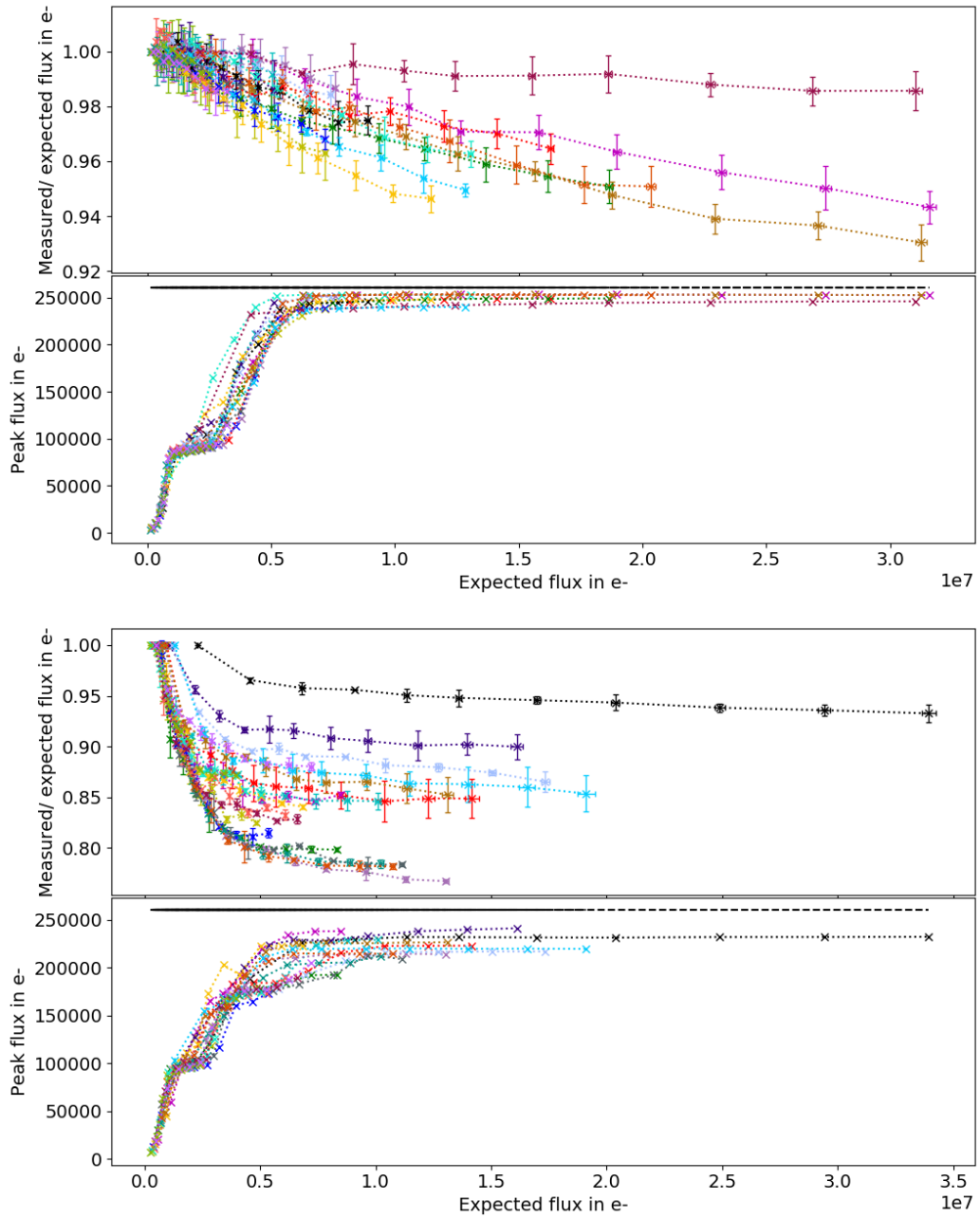


Figure 3.22: Flux vs expected flux values using gain setting PAG1 and other voltages for camera 809. The top figure shows VI190 and the bottom shows VI168. The top panel of each figure shows the ratio of mean measured flux/ expected flux, while the bottom shows peak pixel values. The black horizontal line shows the theoretical maximum pixel value in electron units.

Camera	PAG1 gain (e^-s/ADU)	PAG2 gain (e^-s/ADU)
801	3.63	1.95
802	5.36	2.78
803	5.46	2.89
804	3.60	2.01
805	11.27	3.10
806	3.87	2.29
807	3.90	2.10
808	3.96	2.14
809	3.97	2.05
810	3.72	2.01
811	4.09	2.18
812	3.87	2.08
813	4.02	2.16

Table 3.3: Table shows measured gain values from both PAG settings for all cameras.

Plots of mean flux against variance show a linear increase up until variance drops again due to saturation. A straight line is fitted to the linear increase, ignoring any clear outlying points. Gain in units of electrons per ADU is 1 over the slope of the mean count vs variance graph. Plots for gain setting PAG1 using voltage setting VI227, can be seen for each camera in Figure 3.23, a similar plot for PAG2 is not shown. Gain values for both PAG1 and PAG2 are recorded in Table 3.3.

Gain values were calculated for all cameras using voltage setting VI227 and gain settings PAG1 and PAG2. As expected, gain values are lower in PAG2, meaning fewer electrons produce one ADU. There is clear variety in the actual gain values, especially for PAG1, with camera 805 in particular having a much higher gain value than other cameras. These gain values are used to calculate the expected flux in Section 3.5.3, allowing us to compare charge conservation in different gain settings.

3.7 Conclusions

3.7.1 Investigation of saturated stars' nature

To determine the nature of the saturated stars, they were crossmatched with Gaia DR2 as discussed in Section 3.4.3 to provide Gaia colours (bp_rp) and absolute magnitudes and plot on a HR diagram. As Gaia DR2 was only released after the bulk of the work on this chapter had been completed, it was not possible to do this

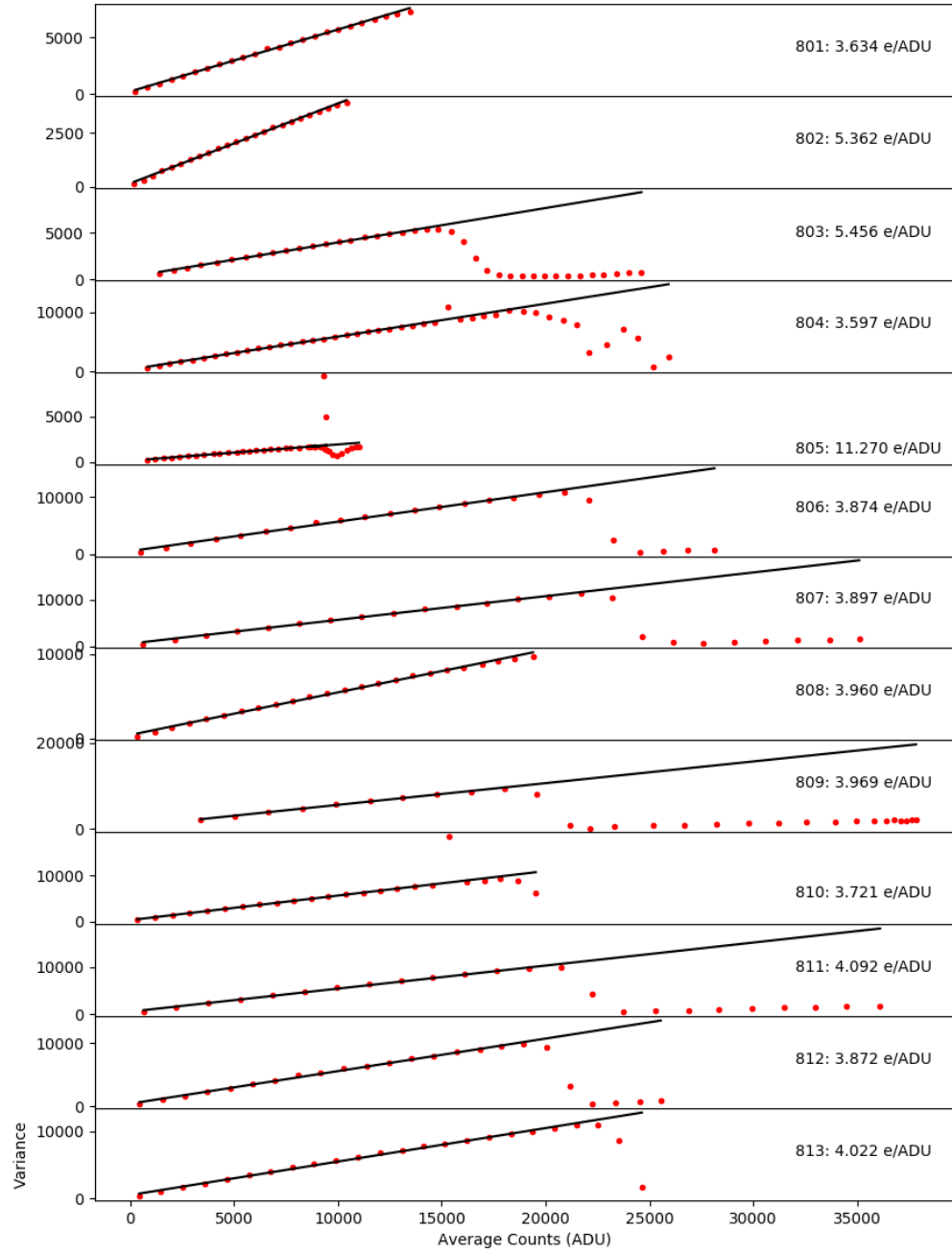


Figure 3.23: Plots of mean flux against variance used to calculate the gain for VI227, PAG 1 (both in units of ADU). Each subplot shows a different camera.

at the start of the project. This identified one saturated star as a clear giant, and suggested three are sub-giants with the remaining seven likely main sequence stars. None of the stars are identified as variable in Gaia DR2.

3.7.2 Summary

- I studied the NGTS survey field NG0304-1115 and found 11 saturated objects, with R magnitudes lower than 9.
- Stable, consistent photometry with a fractional RMS below 0.005 can be recovered for 8 of them, reaching a R magnitude of 8.35, if larger circular apertures (of 5 pixel radius) are used, at the expense of degraded photometry below a R magnitude of 11.6.
- Adoption of rectangular apertures allows reliable photometry to be recovered for all the saturated stars in this field, which reach R magnitudes of up to 7.5.
- Although the photometry in rectangular apertures is stable to the 1.5% level or better, this is expected to improve if the photometry is further processed in the pipeline using SYSREM, as bright unsaturated stars are expected to have similar RMS values between the pipeline and rectangular apertures. In this case, the fractional RMS of saturated stars is likely to decrease to the 0.5% level, giving similar data quality to bright unsaturated stars. Detecting planets at depths around 0.5% should therefore be possible, as shown by the rest of the NGTS survey. However it does not recover reliable absolute flux values due to non-linearity of detectors (where for the brighter stars, the measured flux is up to 20% lower than would be expected).
- The effect of changing gain to acquire photometry of the saturated stars would recover these 11 bright valuable targets in this field. It would slightly reduce the sensitivity to detect small changes in flux, which would likely decrease the sensitivity to detect transits but only for the faintest targets in the target luminosity range.
- The disadvantage of changing the gain setting is that data would not be consistent with previous data taken and this distinction would be hard to track. This is especially the case as fields are shifted on and off the survey schedule (as two fields are observed on the same night) causing issues with operational logistics. Hence it was decided to retain the current settings.

- Potentially hundreds of saturated stars could be recovered a year. As NGTS observes 3 fields per telescope per year this gives 36 fields a year. Assuming this field with 11 saturated stars is typical then gives $36 \times 11 = 396$ objects a year. Assuming this field is typical and SYSREM improves the photometric precision as expected, 0.5% unbinned photometry could be recoverable. A 0.5% transit around an early M dwarf (M1) gives a $3.5 R_{\oplus}$ planet, which should then be detectable over multiple transits. However, saturated stars are more likely to be earlier type stars as few M dwarfs will be sufficiently bright to saturate. In this case, a 0.5% transit of a solar-type star would be caused by a $0.7 R_J$ planet, which is smaller than Saturn.
- However, whether images could be post-processed to recover saturated stars using current settings is less straight forward. True linearity is not essential, it needs only be sufficient to capture the small range of variability in the transit light curve. Therefore, it only needs to be linear over that small range of brightness. The main issue is correcting for airmass, which non-linearity can make more complicated. This might need additional special-case processing for saturated stars, requiring additional work to understand what is needed.
- These objects will not currently be studied further by the NGTS survey using this method.
- The results here are in principle generalisable to other telescopes. However this work highlights that for studying saturated stars to be practical, the instrument really needs to be understood: both the detector and the read-out electronics. Ideally the instrument will have been designed with study of saturated stars in mind. For commercial off-the-shelf instruments such as NGTS, this is not easy, even with supplier engagement in modifications.
- Looking at other surveys, saturated star photometry is being studied for the future PLATO mission (Rauer et al., 2016), which is interested in finding planets around the brightest stars out to the habitable zone and determining the properties of their stars. For this mission, the electronics are being designed from scratch with a focus on charge conservation.

3.7.3 End state

After discussion, it was decided that the gain settings for NGTS would not be changed to allow for charge conservation in the normal surveying mode. This decision was made to keep the data consistent with earlier observations. This means

that currently NGTS observations cannot be used to investigate saturated stars using the proposed method of specialised apertures in Section 3.4.5. If this decision is reviewed in the future then the gain setting could be changed to PAG1 to investigate these valuable targets. Saturated stars could then be processed in a separate pipeline with rectangular apertures to achieve higher precision photometry than in the standard pipeline, as demonstrated in this chapter.

Chapter 4

A Transiting Exoplanet Survey in the Habitable Zones of six mid-to-late M dwarfs with NITES

4.1 Introduction

In recent years, M dwarfs have become attractive targets for transit surveys. In part, this is due to their small size and the resulting relative ease of detection for rocky planets. For example, an Earth-sized planet around a late M dwarf (M8) would produce a transit depth of 1 % – 100 times deeper than the transit of the same planet around a solar-sized host. Furthermore, as M dwarfs are less luminous than solar-type stars, their habitable zones (defined as the orbital distance where the equilibrium temperature range allows terrestrial-mass planets with a $\text{CO}_2\text{--H}_2\text{O--N}_2$ atmosphere to sustain surface liquid water (e.g. Kasting et al., 1993; Kopparapu et al., 2013)) are much closer-in. M dwarf habitable zones are therefore more favourable for transit detection in a given observing season due to the shorter orbital periods, and any planets therein are more likely to transit due to the more favourable transit geometry. Combined, these factors mean that discovering transiting terrestrial planets in the habitable zone is much more likely around M dwarfs than around larger solar-type stars.

However, despite M dwarfs comprising over 70 % of stars in our solar neighbourhood (Henry et al., 2006; Winters et al., 2019), comparatively few exoplanets have been found around them. Most transiting exoplanets have been found in wide

field surveys. Traditionally, these surveys have been focused on brighter solar-type stars, and have used bluer filters not optimised for M dwarfs, hence most discoveries by surveys from SuperWASP (Pollacco et al., 2006) to Kepler (Borucki et al., 2010) have been around FGK dwarfs. Furthermore, as M dwarfs are intrinsically faint they generally have fainter apparent magnitudes, making it more difficult to measure the small change in flux caused by a transit. This is especially true in wide field surveys where exposure time is optimised to maximise the number of observable targets.

More recent exoplanet surveys such as NGTS (Wheatley et al., 2018) and TESS (Ricker et al., 2015) have been using red sensitive cameras more favourable to the infrared wavelengths where M dwarfs are brighter. Red sensitive cameras aid in NGTS’ goal to find smaller exoplanets from the ground, specifically increasing sensitivity to Neptune-sized planets, and also aid TESS’ primary mission to discover 50 small planets with measurable masses. Small planets are easier to discover around smaller stars where they produce larger transit signals. Hence, TESS observes in the 600–1000 nm bandpass, optimised for early-to-mid M dwarfs (M0–M5), which are also abundant in our solar neighbourhood and relatively understudied in exoplanet searches (Ricker et al., 2015). While both NGTS and TESS have discovered exoplanets around M dwarfs (Bayliss et al., 2018; Crossfield et al., 2019; Vanderspek et al., 2019), they both have relatively large fields of view and are best suited to brighter stars. Both surveys use small aperture telescopes (20 and 10cm respectively), limiting their collection of photons and making it difficult to reach sufficient precision for fainter, later type M dwarfs. In addition, TESS has large pixels spanning 21 arcseconds meaning there are multiple stars within the same pixel (Ricker et al., 2015). This will lead to more false positives and requires additional vetting to confirm whether the signal originates from the brighter TESS target. This is achieved through a combination of follow up observations, centroid analysis and calculation of the flux contribution from other stars. The challenges of large pixels for transit surveys are discussed further in e.g. Sullivan et al. (2015); Collins et al. (2018); Giacalone and Dressing (2020).

A small number of targeted M dwarf surveys have either taken place or are ongoing, including the MEarth project (Irwin et al., 2009b; Nutzman and Charbonneau, 2008), which has a northern observatory at the Fred Lawrence Whipple Observatory (FLWO) on Mount Hopkins, and a southern observatory at the Cerro Tololo Inter-American Observatory in Chile. MEarth’s observing strategy is to monitor a number of M dwarf stars simultaneously by cycling between them and taking photometric measurements every 20–30 minutes (Irwin et al., 2009b, 2014). Data is reduced in real time, and if a dimming event is detected then high cadence obser-

vations are triggered allowing closer monitoring of a potential transit event. This allows the project to monitor a large number of stars in a given night, but trigger events are more susceptible to being false alarms such as stellar activity, and data analysis is more challenging. Nevertheless, MEarth has discovered three exoplanets to date, including the highly studied GJ 1214b (Charbonneau et al., 2009), and has also been used in the confirmation of exoplanets discovered by other telescopes.

A number of compact multi-planet systems have also been found around M dwarfs, most notably Trappist-1 (Gillon et al., 2016), allowing investigation of their dynamics and evolution. Transits around the M8 dwarf Trappist-1 were initially detected (Gillon et al., 2016) in a targeted survey of M dwarfs by TRAPPIST (Gillon et al., 2011), a small aperture telescope (60cm) at a prime observing site (La Silla). Follow-up observations uncovered that Trappist-1 has a compact system of seven transiting Earth-sized planets, all orbiting within 19 days, and with three planets having equilibrium temperatures consistent with the habitable zone. The impact of this system’s discovery, with its seven Earth-sized planets, has been huge, with an entire four day conference in June 2019 dedicated to this one system¹. Since the announcement of planets in the Trappist-1 system (Gillon et al., 2016), 69 papers have been published on the system. The original Trappist-1 planet discovery paper has been cited 254 times, and the announcement of seven Earth-sized planets (Gillon et al., 2017) 493 times².

Flaring rates can also have a large impact on the potential habitability of planets, with mid-to-late M dwarfs displaying much higher flaring rates than for solar-type stars. Large fractions of late-type M dwarfs have been known to exhibit activity signatures that indicate flaring, namely $H\alpha$, with Schmidt et al. (2007) finding this for 95 % of M7 dwarfs in their volume limited sample of ultracool dwarfs from 2MASS. The Kepler mission was transformative for the studies of flares, providing the most data on flares to date, with The Kepler Flare Catalog (Davenport, 2016) producing 4041 targets with at least 100 flares. However due to the Kepler bandpass, most of these targets are F, G and K dwarfs and the number of flaring late M dwarfs is in single figures. Hawley et al. (2014) analysed the Kepler short cadence data of six sufficiently bright stars with spectral types M1–5, three of the most active and three of the most inactive M dwarfs, as determined by $H\alpha$ emission. They found these stars span a large range of flare energy and frequency, blurring the distinction between active and inactive M dwarfs but later type active M dwarfs displayed more frequent flares than earlier inactive M dwarfs. TESS observations are

¹<https://events.uliege.be/trappist-1/>

²All as of 27th January 2020

now extending flare observations to M dwarfs, with Gunther et al. (2020) identifying 632 flaring M dwarfs in the first two months of short cadence data, of which 179 are later than M4.5. They find M4–M6 dwarfs are most likely to flare, with up to 30 % of them flaring. However the number of targets, and therefore flare detections, for spectral types M7 and later are limited.

Flares are also being studied from the ground in transit surveys. The ground-based wide-field surveys, including the Next Generation Transit Survey (NGTS) is contributing to flare catalogues, aided by its short cadence and red-sensitive cameras, including the detection of a $\Delta V \sim -10$ flare from a L2.5 dwarf (Jackman et al., 2018). MEarth has also studied flaring rates from their targeted search of M dwarfs, finding 34 stars with large flares out of 2226 surveyed (Mondrik et al., 2019). With typical cadence of 20 minutes, they were restricted to larger longer duration flares. The targeted survey with the Near-Infrared Transiting ExoplanetS (NITES) telescope can contribute to flare observations of mid-to-late M dwarfs, with its red-sensitive bandpass and high cadence observations.

The habitability of planets around M dwarfs has long been debated but has become more relevant in recent years with Keplers discovery of closely packed planetary systems of small planets, with a third of these rocky planets within the habitable zone (Shields et al., 2016). M dwarfs exhibit significant X-ray and UV emission along with flare activity, even M dwarfs which are less active (France et al., 2013, 2016). Extreme XUV radiation is especially an issue during the extended pre-main sequence phase of M dwarfs (Baraffe et al., 1998, 2015), where later-type M dwarfs exhibit saturated emission levels for over 1 Gyr (Scalo et al., 2007; Buccino et al., 2007), extending the period over which close in habitable zone planets may be bombarded with the XUV radiation. Higher flare rates and XUV radiation are generally considered to adversely affect habitability, as repeated flaring can erode protective planetary atmospheres (Lammer et al., 2007), significantly deplete ozone layers (Segura et al., 2010; Lingam and Loeb, 2017; Tilley et al., 2019) and cause runaway greenhouse and hydrodynamic escape, potentially losing oceans worth of water and being left desiccated (Luger and Barnes, 2015). High flaring and XUV flux levels are generally considered to be negative for life, causing detrimental DNA mutation and frequent sterilisation events (Atri, 2017). However numerical modelling and tests on microorganisms suggest a small percentage of organisms will survive (Atri, 2017; Abrevaya et al., 2020). Additionally flares may be the only way for M dwarfs to provide the required UV radiation during stages of prebiotic chemistry (Rimmer et al., 2018) that are necessary for life to later develop.

Though currently few in number, nearby M dwarf exoplanets are extremely

valuable as they represent our best chance of characterising terrestrial exoplanets and constraining their atmospheres with near future instruments such as the James Webb Space Telescope (JWST) (Barstow and Irwin, 2016; Morley et al., 2017; Fujii et al., 2018; Fauchez et al., 2019; Lustig-Yaeger et al., 2019; Wunderlich et al., 2019). The enormous impact these types of discoveries can have warrants their observation in targeted surveys.

This chapter describes one such survey. Section 4.2 presents the survey strategy and data collection. In Section 4.3 manual inspection of nightly lightcurves, including observations of interest are discussed, along with the calculation of phase coverage and habitable zone boundaries. An automated search for planets using the Box Least Squares (BLS) algorithm and transit injections are described in Section 4.4. I discuss the findings in Section 4.5.

4.2 Observations

4.2.1 Survey strategy

An initial set of targets were selected from spectroscopically confirmed M6-9 dwarfs sourced from J Gagne’s webpage³, which made use of the Database of Ultracool parallax (Dupuy and Liu, 2012). I filtered for targets brighter than $J = 13$ mag and with declination north of -15 degrees to suit observing from the Roque de Los Muchachos site. Potential targets were checked on Simbad (Wenger et al., 2000) to remove known multiple star systems (to avoid confusion with eclipsing binary systems), and to ensure observations would not be obscured by any close bright stars. This resulted in 31 targets for our initial target list. After the Gaia DR2 data release (Gaia Collaboration et al., 2016, 2018), additional red dwarf targets were identified from stars brighter than $G_{RP} = 12$, and with colour $G_{BP} - G_{RP} > 3.3$, and I added two stars to the target list.

In contrast to MEarth, our strategy was to stay on the same target for as long as possible, simplifying the observation and analysis pipelines. This strategy also made false alarms much less likely, as a few spurious points of lower flux could be ignored, and with full night coverage activity signals were easier to identify. One or two targets were scheduled on any given night depending on their observability. Where two targets were scheduled and their observability overlapped, one was chosen as the priority target and observed until it set. In the initial survey, brighter stars and those that were visible for longer were favoured on a given night, while trying to observe most of the targets. In the full survey, target selection was based on the

³<https://jgagneastro.com/list-of-m6-m9-dwarfs/>

expected increase in phase coverage of a given night’s observations (see Section 4.3.3 for details).

Initial observations for the survey began in May 2016, with the full survey commencing in April 2017 and ending in October 2019 with observations between the two surveys overlapping. In the initial survey we observed 22 targets, with priority given to brighter targets and those with more favourable observability over the year. The remaining targets were not observed owing to either their lower priority compared to others or their magnitude, as initial observations showed that observing targets fainter than $J = 11.5$ produced lower precision light curves (root mean square (RMS) less than 1 % over the night).

The full survey focused on increasing the phase coverage of the six Mdwarfs presented in the rest of this chapter. These six targets were chosen based on their observability throughout the year from our observing site, brightness, and any potential features which had previously been observed. The data for these objects from the initial survey was also included. Spectral type was also considered, with preference given to later type Mdwarfs, as their habitable zones are at shorter orbital distances. Stellar parameters for the selected stars are listed in Table 4.1. The breakdown of the number of nights each target was observed is given in Table 4.3, and the number of hours (including flares) in Table 4.2. In total, there are 1484.8 hours of observations across the six targets, after filtering out noisy nights from the analysis (see Section 4.4.1). The median number of hours per target is 282.9, with minimum of 249.0 and maximum of 337.1 hours.

4.2.2 Observations

The Near-Infrared Transiting ExoplanetS (NITES) 0.4m telescope is situated at the Roque de Los Muchachos Observatory in La Palma. NITES consists of a Meade 16 inch LX200R telescope with attached FLI ProLine PL4710 camera. NITES has a field of view of 11.26×11.26 arcminutes and a pixel scale of 0.66 arcseconds per pixel. The detector has peak quantum efficiency greater than 90 % around 800 nm, and is sensitive out to 1 micron (McCormac et al., 2014), making it optimal for cooler, redder Mdwarfs. More details about the telescope can be found in McCormac et al. (2014). It is run remotely by members of the NITES observing team at the University of Warwick.

Observing plans, including target, calibration and flat observations, were made and run using the ACP Observatory Control software⁴. This uses MaxIm DL

⁴<http://acp.dc3.com/index2.html>

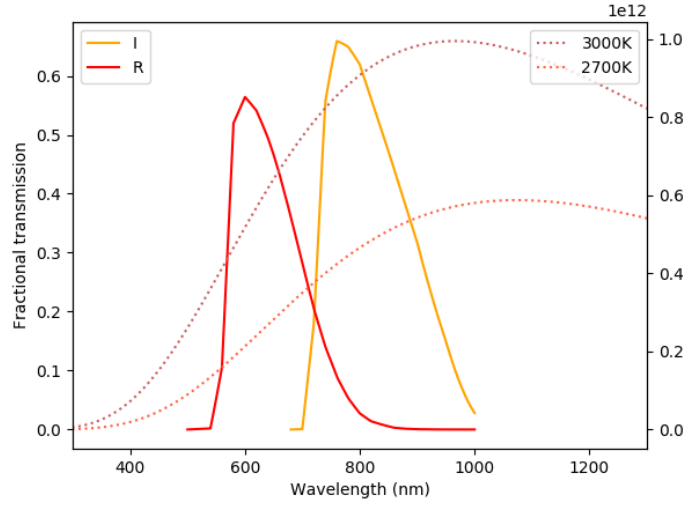


Figure 4.1: Calculated throughput (transmission vs wavelength) for the NITES I and R filters. The blackbody spectrum for stars with temperatures 2700 and 3000 K are also plotted.

Pro 6⁵ as the camera software and FocusMax v4⁶ to control the focuser position. The target was recentred between frames using the DONUTS autoguiding software (McCormac et al., 2013).

Exposures were taken using a FLI Johnson-Bessel I-band filter. The zero point magnitude of the telescope in the I band is 21.3 mag. The calculated transmission for the NITES I and R filters as a function of wavelength is shown in Figure 4.1. This combines the transmission from the filter, quantum efficiency of the camera and the telescope, where the manufacturer provided quantum efficiency values are interpolated to our operating temperature of -40°C and the telescope values are quadratically extrapolated beyond 750 nm. Also plotted is the blackbody spectrum for stars with temperatures 2700 K and 3000 K, indicating the I filter is the best match available to us for the peak flux of these stars. 30 second exposure times were used for all targets apart from the brightest target in the sample, MD20+58, where an exposure time of 15 seconds was used to avoid saturation and obtain maximum pixel counts in the region of 25000–30000 ADU.

⁵<http://diffractionlimited.com/product/maxim-dl/>

⁶<http://www.ccdware.com/products/focusmax/>

4.2.3 Data Reduction

The data are reduced using the Python data reduction package, CCDPROC (Craig et al., 2015), with a master bias, dark and flat. At least 21 frames are used to make each master frame. Apertures are placed over manually selected comparison stars, and repositioned by light centroiding within Source Extractor in Python (SEP) (Barbary, 2016; Bertin and Arnouts, 1996) before aperture photometry is extracted. The autoguiding algorithm, DONUTS (McCormac et al., 2013), measures the pixel shifts between images, allowing photometry apertures to be recentered between frames with subpixel precision. Light curves are plotted using the differential flux between the target and the summed comparison stars (3–5 stars was typical). Variations of comparison stars were checked against each other by eye. A threshold of less than 1 % variations over the course of the night was required for stars to be included.

As our targets are extremely cool we have to be mindful of second order colour terms affecting the differential photometry at changing airmass. This arises as the comparisons are generally bluer in colour than the targets. As colour terms are airmass dependent, it is expected to produce a slow continuous change when the colour term becomes more significant (i.e. at high airmass). As our observing altitude was limited to 35 degrees above the horizon (approximately airmass 1.7) the effects of colour differences between the comparison stars and target is limited. No significant trends with airmass were identified in the selected comparison stars as any showing trends with the target and other comparison stars with airmass were rejected.

Observations for each object on each night are fitted to a linear trend. Where a partial or full transit-like event is identified, the linear trend is fitted to the out of transit data. X and y position of the target on the CCD sensor, airmass, full width half maximum, and background sky level are all plotted with the light curve to allow any correlations to be identified manually. Potential features were checked against the observational parameters to see if any correlations could be identified at that point. Any feature in the lightcurve of less than half a percent was viewed suspiciously if correlations occurred on the same time scale as the feature and if they could result in this feature shape.

Nightly fluxes are normalised to 1 to account for comparison stars sometimes changing between different nights due to tracking or pointing errors. The final, optimal aperture size is chosen to minimise the RMS of out-of-transit data in that night’s light curve. Aperture size varied between nights due to changes in seeing. Normalised fluxes for all nights for a given object are combined for further analysis.

Table 4.1: Stellar parameters of targeted Mdwarfs, where T shows the effective temperatures and L the luminosity. Source: ^a: Gaia DR2, ^b: 2MASS, ^c: Simbad, ^d: TESS Candidate Target List (*CTL*) v8.0. All magnitudes are Vega magnitudes apart from I magnitudes for MD20+58 and MD22+40, which are AB magnitudes.

Name	RA ^a	Dec ^a	J mag ^b	I mag ^b	R mag ^b	Spectral type ^c	T ^d / K	Mass ^d / M_{\odot}	L ^d / L_{\odot}	Radius ^d / R_{\odot}
MD02+22	02 36 44.13	+22 40 26.20	10.0	11.4	14	M5	3002	0.152	0.0024	0.182
MD07+16	07 52 23.93	+16 12 14.96	10.9	-	15.8	M6	2854	0.146	0.0018	0.176
MD11+06	11 53 52.68	+06 59 56.26	11.3	13	17.7	M8	2807	0.102	0.0009	0.127
MD18+29	18 39 33.07	+29 52 16.48	11.0	13.6	16.8	M7	2722	0.097	0.0007	0.121
MD20+58	20 26 05.30	+58 34 22.68	9.0	10.4	13.8	M4.95	3025	0.165	0.0029	0.196
MD22+40	22 11 24.16	+40 59 58.70	9.7	-	14.9	M5.5	2950	0.158	0.0024	0.189

4.3 Results

Data was reduced on a night by night basis, and the resulting nightly light curves visually inspected. Plots were displayed interactively, allowing for adjustment of the axes scale for additional inspection and clipping of individual outlying points more than 5 sigma from the light curve. If light curves displayed features or anything anomalous, these were further examined by two other members of the team. I report on some interesting events observed on individual nights: transit-like features in Section 4.3.1 and flares in Section 4.3.2. I calculate and compare the phase coverage of our observations and the habitable zone boundaries in Section 4.3.3. The manual inspection of nightly light curves discussed in this section was complemented by an automated BLS discussed in Section 4.4.1.

4.3.1 Transit-like features

Several potential transit candidates were observed in lightcurves from individual nights, which are shown in Figures 4.2 and 4.3. A full list of individual events, including transit-like features, is given in Section 4.7.

Parameters of the initial transit candidates were estimated by fitting transit models to the lightcurves to determine their parameters and judge whether they were significant. As these are only single transit-like events, the period is estimated from the total duration of the transit (t_t , from t_1 to t_4) and the duration of full transit (t_f , from t_2 to t_3), transit depth and stellar mass (M_*) and radius (R_*). Assuming a circular orbit, this is found as:

$$P = \frac{G\pi M_*}{32 R_*^3} \frac{(t_t^2 - t_f^2)^{3/2}}{\Delta F} \quad (4.1)$$

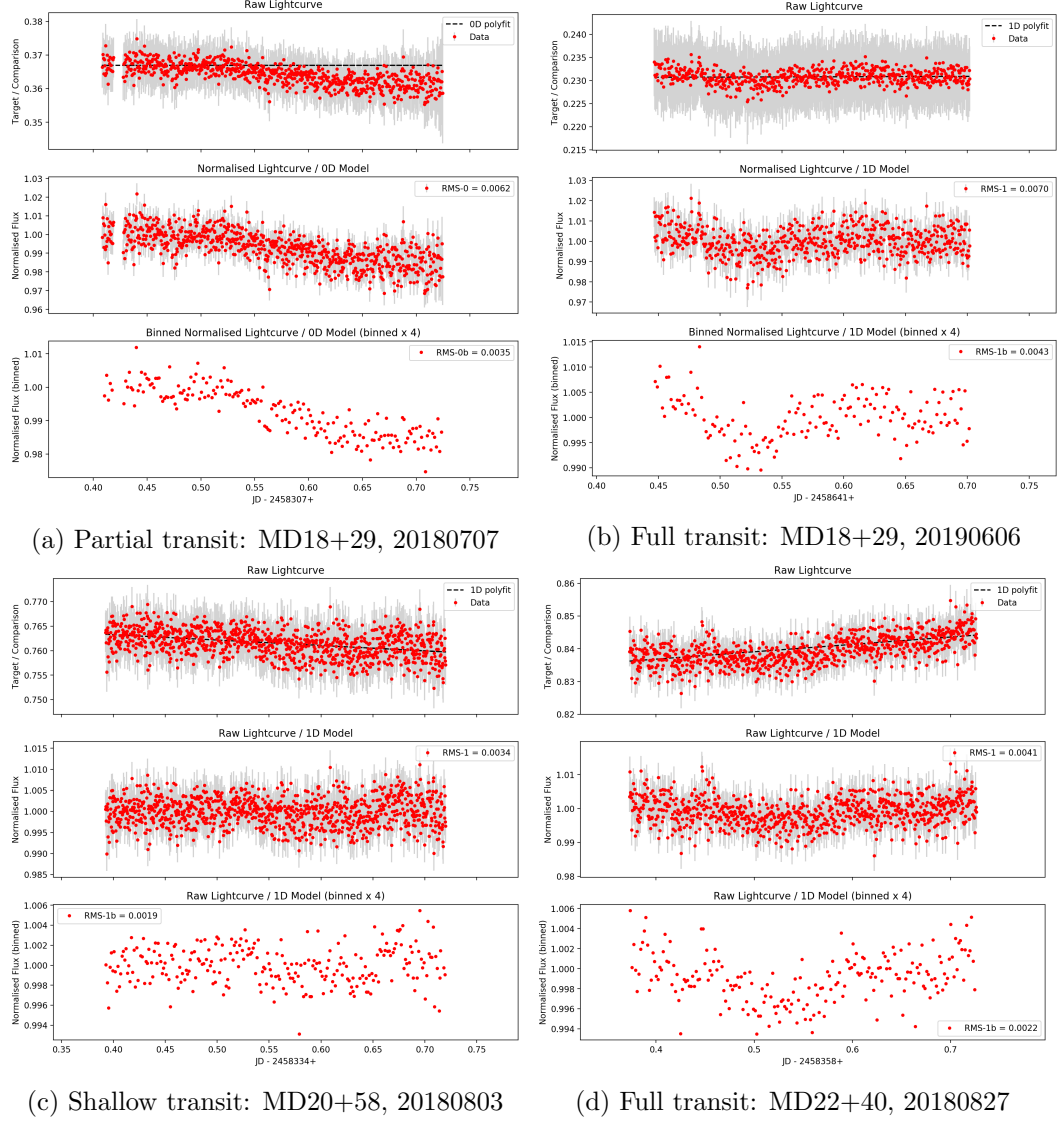


Figure 4.2: Plots of example individual nightly light curves displaying initial candidates identified with transit-like features. The raw data with 30 second exposures is in the top row, the middle row shows data fitted to the linear trend in the top row. The bottom row shows the fitted data binned to a factor of 4. The residual RMS compared to a linear fit is given for the out of transit data for both the unbinned and binned data. The caption for each gives the target and the night of observation.

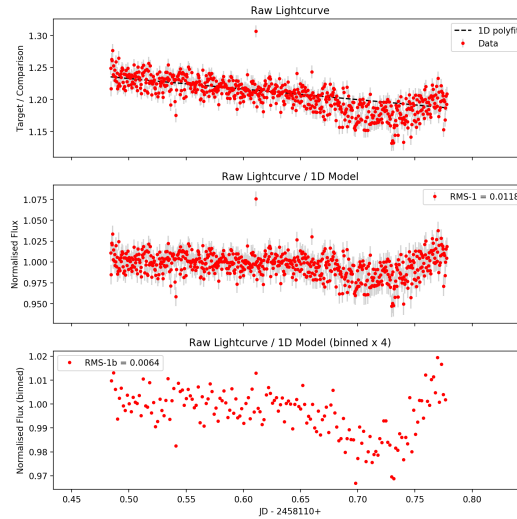


Figure 4.3: As per Figure 4.2. Plot of initial candidate transit for MD07+16, 20171222.

Stellar parameters were taken from the TESS Candidate Target List v8.0 (*CTL* Stassun et al., 2018, 2019). Limb darkening parameters were calculated by inputting stellar temperature and log g values and errors into the limb darkening toolkit (Parviainen and Aigrain, 2015). Solar metallicity, $[Fe/H] = 0$, with uncertainty of 0.1 were assumed as these values are not available in the TESS CTL v8.0 catalogue. Transit models assumed circular orbits (i.e. zero eccentricity) and edge-on transits (90 degrees inclination). Timings and depths were initially estimated by eye from the lightcurve. After which, PyTransit models (Parviainen, 2015) were fitted to the lightcurves to determine the transit depth and transit duration timings, which together give the period. The depth and transit timings were optimised by iteratively fitting models to minimise the residual rms between the model and the data. Depths were tested at 0.1 % steps and individual timings at 0.002 days. After inspection of lightcurves, uncertainties on depth and period were calculated as within 1 % of the minimum RMS value.

The fitted transits are shown in Figure 4.4. For MD07+16 on 20171222, the linear trend in the lightcurve was normalised before transit fitting. The linear trend may be a very small colour effect given the likely colour difference between the comparisons and target. This will cause some uncertainty as the transit shape could be a function of it. From the fitted transits, I find transit depth $1.7 \pm 0.3\%$ and period $24.4^{+24.9}_{-7.0}$ days. This depth leads to an estimated radius of $2.5 \pm 0.2 R_{\oplus}$. This remains a candidate transit.

For the light curve of MD18+29 on 20190606, transit models find depths of

$0.4 \pm 0.1\%$ with period $31.6_{-12.5}^{+7.6}$ days, with the depth leading to estimated radius of $0.8 \pm 0.1 R_{\oplus}$. Similarly, the lightcurve of MD22+40 on 20180827 gives a depth of $0.3 \pm 0.1\%$ and period $38.0_{-13.0}^{+23.0}$ days, which corresponds to radius $1.1 \pm 0.2 R_{\oplus}$. While transit fits for both lightcurves had decreased residual RMS values compared to a linear fit, both have best fits with low signal to noise ratios of less than 1, making them weak candidates.

Fits for the very shallow event for MD20+58 on 20180803 were inconclusive due to the low transit SNR. The transit fit to the partial event for MD18+29 on 20180707 was also inconclusive. We consider both of these to be unlikely candidates.

4.3.2 Flares

During our search for transiting exoplanet signals, visual inspection of the light curves revealed a number of flaring events. Flaring frequency has an important effect on the habitability of close-in planets. Table 4.2 gives a summary of number of flares seen and the observed flare frequency in our survey for each target star. Three of the stars were very quiet, with only one observed flare in the entire run for MD11+06 and MD18+29, out of 90 and 81 nights respectively. No flares were observed for MD20+58. The other three targets were much more active, with MD07+16 (the most active) showing 45 flares observed over 99 nights of observation, giving an average flare frequency of 0.14/hour. I calculate flare energies based on the method of Davenport et al. (2014) using TESS *CTL* stellar radii and temperatures. The method assumes that both the star and the flare radiate like blackbodies, with an assumed flare blackbody temperature of 9000 ± 500 K, consistent with other studies (e.g. Jackman et al. (2019, 2018); Howard et al. (2018); Gunther et al. (2020))

A selected number of interesting flaring events can be seen in Figure 4.5. Flares were identified where flux values were 3 sigma above the baseline level, with the light curve displaying time resolved structure characteristic of flares: a sudden rise in brightness followed a more gradual decline. We observe what appears to be a complex flare for MD02+22 on 20190205 (see Figure 4.5a). This flare causes a peak brightness of 1.02 times the quiescent level and lasts for at least half an hour, from which I find a minimum flare energy of 1.30×10^{31} erg. The flare with the largest peak brightness observed in our standard I filter was for MD07+16 on 20180217, Figure 4.5b. A peak brightness of 2.7 times quiescent level was observed, corresponding to a minimum flare energy of 9.63×10^{31} erg.

After observing a number of flares for MD07+16, we observed a flare in

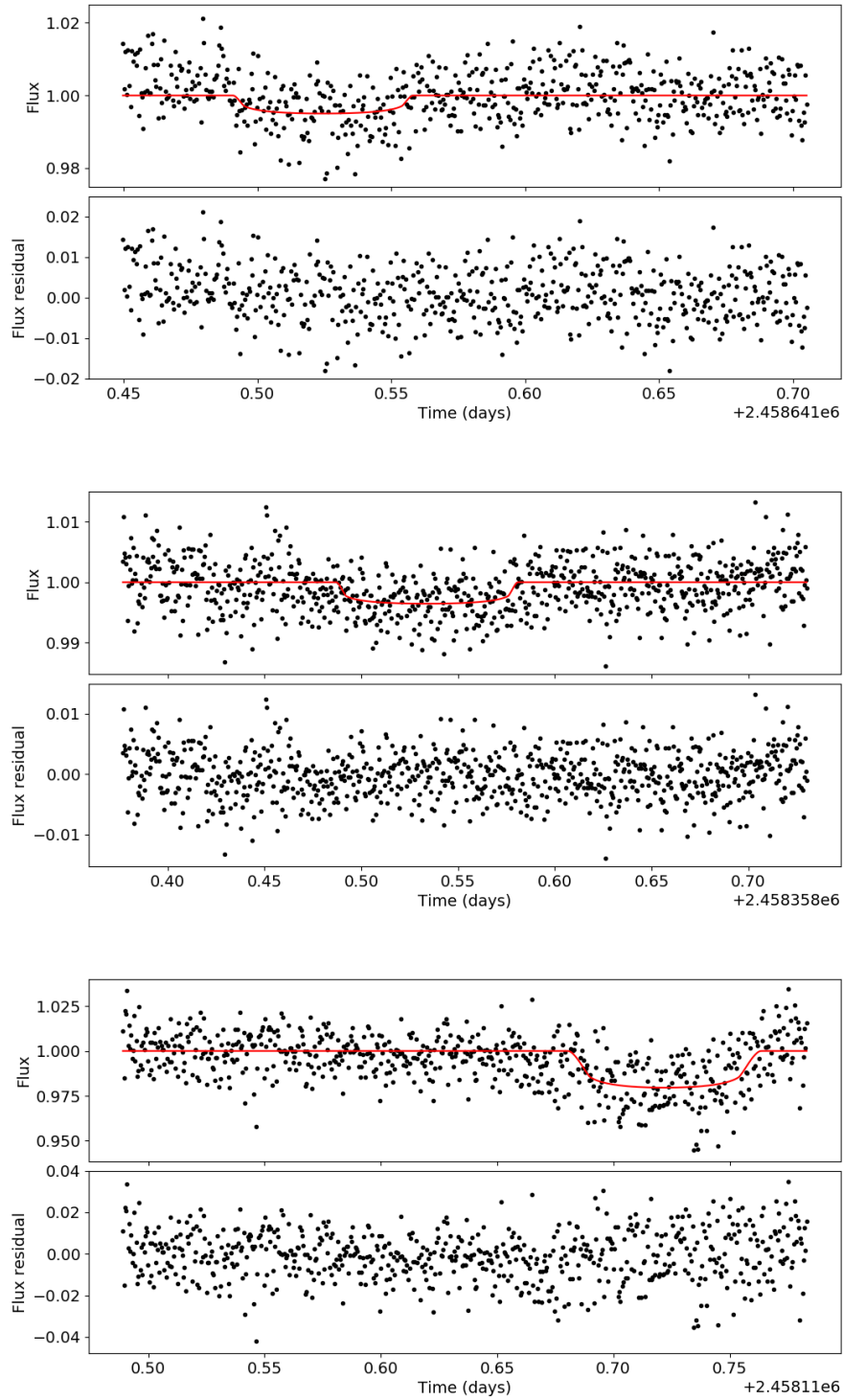


Figure 4.4: Single night lightcurves with fitted transit models and their residuals. Top: MD18+29, night 20190606. Middle: MD22+40, night 20180827. Bottom: MD07+16 on night 20171222.

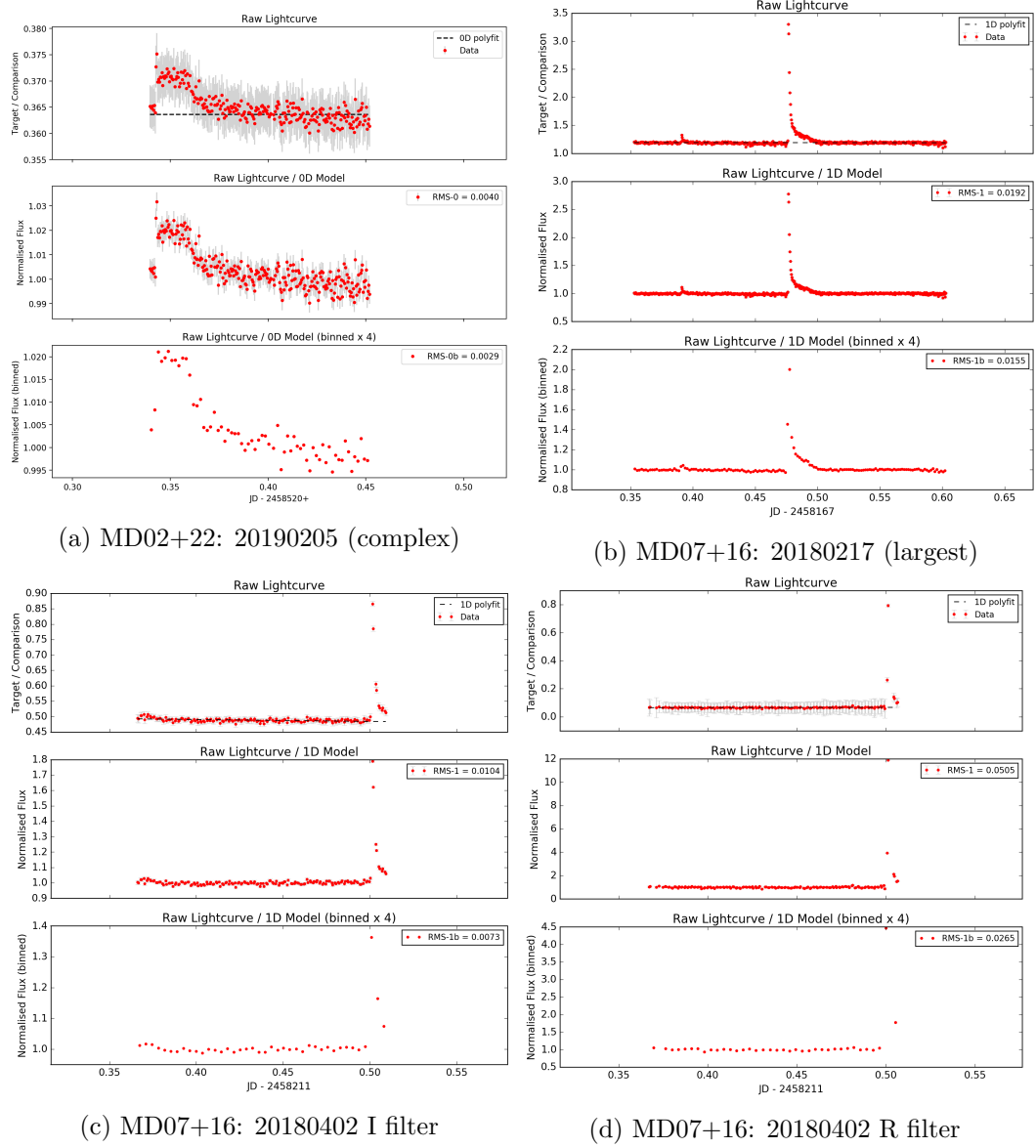


Figure 4.5: As per Figure 4.2, with RMS values given for out of flare data. Plots of example individual nightly light curves showing flares.

Table 4.2: Flare information on targeted Mdwarfs. Hours observed includes all data, including flares and noisy data. Targets were observed for an average of 3.4 hours per night, with the mean hours of observation varying from 2.8 to 4.9 hours, depending on the object. Average flare frequencies are given per night of observation (rather than 24 hours) and per hour of observation.

Name	Nights	Flaring nights	Total flares	Hours observed	Flare frequency /night	Flare frequency /hour
MD02+22	82	10	11	259.5	0.13	0.04
MD07+16	99	34	45	318.0	0.45	0.14
MD11+06	90	1	1	253.9	0.01	0.00
MD18+29	81	1	1	337.1	0.01	0.00
MD20+58	81	0	0	249.0	0.00	0.00
MD22+40	62	15	18	306.2	0.29	0.06

multiple filters on 20180402. We observed in R and I filters (see Figures 4.5c and 4.5d), switching filter after two exposures. I find a peak brightness in I of 1.8, and in R of 12 times quiescent flux level. This equated to a minimum energy of 3.06×10^{31} erg in I and 1.34×10^{32} erg in R. We observed the start of a flare on MD07+16 in both filters on one other night, but this was only a marginal detection in R. Section 4.7 contains a full list of flares observed in the survey.

4.3.3 Phase coverage and the Habitable Zone

While the number of hours observed gives us some indication of the data coverage, we are interested in determining how much coverage there is at specific periods, namely those covering the habitable zone of each star.

I calculate the habitable zone boundaries for each of our stars to determine phase coverage at these periods. I calculate these boundaries using stellar parameters from the TESS Candidate Target List v8.0 (*CTL*). For all six targets, the temperatures in the *CTL* come from the Cool Dwarfs Catalogue 2 (CDC2), the updated version of the Cool Dwarf Catalogue from Muirhead et al. (2018), that is discussed in Stassun et al. (2019). The CDC2 compiles stars cooler than 4000 K and with $V - J > 2.7$. Dwarfs are distinguished from giants based on parallax or proper motion. Effective temperatures are calculated from Gaia G_{BP} and G_{RP} using relations developed from photometrically-calibrated spectra of nearby late K and M dwarfs from Mann et al. (2013). Errors of 157 K are given for all six targets, and temperatures are in good agreement with those derived from the standard methodology of Stassun et al. (2019). Stellar mass and radii were calculated using

mass- M_K relations from Mann et al. (2019) and radius- M_K relations from Mann et al. (2015) respectively. Stellar luminosities are calculated from the stellar radii and temperatures. All stellar parameters do not account for extinction or reddening.

Fluxes at the habitable zone boundaries were calculated using values from Kopparapu et al. (2013) and stellar temperatures from the TESS Candidate Target List v8.0 (*CTL*). These fluxes were converted into habitable zone boundary distances using stellar luminosities from the *CTL*. Habitable zone distances were converted into their corresponding periods using Kepler’s third law and stellar masses from the *CTL*. Runaway and maximum greenhouse boundaries, representing the inner and outer habitable zone boundaries respectively, are shown in Table 4.3 and are represented by shaded regions in Figure 4.6.

I calculate the phase coverage for each object from periods of 0.8–35 days to encompass the habitable zone of each star. For each object, I filter out nights with nightly RMS above the threshold values given in Table 4.3. The remaining nights (listed as filtered nights in Table 4.3) were used to calculate the phase coverage. The timestamps of these observations were folded onto periods from 0.8 to 35 days at 0.2 day intervals. Each period was then divided up into 1 % chunks of phase and compared to the phases in which data was present. If phase folded light curves had at least one data point in a 1 % chunk of phase, then this 1% of phase was covered. This is discussed further in the methods: Section 2.3.1. For each object, the fraction of 1 % phase chunks which contained observed data for each period are shown in Figure 4.6. The maximum period where at least 50 % phase coverage is observed (excluding 1 day aliases) is given in Table 4.3, showing that the six Mdwarfs each have 50 % phase coverage for a minimum period of 16.8 days.

Figure 4.6 shows that there is at least 50 % phase coverage for periods midway into the habitable zone for four of the six targets. All targets show at least 35 % phase coverage covering the entirety of their habitable zones. For MD11+06, nearly all of the habitable zone has at least 50 % phase coverage, and for MD18+29, which has the closest habitable zone, has 68 % phase coverage at a period of 15.8 days, showing high coverage at the maximum greenhouse limit (the outer edge) of 15.9 days. This means that for all our targets we have at least 50 % phase coverage for about half or more of the orbital periods which fall within the habitable zone, allowing us to place some constraints on transiting planet occurrence within it.

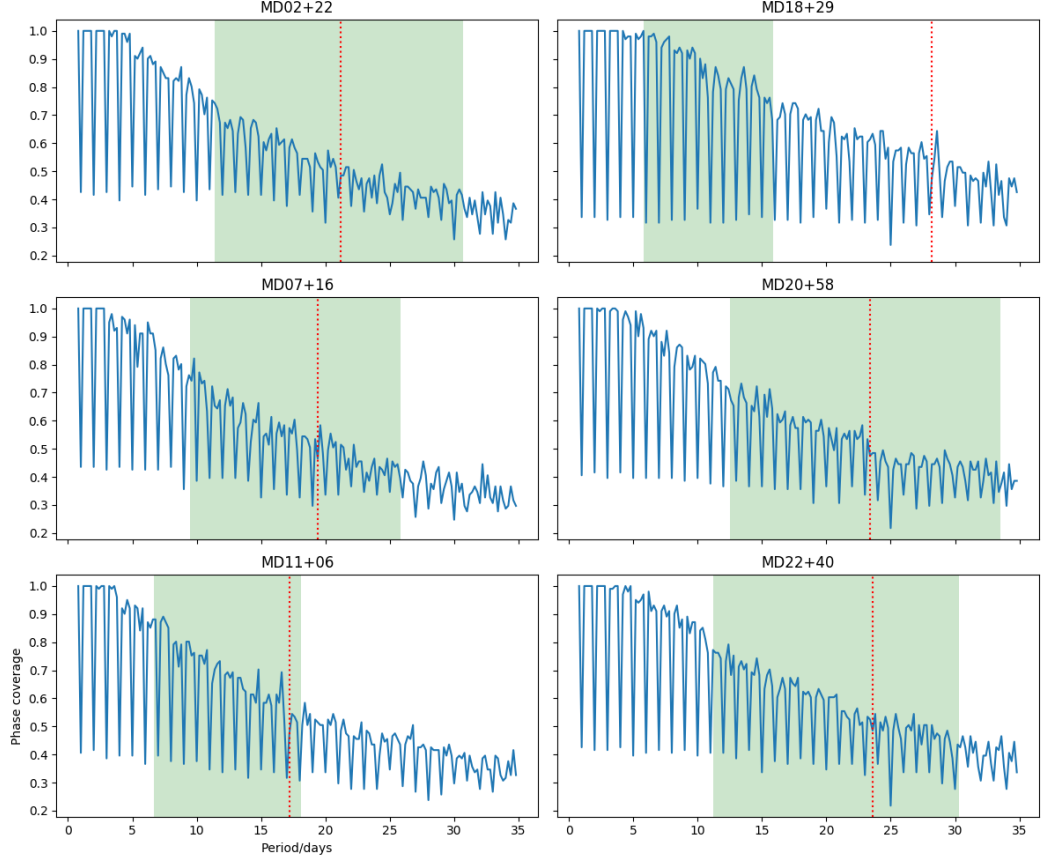


Figure 4.6: Phase coverage of the targeted M dwarfs. Each subplot shows the phase coverage of one of the six M dwarfs. The shaded region shows the extent of the habitable zone, calculated using runaway greenhouse and maximum greenhouse boundaries, with parameters from the TESS *CTL*. The first period with phase coverage below 50 % (excluding 1 day aliases) is indicated by the vertical red dotted line. Phase coverage includes flare data but excludes data with higher RMS values.

Table 4.3: Number of observed hours, phase coverage and calculated habitable zone limits of targeted M dwarfs. Filtered nights excludes nights with nightly RMS above the values specified in the max RMS column. The habitable zone limits are calculated from TESS *CTL* v8.0 and are indicated by Runaway GH (runaway greenhouse) and Max GH (maximum greenhouse). 50 % phase coverage period includes flares, but excludes filtered RMS.

Name	Nights observed	Max RMS	Filtered nights	Filtered hours observed	50% phase coverage (days)	Runaway GH (days)	Max GH (days)
MD02+22	82	0.006	74	238.7	20.8	11.4	30.7
MD07+16	99	0.009	70	217.4	19.2	9.5	25.8
MD11+06	90	0.01	81	221.0	16.8	6.7	18.1
MD18+29	81	0.01	76	316.1	27.8	5.8	15.9
MD20+58	81	0.005	70	213.9	23.2	12.5	33.5
MD22+40	62	0.005	54	277.7	23.4	11.2	30.3

Table 4.4: Parameters used in injection and for BLS search. The frequency factor controls the frequency spacing, defining the coarseness of the BLS search. Limb darkening constants for transit injection were calculated using the limb darkening toolkit (LDTk) (Parviainen and Aigrain, 2015) with TESS *CTL* temperature and $\log g$ values and zero metallicity.

BLS Parameters	Value
P_{min} (days)	0.7
P_{max} (days)	50% phase coverage period
Frequency factor	5000
Min. duration (days)	0.01
Max. duration (days)	0.2
No. durations (days)	10
Injection Parameters	Values
Planet/star radius ratios	0.075,0.1,0.15,0.2
Minimum orbital period (days)	0.8
Maximum orbital period (days)	50% phase coverage
Eccentricity	0
Inclination (degrees)	90
Argument of Periastron (degrees)	90

4.4 Analysis

4.4.1 BLS search

Light curves were searched for periodic transit-like signals using the astropy Box Least Squares (BLS) algorithm (The Astropy Collaboration et al., 2013, 2018), based on Kovács et al. (2002). BLS searches for a periodic box-like step signal where much less time is spent at the lower level. The BLS search parameters are listed in Table 4.4. The period range searched was tailored to each star, with the maximum period set at the longest period with 50 % phase coverage.

Prior to our BLS search, I excluded lower quality data by excluding nights where the nightly RMS was greater than some threshold value, which was determined on a star-by-star basis by examination (see Table 4.5). Individual data points where the error bar was greater than three times the nightly median flux error of the light curve were also excluded. All remaining data were combined into one light curve per object for the BLS search.

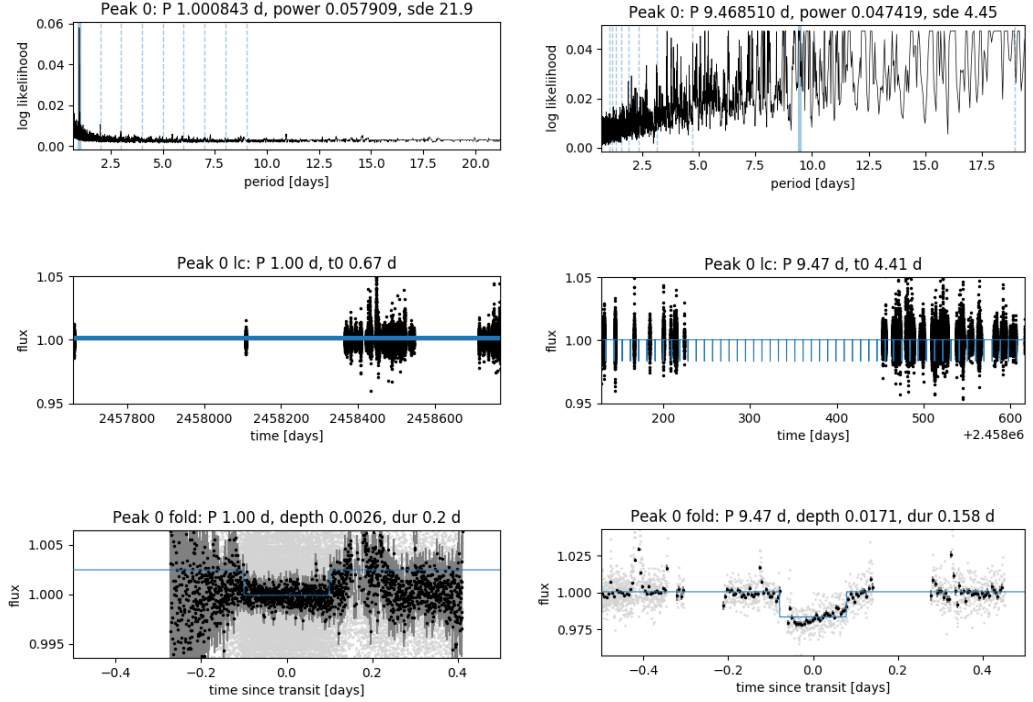


Figure 4.7: BLS results. (a) MD02+22: a clear significant peak is seen at 1 day, most likely due to the day-night cycle. (b) MD07+16: no significant peak is seen in the BLS spectrum.

4.4.2 BLS results

The relative power of different periods, and, by extension, the likelihood that a given period is real, can be characterised by finding the period’s Signal Detection Efficiency (SDE). The SDE is calculated based on the relative strength of the peaks in the BLS power spectrum:

$$\text{SDE} = \frac{\text{test power} - \text{mean power}}{(\text{standard deviation of power})^2} \quad (4.2)$$

BLS output parameters for the periods with the highest BLS power are given in Table 4.5, and example plots for two of the M dwarfs can be seen in Figure 4.7. No significant peaks attributable to transits are identified. Qualitatively, only MD02+22 has a peak in the BLS power spectrum that stands out from the background level, hence its much higher SDE. Unfortunately this peak is at exactly one day, and visual inspection confirms that the signal does not appear to be a transit but is likely due to the day-night cycle.

MD07+16 is an example where the power of the highest peak is not above the

Table 4.5: BLS results. Nightly RMS values greater than the max RMS were not included in the BLS analysis. Other parameters are obtained from the BLS. Results from the highest peak for each object are shown.

Object	Max RMS	No. transits in data	SDE	Retrieved radius (R_{\oplus})	Period (days)	Depth	Power
MD02+22	0.006	59	21.9	1.00	1.00084	0.0026	0.058
MD07+16	0.009	2	4.45	2.50	9.46851	0.0171	0.047
MD07+16	none	2	6.83	2.28	22.3231	0.0142	0.0623
MD11+06	0.01	12	5.57	0.57	1.28480	0.0017	0.002
MD18+29	0.01	3	5.32	1.38	18.66021	0.0109	0.025
MD20+58	0.005	2	4.89	1.57	9.30576	0.0054	0.007
MD22+40	0.005	41	7.27	0.61	0.76280	0.0009	0.004

background level, hence a low SDE. While BLS identifies two transit-like features in the MD07+16 lightcurve, examination of the individual nights revealed that one of these contained just a couple of data points at the end of a night, effectively leaving this as a detection of a single partial transit-like feature, making it less certain it is a true transit. Preliminary fitting of transit models to this individual transit (observed on the night of 20190128) was carried out as described in Section 4.3.1, with the best fit shown in Figure 4.8. This suggested a transit depth of $1.5 \pm 0.1\%$, which gives a SNR of 1.9 and corresponds to a radius of $2.4 \pm 0.1 R_{\oplus}$. The best fit period identified was 527.9 ± 24.9 days, much longer than periods searched using BLS. Uncertainties are very difficult to estimate as the transit start time is unknown so this is likely an underestimate.

The individual lightcurve for MD07+16 on 20171222, discussed in Section 4.3.1 was not included in the standard BLS search as its RMS was greater than the filtering value. Its transit depth is very similar to the single transit identified by BLS. Running BLS again and including the noisier data did identify just these two lightcurves in the phase folded transit and at higher significance. However, inspection of the phase folded lightcurve (Figure 4.9) showed that the durations of the transit candidates are very different, which they could not be if they resulted from a single transiting exoplanet.

4.4.3 Transit injection

I performed transit injections to test our sensitivity to transiting planets. Transits were considered recovered if the time retrieved by BLS was within 0.02 days of that injected and we required that at least 20 % of retrieved times to be ‘true’ transits. We performed three separate injection tests to test our sensitivity.

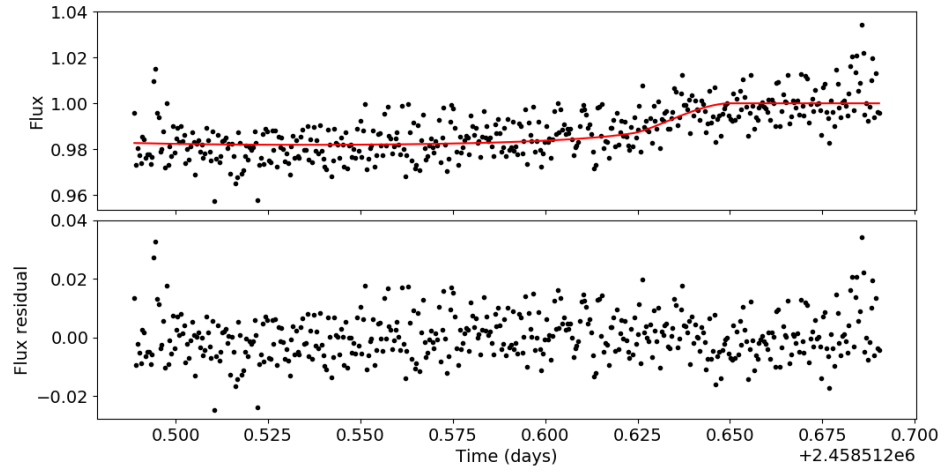


Figure 4.8: Transit model fit to the individual transit identified by BLS for MD07+16, which was observed on the night of 20190128.

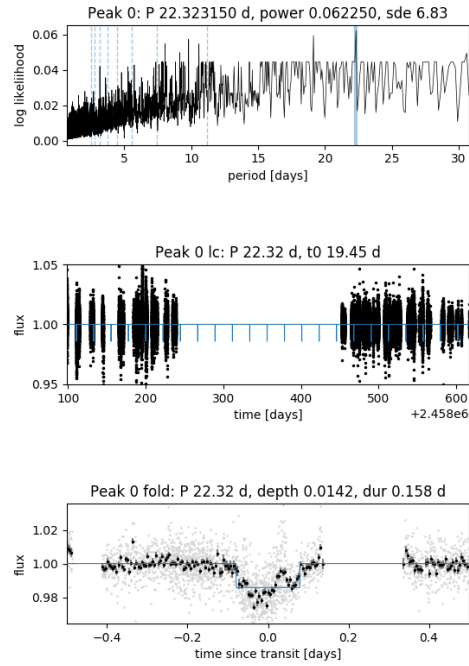


Figure 4.9: BLS results for MD07+16 without filtering the data. Two transits of similar depth are identified by BLS in the data but the phase folded light curve shows their durations are very different.

Injected transit shape and depth were calculated using the quadratic model in PyTransit (Parviainen, 2015), with the parameters specified in Table 4.4. Inclination was fixed to 90 degrees, so only edge-on transits are considered, meaning we do not model the recoverability of grazing transits where only part of the planet’s disk crosses its star. The limb darkening constants for the NITES telescope I filter were calculated for each star by inputting TESS *CTL* temperature and $\log g$ values into the limb darkening toolkit (LDTk) (Parviainen and Aigrain, 2015). *CTL* metallicity values are missing for all our objects, so a metallicity of 0 (i.e. solar metallicity) was assumed. For each object, noise was added to the transits using the median of the nightly RMS values as the standard deviation of injected points. These artificial transits were then injected into the observed NITES data.

The injected light curves were then searched using BLS as described in Section 4.4.1 using the parameters given in Table 4.4. The transit mid-point times detected by BLS were then compared to the injected mid-point times. Through visual inspection of the light curves, I tested different timing thresholds (the difference between injected and BLS recovered transit mid-point) between 0.01 and 0.2 days through visual inspection of the light curves, finding the optimum value of 0.02 days to maximise the number of true transits and minimise the number of false signals. The number of recovered transits was found by summing how many BLS detected mid-points were within 0.02 days of the injected mid-point. Where BLS identified additional false signals, we required that at least 20 % of timings matched the injected time, otherwise this was classed as a false detection.

If at least two transits were detected for a given period and radius ratio (with mid-point times matching those injected), and if these ‘true’ detections made up at least 20 % of BLS detections, then this period and radius ratio combination was considered successfully recovered. Figure 4.10 shows example BLS injection recovery plots.

Injection at the inner edge

I injected transits at periods at the inner edge of the habitable zone (the runaway greenhouse limit calculated using *CTL* values) for each object given in Table 4.6. Transits were injected using the radius ratios given in Table 4.4 at phases 0, 0.2, 0.4, 0.6 and 0.8, and tested for the minimum radius ratio recoverable.

Table 4.6 shows the smallest planet that is detectable in our data at the inner edge of the habitable zone, where transits were recovered in any of the injected phases. This enables us to rule out the presence of transits in the data at the runaway greenhouse limit, with minimum radii as given in Table 4.6.

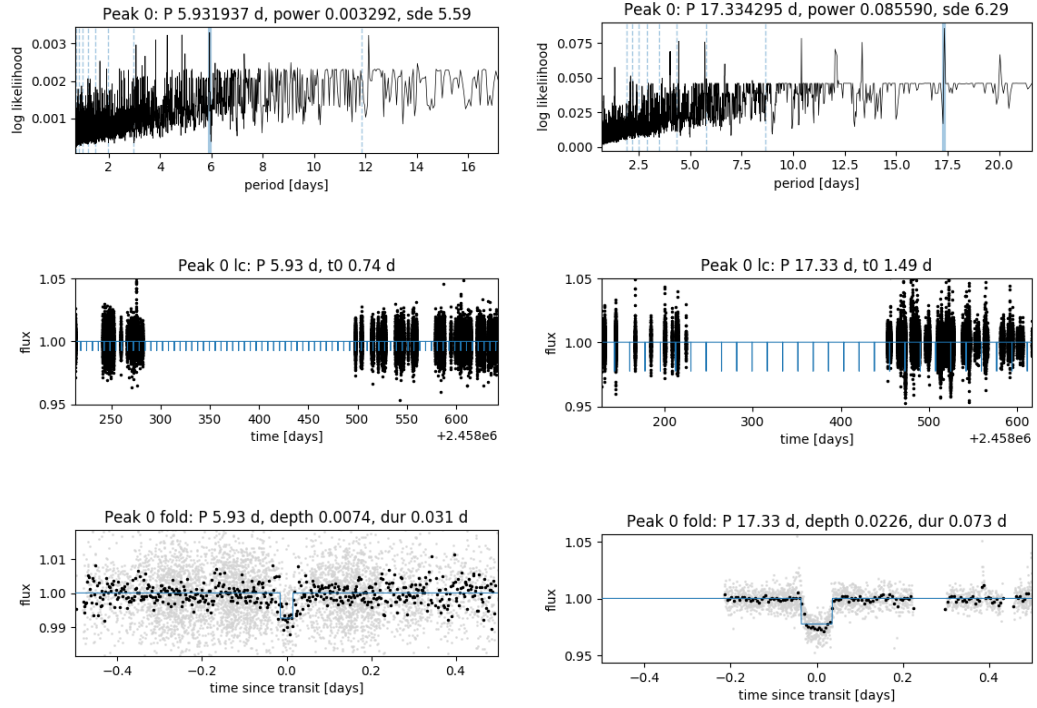


Figure 4.10: Examples of BLS injection recovery results (a) Injected transits are recognisable for MD11+06 for an injected planet with radius ratio 0.075 and period 8.09 days, although BLS recovers a period of 5.93 days. (b) The correct period of 17.73 days is recovered by BLS for MD07+16 with injected planet radius ratio of 0.15.

Table 4.6: Results from injection tests at the inner edge of the habitable zone (runaway greenhouse limit) for all target stars. For each target, the runaway greenhouse period, minimum radius ratio recovered at any injected phase, and corresponding minimum radius (calculated using TESS *CTL* v8.0 parameters) are given. The probability of transit at the inner edge is calculated for the given minimum radius using equation 4.5, as described in Section 4.5.4.

Object	Runaway Greenhouse limit (days)	Min. radius ratio	Min. radius (R_{\oplus})	Probability of transit %
MD02+22	11.4	0.15	2.98	1.8
MD07+16	9.5	0.20	3.83	2.1
MD11+06	6.7	0.075	1.04	2.0
MD18+29	5.8	0.15	1.98	2.2
MD20+58	12.5	0.10	2.14	1.7
MD22+40	11.2	0.075	1.55	1.8

Injection - multi-period

I next tested sensitivity at different periods up to the 50 % phase coverage period for each object. I injected transits at randomly generated phases for 10 periods linearly spaced between the minimum and maximum orbital periods given in Table 4.4. These transits were injected using the same radius ratios as in Section 4.4.3, which are given in Table 4.4.

Table 4.7 gives the results of multi-period injections. Table 4.7 shows the minimum radius ratio we are sensitive to at any period, which is equivalent to $1.04\text{--}2.98 R_{\oplus}$ for the different M dwarfs. I calculate the signal to noise ratio (SNR) for these minima as the radius ratio squared over the mean of the nightly rms values. Period sensitivity is given in Table 4.7 as the maximum period where at least 2 transits for each radius ratio were recovered. Generally, sensitivity to longer periods improves for larger planets as expected.

Injection- multi-phase

I also performed a multi-period, multiple-phase test by injecting transits for a planet with radius ratio of 0.2 using the same periods but for phases 0, 0.2, 0.4, 0.6 and 0.8. I checked in how many phases at least 2 injected transits were recovered.

If the transit injection of a planet is recovered at all five injected phases, and the signal is not seen in the non-injected data, we can rule out the presence of a planet of given radius at that period in the data. The final column of Table 4.7 gives the maximum period where a planet with radius ratio of 0.2 can be ruled out. While the injections show sensitivity to planets within the habitable zone of these stars, ruling out the existence of transiting planets is much more difficult as it essentially requires 100 % phase coverage at that period. Hence, only very short period transiting planets can be ruled out in these systems, with the caveat that periods at multiples of 1 day cannot be tested due to the 1-day alias that is a drawback of observing from the ground.

4.4.4 Lomb Scargle

Photometric light curves can also be investigated to search for the rotational periods of stars. M dwarfs can be divided into fast rotators (< 10 days) and slow rotators (> 70 days) (e.g Newton et al., 2016, 2018). Rotational periods can be seen as sinusoidal variation in the light curve. I used astropy’s Lomb-Scargle periodogram function, which uses the formulation from Press and Rybicki (1989), to search for sinusoidal signals in the filtered data after removing flares. The light curve

Table 4.7: Results from multi-period injection tests. All but the last column give results from injection at a random phase to find maximum period and minimum radius sensitivity for each target. Columns 2–4 give the minimum radius ratio recovered in the injection tests, its SNR, and the corresponding minimum radius (calculated using TESS *CTL* v8.0 parameters). Columns 5–8 give the maximum period where at least two transits are correctly detected for each radius ratio (RR) at the random injected phase. The rightmost column shows the results from the multi-period, multiple phase test, and gives the maximum period where transits of radius ratio 0.2 were recovered at all five phases. This required all shorter tested periods to be recovered.

Object	Min. radius ratio	SNR	Radius (R_{\oplus})	Period sensitivity (days) for RR				Max. period all recovered (days)
				0.075	0.1	0.15	0.2	
MD02+22	0.15	5.4	2.98	-	-	18.9	18.9	3.1
MD07+16	0.15	3.2	2.87	-	-	17.3	17.3	0.8
MD11+06	0.075	0.7	1.04	8.1	9.9	8.1	8.1	2.6
MD18+29	0.10	1.5	1.32	-	0.8	6.9	6.9	3.8
MD20+58	0.075	1.5	1.60	0.8	13.4	13.4	13.4	3.3
MD22+40	0.075	1.5	1.55	8.4	16.0	16.0	16.0	3.3

of MD02+22 shows sinusoidal signals, which is confirmed by the Lomb-Scargle results, with sinusoidal semi-amplitude of 0.2 %. Its Lomb-Scargle periodogram had a best peak frequency of 4.7/day, with power more than 10 times the 0.1 % false alarm probability rate. Overall there were four prominent peaks at frequencies of 5.6, 3.7, 4.7 and 2.7 per day. This sinusoidal variation may be caused by rotation and is consistent with MD02+22 being identified as a young star in our source catalogue. Other targets had less well defined highest peak frequencies, and in particular the highest peak frequency for MD11+06 was below even the 10 % false alarm probability, indicating that is unlikely there is a sinusoidal signal in the light curve. However, nightly normalisation to optimise transit searches will affect our ability to search for stellar rotation periods.

4.5 Discussion

4.5.1 MEarth data

Observations of five of our six targets are publicly available on the MEarth website. These observations cover the period from 2008–2017, although observations are not necessarily available for each object every year. The MEarth data did not overlap with our own. I examined all available data but the sparsity of the data – ≤ 30 points/night, and an average up to 7.6 points per night – meant I was unable to identify and model transits. Variations in the baseline magnitude are also seen between nights, so I did not use the MEarth data in the analysis.

4.5.2 TESS data

During the preparation of this manuscript, TESS data for three of the six targets became available: MD20+58 in Sectors 15, 16 and 17, MD22+40 in Sector 16 and MD02+22 in Sector 18. Examination of the MD20+58 data using BLS revealed a periodic sinusoidal trend. Analysis using astropy’s Lomb-Scargle function revealed that this sinusoidal trend had a period of 2.65 hours and an amplitude of 0.15 %. However, closer investigation and comparison with our own data uncovered that this signal is coming from another nearby star 45 arcseconds away. I searched Gaia DR2 (Gaia Collaboration et al., 2016, 2018) within a 5 arcsecond radius of the nearby star’s coordinates, revealing a 12.6 Gmag star with a BP–RP colour of 0.837, a temperature of 5775 K and a radius of $3.1 R_{\odot}$, implying a sub-giant. During data reduction, I noticed that this star was variable, with a sinusoidal period of 2.6 hours and amplitude of a few percent, so I excluded it from our choice of comparison stars. This variable star lies at the edge of the TESS aperture for this object, contaminating the signal from the Mdwarf. The contaminant has a flux ratio of approximately 0.28 in the NITES I filter band, so we observe a smaller amplitude of variation due to blending in the TESS data.

Running BLS on the MD02+40 TESS data, the strongest signal was sinusoidal, with a period of 0.74 days and depth of 0.2 %. We then used the astropy Lomb-Scargle function, identifying a period of 8.9 hours or 0.37 days (or 2.7/day), half that found by BLS. This frequency was also identified as a prominent peak in the NITES data. The semi-amplitude of the sinusoidal signals is of order 0.2 %, similar to the NITES data. This sinusoidal trend in the TESS data had power significantly above the false alarm probability limit of 0.1 %. I checked Gaia DR2 and identified no additional stars within 30 arcseconds of this target and only 20th Gaia magnitude stars within 45 arcseconds, suggesting this is not due to contamination by another star. I identify 10 flares with peak flux increase of at least 2 % in the 496.3 hours of TESS observations, giving a flare frequency of 0.020 flares/hour. Two other events with more symmetrical brightenings (peak flux 2 %) appear to be passings of a solar system object from inspection of the target pixel files using lightkurve (Lightkurve Collaboration et al., 2018).

I ran BLS on the MD22+40 TESS data, finding a best period of 0.79 days, with depth 0.07 %, corresponding to $0.5 R_{\oplus}$. This is much shallower than the transits depths we are sensitive to in the NITES data. However, this signal did not appear to be real as the duration varied wildly in the individual events. Instead, it appeared potentially correlated with a small centroid shift in the data. I also found twelve flares in the TESS data for this target, with peak flux increase of at least 2 % in

the 529.73 hours of TESS observations, giving 0.023 flares/hour — curiously much lower than we observed with NITES, despite our sensitivity to smaller flares. This may be a factor of our increased cadence.

4.5.3 Habitability

High flaring rates may be sufficient to strip the atmospheres of habitable zone planets. Tilley et al. (2019) model the effect of repeated flaring by a M4 dwarf on an Earth-like planet in the habitable zone. Tilley et al. (2019)’s simulations show that the electromagnetic radiation from flares had little impact on the Earth-like planet’s atmosphere. However, solar flares with energies greater than $10^{28.3}$ erg (GOES class X2) are nearly certain to have a large flux of energetic particles associated with them (Yashiro et al., 2006; Hudson, 2011; Dierckx et al., 2015). When the associated proton flux was included, Tilley et al. (2019) found these could rapidly deplete the planet’s atmosphere if it hit the planet frequently enough.

Following Tilley et al. (2019), I consider the impact of flares and their associated proton fluence for flares with energies greater than $10^{30.5}$ erg. I calculated flare energies in Section 4.3.2. In the 318.0 hours of observation of MD07+16, the target with the highest flaring rate, we observe 18 flares with calculated energies greater than this value, giving an occurrence rate of 0.056/ hour or 1.36 a day. Tilley et al. (2019) show that the proton flux associated with flares of this energy occurring once a day rapidly deplete the atmospheric ozone of an Earth-like planet, however this assumes that every flare and coronal mass ejection (CME) hits the planet.

The geometric probability that a coronal mass ejection will hit a planet is given by Khodachenko et al. (2007):

$$P_{\text{CME}} = \frac{(\Delta\text{CME} + \delta_{pl}) \cdot \sin \left[\frac{\Delta\text{CME} + \delta_{pl}}{2} \right]}{2\pi \sin \Theta} \quad (4.3)$$

where P_{CME} is the probability of a coronal mass ejection with angular size ΔCME hitting a planet which subtends a solid angle of δ_{pl} . Θ is the hemispheric latitude range of CME activity on the star. After Tilley et al. (2019), with the restrictive $5\pi/18$ (permissive $\pi/2$) CME angular size and $\Theta \pm \pi/4$, I find probabilities of hitting a planet at the inner edge of the habitable zone of 0.08 (0.25). This reduces the rate CMEs would hit the planet to every 9.2 (3) days. Tilley et al. (2019) found CMEs associated with flares of energy $10^{30.5}$ erg for all interflare frequencies of once a month or more rapidly depleted the Earth-like planet’s ozone, assuming all directly impact the planet and fully affect the atmosphere. Specifically their simulations of

just 100 of these CME events reduced the ozone fraction by 40 % within $\sim 10^8$ seconds, or just over 3 years. Extrapolation suggests additional CME events may deplete the ozone further.

However, these depletion rates are expected to be lower limits as our flare energies have been calculated in the NITES I band, whereas Tilley et al. (2019) use the more typical U band energies. Flares emit much of their energy at bluer wavelengths than M dwarfs, and are typically modelled with blackbody temperatures of 9000K (e.g. Jackman et al., 2019). Calculated energies for flares observed in bluer bands are observed to be higher: e.g. Lacy et al. (1976) found $E_u = 1.8E_v$ in their multi-filter study of UV Ceti flare stars. We therefore expect the frequency of flares with U band energy $10^{30.5}$ erg to be higher and cause greater depletion of a habitable zone planet’s atmosphere.

The combination of high flaring rates and high probability that a flare hits the planet means that any habitable zone planet with an Earth-like atmosphere likely has had its ozone heavily depleted. This could be common around mid-to-late M dwarfs as Gunther et al. (2020) found up to 30 % of mid-to-late M dwarfs (M4.5–M10) have strongly detected flares observable in TESS short cadence data in sectors 1 and 2. In comparison, only 5 % of M dwarfs earlier than M4.5 flared. However the fraction of flaring stars, especially for late M dwarfs will be affected by TESS target selection and the signal-to-noise constraints in flare detection.

4.5.4 Comparison to expected number of detections

There has been limited investigation into the planet occurrence rate around mid-to-late M dwarfs. Demory et al. (2016) ran BLS analysis on K2 long cadence data for 189 spectroscopically confirmed M5.5–M9 targets (with approximately half being spectral type M6), and found no transiting candidates at 4σ . However, Kepler/K2 may not have been sensitive enough to detect them as they are faint targets in the Kepler band (14.5–23.9 Kmag) and planets with periods of 1 day have transit durations shorter than the 30 minute cadence of observations. Demory et al. (2016) tested the sensitivity of K2 to Trappist-1 b and c like planets (with approximately Earth radii), with periods 1.51 and 2.42 days. Their injection tests found recovery rates of 11 % and 6 % respectively, which increased to 71 % and 67 % when the radii increased to the mini-Neptune size of GJ 1214 b ($2.68 R_\oplus$, (Charbonneau et al., 2009)). They calculate the number of planets they expected to recover as:

$$\text{no. planets} = \text{recovery fraction} \times \text{no. stars} \times \text{transit probability} \times \text{occurrence rate} \quad (4.4)$$

Assuming that every star has a Trappist-1b like planet (occurrence rate =1), they would only expect 0.95 planets from their sample. This increases for greater planet sizes as the recovery percentage increases, so 7.2 mini-Neptune planets with Trappist-1b's period are expected, where they see none. This suggests that mini-Neptunes are rare around mid-to-late M dwarfs, similar to earlier M dwarf spectral types. Additionally Demory et al. (2016) find that K2 is inefficient at detecting planets with $R_p < 1.4R_\oplus$, where the occurrence rate is expected to peak at these short periods.

I calculate the transit probabilities at the inner edge of the habitable zone for the minimum radius detected in injection tests, as given in Table 4.6. The geometric probability of a planet transiting its star is calculated as the fraction of the star's face the planet casts a shadow over:

$$p = \frac{R_* + R_p}{a} \quad (4.5)$$

where R_* and R_p describe the radius of the star and planet respectively and a the semi-major axis (Haswell, 2010). I find transit probabilities of 1.7–2.1 % at the inner edge of the habitable zones for our M dwarf targets.

Little is known about the transiting planet frequency of mid-to-late M dwarfs, hence why dedicated searches of them continue. TESS is more red sensitive, so more M dwarf planet discoveries are expected, though this will be easier for earlier M dwarfs. Trappist-1 was found after searching ~ 50 targets (Demory et al., 2016). Trappist-1 was monitored for 245 hours over 62 nights, which is comparable to what NITES observed, although their observations were over one observing season only. From this they observed 11 transits with amplitude 1 %. Transiting planet frequency for earlier type M3–5 dwarfs from Kepler suggest 1.3 % have planets with periods up to 10 days (Hardegree-Ullman et al., 2019).

Dressing and Charbonneau (2015) calculate planet occurrence rates by dividing the detected planet candidate population by their search completeness. They find 27 % of stars had at least one planet in the habitable zone with radii between $1\text{--}2 R_\oplus$ and 15 % of stars had one with $2\text{--}4 R_\oplus$ for the entire M dwarf range. However only a handful of stars in the Dressing and Charbonneau (2015) sample cover the same temperature range as our own (13/2543 stars have temperature less than 3100 K) so this may not be representative of mid-to-late M dwarfs. Based on purely

geometric arguments, we would expect a higher fraction of habitable zone M dwarf planets to be transiting for later M dwarf types, as indicated in the equation above.

I take the geometric probability of transit at the inner edge of the habitable zone for the minimum planet size detected and assume the Dressing and Charbonneau (2015) habitable zone occurrence rate for that size planet. Each M dwarf has a probability of hosting an exoplanet in the habitable zone of less than 1 %. The probability of any of the six Mdwarfs hosting a transiting habitable zone exoplanet is about 2.5 %. This assumes that the occurrence rate for earlier type Mdwarfs holds for later type Mdwarfs and of course does not include the probability of hosting transiting exoplanets interior (or exterior) to the habitable zone. This is consistent with not finding any transiting planets in the habitable zones of the six targets.

I also calculated the predicted radial velocity semi-amplitude for the minimum detectable planet radii at the inner edge of the habitable zone from transit injections, shown in Table 4.3. I estimated planet masses for these radii using the mass-radius relationships from Weiss and Marcy (2014) and Wolfgang et al. (2016). I found the range of RVs was $1.7\text{--}9.1\text{ ms}^{-1}$ or $3.9\text{--}15\text{ ms}^{-1}$ respectively using TESS CTL v8 parameters and assuming circular orbits and edge-on transits ($i=90$ degrees). In comparison, the Habitable Planet Finder (HPF) (Mahadevan et al., 2012) and the Infrared Doppler instrument on Subaru telescope (Kotani et al., 2014) have design precisions between 1 and 3 ms^{-1} . Our targets are bright with J magnitudes between 9–11, making them good targets for these surveys.

4.6 Conclusions

We surveyed six mid-to-late Mdwarfs for transiting exoplanets using the NITES 0.4m telescope. We obtained high precision data with coverage into the habitable zones of these objects, with 50 % phase coverage at least midway into the range of habitable zone periods. BLS results do not reveal any significant signals of transits which are detected in multiple epochs, so no strong exoplanet candidates are identified.

Several candidate individual transits are identified and through fitting transit models, two are rejected. Two remain very weak candidates with very low SNR. The two candidate transits identified for MD07+16, one of which was identified from the BLS search, are slightly stronger, although their differing transit durations mean they could not be from the same exoplanet. All exoplanet signals identified through photometry remain candidates until confirmation with radial velocity signals. Radial velocity observation time remains the bottleneck for photometric transit surveys,

leaving many transit signals as candidate planets (which is an important factor in why many planets from the Kepler space telescope are validated by statistical tests rather than spectroscopically confirmed). As these are only individual candidate transits and do not have especially high SNR, they would be considered low priority for spectroscopic follow up observations, with the uncertainty on the period and low expected signal requiring large numbers of observations.

Transit injection tests reveal that we are sensitive to Earth to Neptune-sized planets ($1-3.8 R_{\oplus}$), depending on the star, at the inner edge of the habitable zone, so we would expect to have detected these had two or more transits been present in our data. I found planets with the minimum planet radii detectable in transit injections at the inner edge of the habitable zone should be detectable in radial velocity surveys with the Habitable Planet Finder and the Infrared Doppler instrument on Subaru telescope. The targets observed here would be good candidates for these surveys.

During the survey, a number of flares were also observed for which I calculated the flare frequency. I identify MD07+16 as having a high flaring rate and MD11+06 and MD18+29 as very low flaring rates. I investigate whether the high flaring rate of MD07+16 could affect the habitability of any planets around it. Investigation of the impact of high energy flares at this frequency illustrated that if any habitable zone planets existed around this star, their atmospheres would likely be stripped, rendering them uninhabitable.

Few transit surveys have targeted mid-to-late M dwarfs due to their inherent faintness, making this survey a valuable contribution. The larger aperture compared to wide-field surveys like TESS and NGTS, allows more photons to be captured for these faint stars. This survey targets a few stars but provides high phase coverage, reaching into the habitable zones of these stars. The high cadence of observations gives higher time resolution to help characterise transit events and flares, compared to the two minute cadence of TESS. Ongoing and future targeted surveys from the ground continue with the two TRAPPIST telescopes and their successor, the four 1m telescopes of SPECULOOS (Delrez et al., 2018). SPECULOOS aims to find late M dwarf exoplanets suitable for atmospheric characterisation, which would allow us to see whether they might be habitable.

4.7 Tables of individual events

Table 4.8: Filtered table of interesting events, listing transit-like features, including their depth and periods estimated from the single transit where available.

Target	Date	Type	Depth (%)	Estimated period (days)
MD07+16	20171222	Full	1.7 ± 0.3	$24.4^{+24.9}_{-7.0}$
MD07+16	20190128	Partial	1.5 ± 0.1	527.9 ± 24.9
MD18+29	20180707	Partial	~ 1.5	-
MD18+29	20190606	Full	0.4 ± 0.1	$31.6^{+7.6}_{-12.5}$
MD20+58	20180803	Full	~ 0.2	-
MD22+40	20180827	Full	0.3 ± 0.1	$38.0^{+23.0}_{-13.0}$

Table 4.9: All flares identified in the survey. None were observed for MD20+58. Flare peak fluxes are given, where fluxes outside the flare are normalised to 1. Calculated energies are in erg.

Target	Date	Comment	Peak flux	Calculated energies
MD02+22	20160926		1.125	
	20181001		1.015	
	20181103		1.08	
	20181106		1.35	
	20181125	double-peak	1.8	
	20190123		1.03	
	20190204		1.04	
	20190205	complex	1.03	
	20190925	two flares	1.045,	
	20191011		1.045	
MD07+16	20180125		1.10	1.638e+30
	20180126	long	1.20	2.792+31
	20180215		1.60	2.912e+31
	20180216		1.07	2.221e+30
	20180217	two flares	2.7, 1.1	5.734e+31,
	20180309		1.30	7.001e+30
	20180311		1.30	2.341e+31
	20180312		1.03	
	20180329		1.15	
	20180331	two flares	1.08, 1.12	,1.072e+31
	20180402	multifilter	1.8	1.820e+31 (I), 1.246e+32 (R)
	20180403		1.10	3.285e+30

Target	Date	Comment	Peak flux	Calculated energies
	20180405		1.10	
	20181202		1.05	
	20181214		1.05	
	20181217		1.04	
	20181218		1.06	2.671e+30
	20181226		1.20	1.168e+31
	20181228	two flares	1.30,1.05	7.040e+30,
	20190101	two flares	1.03,1.07	,4.112e+30
	20190102		1.06	1.522e+30
	20190203		1.06	1.330e+30
	20190206		1.30	1.865e+31
	20190207		1.25	5.274e+30
	20190223		1.08	1.398e+30
	20190225		1.04	
	20190226	three flares	1.05,1.05,1.30	,,7.395e+30
	20190227		1.06	
	20190301		1.04	
	20190320		1.06	
	20190321	two flares	1.28, 1.04	7.545e+30,
	20190408		1.8	2.902e+31
	20190417		1.04	
	20190420		1.08	1.1572e+30
MD11+06	20180605		1.15	
MD18+29	20190626		1.03	
MD22+40	20180721		1.08	
	20180818	two flares	1.03,1.01	
	20180820	two flares	1.10, 1.03	
	20180826	two flares	1.07,1.08	
	20180919		1.10	
	20180930		1.02	
	20181013		1.02	
	20181015		1.015	
	20190722		1.025	
	20190727		1.10	
	20190801		1.20	
	20190802		1.015	
	20190913		1.025	
	20190918		1.20	
	20191012		1.025	

Chapter 5

Characterisation of Two Low Mass Eclipsing Binaries (EBLMs) from *SuperWASP*

5.1 Introduction

5.1.1 Low mass stars

Mass-radius diagrams for stars $< 0.4 M_{\odot}$ are much less populated than for more massive stars as their intrinsic faintness makes accurate measurements difficult. Astronomers are particularly interested in accurately characterising low mass (M dwarf) stars to investigate what mass distribution separates stars from planets and the relative frequencies over masses of stars, brown dwarfs and planets. Astronomers are also interested in better understanding low mass stars as hosts of exoplanets, especially habitable zone rocky planets amenable to atmospheric follow up by the James Webb Space Telescope, *JWST*, in the near future.

The lack of well characterised M dwarf stars has led to a long time discrepancy between observations and models, e.g. Baraffe et al. (1998). These models consistently predicted M dwarfs as having 5–10% smaller radii and temperatures a few 100 K hotter than observed (Morales et al., 2009). This is most apparent around $0.35 M_{\odot}$, where M dwarfs transition from partially convective to fully convective cores (López-Morales, 2007), and could be caused by our lack of complete understanding of how this affects the mass-radius relation. High levels of stellar magnetic activity or unaccounted for sources of opacity at increased stellar metallicities have been suggested to inhibit convection in the cores of these stars. Strong magnetic fields may suppress the temperatures and cause the radii to inflate to maintain ra-

diative and hydrostatic equilibria (Lopez-Morales, 2005; Torres et al., 2014). Tidal interactions may induce strong magnetic fields and therefore inflate the radii of close binary systems (Kraus et al., 2011), although studies of single M dwarfs with interferometry have also seen inflated radii (Boyajian et al., 2012). Alternatively, higher than expected metallicities may also increase the stellar radius (Berger et al., 2006). These factors may lead to discrepancies between model predictions and eclipsing binary observations (Ribas, 2006).

Baraffe et al. (2015) released updated stellar models in 2015, computing mass-luminosity, mass-radius and colour-magnitude diagrams, covering stars with $0.07\text{--}1.4\ M_{\odot}$. The models incorporated updated molecular linelists (most importantly TiO) and updated solar abundances (significantly oxygen). Previous models predicted V–I colours which were too blue for a given magnitude of M dwarfs, which this model aimed to improve upon. Baraffe et al. (2015) note that more systematic tests of models against observations are necessary to identify remaining uncertainties, hence the need for more observational data of M dwarfs.

Discovery of planets around M dwarfs has been of particular interest recently because their small size is more favourable for detecting Earth-sized planets and their lower luminosity means the habitable zone is more amenable to transit photometry, as discussed in Chapter 4. The most common techniques for finding and determining exoplanet properties are transit photometry and radial velocity, which give radius ratios and minimum mass ratios respectively relative to the host star. Transit photometry cannot give stellar properties itself. Spectroscopy, from which radial velocities are calculated, can give stellar effective temperature, $\log g$ and metallicity, which are used in stellar evolutionary models to determine mass and radius. However, if the models are inaccurate, then inaccurate stellar, and therefore planetary, properties will be given.

5.1.2 Low mass stars in binaries

Low mass eclipsing binaries (EBLMs) are binary systems containing a M dwarf star (or Brown Dwarf) eclipsing a F/G/K star. EBLMs can help us to fill in the mass-radius diagram and test stellar models. In an eclipsing system, the relative radius and mass ratios can be found from the eclipse depth and the relative shift in radial velocities respectively as the M dwarf orbits the more massive star. As stellar evolutionary models of more massive stars are better understood and binary stars should have formed at the same time, EBLMs give us observed mass, radius and ages of M dwarf stars, independent of M dwarf models. For double-lined spectroscopic binaries (SB2s) this means model independent masses and radii can be calculated

for both stars with accuracies of 1–2%. Model independent observed masses and radii can then test the accuracy of stellar models for single stars and improve our understanding of the structure and evolution of stars.

Studying the effect of large mass differences in EBLMs may also help expand our knowledge to exoplanets. For example do EBLMs, especially those in tight orbits, form by the same process as for stars and exoplanets? Investigating mutual inclinations of EBLM systems using the Rossiter-McLaughlin effect may place constraints on this (Triaud et al., 2013). This effect can also test for tidal heating and investigating low mass stars may further our understanding of planetary spin orbit angle distribution.

5.1.3 Identification of EBLMs from SuperWASP

A number of EBLMs have been identified from transit surveys such as *SuperWASP* (Pollacco et al., 2006). The box least squares (BLS) algorithm detects their periodic transit-like signal. During visual inspection of BLS candidates (colloquially known as ‘eyeballing’), they are identified as a candidate exoplanet as they have similar radii to hot Jupiters and in surveys such as *SuperWASP* no secondary eclipse can be seen. Good quality candidates are then selected for initial spectroscopy measurements.

These initial spectra are collected using spectrographs, typically observed at phases close to 0.25 and 0.75 to measure the semi-amplitude of the radial velocity signal. One spectrum can identify a double-lined spectroscopic binary, SB2, where each component in the system produces a set of spectral lines. An object is ruled out as an exoplanet if an SB2 is observed or if the single line emitting object shows quadrature phase velocity shifts of order kilometres a second. In the latter case (an SB1), the secondary must be too large to be an exoplanet. An EBLM is implied if the primary star is found to be a FGK dwarf.

5.1.4 Contributions

James McCormac compiled a list of EBLMs from the *SuperWASP* data and organised follow up observations. Guillaume Hébrard follow up spectra and measured their radial velocities. James McCormac adapted ELLC (Maxted, 2016) for modelling the *SuperWASP* EBLMs. Amanda Doyle ran spectral fitting for WASPJ23+29. James McCormac ran initial fitting for WASPJ23+29, fitting the NITES photometry, as presented in Figure 5.4, and radial velocity data as presented in Figure 5.3. I was given two EBLMs to analyse. I ran spectral analysis for WASPJ02+40, modelled the data for both EBLMs and analysed the results.

5.2 Initial Observations

1SWASPJ020910.55+402407.2, hereafter WASPJ02+40, was initially identified as a candidate planet from *SuperWASP* (Pollacco et al., 2006) with 6062 data points collected between 2004 and 2007, each with an exposure time of 30 seconds. Data was reduced and the candidate identified using standard *SuperWASP* pipeline analysis (Collier Cameron et al., 2007). The reduced data lightcurve is shown in Figure 5.1.

1SWASPJ234318.41+295556.5, hereafter WASPJ23+29, was initially identified as a candidate planet from *SuperWASP* photometry in Christian et al. (2006) before being published as a candidate low mass eclipsing binary (EBLM) in Collier Cameron et al. (2007). It was published as a confirmed EBLM in Chaturvedi et al. (2016), using the eight partial eclipses in the *SuperWASP* data, which are shown in Figure 5.2. The catalogue stellar properties for both stars are given in Table 5.1.

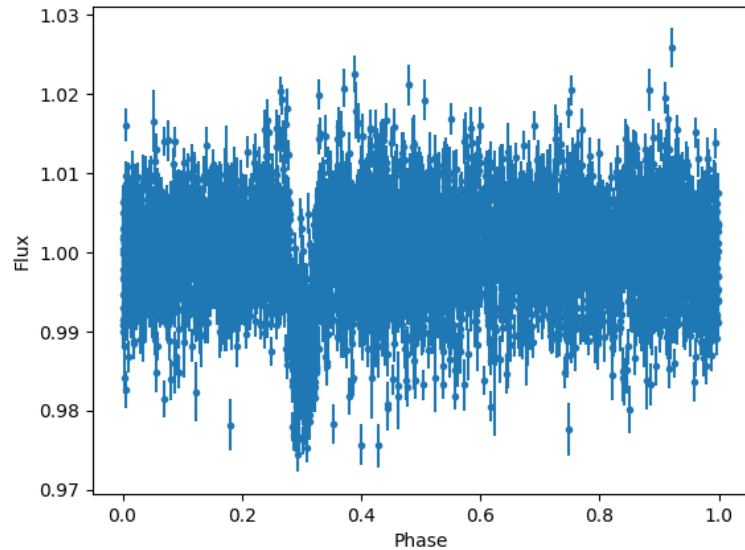


Figure 5.1: Phase folded light curve of all *SuperWASP* data for WASPJ02+40. Primary transit can be clearly seen around phase 0.3 and no secondary is visible.

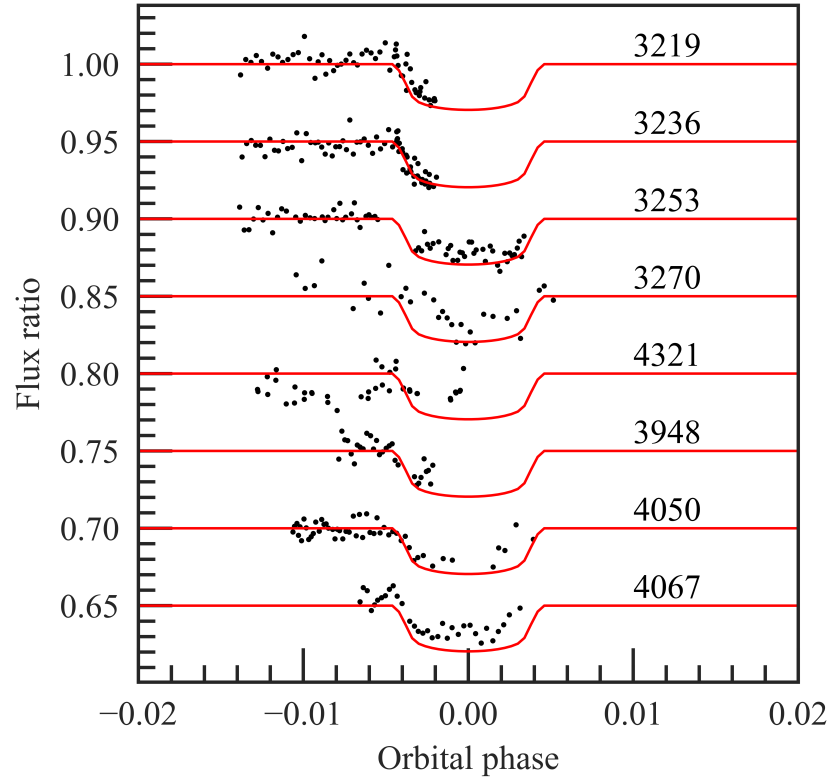


Figure 5.2: Individual *SuperWASP* light curves for WASPJ23+29. Produced by James McCormac.

Table 5.1: Stellar properties. ^a: Gaia DR2. ^b: Simbad

Parameter	WASPJ02+40	WASPJ23+29
RA ^a	02 09 10.55	23 43 18.41
Dec ^a	+40 24 07.21	+29 55 56.62
V mag ^b	9.72	10.59
Gaia G mag ^a	9.62	10.34
Gaia BP mag ^a	9.9182	10.85
Gaia RP mag ^a	9.2125	9.7185
Parallax ^a (mas)	6.7902 ± 0.0401	11.9010 ± 0.1036
Spectral type ^b	F5	K0
Gaia Radius ^a (R_{\odot})	1.34	0.88
Gaia T_{eff} ^a (K)	6101	4964

5.3 Spectral follow up observations

5.3.1 Spectral follow up of WASPJ02+40

SOPHIE is a cross-dispersed échelle spectrograph on the Observatoire de Haute-Provence 1.93m telescope. Spectra were collected in high resolution mode ($R = 75000$) to optimise radial velocity precision and reduced using standard pipeline procedures (Perruchot et al., 2008; Bouchy et al., 2009). Two SOPHIE spectra were observed in September 2011 finding a single-lined system with radial velocity (RV) shifts too large to be a planet. RVs suggested WASPJ02+40 was a single-lined binary system with the secondary’s mass at the base of the stellar main sequence. A further SOPHIE data point was collected in February 2018. Radial velocities and their errors are given in Table 5.2.

The Intermediate Dispersion Spectrograph (IDS) is a long-slit spectrograph on the 2.5m Isaac Newton Telescope. While lower resolution than SOPHIE, IDS is capable of detecting the few kms^{-1} shift due to the gravitational pull of an orbiting brown dwarf or late M dwarf. 10 IDS data points were collected between August and October 2016 and reduced using standard pipeline procedures. Radial velocity measurements for WASPJ02+40 are given in Table 5.2.

Table 5.2: Summary of 13 new spectral radial velocities for WASPJ02+40.

HJD_mid	RV (km/s)	RV _{error} (km/s)	Spectrograph
2457626.64786	18.42	1.1	IDS
2457627.73148	-14.06	0.91	IDS
2457669.49998	1.45	0.49	IDS
2457669.61846	4.82	1.04	IDS
2457670.47956	12.75	0.5	IDS
2457671.45183	-8.27	0.57	IDS
2457672.46066	18.2	0.75	IDS
2457672.60335	11.74	0.43	IDS
2457673.5515	-8.05	1.06	IDS
2457674.51323	20.96	0.72	IDS
2455830.5825	14.02	0.05	SOPHIE
2455831.5888	-15.62	0.05	SOPHIE
2458171.2616	-2.17	0.05	SOPHIE

5.3.2 FIES Spectroscopy of WASPJ23+29

19 spectra of WASPJ23+29 were obtained between 2011 August 24 and 2012 August 18 using the FIES Spectrograph (Telting et al., 2014). The data were acquired with the medium resolution fiber 3. Each science spectrum was flanked on both sides by a ThAr arc exposure to increase the accuracy of wavelength calibration.

Spectra were reduced, extracted, and wavelength calibrated using the *CERES* échelle spectroscopy reduction package (Brahm et al., 2017). The extracted 1D spectra were cross-correlated using a K5 mask to obtain radial velocity measurements, again using *CERES*. Radial velocities are listed in Table 5.3. More information on the reduction and extraction process can be found in Brahm et al. (2017).

Archival SOPHIE data and radial velocities from Chaturvedi et al. (2016) were also used. The initial fitting of radial velocity values for WASPJ23+29 using *FIES*, *SOPHIE* and *PARAS* spectra can be seen in Figure 5.3.

Table 5.3: Summary of 19 new *FIES* radial velocities (RVs) for WASPJ23+29.

BJD _{TDB} (-2450000)	RV (km/s)	RV _{error} (km/s)
5798.59644043	-27.5993	0.009
5799.62500832	-29.1452	0.009
5800.57383053	-29.2866	0.009
5924.33026010	-20.6274	0.009
5925.33125608	-18.3134	0.009
5925.39598176	-18.1655	0.009
5926.34097238	-16.0635	0.009
5926.40143116	-15.9338	0.009
5927.33393079	-14.1373	0.009
5941.31377983	-20.5626	0.009
5942.31477763	-18.2492	0.009
5943.31781041	-16.0209	0.009
6133.72041144	-13.6193	0.009
6134.65592547	-16.3270	0.009
6135.63099651	-20.2874	0.009
6136.65462402	-24.5146	0.009
6150.56215441	-13.4050	0.009
6151.62957382	-16.3919	0.009
6152.61978457	-20.4000	0.009

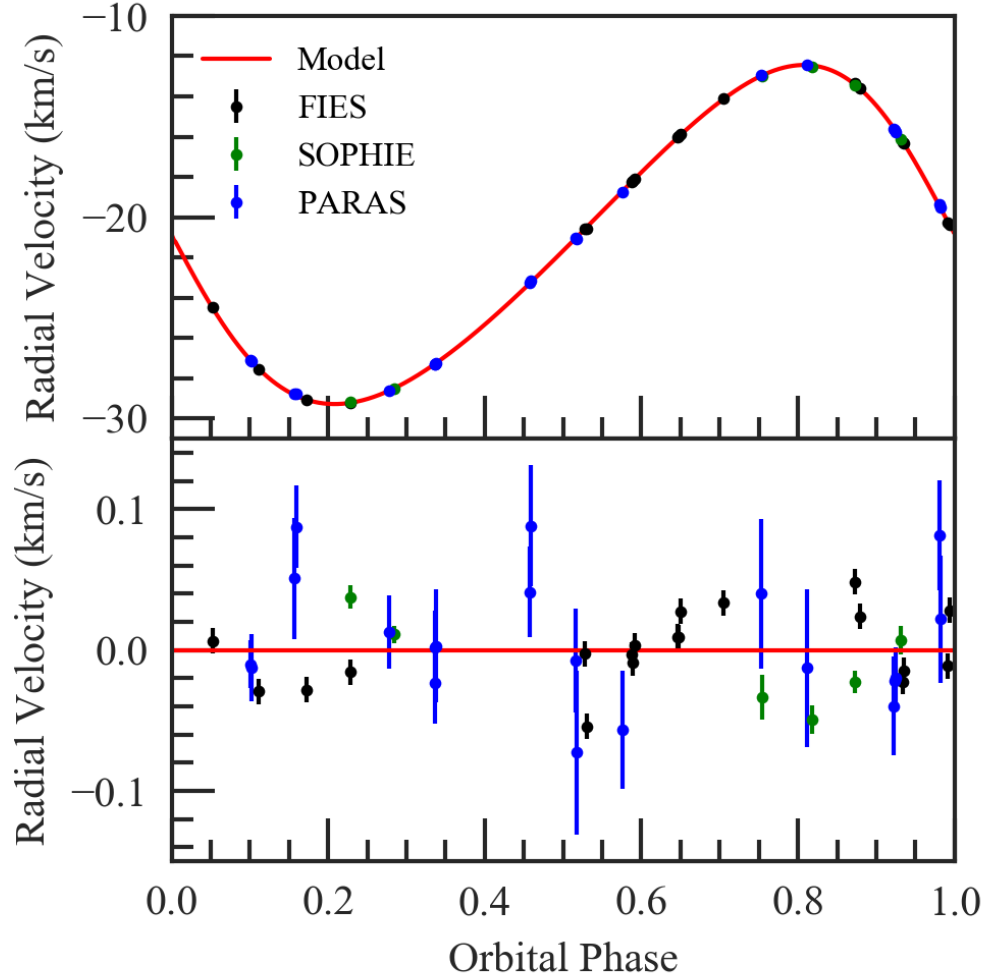


Figure 5.3: RV measurements of WASPJ23+29. The top panel shows the phased RV measurements from the *FIES*, *SOPHIE* and *PARAS* spectrographs in black, green and blue points respectively. The *SOPHIE* and *PARAS* data are taken from Chaturvedi et al. (2016) and have been included in the global modelling in Section 5.5.2. The bottom panel shows the residuals after subtracting the best fitting model. Note that error bars are plotted on the upper plot but are smaller than the point size used in the figure. Relative scales of the error bars are more clearly seen in the lower panel. Produced by James McCormac.

5.4 Follow up photometry

Follow up photometry was obtained for WASPJ23+29 as only partial eclipses are present in the SuperWASP data. A total of 4 eclipses (3 full and 1 partial) of WASPJ23+29 were obtained using the Near-Infrared Transiting ExoplanetS telescope [*NITES*] in La Palma (McCormac et al., 2014). A summary of the observations is given in Table 5.4. The data were reduced in Python using *CCDPROC* (Craig et al., 2015). A master bias, dark and flat were created using the standard process on each night. A minimum of 21 frames was used to create each master calibration frame. Two non-variable, nearby comparison stars were selected by hand, and aperture photometry extracted using *SEP* (Barbary, 2016; Bertin and Arnouts, 1996). The shift between each defocused image was measured using the *DONUTS* algorithm (McCormac et al., 2013); this was used to recentre photometry apertures on the target in each frame. The aperture sizes listed in Table 5.4 were chosen to minimise the RMS of the light curve scatter out-of-transit.

Additional data was obtained on 20120829 but the light curve showed a systematic change in the eclipse depth that anti-correlated with an instantaneous offset in the X direction caused by an uncorrected jump in the telescope position. Shortly after this jump in stellar positions the telescope was closed due to a weather alert. After 20 minutes the telescope reacquired WASPJ23+29 but again on a different region of the CCD. The affected data have been removed from the modelling process in Section 5.5.2 but are plotted in Figure 5.4 (grey points) for completeness.

Table 5.4: Summary of *NITES* follow-up photometry of WASPJ23+29. The exposure time, out of transit RMS values and aperture radius are given for each night.

Date	Filter	Images	Exptime (s)	RMS _{OOT} (mmag)	R _{phot} (pixels)
20120829	Clear	1798	15	3.2	14
20130923	Clear	1803	10	3.8	14
20131010	Clear	1333	15	2.9	14
20141001	Clear	1071	20	3.4	14

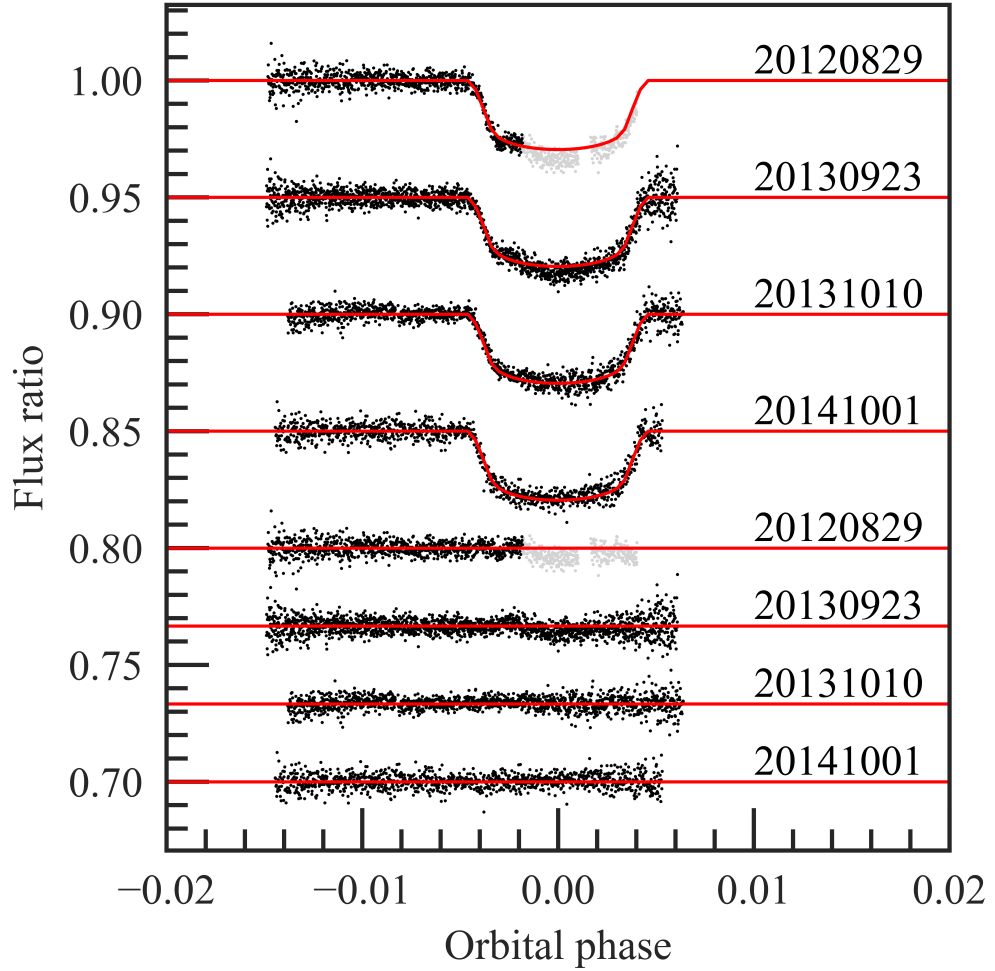


Figure 5.4: *NITES* eclipse photometry of WASPJ23+29. Black points are the photometric data. Red lines show the best fitting model from Section 5.5.2. Four individual transits observed by *NITES* are shown offset from a flux ratio of 1, labelled by the date of observation. The residuals to the best fitting model are shown in the lower section of the figure, again labelled by date of observation. The grey points on night 20120829 were affected by a jump in the telescope position at the time of the second dip during the eclipse. Grey points were excluded from the global model in Section 5.5.2. Produced by James McCormac.

5.5 Analysis and results

5.5.1 Stellar parameters

Stellar Parameters of WASPJ23+29

Spectral analysis of WASPJ23+29, including determining stellar mass, radius and age, was performed by Amanda Doyle using the methods given in Doyle et al. (2017). 10 individual FIES spectra of WASPJ23+29 were co-added to produce a single spectrum with typical S/N of around 100:1. The effective temperature (T_{eff}) was determined from the excitation balance of the Fe I lines, and $\log g$ was determined from the ionisation balance of Fe I and Fe II lines. A value for microturbulence (v_{mic}) was determined from Fe I lines, by requiring zero slope (i.e. no correlation) between the abundance and equivalent widths. Parameters obtained from the analysis are listed in Table 5.5. The projected stellar rotation velocity ($v \sin i$) was determined by fitting the profiles of several unblended Fe I lines. A value for macroturbulence of $2.82 \pm 0.73 \text{ km s}^{-1}$ was determined from the calibration of Doyle et al. (2014). A best fitting value of $v \sin i = 3.68 \pm 0.88 \text{ km s}^{-1}$ was obtained. Doyle et al. (2017) found systematic uncertainties in temperature of $70 \pm 80 \text{ K}$, 0.04 ± 0.11 in $\log g$, $0.11 \pm 0.04 \text{ km s}^{-1}$ for v_{mic} and 0.08 ± 0.02 for metallicity $[Fe/H]$ for a set of 23 FGK standard stars.

Mass and radius parameters were calculated from the T_{eff} , $\log g$ and metallicity ($[Fe/H]$, defined as $\log_{10}([Fe/H]_{\text{star}}/[Fe/H]_{\text{sun}})$ throughout the chapter) values using the Torres et al. (2010) relation. Torres et al. (2010) derived empirical relations of mass and radius for main sequence stars above $0.6 M_{\odot}$. They used 95 detached binary systems (of which 94 were eclipsing) where mass and radius of both stars were known to at least $\pm 3 \%$. They recompute stellar parameters with a consistent set of assumptions. As a result they find functions of T_{eff} , $\log g$ and metallicity which yield mass and radius with errors of 6% and 3% respectively.

There is no significant detection of lithium in the spectra, with an equivalent width upper limit of $14 \text{ m}\text{\AA}$ corresponding to an abundance upper limit of $\log A(\text{Li}) < 0.60 \pm 0.09$. This implies an age of several hundred Myr (Sestito and Randich, 2005). The rotation rate ($P = 15.1 \pm 4.7 \text{ days}$) implied by the $v \sin i$ gives a gyrochronological age of $0.67^{+0.60}_{-0.38} \text{ Gyr}$ using the Barnes (2007) relation.

Spectral analysis of WASPJ02+40

Spectral parameters for WASPJ02+40 were determined from the 1D averaged SOPHIE spectrum by fitting synthetic spectra with resolution 75000 using SPEC-

Table 5.5: Stellar parameters of WASPJ23+29 from spectroscopic analysis.

Parameter	Value
T_{eff}	$5053 \pm 65 \text{ K}$
$\log g$	4.40 ± 0.17
v_{mic}	$0.92 \pm 0.05 \text{ km s}^{-1}$
$v \sin i$	$3.68 \pm 0.88 \text{ km s}^{-1}$
[Fe/H]	0.27 ± 0.11
$\log A(\text{Li})$	$< 0.60 \pm 0.09$
Mass	$0.92 \pm 0.08 M_{\odot}$
Radius	$0.98 \pm 0.21 R_{\odot}$

Note: Mass and radius are estimated using the Torres et al. (2010) calibration. Abundances are relative to the solar values obtained by Asplund et al. (2009).

TRUM within iSpec (Blanco-Cuaresma, 2015; Gray and Corbally, 1994). These used MARCS model atmospheres (Gustafsson et al., 2008), solar abundances from Grevesse et al. (2007) and VALD linelists (Kupka et al., 2011). I determined the T_{eff} from fitting synthetic spectra to the wings of the $H\alpha$ line. I fitted for the metallicity, $[Fe/H]$, and $v \sin i$ using Fe I lines, finding the star is a fast rotator. I find a solar-like $\log g$ using the sodium doublet around 589 nm. I do not identify lithium in the spectrum at 670.7 nm, implying this is not a young star. Blanco-Cuaresma et al. (2014) investigated systematic uncertainties by finding the difference between parameters determined with iSpec and reference values. They did this for 34 Gaia FGK benchmark stars whose temperature and $\log g$ were determined independently of spectroscopy. They found the synthetic spectral fitting technique used here had systematic offsets in temperature of $-24 \text{ K} \pm 124 \text{ K}$, $\log g$ of -0.11 ± 0.21 and metallicity of 0.01 ± 0.14 . They also investigated the dispersion in analysing different spectra of the same star with the same method, finding uncertainties in temperatures of 15 K, $\log g$ of 0.06 and metallicity of 0.01.

I used the isochrones package (Morton, 2015) with the MIST evolutionary models (Choi et al., 2016) to determine the stellar mass and radius. I input the temperature, $\log g$ and metallicity determined from spectral fitting as well as parallax and Gaia G , G_{BP} and G_{RP} magnitudes from Gaia DR2 (Gaia Collaboration et al., 2016, 2018), as given in Table 5.1. For comparison, I also calculated the primary star mass and radius from the spectral parameters using the Torres et al. (2010) relation. Stellar parameters are given in Table 5.6.

Table 5.6: Stellar parameters of WASPJ02+40 from spectral analysis. Parameters ‘Spectra’ were determined in iSpec with abundances relative to solar values in Grevesse et al. (2007). Resulting stellar parameters of WASPJ02+40 output by the isochrones package (Morton, 2015) are given under ‘Isochrones’, see text for details. *Note: Mass and radius in this column are calculated using the Torres et al. (2010) relation.

Parameter	Spectra	Isochrones
T_{eff} (K)	6100 ± 150	6038 ± 144
$\log g$	4.4 ± 0.2	4.37 ± 0.10
$v \sin i$ (km s $^{-1}$)	50 ± 5	-
[Fe/H]	0.1 ± 0.1	0.06 ± 0.09
Age (Gyr)	-	2.7 ± 1.9
A_V	-	0.50 ± 0.29
Mass (M_{\odot})	$1.175 \pm 0.131^*$	1.117 ± 0.078
Radius (R_{\odot})	$1.124 \pm 0.320^*$	1.145 ± 0.168

5.5.2 Global modelling with ellc

ELLC is a lightcurve modelling code described by Maxted (2016) which models eclipsing binaries and transiting exoplanets. It can model photometry and radial velocity measurements together to fit the system parameters. ELLC finds the best fitting parameters using the initial parameters (as discussed in Section 5.5.2) and the observed data. EMCEE (Foreman-Mackey et al., 2013) is an MCMC method which iterates the ELLC modelling using a user defined number of walkers over a user defined number of steps to find the best fitting model. MCMCs are discussed further in Methods (Section 2.4.1).

Types of Initial Parameters

There are several types of initial parameter given to ELLC: i. ‘no prior’ parameters are given with their seed value and weight, which determine the initial distribution of walkers. ii. uniform parameters which also have seed value and weights but also have lower and upper priors to limit the range of values the walkers can explore. iii. fixed parameters, whose values are used in the fitting but are not changed by it. iv. external parameters which add constraints to the possible parameters as the model must balance fitting the data with parameters being physically feasible and consistent with parameters determined from e.g. spectral analysis.

Uniform parameters fitted in ELLC are: primary stellar radius in units of semi-major axis r_1/a ; radius ratio between primary and secondary object, r_2/r_1 ,

determined from the transit depth; radial velocity semi-major amplitude, K ; inclination angle i ; eccentricity, e ; longitude of periastron, ω ; mass ratio, q ; and systematic velocity in each spectrograph, v_{sys} .

‘No prior’ parameters are the period, P , and the transit mid-point, t_0 . Limb darkening constants are calculated using the limb darkening toolkit (LDTk, Parviainen and Aigrain (2015), see Methods, Section 2.6.1) with parameters found in spectral analysis (T_{eff} , $\log g$ and metallicity) in a custom filter for NITES and *SuperWASP* bands as appropriate. Quadratic limb darkening parameters were input as fixed parameters. External parameters for primary star mass, radius and $\log g$ with their uncertainties were also input into ELLC.

Determining Initial Parameters

For WASPJ02+40, initial values for the period, t_0 and r_2/r_1 were determined using the photometry, with r_2/r_1 calculated from the light curve transit depth and using the primary stellar radius (r_1) found in spectral analysis. Initial values for the systematic velocities for the different instruments (v_{sys}), radial velocity semi-amplitude (K) and the mass ratio (q) were calculated from the radial velocity measurements.

Initial parameters for WASPJ02+40 were estimated based on the *SuperWASP* photometry, radial velocities and spectral analysis, as indicated in Table 5.7. Specifically, the radius ratio (r_2/r_1) was calculated from the box least squares (BLS) transit depth (ΔF) reported by the *SuperWASP* pipeline using Equation 5.1.

$$\frac{r_2}{r_1} = \sqrt{\Delta F} \quad (5.1)$$

An estimate of the semi-major axis was calculated from the period from *SuperWASP* (P) and the primary star mass (M_1) using Kepler’s third law and assuming secondary mass of 0, as shown in Equation 5.2.

$$a = \sqrt[3]{\frac{P^2 G M_1}{4\pi^2}} \quad (5.2)$$

As IDS has coverage at quadratures, the maximum semi-amplitude of the radial velocities was estimated as half the difference between maximum and minimum radial velocity values measured by IDS. The mass ratio (q) was found by estimating the minimum mass of the secondary (M_2) and dividing by the primary star mass (M_1) found in spectral analysis. M_2 was calculated in units of Jupiter mass (before being converted to units of solar mass) and P in units of years, assuming zero eccentricity using Equation 5.3 (Perryman, 2018).

$$M_2 = \frac{KM_1^{2/3}P^{1/3}}{28.4} \quad (5.3)$$

The IDS systematic velocity was estimated by summing the minimum and maximum measured radial velocities and taking half this value. There are only 3 SOPHIE points and no large offset is seen, so I use a starting systematic velocity of zero.

Table 5.7: Initial parameters used for WASPJ02+40. SuperWASP = determined from SuperWASP photometry. RVs = radial velocities. Spectra = from spectral analysis. v_{sys} = systematic velocity. Ldc = limb darkening constant.

Initial parameter	Value	Weight	Source
r_2/r_1	0.124	0.01	SuperWASP
period (days)	2.17204	0.0001	SuperWASP
a (m)	5.0901909e+09	-	SuperWASP and spectra
K (km s ⁻¹)	17.51	0.1	IDS RVs
q	0.10288	0.005	RVs, spectra, SuperWASP
t_0 (days)	2453969.4577	0.001	SuperWASP
r_1/a	0.15621911	0.01	SuperWASP and spectra
M_1 (M_\odot)	1.114	0.08	Spectra
R_1 (R_\odot)	1.143	0.18	Spectra
log g	4.4	0.2	Spectra
v_{sys} IDS (km s ⁻¹)	3.45	0.5	IDS RVs
v_{sys} SOPHIE (km s ⁻¹)	0	0.5	SOPHIE RVs
eccentricity	0	-	Fixed to 0
inclination (°)	0	-	Fixed to 90
omega (°)	90	-	Fixed to 90
ldc1	0.6148	-	Fixed: value from LDTk
ldc2	0.0963	-	Fixed: value from LDTk

Initial parameters for WASPJ23+29 used values from Chaturvedi et al. (2016), with initial parameters for systematic velocities for SOPHIE and FIES estimated in the same way as discussed for IDS above.

Running ellc

Starting positions of walkers were determined from the initial positions based on a normal distribution, with mean values from the initial values and widths from the

Table 5.8: Initial parameters used for WASPJ23+29. RVs = radial velocities. Spectra = from spectral analysis. v_{sys} = systematic velocity. Ldc = limb darkening constant.

Initial parameter	Value	Weight	Source
r_2/r_1	0.1471	0.01	Chaturvedi 2016
period (days)	16.95350	0.00005	Chaturvedi 2016
K (km s^{-1})	8.407	0.01	Chaturvedi 2016
q	0.1134	0.005	Chaturvedi 2016
t_0 (days)	2453592.7443	0.003	Chaturvedi 2016
eccentricity	0.16100	0.005	Chaturvedi 2016
inclination ($^\circ$)	89.55	0.2	Chaturvedi 2016
omega ($^\circ$)	77.48	1	Chaturvedi 2016
r_1/a	0.03115	0.001	From a/r_1 Chaturvedi 2016
M_1 (M_\odot)	0.92	0.08	Spectra
R_1 (R_\odot)	0.98	0.21	Spectra
$\log g$	4.4	0.17	Spectra
v_{sys} PARAS (km s^{-1})	-21.0314	0.02	Chaturvedi 2016
v_{sys} SOPHIE (km s^{-1})	-20.836	0.1	SOPHIE RVs
v_{sys} FIES (km s^{-1})	-21.290	0.1	FIES RVs
ldc1	0.5760	-	Fixed: value from LDTk
ldc2	0.0772	-	Fixed: value from LDTk

weights, both given in Tables 5.7 and 5.8. The walker scaling factor gives the number of walkers, with a walker scaling factor of 1 setting the number of walkers as 4 times the number of modelled parameters. The thinning factor decreases autocorrelation between parameters by using only every n th step in the chain, it can also help memory or time constraints in post-chain processing.

ELLC models were ran for 10000 steps using a walker scaling factor of 5 and thinning factor of 5, resulting in 2000 steps in the final result. Upon inspection of the model parameter chains, a burn in period of 10% (200 steps) was used to determine the posterior probability distribution, represented in a corner plot, and to produce the fitted light curve and radial velocity models.

5.6 Results

5.6.1 WASPJ23+29

Parameters

Figure 5.5 shows the best fitting transit lightcurve and radial velocity model, folded on the best period identified by ELLC given with the other output parameters in Table 5.9. I derive the uncertainty on the secondary mass by combining the errors on mass ratio and primary mass in quadrature and similarly for the secondary radius.

The corner plot produced from MCMC analysis in Figure 5.6 shows that the parameters are well constrained. The radial velocity semi-amplitude, K , is weakly correlated with the orbital period and weakly anticorrelated with t_0 , ω and the systemic velocity from the FIES instrument. Period and t_0 will be more precisely constrained by the lightcurve however. A strong correlation is seen between the inclination and radius parameters r_1/a and r_2/r_1 , with their relationship described in Equation 1.2 in Section 1.2.1. The range of possible inclination values is small as the system geometry is constrained by the eclipse lightcurve. This provides a strong lower limit on inclination seen in the posterior probability distribution, which is consistent with edge-on (90 degrees). However inclination is an important source of uncertainty in the radius ratio and therefore the secondary star radius.

Fitting for inclination is the approach taken in Maxted (2016). An alternative is to fit for a parameter which more weakly correlates with the radius. Gill et al. (2019) fitted EBLM systems using the full-width half maximum of the transit given in Equation 5.4. Some studies alternatively fit for the impact parameter, b , which is a function of a/r_1 and derive the inclination from this (e.g. Casewell et al., 2018; von Boetticher et al., 2019). This could be investigated in future work.

$$w = \frac{R_*}{a} \frac{\sqrt{1 - b^2}}{\pi} \quad (5.4)$$

Table 5.9: Output parameters derived from ELLC for WASPJ23+29, using primary star parameters from the Torres et al. (2010) relation.

Parameter	Value	Uncertainty
Model parameters	-	-
r_1/a	0.0293	0.0003
r_2/r_1	0.1554	0.0006
K (km s ⁻¹)	8.422	0.003
inclination (°)	90.0	0.1
eccentricity	0.1604	0.0003
omega (°)	78.37	0.09
q	0.112	0.004
vsys PARAS (km s ⁻¹)	-20.896	0.007
vsys SOPHIE (km s ⁻¹)	-21.122	0.004
vsys FIES (km s ⁻¹)	-21.133	0.002
t_0 (days)	2453592.742	0.002
period (days)	16.95355	0.00001
Derived parameters	-	-
secondary mass (M_J)	108.1	10.0
secondary radius (R_J)	1.48	0.32

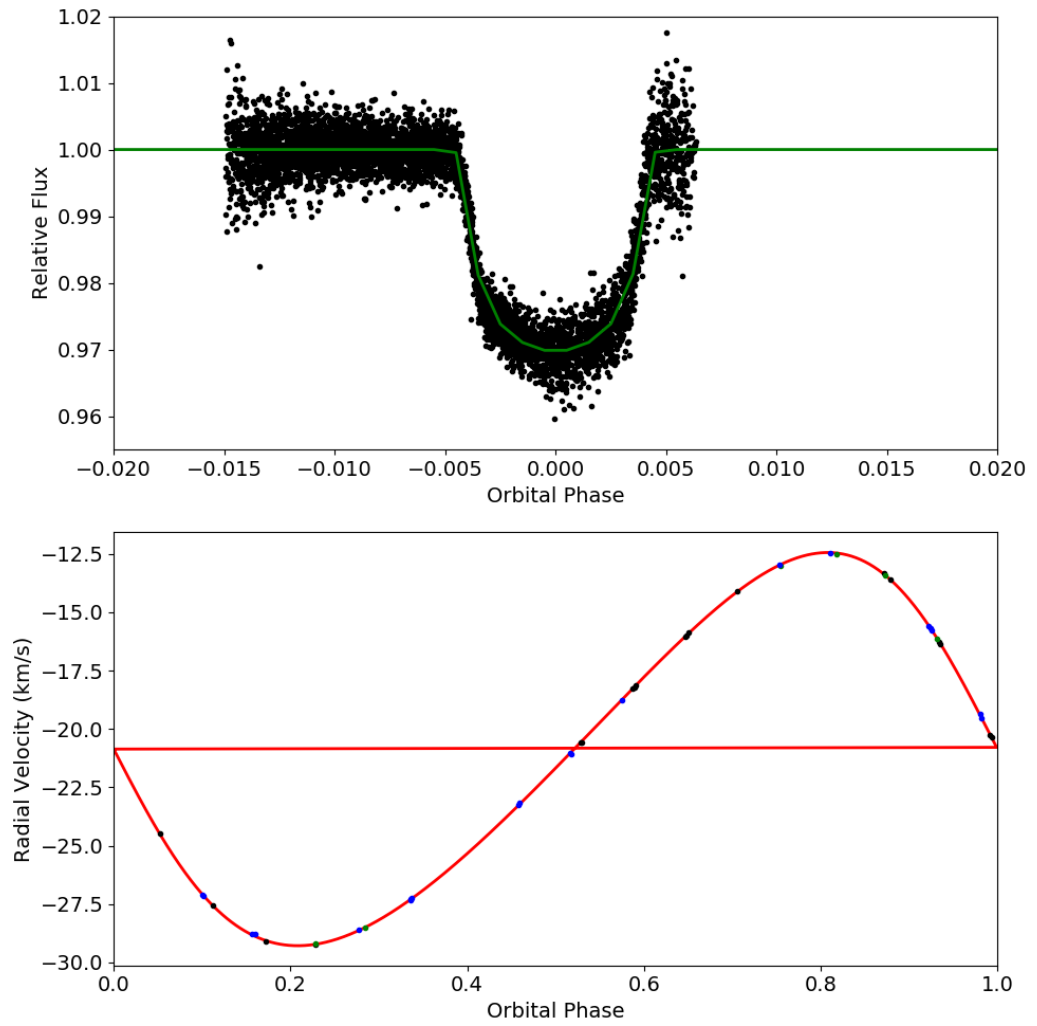


Figure 5.5: WASPJ23+29 fitted light curve and radial velocity model using spectral parameters derived from Torres et al. (2010).

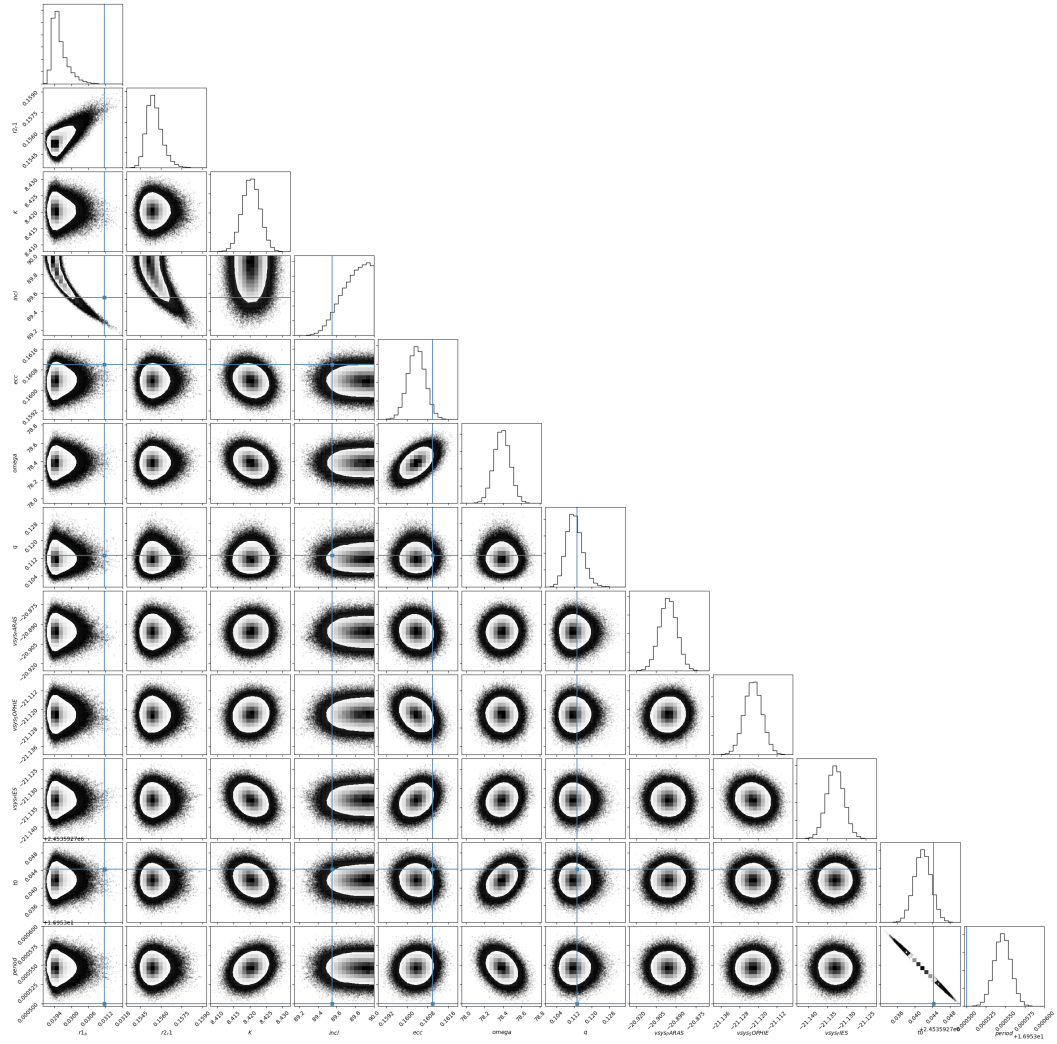


Figure 5.6: WASPJ23+29 corner plot for the fitted model shown in Figure 5.5. Parameters from left to right: r_1/a , r_2/r_1 , K , inclination, eccentricity, ω , q , v_{sys} PARAS, v_{sys} SOPHIE, v_{sys} FIES, t_0 .

Comparison of WASPJ23+29 to literature values

The parameters obtained using ELLC and the Torres et al. (2010) relation are compared to those from the combined radial velocity and transit fit in Chaturvedi et al. (2016) in Table 5.10. Our spectral analysis gives larger primary stellar mass and radius values than those in Chaturvedi et al. (2016), with errors on the primary stellar radius much larger. This is surprising given our higher signal to noise spectrum (SNR 100 vs ~ 80 that Chaturvedi et al. (2016) report). T_{eff} and $\log g$ are lower and metallicity is higher than those from Chaturvedi et al. (2016) though these values overlap within the errors.

The results from ELLC give a very similar mass ratio and period to those in Chaturvedi et al. (2016) which agree within the errors. Significantly, ELLC identifies a larger radius ratio with nearly an order of magnitude lower uncertainty. Thanks to the high precision NITES photometry, the transit depth and shape can be more precisely constrained than in the *SuperWASP* data with only partial eclipses used by Chaturvedi et al. (2016), which reduces uncertainty on the radius ratio and inclination.

The larger derived secondary radius compared to Chaturvedi et al. (2016) is due to both the larger primary stellar radius and the larger radius ratio identified. The larger radius ratio cannot be explained due to inclination as Chaturvedi et al. (2016) find a lower inclination value and the posterior plots (e.g. Figure 5.6) shows lower inclination correlates with higher radius ratios. Our larger secondary radius does still agree within the uncertainties with that of Chaturvedi et al. (2016). Unfortunately our secondary radius uncertainty is larger than that of Chaturvedi et al. (2016) due to our larger uncertainty on the primary stellar radius identified in spectral analysis.

Investigation into Chaturvedi et al. (2016) parameters

It is surprising that our results from ELLC and the Torres et al. (2010) relation produced significantly larger error bars, so I investigated Chaturvedi et al. (2016)'s method. For spectral analysis, they co-add PARAS spectra to give a signal to noise ratio of 65–70 at the blue end (500–600 nm) and 80 at the red end (600–650 nm). They report co-adding 28 spectra but only 20 are listed in their observation log (their Table 3). The relative uncertainties between PARAS and FIES spectra radial velocities can be seen in Figure 5.3, which suggests that co-adding 10 FIES spectra should produce higher signal to noise than 20 or 28 PARAS spectra. Chaturvedi et al. (2016) consider different systematic uncertainties in synthetic spectrum gen-

Table 5.10: Derived parameters comparison for WASPJ23+29. All parameters for Chaturvedi et al. (2016) come from joint modelling with EXOFAST apart from T_{eff} , $\log g$, $[Fe/H]$ and primary stellar mass and radius which are reported to come from spectral analysis using PARAS data. ‘ELLC Torres’ shows ELLC results using primary star mass and radius calculated from spectra using the Torres et al. (2010) relation.

Parameter	Chaturvedi et al. (2016)	ELLC Torres
Primary stellar mass (M_{\odot})	$0.864^{+0.097}_{-0.098}$	0.92 ± 0.08
Primary stellar radius (R_{\odot})	$0.854^{+0.050}_{-0.060}$	0.98 ± 0.21
Secondary mass (M_{\odot})	0.098 ± 0.007	0.1032 ± 0.0096
Secondary radius (R_{\odot})	0.127 ± 0.007	0.1523 ± 0.0326
Secondary mass (M_J)	102 ± 7	108 ± 10
Secondary radius (R_J)	1.24 ± 0.07	1.48 ± 0.32
Mass ratio	$0.1134^{+0.0056}_{-0.0060}$	0.112 ± 0.004
Radius ratio	$0.1471^{+0.005}_{-0.004}$	0.1554 ± 0.0006
Period (days)	16.95350 ± 0.00005	$16.95355 \pm 1\text{e-}5$
inclination ($^{\circ}$)	$89.55^{+0.12}_{-0.40}$	90.0 ± 0.1
T_{eff} (K)	5125 ± 67	5053 ± 65
$[Fe/H]$	0.1 ± 0.14	0.27 ± 0.11
$\log g$	4.6 ± 0.14	4.4 ± 0.17

eration for signal to noise (S/N) <100 to determine errors on effective temperature of 67 K, $\log g$ of 0.11 and metallicity, $[Fe/H]$, of 0.11. Using synthetic spectrum generation, they calculate T_{eff} (5100 ± 84 K) and metallicity ($[Fe/H] = 0.1 \pm 0.14$) but say they do not have sufficient precision in magnesium lines for $\log g$ measurement. Instead they measure the equivalent width of Fe I and Fe II lines from Sousa et al. (2014) linelists, fixing metallicity to the value found from synthetic spectra, inputting these into the SPECTRUM abundance routine to determine T_{eff} , $\log g$ and microturbulence values. Their mass and radius values are derived from spectral parameters using the Torres et al. (2010) relation.

I repeat their parameter derivation, inputting the parameters from their spectroscopic fit (T_{eff} , $\log g$ and metallicity, as given in Table 5.10) into the Torres et al. (2010) relation, and find mass $0.869 M_{\odot}$ and radius $0.770 R_{\odot}$. This radius is noticeably lower than their reported value from spectral fitting ($0.854 R_{\odot}$), although a radius of $0.78 \pm 0.1 R_{\odot}$ is reported in their Table 5 for fitting using only radial velocity data. Chaturvedi et al. (2016) use EXOFAST (Eastman et al., 2013) to fit primary star parameters at the same time as relative system parameters, which

Table 5.11: Stellar parameters of WASPJ23+29 from Chaturvedi et al. (2016). Parameters within the PARAS column were calculated by Chaturvedi et al. (2016) using PARAS spectra. Parameters within the SOPHIE column were calculated using archival SOPHIE spectra. They estimate mass and radius using the Torres et al. (2010) calibration.

Parameter	PARAS	SOPHIE
$T_{\text{eff}}(\text{K})$	5125 ± 67 (EW) 5100 ± 84 (synthetic)	5150 ± 67 (EW) 5000 ± 84 (synthetic)
$\log g$	4.6 ± 0.14	4.5 ± 0.14
$v_{\text{mic}} (\text{km s}^{-1})$	1.2 ± 0.1	1.2 ± 0.1
$v \sin i (\text{km s}^{-1})$	3.2 ± 0.5	-
$[\text{Fe}/\text{H}]$	0.1 ± 0.14	0.2 ± 0.14
Rotational period (days)	13.6 ± 0.5	
Age (Gyr)	1.5 ± 0.5	-
Mass (M_{\odot})	$0.864 \pm_{-0.098}^{+0.097}$ (combined) $0.868 \pm_{-0.05}^{+0.07}$ (RV only)	-
Radius (R_{\odot})	$0.854 \pm_{-0.060}^{+0.050}$ (combined) $0.78 \pm_{-0.1}^{+0.11}$ (RV only)	-

requires priors on T_{eff} , $\log g$ and metallicity. EXOFAST uses the Torres et al. (2010) relation to determine the primary star mass and radius at each step in the Markov chain. Their errors are then determined from the posterior probability distribution. A caveat is that EXOFAST is an exoplanet fitting routine that ignores the secondary mass while calculating orbital separation, which as Chaturvedi et al. (2016) say, may affect the accuracy of the derived secondary radius. This is why Eastman et al. (2013) note EXOFAST ‘should only be applied to single (post-) main sequence stars above $0.6 M_{\odot}$ ’. I considered minimum and maximum possible masses and radii from Chaturvedi et al. (2016)’s spectral parameters and errors by inputting all permutations of these parameters into the Torres et al. (2010) relation. From this, I found the uncertainty on mass is $0.06 M_{\odot}$ and radius is $0.14 R_{\odot}$ when considering the full range of errors rather than the errors from fitting in EXOFAST. The resulting values for mass and radius of the primary and secondary star from Chaturvedi et al. (2016) and our calculation using their parameters, are compared in Table 5.13.

Combining the error on primary radius, $0.14 R_{\odot}$, in quadrature with their measured radius ratio error (as given in Table 5.10) under the assumption this does not change, I find the error on their secondary radius increases to 18.5%. This is comparable to our error on secondary radius of 21.4%, which also considers the range

of possible primary star radius parameters from the Torres et al. (2010) relation. An 18.5% error corresponds to an increase from $0.007 R_{\odot}$ to $0.023 R_{\odot}$. This explains a large part of the difference in uncertainties between our own and Chaturvedi et al. (2016)’s secondary radii. Chaturvedi et al. (2016) measure a lower uncertainty on $\log g$ of 0.14 compared to our 0.17. Finding the range of possible parameters using the Torres et al. (2010) relation using our measured spectral parameters but replacing our $\log g$ uncertainty of 0.17 with 0.14, the error on our secondary radius decreases to 20.0%, going some way to explaining the difference between the two uncertainties. The remaining difference between their and our uncertainty may be inherent due to a larger range of masses and radii fitting the measured spectral parameters. Our calculation finds that the mass of the secondary is almost the same, with a slightly larger error bar ($103 \pm 9 M_J$ vs $102 \pm 7 M_J$), but that the smaller primary radius with a larger error bar impacts on the secondary, decreasing the secondary star radius ($1.10 \pm 0.20 R_J$ vs $1.24 \pm 0.07 R_J$).

Alternative parameter calculation

I investigated using isochrones as an alternative to the Torres et al. (2010) relation for calculating primary star parameters for WASPJ23+29. The Torres et al. (2010) relation is not mathematically self-consistent, as input $\log g$ does not precisely equal the resulting $\log g$ value (Eastman et al., 2013). I calculated parameters from stellar evolution models, specifically the isochrones package (Morton, 2015) with MIST evolutionary models (Choi et al., 2016), as for WASPJ02+40. This used T_{eff} , $\log g$ and $[Fe/H]$ from spectral analysis, age derived from lithium abundance, mass from Torres et al. (2010) relation, and Gaia DR2 parallax, G , G_{RP} and G_{BP} magnitudes. Taking the median and standard deviation as the derived parameter and its uncertainty, gave lower resulting mass and radius values, shown in Table 5.12. However the calculated age: 6.53 ± 3.9 Gyr is both inconsistent with that found from spectroscopy and has a large uncertainty, questioning the validity of the mass and radius.

Global modelling results from ELLC using mass and radius from isochrones are given in Table 5.13. Primary star mass from isochrones is much more similar to that of Chaturvedi et al. (2016), though the isochrones method gives smaller errors. As mass ratio is almost identical to that of Chaturvedi et al. (2016), this results in a very similar secondary mass value, though the isochrones method has smaller error bars due to smaller errors on both primary star mass and mass ratio. Primary star radius is slightly smaller than that given by Chaturvedi et al. (2016) with comparable error bars. The isochrones method finds a larger radius ratio compared to that of

Chaturvedi et al. (2016), but this results in the same secondary radius as the effect of a larger radius ratio is cancelled out by the smaller primary radius. Despite our radius ratio having an error bar 7 times smaller, indicating smaller random errors in the superior *NITES* photometry, the error on primary radius from systematics in the calibrations dominates, resulting in comparable secondary radius error to that reported in Chaturvedi et al. (2016).

Table 5.12: Stellar parameters of WASPJ23+29 calculated using the isochrones package (Morton, 2015), see text for details.

Parameter	Value
Mass	$0.86 \pm 0.03 M_{\odot}$
Radius	$0.82 \pm 0.05 R_{\odot}$
Age	6.5 ± 3.9 Gyr
A_V	0.52 ± 0.29
[Fe/H]	0.20 ± 0.09
$\log g$	4.54 ± 0.04
T_{eff}	5055 ± 65 K

5.6.2 WASPJ02+40

Figures 5.7 and 5.8 give the model fit and corresponding corner plot using parameters determined from spectral analysis, using isochrones. The corner plot shows the parameters are well constrained. The best fitting parameters and their uncertainties are given in Table 5.14. Uncertainties for derived parameters are calculated as for WASPJ23+29, calculating errors in quadrature. Derived parameters show 7 % uncertainty on the secondary star’s mass and 15 % uncertainty on its radius. For comparison, I also ran ELLC modelling with primary star mass and radius calculated using the Torres et al. (2010) relation. The larger primary star mass and smaller primary star radius lead to a secondary star with a larger mass and smaller radius. Using the larger uncertainties on the primary star from the Torres et al. (2010) relation also led to increased secondary star uncertainties, so uncertainty is 12 % for mass and 28 % for radius.

Table 5.13: Derived parameters comparison for WASPJ23+29. The second column (Chat. 2016) gives parameters as reported in Chaturvedi et al. (2016) come from joint modelling with EXOFAST apart from T_{eff} , $\log g$, $[Fe/H]$ and primary stellar mass and radius reported from spectral analysis using PARAS data. Where there is a second row of data, these record our calculation of errors based on their spectral parameters, and marked by ‘this work’. The third column (ELLC Torres) shows ELLC results using mass and radius derived from Torres et al. (2010) as external parameters. The fourth column shows ELLC results using mass and radius derived from isochrones.

Parameter	Chat. 2016	ELLC Torres	ELLC isochrones
$M_1 (M_{\odot})$	$0.864^{+0.097}_{-0.098}$ (Chat2016)	0.92 ± 0.08	0.86 ± 0.03
	0.869 ± 0.06 (this work)		
$R_1 (R_{\odot})$	$0.854^{+0.050}_{-0.060}$ (Chat2016)	0.98 ± 0.21	0.82 ± 0.05
	0.77 ± 0.14 (this work)		
$M_2 (M_{\odot})$	0.098 ± 0.007 (Chat2016)	0.1032 ± 0.0096	0.0978 ± 0.0036
	0.099 ± 0.009 (this work)		
$R_2 (R_{\odot})$	0.127 ± 0.007 (Chat2016)	0.1523 ± 0.0326	0.1274 ± 0.0078
	0.113 ± 0.023 (this work)		
$M_2 (M_J)$	102 ± 7 (Chat2016)	108 ± 10	102 ± 4
	103 ± 9 (this work)		
$R_2 (R_J)$	1.24 ± 0.07 (Chat2016)	1.48 ± 0.32	1.240 ± 0.078
	1.10 ± 0.20 (this work)		
Mass ratio	$0.1134^{+0.0056}_{-0.0060}$	0.112 ± 0.004	0.1138 ± 0.0014
Radius ratio	$0.1471^{+0.005}_{-0.004}$	0.1554 ± 0.0006	0.1553 ± 0.0006
Period /day	16.95350 ± 0.00005	$16.95355 \pm 1\text{e-}5$	16.95355 ± 0.00001
T_{eff}/K	5125 ± 67	5053 ± 65	5053 ± 65
$[Fe/H]$	0.1 ± 0.14	0.27 ± 0.11	0.27 ± 0.11
$\log g$	4.6 ± 0.14	4.4 ± 0.17	4.4 ± 0.17

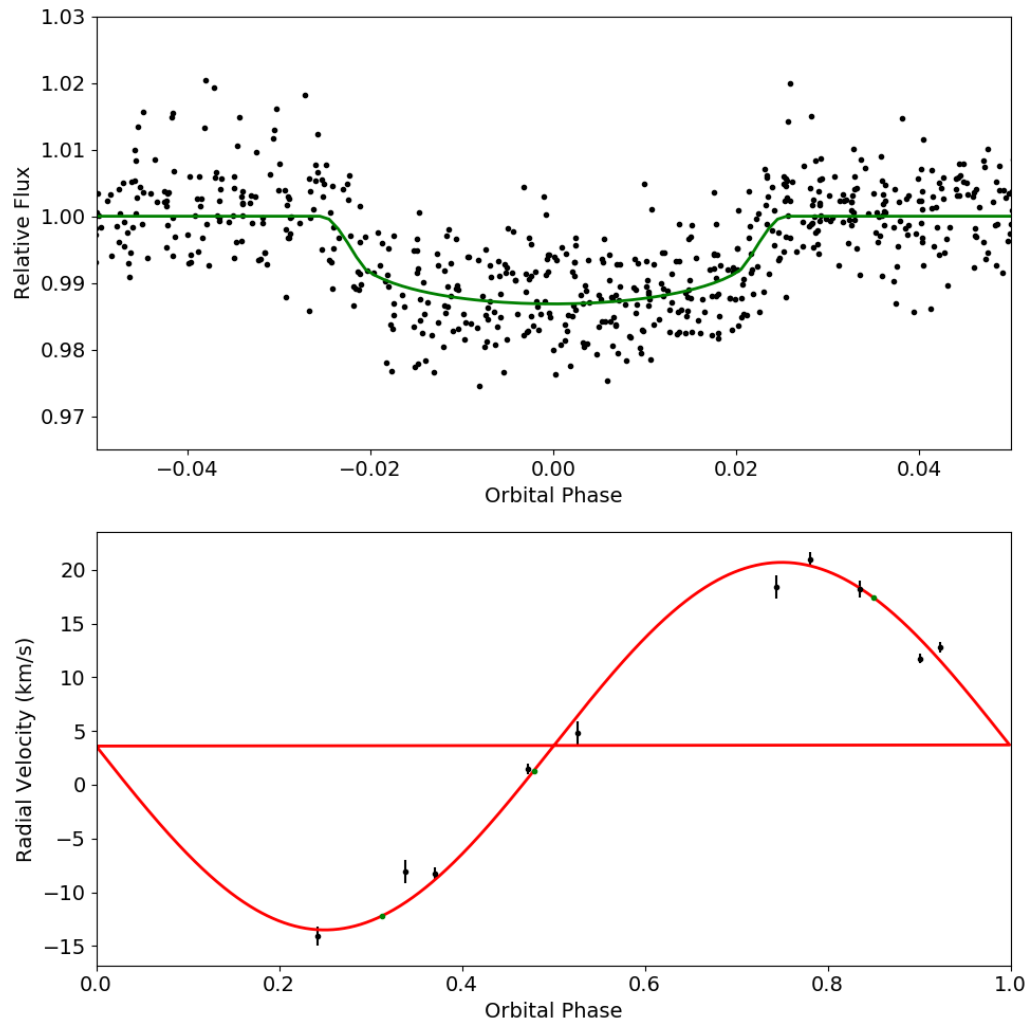


Figure 5.7: WASPJ02+40 fitted light curve and RV model output from ELLC using external parameters from isochrones.

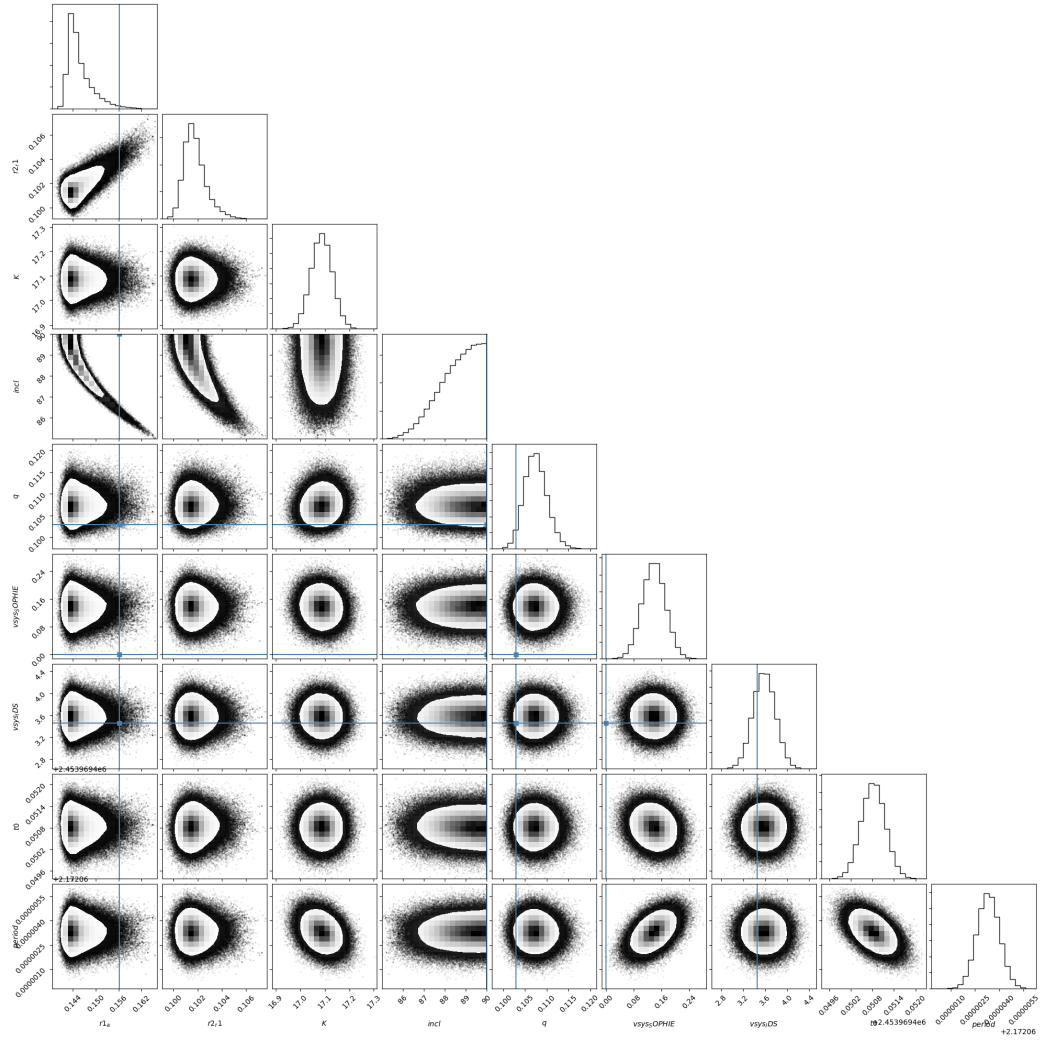


Figure 5.8: WASPJ02+40 corner plot for model parameters output from ELLC using external parameters from isochrones. Parameters from left to right: r_1/a , r_2/r_1 , K , inclination, q , v_{sys} SOPHIE, v_{sys} IDS, t_0 .

Table 5.14: Output parameters derived from ELLC for WASPJ02+40. ‘Isochrone R’ gives results using the radius derived from isochrones as an external parameter, ‘Torres RM’ gives results using the parameters derived using the Torres et al. (2010) relationship and ‘Gaia R’ gives results using the Gaia DR2 radius. Primary star mass and radius parameters used in ELLC are also given for reference.

Parameter	Isochrone R	Torres RM	Gaia R
Primary star	-	-	-
M_1 (M_\odot)	1.12 ± 0.08	1.18 ± 0.13	1.12 ± 0.08
R_1 (R_\odot)	1.15 ± 0.17	1.12 ± 0.32	1.34 ± 0.13
Model parameters	-	-	-
r_1/a	0.1432 ± 0.0034	0.1432 ± 0.0035	0.1444 ± 0.0041
r_2/r_1	0.10134 ± 0.00093	0.10102 ± 0.00094	0.1014 ± 0.0011
K (km s^{-1})	17.091 ± 0.043	17.076 ± 0.043	17.098 ± 0.044
incl ($^\circ$)	89.68 ± 0.95	89.70 ± 0.96	88.80 ± 1.06
q	0.1075 ± 0.0026	0.1055 ± 0.0044	0.1067 ± 0.0025
v_{sys} SOPHIE (km s^{-1})	0.149 ± 0.033	0.140 ± 0.034	0.130 ± 0.034
v_{sys} IDS (km s^{-1})	3.59 ± 0.20	3.50 ± 0.20	3.57 ± 0.20
t_0 (days)	$2453969.450833 \pm 0.000333$	$2453969.450825 \pm 0.000331$	$2453969.450780 \pm 0.000332$
period (days)	2.172063 ± 0.000001	2.172063 ± 0.000001	2.172063 ± 0.000001
Derived parameters	-	-	-
M_2 (M_\odot)	0.120 ± 0.009	0.124 ± 0.015	0.119 ± 0.009
R_2 (R_\odot)	0.116 ± 0.017	0.114 ± 0.032	0.136 ± 0.014
M_2 (M_J)	126 ± 9	130 ± 15	125 ± 9
R_2 (R_J)	1.13 ± 0.17	1.10 ± 0.31	1.32 ± 0.13

As there is a large difference between the spectroscopically derived radius and the radius presented in Gaia DR2, I investigated instead using the Gaia radius as an external parameter in global modelling. Gaia fluxes in the G , G_{BP} and G_{RP} bands give the effective temperature which, combined with the measured parallax and a bolometric correction, gives the luminosity and therefore radius. One of source of potential error is that Gaia DR2 assumes all sources are single stars in its calculation (Andrae et al., 2018), and only the primary star of WASPJ02+40 is identified as a source in Gaia DR2. Additionally, Gaia’s calculation of radius does not account for extinction, A_G , as it is not accurate on an individual star basis (Andrae et al., 2018). Gaia measures A_G of $0.1895^{+0.1115}_{-0.1031}$ for WASPJ02+40. Andrae et al. (2018) give the relation to find the radius assuming a non-zero extinction as:

$$R = R_0 \times 10^{0.2 \times A_{G_{new}}} \quad (5.5)$$

Inputting Gaia A_G values, the calculated radius increases: $1.09^{+0.06}_{-0.05}$ times larger than the $A_G = 0$ value, actually increasing the discrepancy between the Gaia and spectroscopically determined radii from isochrones. Another possible cause of the discrepancy is that Gaia stellar parameters are estimated from the photometry, as described in Andrae et al. (2018). Specifically, temperatures are estimated from the $G_{BP} - G$ and $G - G_{RP}$ colours using EXTRATREES, a machine learning algorithm. EXTRATREES is trained on Gaia photometry and catalogue T_{eff} from spectroscopic and photometric sources. The reference sample of 65000 stars, which is divided equally between training and testing sets, contains only near-solar metallicity stars ($-2 < [\text{Fe}/\text{H}] < 0.5$) with low extinction, estimated $\log g$ values and T_{eff} uncertainty < 200 K. Nevertheless, the colour-colour diagrams show a larger scatter than expected from the flux uncertainties which is due to astrophysical diversity not accounted for in the models, such as metallicity. This affects the accuracy of temperature, luminosity and radius values. They conclude that typical accuracies in Gaia are 324 K for temperature and 10 % for radius, which are larger than the uncertainties in the Gaia DR2 catalogue for WASPJ02+40. The full spectrophotometry available in future Gaia data releases will enable estimation of extinction without relying on parallax and estimation of $\log g$ and $[\text{Fe}/\text{H}]$ (Andrae et al., 2018), allowing more accurate determination of all stellar parameters.

As Andrae et al. (2018) advise A_G estimates should not be used for individual stars, I take the reported Gaia radius, i.e. using $A_G = 0$. I consider the 10% accuracy of the Gaia radius as the uncertainty and model using ELLC as above. Results using the Gaia and the spectroscopic radii are compared in Table 5.14. In terms of the fit itself, fitted radius and mass ratios were almost identical, with less than 1 % change.

As the same primary mass was used, the secondary mass is almost identical ($0.119 \pm 0.009 M_{\odot}$ compared to $0.120 \pm 0.009 M_{\odot}$). Calculating secondary radius with the larger Gaia primary radius gave $0.136 \pm 0.014 R_{\odot}$, i.e. a 17 % larger star and a 18 % smaller error. This clearly demonstrates that a large part of the error in the secondary radius is dependent on the primary radius error.

5.7 Discussion

5.7.1 EBLMs in context

I identified other systems with measured mass and radius with masses less than $0.6 M_{\odot}$ and that contained errors on both. These systems were identified by searching arXiv¹ and ADS² for published papers mentioning low mass eclipsing binaries, searching DEBCat³ (Southworth, 2015), and references within. These include single-lined (von Boetticher et al., 2017; Gomez Maqueo Chew et al., 2014; Triaud et al., 2013; Chaturvedi et al., 2018; Beatty et al., 2007; Ofir et al., 2012; Fernandez et al., 2009; Bouchy et al., 2005; Siverd et al., 2012; Diaz et al., 2014; David et al., 2019; Torres et al., 2014; Kaluzny et al., 2014; von Boetticher et al., 2019; Gill et al., 2019; Ratzloff et al., 2019; Kuzlewicz et al., 2019; Gill et al., 2020a) and double-lined low mass eclipsing binaries (Nefs et al., 2013; Morales et al., 2009; Hartman et al., 2011; Irwin et al., 2011, 2009a; Birkby et al., 2012; Kraus et al., 2011; Ribas, 2003; Blake et al., 2008; Creevey et al., 2005; Hebb et al., 2006; Helminiak et al., 2012; Windmiller et al., 2010; Han et al., 2017; Kraus et al., 2011; Hartman et al., 2018; Kraus et al., 2017; David et al., 2019; Dimitrov and Kjurkchieva, 2010; Casewell et al., 2018; Han et al., 2019; Gillen et al., 2017; Murphy et al., 2020), Kepler circumbinary planet systems (Orosz et al., 2012; Schwamb et al., 2013; Doyle et al., 2011; Welsh et al., 2015), multiple star systems (Carter et al., 2011; Johnson et al., 2011), and interferometric measurements (Segransan et al., 2003; Demory et al., 2009; Vaccaro et al., 2007). Note these systems are taken as presented, and will have their own assumptions and uncertainties.

WASPJ02+40 is shown in the top mass-radius plot of Figure 5.9 along with other systems with orbital periods less than 10 days. Isochrone models from Baraffe et al. (2015) for ages 0.1, 0.5, 1, 5 and 10 Gyr, which assume solar metallicity, are also plotted. This plot shows that M dwarf stars with measured mass and radius are rare below $0.15 M_{\odot}$. Results from ELLC using primary star parameters calculated

¹<https://arxiv.org/search/astro-ph>

²<https://ui.adsabs.harvard.edu/>

³<https://www.astro.keele.ac.uk/jkt/debcats/>

from the isochrones package (Morton, 2015) show WASPJ02+40 sits above all the Baraffe et al. (2015) isochrone lines. However, the isochrones package, using MIST models (Choi et al., 2016), and Baraffe et al. (2015) models are both built using different calculations for stellar structure and parameters such as line opacities, so they may be affected by systematics. Results from ELLC using mass and radius calculated from the Torres et al. (2010) relation similarly sits above the isochrone line, although larger radius error bars mean it is closer to the isochrone lines. These results are inconsistent with Baraffe et al. (2015) models, though additional factors likely need to be considered. The inconsistency of the isochrones and Torres et al. (2010) models may be an effect of potential previous interaction with its primary star – as its period is relatively short – or due to its metallicity, if its metallicity is greater than 0 (WASPJ02+40’s metallicity is 0.1 ± 0.1 , so is consistent with 0). Results from ELLC using the Gaia radius show WASPJ02+40 is consistent with the isochrone lines for stars with ages of at least 0.5 Gyr. However, there are additional assumptions in the Gaia radius, including that it assumes sources are single stars.

WASPJ23+29 is shown in the bottom plot of Figure 5.9, against other systems with long orbital periods (more than 10 days). Far fewer systems have been identified at longer periods, due to the reduced probability of both an eclipse occurring and it being observed in a given observing season. I identify only five other long period systems with masses below $0.15 M_{\odot}$ and radii below $0.20 R_{\odot}$. Results using parameters derived using the Torres et al. (2010) relation show the position of WASPJ23+29 on the mass-radius diagram is consistent with it being a young star, although the large error on radius means this cannot be confirmed. Chaturvedi et al. (2016) parameters are plotted (in brown) using parameters as derived in their paper using EXOFAST. While results from ELLC using primary star parameters from the Torres et al. (2010) relation find a larger radius than Chaturvedi et al. (2016), they are still consistent with the Chaturvedi et al. (2016) parameters due to our large error bars on primary star radius. Considering our calculation of the primary and secondary star masses from the Chaturvedi et al. (2016) spectral parameters, as shown in Table 5.13, these would push the secondary star to a lower radius so it is above the 10 Gyr isochrone line on the mass-radius diagram, but with a larger error making it still consistent with the 0.5–10 Gyr lines and with the value published in Chaturvedi et al. (2016). Our errors from ELLC and the Torres et al. (2010) relation using FIES spectra, and those found in this work for Chaturvedi et al. (2016) are too large to distinguish between different evolutionary ages. Results using parameters derived using isochrones show the position of WASPJ23+29 on the mass-radius diagram is consistent with a 0.5 Gyr star but the difference in radius between stars

of different ages is very small at this mass so this is insufficient in itself to exclude older ages in the Baraffe et al. (2015) models. Note we find WASPJ23+29 has a non-zero metallicity which likely causes additional scatter.

EBLMs with periods of 10 days or more show good agreement with the Baraffe et al. (2015) models. These stellar evolutionary models are for single stars so the agreement of the EBLMs implies that at these longer periods, the lower mass star is available to evolve sufficiently independently of the higher mass star to not strongly affect its mass to radius ratio. Low mass stars have evolutionary lifetimes longer than the age of the Universe (Eggleton, 2006), and binaries with periods longer than 10 days are not expected to have interacted during their lifetime, with which our mass-radius plot agrees, but there is no guarantee this is true for shorter periods. For EBLMs with periods shorter than 10 days the fit to the mass radius plot is less good, which could be due to interactions between the stars. Torres (2013) notes that discrepant low-mass binary systems typically have orbital periods of less than three days, which could be explained by tidal forces in the tight systems synchronising stellar spins with the orbital motion, leading to rapid rotation and increased magnetic activity. Modelling with binary star evolutionary models to provide isochrones of M dwarfs in EBLMs could potentially resolve this issue. However, while binary star evolution models exist for higher mass stars (e.g. Wolf-Rayet stars with BPASS, Eldridge and Stanway (2009)), I was unable to identify existing models optimised for stellar masses so low.

The two EBLMs studied in this chapter provide extra data points to compare evolutionary models to, although the precision on these measurements may need improvement. As can be seen in Figure 5.9, the precisions on mass and radius for the lowest mass stars could be improved, especially for shorter periods. The different models in Figure 5.9 also highlight that secondary star parameters in SB1s are dependent on models for higher mass stars, e.g. between empirical relations, such as Torres et al. (2010), or evolutionary models, which can cause discrepancies. This is illustrated by the systematic uncertainties in determining mass and radius of the primary star using the different models, which can play an important role in producing scatter in the secondary star’s mass-radius diagram. Systematic uncertainties in the parameters directly determined from spectra likely introduce some scatter also, as in some cases the systematic uncertainties are comparable to the measured parameter uncertainty. As the isochrones are for solar metallicity, and the EBLMs are not necessarily so, this introduces additional uncertainty in determining whether the M dwarfs agree with isochrones. The two EBLMs discussed in this chapter are among the lowest mass stars at 0.12 and 0.10 M_{\odot} . WASPJ23+29 in

particular sits close to the hydrogen-burning minimum mass limit $0.07 M_{\odot}$. These systems are of particular interest as they can help constrain models which try to explain parameters at the transition between stars and brown dwarfs.

5.8 Conclusions and Future work

I fitted two low mass eclipsing binary systems initially identified in *SuperWASP* lightcurves. Follow up spectroscopy was obtained and spectral analysis used to derive primary star parameters. Follow up photometry was also obtained for WASPJ23+29 as *SuperWASP* lightcurves did not have full coverage of the eclipse. Noticeably different primary star parameters are obtained depending on the method and these have a large effect on the derived secondary star parameters. For WASPJ23+29, despite inputting the same T_{eff} , $\log g$ and metallicity values from spectral analysis, very different mass and radius values and errors are found depending on whether they are determined using empirical relations based on observational data (Torres et al., 2010) or using evolutionary models (Morton, 2015; Choi et al., 2016). For WASPJ02+40, using the spectroscopically determined radius, or that from Gaia makes a large difference to the secondary radius and its error bar. WASPJ02+40 also has a lower precision on its temperature, which is carried forward to its radius error, as it is a fast rotating star. As there are so few systems with measured mass and radii that do not rely on low mass star evolutionary models, these EBLMs are valuable, with M dwarf parameters relying only on model determined parameters of their primary star, but their use in testing evolutionary models likely requires more precise determination of their parameters.

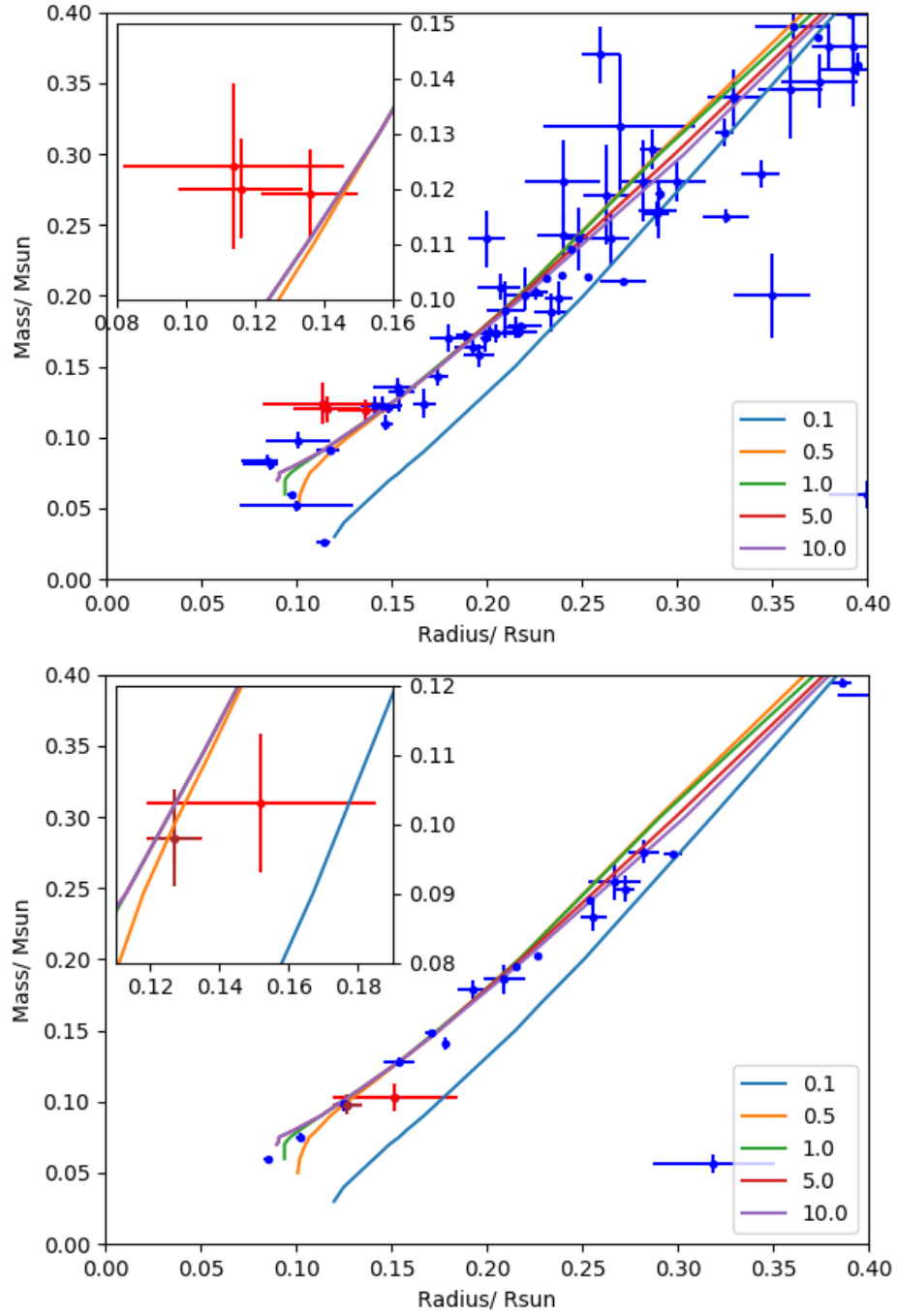


Figure 5.9: Mass radius plot for low mass stars (less than $0.4 M_{\odot}$) split by orbital period. Plotted lines are isochrones from Baraffe et al. (2015) with ages in Gyr as indicated. The inset plots show a zoomed-in region comparing the modelled EBLMs to the isochrone lines, see text for details. Top: orbital periods less than 10 days. WASPJ02+40 values from ELLC are in red. Bottom: orbital periods more than 10 days. WASPJ23+29 values from ELLC are in red, and Chaturvedi et al. (2016)’s value is in brown. Note: Chaturvedi et al. (2016)’s value nearly entirely overlaps with our calculated value using isochrones.

Chapter 6

Conclusions and Prospects

6.1 Conclusions

6.1.1 Investigation into Saturated Stars in the Next Generation Transit Survey

NGTS is a wide-field ground-based survey designed to achieve higher precision photometry to build on the success of surveys such as *SuperWASP*, HAT-NET and HAT-SOUTH, and extend detections down to Neptune-sized exoplanets. NGTS was designed to find exoplanets with sufficiently bright stars to enable radial velocity characterisation, especially stars brighter than I magnitude of 13. As it is a wide-field survey, exposure lengths are selected to maximise the number of stars with sufficient signal to noise ratio to enable exoplanet detection. As a result, the brightest stars are saturated.

In Chapter 3, I investigated saturated stars within NGTS and whether different sized apertures could recover the photometry. I used a plot of flux mean vs fractional flux root mean square (RMS) to identify stars which are saturated when processed using the standard pipeline aperture. Generally brighter stars are less noisy (having lower RMS values) but when the flux reaches sufficient levels, the flux can no longer be contained within the aperture and so the noise increases. I investigated whether larger circular apertures could capture the flux that escapes from the standard pipeline aperture. This helped decrease the noise slightly, but thumbnails of brighter saturated stars showed that larger circular apertures did not contain all their flux and contained a large amount of sky background, increasing the chance of contamination.

I then investigated using rectangular apertures tailored to the vertical extent of different saturated stars, finding a relationship between vertical extent and star

magnitude from external catalogues. Thumbnails showed that these apertures were better suited to the extended shape of saturated stars on the CCD but lightcurves revealed a number of frames where flux dropped significantly for all saturated and bright unsaturated stars in the same frame when using an aperture width of 6 pixels. Investigation into these drop out fluxes revealed correlation with larger autoguider errors, compared to the reference frame, so frames where the autoguider error was more than 3σ from the mean were filtered out. Comparing median fluxes from rectangular aperture lightcurves to those from circular apertures, I show that rectangular apertures capture the large fractions of flux lost, especially in brighter saturated stars. To account for atmospheric effects, I created a standard star using the bright unsaturated stars and divided the saturated and bright unsaturated star by it. I calculate the mean and fractional RMS flux from these relative lightcurves and find saturated and bright unsaturated stars show comparable fractional RMS values when using an aperture width of 6 pixels. I find that saturated stars are much less noisy using rectangular apertures than circular ones, indicating their suitability for these stars. While bright unsaturated stars produce a higher fractional RMS using rectangular apertures than in the standard NGTS pipeline, I expect these differences to disappear with more sophisticated processing using SysRem.

However, in order to measure absolute fluxes of saturated stars, charge must remain conserved. Where charge is conserved, as pixels near saturation, additional induced electrons are redirected into neighbouring pixels. Charge conservation is influenced by the gain and voltage settings that the camera uses. I tested whether the current operating settings of NGTS conserve charge by comparing the measured flux for different exposure lengths to the expected flux calculated by scaling up the measured flux in the shortest exposures. If charge is conserved, then the measured flux/expected flux ratio should be close to 1. Custom rectangular apertures were created for selected stars to capture all stellar flux in the longest exposure frame. I found that for the current NGTS voltage and gain settings, measured flux/expected flux dropped off at higher fluxes, meaning charge is not conserved. Repeating the process using exposures taken with the same voltage but gain setting PAG1, I found with these settings, flux was conserved to 1%. Testing higher voltages with gain setting PAG1, I found flux was no longer conserved.

While it was decided to not change NGTS' gain setting in its survey mode to allow charge conservation of saturated stars, if this decision is reviewed then saturated star photometry using rectangular apertures will be possible. Similar photometric precision to bright unsaturated stars could be expected, which would give RMS values of around 0.5%. For this level of precision, transits of 0.5% should

be detectable which for a solar-type star corresponds to a $0.7 R_J$ planet, i.e. sub-Saturn.

In terms of addressing the key question: can saturated stars be included in transit searches, I found in principle they likely can be if the detector settings allow charge to be conserved, which is not the case for the current NGTS settings. Custom apertures improved the lightcurve precision by up to a factor of 2 and further processing using SysRem is expected to improve this further, likely to similar precision to target stars in the survey. However, charge conservation is also necessary as trying to correct for this in post-processing can cause systematics in the lightcurves. The chapter highlights that for studying saturated stars to be practical, the instrument really needs to be understood, and would ideally have been designed with study of saturated stars in mind.

6.1.2 A Transiting Exoplanet Survey in the Habitable Zones of six mid-to-late M dwarfs with NITES

M dwarfs are attractive targets for searching for potentially habitable exoplanets, as their habitable zones are more accessible to transit surveys, being closer to their star and planets are more likely to transit. Earth-sized planets also produce deeper transits around M dwarfs than Sun-like stars. Together these factors make it more likely that Earth-sized planets in the habitable zone will be found around a M dwarf than a solar type star. However M dwarfs are intrinsically faint, which makes achieving a sufficient signal to noise ratio for transit discovery in wide-field transit surveys more difficult, hence the need for targeted surveys using red-sensitive detectors. These factors are especially true for spectral types later than M5, which is why I focused on these stars.

In Chapter 4, I discussed one such targeted survey, which used the NITES 0.4m telescope to observe six mid-to-late M dwarfs looking for transiting exoplanets. Targets were selected by calculating the increase in phase coverage by observing a given target on a given night. Each night's data was processed individually by finding the relative flux compared to hand-selected comparison stars. We obtained over 200 hours of high precision data for each target. With this amount of data, we gained coverage into the habitable zones of these objects, with 50% phase coverage at least midway into the range of habitable zone periods. I looked for periodic signals indicative of a transiting exoplanet using the box least squares (BLS) algorithm but did not identify any significant signals with multiple transits, meaning no strong exoplanet candidates were found. Through inspection of individual night lightcurves, I identified some single transit-like events. By fitting transit models, I

determine that some of these are weak exoplanet candidates, which would be considered low priority for spectroscopic confirmation with their period uncertainty and low expected signal.

I considered previous studies of M dwarf planet frequency (Dressing and Charbonneau, 2015) and found these consistent with no detection of exoplanets in the NITES data. As data from the Transiting Exoplanet Survey Satellite (TESS) became available for these targets, I also ran the BLS algorithm on this, and again identified no periodic transit-like signals. I performed transit injection tests on the NITES data to address the key question of what exoplanet radii and periods would be detectable from a targeted survey with a red-sensitive camera. I found that at the inner edge of the habitable zone, we are sensitive to Earth to Neptune-sized planets ($1 - 3.8 R_{\oplus}$), depending on the star, so these should have been detected had two or more transits been present in the data.

Some M dwarfs are known to exhibit high flaring activity and we observed a number of flares within the NITES data. Sufficiently high flaring rates can affect the habitability of any exoplanets within the M dwarf’s closer habitable zone. Investigation of the most frequently flaring star in our survey illustrates that if any habitable zone planets exist around it, their atmospheres are likely stripped, rendering them uninhabitable.

6.1.3 Characterisation of Two Low Mass Eclipsing Binaries (EBLMs) from *SuperWASP*

Low mass M dwarfs are not well described by stellar evolutionary models, so determining M dwarf properties independently of low mass stellar models is required. Observations of low mass eclipsing binaries (EBLMs) offer a way to precisely determine M dwarf masses and radii relative to their primary star. These EBLMs can be identified during transit surveys. Late M dwarfs have similar radii to Jupiter-sized planets so if they eclipse a larger star, they can be identified as exoplanet candidates in transit surveys searching for exoplanets. To distinguish between large exoplanets and small stars, spectra are taken first to confirm whether the system displays two sets of lines, indicating a double-lined spectroscopic binary, and second to measure radial velocity shifts of the primary star around the system barycentre. Stellar objects cause shifts of km s^{-1} between quadratures due to the reflex motion on the primary star. Further spectra are collected at different phases to measure radial velocities and enable characterisation of the secondary star’s orbit.

In Chapter 5, I fitted two of these low mass eclipsing binary systems initially identified in *SuperWASP* lightcurves: WASPJ23+29 and WASPJ02+40. Eclipse

depths and radial velocities only give the relative radii and masses of objects in the system, so spectral analysis was used to derive primary star parameters, with T_{eff} , $\log g$ and metallicity directly determined from the spectra. WASPJ23+29 was analysed by Amanda Doyle using the equivalent widths method. Mass and radius of the primary star were calculated using the Torres et al. (2010) empirical relation, and for comparison these parameters were also calculated using the isochrones package (Morton, 2015). I analysed WASPJ02+40 using synthetic spectra and calculated the primary star mass and radius using the isochrones package. Global fitting for the low mass eclipsing binary systems was then performed using ELLC, using initial estimates of parameters and inputting mass, radius and $\log g$ for the primary star to determine precise system parameters. We find WASPJ02+40 consists of a solar-type star eclipsed by a low mass M dwarf with an orbital period of just over 2 days. WASPJ23+29 is a K dwarf eclipsed by a low mass M dwarf on a longer period, of nearly 17 days.

I find noticeably different primary star parameters are obtained depending on the method and these have a large effect on the derived secondary star parameters. For WASPJ23+29, using T_{eff} , $\log g$ and metallicity from spectral analysis give very different mass and radius values and errors depending on whether they are determined using empirical relations based on observational data (Torres et al., 2010) or if they are determined using evolutionary models. Errors using the empirical relations were much larger from our modelling than those reported by Chaturvedi et al. (2016), who previously modelled the system using partial transits in the lower precision *SuperWASP* photometry. I investigate their method and find larger errors when considering the full range of possible masses and radii from their spectral parameters. When determining primary star mass and radius using the isochrones package (Morton, 2015), I identify very similar mass, radius and their respective errors to those presented in Chaturvedi et al. (2016). For WASPJ02+40, using either of the spectroscopically determined primary star radii (from the Torres et al. (2010) relation or the isochrones package) give very different secondary star radii to using the Gaia DR2 radius. Equally, the Torres et al. (2010) relation gives much larger error bars.

As there are so few systems with measured mass and radii that do not rely on low mass star evolutionary models, these EBLMs are valuable but their use in testing evolutionary models requires more precise determination of their parameters. Plotting mass-radius plots of known M dwarfs, I found EBLMs with periods of 10 days or more showed better agreement with the isochrone models of Baraffe et al. (2015) than those with shorter periods. As these stellar evolutionary models are for single

stars, it implies that the lower mass star on longer periods can evolve sufficiently independently that its mass-radius relation is not strongly affected. Short period EBLMs however do not show such agreement, which could be due to interaction between the stars.

6.2 Future outlook

Transit surveys, and the field of exoplanets more generally, remain a large area of astrophysics and this looks set to continue with ongoing and future missions. In particular, NASA’s Transiting Exoplanets Survey Satellite (TESS, Ricker et al., 2015) will complete its nearly full sky survey this year of 200,000 stars, focused on identifying exoplanets around bright K and M dwarfs. Future data releases from ESA’s Gaia space mission will allow more accurate determination of stellar parameters than in the current DR2 release, and will provide additional stellar parameters, notably mass and age. Looking further ahead, ESA’s PLANetary Transit and Oscillations (PLATO) mission will provide much more accurate planetary radii, with the aim to measure Sun-Earth analogues to 3 %, thanks to more accurate determination of stellar parameters using asteroseismology (Rauer et al., 2014; Morris et al., 2020).

Bright stars remain attractive targets as exoplanet host stars. Two of the brightest exoplanet hosts are among the most studied (HD 189733, $V = 7.65$ and HD 209458, $V = 7.63$ mag). 25 exoplanets around 19 stars brighter than $T_{\text{mag}} = 10$ have found by TESS (as of 20th March 2020), some of which will likely be suitable for more detailed characterisation using techniques such as transmission spectroscopy.

The brightest stars appearing in wide-field transit surveys, which are saturated continue to be of interest. However, Chapter 3 highlighted that investigation of absolute photometry of these saturated stars requires charge to be conserved. This requires the detector and readout electronics to be well understood. Alternative approaches were developed for data from the *Kepler* Space Telescope, whose detector saturates at $K_p \sim 11.3$ (Gilliland et al., 2010). The first method, investigating smear data caused by light falling on the detector during readout, is lower precision and vulnerable to significant contamination (Pope et al., 2016, 2019). The second method of halo photometry uses scattered light to recover relative photometry (Pope et al., 2019). This is more precise; their investigation of ‘bright unsaturated stars’ found similar precisions to the standard pipelines, but required targets to be specifically proposed and did not recover absolute photometry. Looking to the future, saturated star photometry is being studied for the PLATO mission (Rauer et al.,

2016), which will seek planets around the brightest stars out to the habitable zone. Rather than using commercially available off-the shelf instruments as in NGTS, for the PLATO mission, the electronics are being designed from scratch with a focus on charge conservation, which will aid in its study of saturated stars.

TESS has currently discovered 13 planets around 8 M dwarfs less than $0.6 R_{\odot}$, although these are mostly earlier M dwarfs with only three planets around two stars with radii less than $0.2 R_{\odot}$ (TESS Planet Count¹, accessed 20th March 2020). However, there continues to be a place for dedicated surveys of late M dwarfs, such as those with NITES. Chapter 4 demonstrated that in our survey we are sensitive to Earth to Neptune-sized planets and we acquired good phase coverage within the habitable zones. This region is of particular interest due to the human desire to find other habitable worlds, and is more accessible around mid-to-late M dwarfs.

The strategy of observing one target through the night is favoured by recent and current surveys such as TRAPPIST and SPECULOOS (Search for habitable Planets ECliPsing ULtra-cOOl Stars, Delrez et al.(2018)). NITES observed sufficient hours to be sensitive to planets in the habitable zones of the targeted stars and the similar number of hours observed per target to TRAPPIST suggests we could have found them. However, comparison with TRAPPIST-South suggests that much more observing time would be required: the first planetary system, Trappist-1 was discovered in a sample size of 50 stars that took place over 6 years. SPECULOOS, the successor to TRAPPIST, will survey the nearest 1000 ultracool dwarfs for transiting exoplanets over a 10 year period (Delrez et al., 2018), drastically increasing the number of stars observed compared to TRAPPIST. To observe this much higher number of stars with just four telescopes and reach the targeted 70% phase coverage at the equivalent incident flux level received by the Earth (requiring between 80 and 160 hours per target), it aims to identify strong candidates from a single transit. Its larger telescopes (1 m, compared to the 60 cm of TRAPPIST) will increase its sensitivity to help complete this goal. Targeting this number of stars, should increase the number of exoplanets around late M dwarfs, of which few are currently known. In its survey, SPECULOOS aims to identify ultracool dwarf exoplanets which are amenable to atmospheric observation with the James Webb Space Telescope, as so far little is known about them.

Low mass eclipsing binaries (EBLMs) and M-M dwarf binaries continue to be of interest in transit surveys, including in NGTS who have reported several discoveries (e.g. Casewell et al., 2018; Gill et al., 2020a). EBLM studies are also pushing to longer periods, with Gill et al. (2020a) finding a period of 38.2 days by recov-

¹<https://tess.mit.edu/publications/>

ering a single ‘transit’ event identified in TESS by identifying possible periods in *SuperWASP* data and using NGTS to follow up on these and determine the true period. Gill et al. (2020b) similarly later identified an even longer period EBLM of 61.777 days by monitoring TESS single transit events using one NGTS telescope. Additional M dwarfs from low mass eclipsing binaries, especially those at longer periods where few data points exist, will provide more data points to compare stellar evolutionary models to. This will also help determine whether interaction between the stars affects the lower mass star’s mass-radius relationship at different orbital periods. This will enable us to build more accurate models and better understand how changing parameters (e.g. metallicity) affects their properties. Looking further ahead, PLATO will enable precise characterisation of primary star parameters thanks to more precise measurement of $\log g$ and constraining ages using asteroseismology (Rauer et al., 2014). In this thesis, we found large uncertainties in the primary star ages determined using parameters from spectra, so better constrained and independent ages would enable isochrone models to be tested more robustly. Better understanding of the properties of M dwarfs in EBLMs will increase our understanding of single M dwarf evolution and how in EBLMs, they may interact with their primary star.

The field of transit surveys is an exciting area, with numerous exciting discoveries during the course of my PhD. With current and future missions, both in space and from the ground, the next decade of transit surveys looks to be as interesting as the last.

Bibliography

- Abrevaya, X. C., Leitzinger, M., Oppezzo, O. J., Odert, P., Patel, M. R., Luna, G. J. M., Forte-Giacobone, A. F., and Hanslmeier, A.: 2020, *MNRAS Letters* **494**(1), L69
- Agol, E., Steffen, J., Sari, R., and Clarkson, W.: 2005, *MNRAS* **359**(2), 567
- Andrae, R., Fouesneau, M., Creevey, O., Ordenovic, C., Mary, N., Burlacu, A., Chaoul, L., Jean-antoine piccolo, A., Kordopatis, G., Korn, A., Lebreton, Y., Panem, C., Pichon, B., Thévenin, F., Walmsley, G., and Bailer-Jones, C. A. L.: 2018, *A&A* 616(A8)
- Asplund, M., Grevesse, N., Sauval, A. J., and Scott, P.: 2009, *Annual Review of Astronomy & Astrophysics* **47**(1), 481
- Atri, D.: 2017, *MNRAS* **465**(1), L34
- Bakos, G., Noyes, R. W., Kova, G., Stanek, K. Z., Sasselov, D. D., and Domsa, I.: 2004, *Publications of the Astronomical Society of the Pacific* **116**, 266
- Baraffe, I., Chabrier, G., Allard, F., and Hauschildt, P.: 1998, *Astronomy & Astrophysics* **337**, 403
- Baraffe, I., Homeier, D., Allard, F., and Chabrier, G.: 2015, *A&A* 577(A42)
- Barbary, K.: 2016, *The Journal of Open Source Software* **1**(6), 58
- Barnes, S. A.: 2007, *The Astrophysical Journal* **669**(2), 1167
- Barstow, J. K. and Irwin, P. G. J.: 2016, *MNRAS Letters* **461**(1), L92
- Bayliss, D., Gillen, E., Eigmueller, P., McCormac, J., Alexander, R. D., Armstrong, D. J., Booth, R. S., Bouchy, F., Burleigh, M. R., Cabrera, J., Casewell, S. L., Chaushev, A., Chazelas, B., Csizmadia, S., Erikson, A., Faedi, F., Foxell, E., Gansicke, B. T., Goad, M. R., Grange, A., Gunther, M. N., Hodgkin, S. T.,

- Jackman, J., Jenkins, J. S., Lambert, G., Loudén, T., Metrailler, L., Moyano, M., Pollacco, D., Poppenhaeger, K., Queloz, D., Raddi, R., Rauer, H., Raynard, L., Smith, A. M. S., Soto, M., Thompson, A. P. G., Titz-Weider, R., Udry, S., Walker, S. R., Watson, C. A., West, R. G., and Wheatley, P. J.: 2018, *Monthly Notices of the Royal Astronomical Society* **475**(4), 4467
- Beatty, T. G., Fernandez, J. M., Latham, D. W., Bakos, G. A., Kovacs, G., Noyes, R. W., Stefanik, R. P., Torres, G., Everett, M. E., and Hergenrother, C. W.: 2007, *The Astrophysical Journal* **663**(1), 573
- Beaulieu, J., Bennett, D. P., Fouque, P., Williams, A., Dominik, M., Jørgensen, U. G., and Kubas, D.: 2006, *Nature* **439**(7075), 437
- Beichman, C. A., Woolf, N. J., and Lindensmith, C. A.: 1999, *The Terrestrial PlanetFinder*, JPL Publication, Pasadena
- Berger, D. H., Gies, D. R., McAlister, H. A., Henry, T. J., Sturmann, J., Sturmann, L., Turner, N. H., Ridgway, S. T., Aufdenberg, J. P., and Me, A.: 2006, *The Astrophysical Journal* **644**(1), 475
- Bertin, E. and Arnouts, S.: 1996, *A&A Supplement Series* **117**, 393
- Birkby, J., Nefs, B., Hodgkin, S., Kovács, G., Sipocz, B., Pinfield, D., Snellen, I., Mislis, D., Murgas, F., Lodieu, N., de Mooij, E., Goulding, N., Cruz, P., Stoev, H., Cappetta, M., Palle, E., Barrado, D., Saglia, R., Martin, E., and Pavlenko, Y.: 2012, *Monthly Notices of the Royal Astronomical Society* **426**(2), 1507
- Blake, C. H., Torres, G., and Gaudi, B. S.: 2008, *The Astrophysical Journal* **684**(1), 635
- Blanco-Cuaresma, S.: 2015, *iSpec Users Manual*
- Blanco-Cuaresma, S., Soubiran, C., Heiter, U., and Jofré, P.: 2014, *A&A* **569**(A111)
- Borucki, W. J., Koch, D., Basri, G., Batalha, N., Brown, T., Caldwell, D., Caldwell, J., Christensen-Dalsgaard, J., Cochran, W. D., DeVore, E., Dunham, E. W., Dupree, A. K., Gautier, T. N., Geary, J. C., Gilliland, R., Gould, A., Howell, S. B., Jenkins, J. M., Kondo, Y., and Latham, D. W.: 2010, *Science* **327**(5968), 977
- Borucki, W. J. and Summers, A. L.: 1984, *Icarus* **58**(1), 121

- Bouchy, F., Hébrard, G., Udry, S., Delfosse, X., Boisse, I., Desort, M., Bonfils, X., and Eggenberger, A.: 2009, *A&A* **505**(2), 853
- Bouchy, F., Pont, F., Melo, C., Santos, N. C., Mayor, M., Queloz, D., and Udry, S.: 2005, *A&A* **431**(3), 1105
- Boyajian, T. S., Braun, K. V., Belle, G. V., Mcalister, H. A., Brummelaar, T. A., Kane, S. R., Muirhead, P. S., Jones, J., White, R., Schaefer, G., Ciardi, D., Henry, T., Mercedes, L., Ridgway, S., Gies, D., Jao, W.-c., Parks, J. R., Sturmann, L., Sturmann, J., Turner, N. H., Farrington, C., Goldfinger, P. J., and Berger, D. H.: 2012, *The Astrophysical Journal* **757**(2), A112
- Brahm, R., Jordán, A., and Espinoza, N.: 2017, *Publications of the Astronomical Society of the Pacific* **129**(973), 034002
- Buccino, A. P., Lemarchand, G. A., and Mauas, P. J. D.: 2007, *Icarus* **192**(2), 582
- Burrows, A., Marley, M., Hubbard, W. B., Lunine, J. I., Guillot, T., Saumon, D., Freedman, R., Sudarsky, D., and Sharp, C.: 1997, *The Astrophysical Journal* **491**(2), 856
- Carter, J. A., Fabrycky, D. C., Ragozzine, D., Holman, M. J., Quinn, S. N., Latham, D. W., Buchhave, L. A., Cleve, J. V., Cochran, W. D., Cote, M. T., Endl, M., Ford, E. B., Haas, M. R., Jenkins, J. M., Koch, D. G., Li, J., Lissauer, J. J., Macqueen, P. J., Middour, C. K., Orosz, J. A., Rowe, J. F., Steffen, J. H., and Welsh, W. F.: 2011, *Science* **331**(6017), 562
- Casewell, S. L., Raynard, L., Watson, C. A., Gillen, E., Mooij, E. D., Bouchy, F., Thompson, A., Jackman, J. A. G., Burleigh, M. R., Chaushev, A., Belardi, C., Loudon, T., Goad, M. R., Nielsen, L. D., Eigm, P., Maximilian, N. G., Jenkins, J. S., Moyano, M., Queloz, D., Smith, A. M. S., West, R. G., and Wheatley, P. J.: 2018, *MNRAS* **481**(2), 1897
- Charbonneau, D., Berta, Z. K., Irwin, J., Burke, C. J., Nutzman, P., Lars, A., Lovis, C., Bonfils, X., Latham, D. W., Udry, S., and Murray-clay, R. A.: 2009, *Nature* **462**(7275), 891
- Charbonneau, D., Brown, T. M., Latham, D. W., and Mayor, M.: 2000, *The Astrophysical Journal* **529**(1), L45
- Charbonneau, D., Brown, T. M., Noyes, R. W., and Gilliland, R. L.: 2002, *The American Astronomical Society* **568**(1), 377

- Chaturvedi, P., Chakraborty, A., Anandarao, B. G., Roy, A., and Mahadevan, S.: 2016, *MNRAS* **462**(1), 554
- Chaturvedi, P., Sharma, R., Chakraborty, A., and Anandarao, B. G.: 2018, *The Astronomical Journal* **156**(1), A27
- Chazelas, B., Pollacco, D., Queloz, D., Rauer, H., Wheatley, P. J., West, R., Da Silva Bento, J., Burleigh, M., McCormac, J., Eig Müller, P., Erikson, A., Genolet, L., Goad, M., Jordán, A., Neveu, M., and Walker, S.: 2012, in *Proc. SPIE 8444*, No. Ground-based and Airborne Telescopes IV, 84440E, Amsterdam, Netherlands
- Choi, J., Dotter, A., Conroy, C., Cantiello, M., Paxton, B., and Johnson, B. D.: 2016, *The Astrophysical Journal* **823**(2), A102
- Christian, D. J., Pollacco, D. L., Skillen, I., Street, R. A., Keenan, F. P., Clarkson, W. I., Cameron, A. C., Kane, S. R., Lister, T. A., West, R. G., Enoch, B., Evans, A., Fitzsimmons, A., Haswell, C. A., Hellier, C., Hodgkin, S. T., Horne, K., Irwin, J., Norton, A. J., Osborne, J., Ryans, R., Wheatley, P. J., and Wilson, D. M.: 2006, *MNRAS* **372**(3), 1117
- Collier Cameron, A., Pollacco, D., Street, R. A., Lister, T. A., West, R. G., Wilson, D. M., Pont, F., Christian, D. J., Clarkson, W. I., Enoch, B., Evans, A., Fitzsimmons, A., Haswell, C. A., Hellier, C., Hodgkin, S. T., Horne, K., Irwin, J., Kane, S. R., Keenan, F. P., Norton, A. J., Parley, N. R., Osborne, J., Ryans, R., Skillen, I., and Wheatley, P. J.: 2006, *MNRAS* **373**(2), 799
- Collier Cameron, A., Wilson, D. M., West, R. G., Hebb, L., Wang, X. B., Aigrain, S., Bouchy, F., Christian, D. J., Clarkson, W. I., Enoch, B., Esposito, M., Guenther, E., Haswell, C. A., Hébrard, G., Hellier, C., Horne, K., Irwin, J., Kane, S. R., Loeillet, B., Lister, T. A., Maxted, P., Mayor, M., Moutou, C., Parley, N., Pollacco, D., Pont, F., Queloz, D., Ryans, R., Skillen, I., Street, R. A., Udry, S., and Wheatley, P. J.: 2007, *Monthly Notices of the Royal Astronomical Society* **380**(3), 1230
- Collins, K. A., Collins, K. I., Pepper, J., Labadie-bartz, J., Stassun, K. G., Gaudi, B. S., Bayliss, D., Bento, J., Colón, K. D., Feliz, D., James, D., Johnson, M. C., Kuhn, R. B., Lund, M. B., Penny, M. T., Rodriguez, J. E., Siverd, R. J., Stevens, D. J., Yao, X., Zhou, G., Akshay, M., Aldi, G. F., and Ashcraft, C.: 2018, *The Astronomical Journal* **156**(5), A234
- Craig, M., Crawford, S., Deil, C., Gomez, C., Günther, H., Heidt, N., Horton, A., Karr, J., Nelson, S., Ninan, J. P., Punyaslok, P., Rol, E., Schoenell, W.,

- Seifert, M., Singh, S., Sipocz, B., Stotts, C., Streicher, O., Tollerud, E., Walker, N., and contributors, C.: 2015, *Astrophysics Source Code Library* (ascl:1510.007)
- Creevey, O. L., Benedict, G. F., Brown, T. M., Alonso, R., Cargile, P., Mandushev, G., Charbonneau, D., Mcarthur, B. E., Cochran, W., Donovan, F. T. O., Jime, S. J., Belmonte, J. A., and Kolinski, D.: 2005, *The Astrophysical Journal* **625**(2), L127
- Crossfield, I. J. M., Waalkes, W., Newton, E. R., Narita, N., Muirhead, P., Ment, K., Matthews, E., Kraus, A., Kostov, V., Kosiarek, M. R., Kane, S. R., Jenkins, J. M., Hori, Y., Colon, K., and Caldwell, D. A.: 2019, *The Astrophysical Journal Letters* **883**(1), L16
- Davenport, J. R. A.: 2016, *The Astrophysical Journal* **829**(1), A23
- Davenport, J. R. A., Hawley, S. L., Hebb, L., Wisniewski, J. P., Kowalski, A. F., Johnson, E. C., Malatesta, M., Peraza, J., Keil, M., Silverberg, S. M., Jansen, T. C., Scheffler, M. S., Berdis, J. R., Larsen, D. M., and Hilton, E. J.: 2014, *Astrophysical Journal* **797**(2), A122
- David, T. J., Hillenbrand, L. A., Gillen, E., Cody, A. M., Howell, S. B., Isaacson, H. T., and Livingston, J. H.: 2019, *The Astrophysical Journal* **872**(2), A161
- Delrez, L., Gillon, M., Queloz, D., Demory, B.-O., Almleaky, Y., de Wit, J., Jehin, E., Triaud, A. H. M. J., Barkaoui, K., Burdanov, A., Burgasser, A. J., Ducrot, E., McCormac, J., Murray, C., Fernandes, C. S., Sohy, S., Thompson, S. J., Van Grootel, V., Alonso, R., Benkhaldoun, Z., and Rebolo, R.: 2018, *Proc. SPIE* **10700**11, 21
- Demory, B., Ségransan, D., Forveille, T., Queloz, D., Beuzit, J., Delfosse, X., E, D. F., Kervella, P., J, L. B., Perrier, C., Benisty, M., Duvert, G., Hofmann, K., Lopez, B., and Petrov, R.: 2009, *A&A* **505**(1), 205
- Demory, B.-O., Queloz, D., Alibert, Y., Gillen, E., and Gillon, M.: 2016, *The Astrophysical Journal Letters* **825**(2), L25
- Diaz, R., Montagnier, G., Leconte, J., Bonomo, A., Deleuil, M., Almenara, J. M., Barros, S., Bouchy, F., Bruno, G., Diamiani, C., Hébrard, G., Moutou, C., and Santerne, A.: 2014, *A&A* **572**, A109
- Dierckxsens, M., Patsou, I., and Malandraki, O.: 2015, *Solar Physics* **290**(3), 841
- Dimitrov, D. P. and Kjurkchieva, D. P.: 2010, *MNRAS* **406**(4), 2559

- Doyle, A. P., Davies, G. R., Smalley, B., Chaplin, W. J., and Elsworth, Y.: 2014, *MNRAS* **444**(4), 3592
- Doyle, A. P., Smalley, B., Faedi, F., Pollacco, D., and Gómez Maqueo Chew, Y.: 2017, *MNRAS* **469**(4), 4850
- Doyle, L. R., Carter, J. A., Fabrycky, D. C., Slawson, R. W., Howell, S. B., Winn, J. N., Orosz, J. A., Prsa, A., Welsh, W. F., Quinn, S. N., Torres, G., Buchhave, L. A., Marcy, G. W., Fortney, J. J., Ford, E. B., Lissauer, J. J., Ragozzine, D., Rucker, M., Batalha, N., McCauliff, S., Fanelli, M. N., Quintana, E. V., Holman, M. J., Caldwell, D. A., Still, M., Stefanik, R. P., Brown, W. R., Esquerdo, G. A., Tang, S., Furesz, G., Geary, J. C., Berlind, P., Calkins, M. L., Short, D. R., Steffen, J. H., Sasselov, D., Dunham, E. W., Cochran, W. D., Boss, A., Haas, M. R., Buzasi, D., and Fischer, D.: 2011, *Science* **333**(6049), 1602
- Dressing, C. D. and Charbonneau, D.: 2015, *ApJ* **807**(1), A45
- Dupuy, T. J. and Liu, M. C.: 2012, *The Astrophysical Journal Letters* **201**(2), A19
- Eastman, J., Gaudi, B. S., and Agol, E.: 2013, *PASP* **125**(923), 83
- Eggleton, P.: 2006, *Evolutionary Processes in Binary and Multiple Stars*, Cambridge University Press, Cambridge, UK
- Eldridge, J. J. and Stanway, E. R.: 2009, *MNRAS* **400**(2), 1019
- Farr, W. M., Pope, B. J. S., Davies, G. R., North, T. S. H., White, T. R., Barrett, J. W., Miglio, A., Lund, M. N., Antoci, V., Andersen, M. F., Grundahl, F., and Huber, D.: 2018, *The Astrophysical Journal Letters* **865**(2), L20
- Faucher, T. J., Turbet, M., Villanueva, G. L., Wolf, E. T., Arney, G., Kopparapu, R. K., Lincowski, A., Mandell, A., de Wit, J., Pidhorodetska, D., Domagal-Goldman, S. D., and Stevenson, K. B.: 2019, *The Astrophysical Journal* **887**(2), 194
- Fernandez, J. M., Latham, D. W., Torres, G., Everett, M. E., Mandushev, G., Charbonneau, D., O'Donovan, F. T., Alonso, R., Esquerdo, G. A., Hergenrother, C. W., and Stefanik, R. P.: 2009, *Astrophysical Journal* **701**(1), 764
- Foreman-Mackey, D., Hogg, D. W., Lang, D., and Goodman, J.: 2013, *PASP* **125**, 306

- France, K., Froning, C. S., Linsky, J. L., Roberge, A., Stocke, J. T., Tian, F., Mauas, P., Vieytes, M., Walkowicz, L. M., and Bushinsky, R.: 2013, *The Astrophysical Journal* **763**(2), A149
- France, K., Loyd, R. O. P., Youngblood, A., Brown, A., Schneider, P. C., Hawley, S. L., Froning, C. S., Linsky, J. L., Roberge, A., Buccino, A. P., Davenport, J. R. A., Fontenla, J. M., Kaltenegger, L., Kowalski, A. F., and Mauas, P. J. D.: 2016, *The Astrophysical Journal* **820**(2), A89
- Fujii, Y., Angerhausen, D., Deitrick, R., Domagal-goldman, S., Grenfell, J. L., Hori, Y., Kane, S. R., Palle, E., Rauer, H., Siegler, N., Stapelfeldt, K., and Stevenson, K. B.: 2018, *Astrobiology* **18**(6), 739
- Gaia Collaboration, Brown, A., Vallenari, A., Prusti, T., de Bruijne, J., and Babusiaux, C.: 2018, *A&A* 616(A1)
- Gaia Collaboration, Prusti, T., Bruijne, J. H. J. D., Brown, A. G. A., Vallenari, A., and Babusiaux, C.: 2016, *Astronomy & Astrophysics* 595(A1)
- Gelman, A. and Rubin, D. B.: 1996, *Statistical Methods in Medical Research* **5**(4), 339
- Giacalone, S. and Dressing, C. D.: 2020, (eprint arXiv:2002.00691)
- Gibson, N. P., Aigrain, S., Pollacco, D. L., Barros, S. C. C., Hebb, L., Hrudkov, M., Simpson, E. K., Skillen, I., and West, R.: 2010, *MNRAS Letters* **404**(1), L114
- Gill, S., Bayliss, D., Cooke, B. F., Wheatley, P. J., Nielsen, L. D., Lendl, M., McCormac, J., Bryant, E. M., Acton, J. S., Anderson, D. R., Belardi, C., Burleigh, M. R., Cameron, C., Casewell, S. L., Goad, M. R., Maximilian, N. G., Hellier, C., James, A. G., Jenkins, J. S., Moyano, M., Pollacco, D., Raynard, L., Smith, A. M. S., Tilbrook, R. H., Turner, O., and West, R. G.: 2020a, *MNRAS* **491**(2), 1548
- Gill, S., Cooke, B. F., Bayliss, D., Nielsen, L. D., Lendl, M., Wheatley, P. J., Anderson, D. R., Bryant, E. M., Acton, J. S., Belardi, C., Burleigh, M. R., Casewell, S. L., Chaushev, D., Goad, M. R., Jackman, J. A. G., Jenkins, J. S., McCormac, J., Maximilian, N. G., Osborn, H. P., Raynard, L., Smith, A. M. S., Tilbrook, R. H., Turner, O., Vines, J. I., Watson, C. A., and West, G.: 2020b, *MNRAS* **495**(3), 2713

- Gill, S., Maxted, P. F. L., Evans, J. A., Evans, D. F., Southworth, J., Smalley, B., Gary, B. L., Anderson, D. R., Bouchy, F., Cameron, A. C., Dominik, M., Faedi, F., Gillon, M., Maqueo, Y. G., Hebb, C. L., Hellier, C., Martin, D. V., McCormac, J., Pepe, F. V., Pollaco, D., Queloz, D., Ségransan, D., Snodgrass, C., Turner, O. D., Triaud, A. H. M., Udry, S., and West, R. G.: 2019, *A&A* **626**, A119
- Gillen, E., Hillenbrand, L. A., David, T. J., Aigrain, S., Rebull, L., Stauffer, J., Cody, A. M., and Queloz, D.: 2017, *The Astrophysical Journal* **849**(1), A11
- Gilliland, R. L., Jenkins, J. M., Borucki, W. J., Bryson, S. T., Caldwell, D. A., Clarke, B. D., Dotson, J. L., Haas, M. R., Hall, J., Klaus, T., Koch, D., Mccauliff, S., Quintana, E. V., Twicken, J. D., and Cleve, J. E. V.: 2010, *The Astrophysical Journal Letters* **713**(2), 160
- Gillon, M., Jehin, E., Lederer, S. M., Delrez, L., Wit, J. D., Burdanov, A., Burgasser, A., Triaud, A. H. M. J., Opitom, C., Demory, B.-o., Sahu, D. K., Gagliuffi, D. B., Magain, P., and Queloz, D.: 2016, *Nature* **533**(7602), 221
- Gillon, M., Jehin, E., Magain, P., Chantry, V., Hutsem, D., Manfroid, J., Queloz, D., and Udry, S.: 2011, *EPJ Web of Conferences* 06002
- Gillon, M., Triaud, A. H. M. J., Demory, B.-o., Jehin, E., Deck, K. M., Lederer, S. M., Wit, J. D., Burdanov, A., and James, G.: 2017, *Nature* **542**(7642), 456
- Gomez Maqueo Chew, Y., Morales, J. C., Faedi, F., Hebb, L., Rodler, F., Deshpande, R., Mahadevan, S., McCormac, J., Barnes, R., Triaud, A. H. M. J., Skillen, I., Collier, A., Joner, M. D., Laney, C. D., Stephens, D. C., Stassun, K. G., and Montanes-Rodriquez, P.: 2014, *A&A* 572(A50)
- Gray, R. O. and Corbally, C. J.: 1994, *The Astronomical Journal* **107**(2), 742
- Grevesse, N., Asplund, M., and Sauval, A. J.: 2007, *Space Science Reviews* **130**(1-4), 105
- Grillmair, C. J., Charbonneau, D., Burrows, A., Armus, L., Stauffer, J., Meadows, V., Cleve, J. V., and Levine, D.: 2007, *Astrophysical Journal* **658**(2), L115
- Grimm, S. L., Demory, B.-o., Gillon, M., Dorn, C., Agol, E., Burdanov, A., Delrez, L., Sestovic, M., Triaud, A. H. M. J., Turbet, M., Bolmont, É., Caldas, A., Wit, J. D., Jehin, E., Leconte, J., Heng, K., Hernandez, D. M., Ingalls, J. G., Lederer, S., Selsis, F., and Queloz, D.: 2018, *A&A* **613**(A68), 21

- Günther, M. N., Queloz, D., Gillen, E., McCormac, J., Bayliss, D., Bouchy, F., Walker, S. R., West, R. G., Eigmüller, P., Smith, A. M. S., Armstrong, D. J., Burleigh, M., Casewell, S. L., Chaushev, A. P., Goad, M. R., Grange, A., Jackman, J., Jenkins, J. S., Loudon, T., Moyano, M., Pollacco, D., Poppenhaeger, K., Rauer, H., Raynard, L., Thompson, A. P. G., Udry, S., Watson, C. A., and Wheatley, P. J.: 2017, *MNRAS* **472**(1), 295
- Gunther, M. N., Zhan, Z., Seager, S., Rimmer, P. B., Ranjan, S., Stassun, K. G., Oelkers, R. J., Daylan, T., Newton, E., Gillen, E., Rappaport, S., Ricker, G. R., Latham, D. W., Winn, J. N., Jenkins, J. M., Glidden, A., Fausnaugh, M., Levine, A. M., Dittmann, J. A., Quinn, S. N., Krishnamurthy, A., and Ting, E. B.: 2020, *The Astronomical Journal* **159**(2), A60
- Gustafsson, B., Edvardsson, B., Eriksson, K., Jørgensen, U. G., Nordlund, Å., and Plez, B.: 2008, *A&A* **486**(3), 951
- Han, E., Muirhead, P. S., and Swift, J. J.: 2019, *The Astronomical Journal* **158**(3), A111
- Han, E., Muirhead, P. S., Swift, J. J., Baranec, C., Law, N. M., Atkinson, D., Mace, G. N., and Defelippis, D.: 2017, *The Astronomical Journal* **154**(3), A100
- Hardegree-Ullman, K. K., Cushing, M. C., Muirhead, P. S., and Christiansen, J. L.: 2019, *AJ* **158**(2), A75
- Hartman, J. D., Bakos, G. Á., Noyes, R. W., Sipcz, B., Kovács, G., Mazeh, T., Shporer, A., and Pal, A.: 2011, *AJ* **141**(5), A166
- Hartman, J. D., Quinn, S. N., Bakos, G. Á., Torres, G., Kovács, G., Latham, D. W., Noyes, R. W., Shporer, A., Fulton, B. J., Esquerdo, G. A., Everett, M. E., Penev, K., Bhatti, W., and Csubry, Z.: 2018, *The Astronomical Journal* **155**(3), A114
- Hastings, W. K.: 1970, *Biometrika* **57**(1), 97
- Haswell, C. A. .: 2010, *Transiting Exoplanets*, Cambridge University Press, Cambridge, UK
- Hawley, S. L., Covey, K. R., Knapp, G. R., Golimowski, D. A., Fan, X., Anderson, S. F., Long, G. M., Lupton, R. H., Mcgehee, P. M., Gunn, J. E., Harris, H. C., Narayanan, V., Peng, E., Schlegel, D., Schneider, D. P., Spahn, E. Y., Strauss, M. A., Szkody, P., Tsvetanov, Z., Walkowicz, L. M., Brinkmann, J., Harvanek, M., Hennessy, G. S., Kleinman, S. J., Krzesinski, J., Long, D., Neilsen, E. H.,

- Newman, P. R., Nitta, A., Snedden, S. A., and York, D. G.: 2002, *The Astronomical Journal* **123(6)**, 3409
- Hawley, S. L., Davenport, J. R. A., Kowalski, A. F., Wisniewski, J. P., Hebb, L., Deitrick, R., and Hilton, E. J.: 2014, *ApJ* **797(2)**, A121
- Hebb, L., Wyse, R. F. G., Gilmore, G., and Holtzman, J.: 2006, *The Astronomical Journal* **131(1)**, 555
- Helminiak, K. G., Konacki, M., Rózycka, M., Kaluzny, J., Ratajczak, M., Borkowski, J., Sybilski, P., Muterspaugh, M. W., Reichart, D. E., Ivarsen, K. M., Haislip, J. B., Crain, J. A., Foster, A. C., Nysewander, M. C., and Lacluyze, A. P.: 2012, *Monthly Notices of the Royal Astronomical Society* **425(2)**, 1245
- Henden, A. and Munari, U.: 2014, *Contributions of the Astronomical Observatory Skalnaté Pleso* **43(3)**, 518
- Henry, G. W., Marcy, G. W., Butler, R. P., and Vogt, S. S.: 2000, *The Astrophysical Journal* **529(1)**, L41
- Henry, T. J., Jao, W.-C., Subasavage, J. P., and Beaulieu, T. D.: 2006, *Astronomical Journal* **132(6)**, 2360
- Hoaglin, D. C., Mosteller, F., and Tukey, J. W.: 1983, *Understanding of Robust and Exploratory Data Analysis*, Wiley, New York, 1st edition
- Howard, W. S., Tilley, M. A., Corbett, H., Youngblood, A., Loyd, R. O. P., Ratzloff, J. K., Fors, O., del Ser, D., Shkolnik, E. L., Ziegler, C., Goeke, E. E., Pietraallo, A. D., Haislip, J., and Law, N. M.: 2018, *Astrophysical Journal Letters* **860(2)**, L30
- Howell, S. B.: 2006, *Handbook of CCD Astronomy*, Cambridge University Press, Cambridge, UK, 2nd edition
- Huber, D., Chaplin, W. J., Chontos, A., Kjeldsen, H., Christensen-dalsgaard, J., Bedding, T. R., Ball, W., Brahm, R., Espinoza, N., Henning, T., Crossfield, I., Fulton, B., Howard, A. W., Andersen, M. F., Pall, P. L., Isaacson, H. T., Weiss, L. M., Handberg, R., Lund, M. N., Serenelli, A. M., Mosumgaard, J. R., Stokholm, A., Bierlya, A., Buchhave, L. A., Latham, D. W., Quinn, S. N., Gaidos, E., Hirano, T., Ricker, G. R., Vanderspek, R. K., Seager, S., Jenkins, J. M., Winn, J. N., Antia, H. M., Appourchaux, T., Basu, S., Gazeas, K., Giddens, F., Hall, O., and Hekker, S.: 2019, *The Astronomical Journal* **157(6)**, A245

- Hudson, H. S.: 2011, *Space Science Reviews* **158**(1), 5
- Irwin, J., Charbonneau, D., Berta, Z. K., Quinn, S. N., Latham, D. W., Torres, G., Blake, C. H., Burke, C. J., Esquerdo, G. A., Mink, D. J., Nutzman, P., Szentgyorgyi, A. H., Calkins, M. L., Falco, E. E., Bloom, J. S., and Starr, D. L.: 2009a, *The Astrophysical Journal* **701**(2), 1436
- Irwin, J., Charbonneau, D., Nutzman, P., and Falco, E.: 2009b, in F. Pont, D. Sasselov, and M. Holman (eds.), *Transiting Planets, Proceedings of the IAU Symposium*, Vol. 253, pp 37–43, Cambridge, MA
- Irwin, J. M., Berta-Thompson, Z. K., Charbonneau, D., Dittmann, J., Falco, E. E., Newton, E. R., and Nutzman, P.: 2014, in G. van Belle and H. Harris (eds.), *Proceedings of the 18th Cambridge Workshop on Cool Stars, Stellar Systems, and the Sun (Cool Stars 18)*, pp 767–772, Flagstaff, AZ
- Irwin, J. M., Quinn, S. N., Berta, Z. K., Latham, D. W., Torres, G., Burke, C. J., Charbonneau, D., Dittmann, J., Esquerdo, G. A., Stefanik, R. P., Oksanen, A., Buchhave, L. A., Nutzman, P., Berlind, P., Calkins, M. L., and Falco, E. E.: 2011, *The Astrophysical Journal* **742**(2), A123
- Irwin, M. J., Lewis, J., Hodgkin, S., Bunclark, P., Evans, D., Irwin, M. J., Lewis, J., Hodgkin, S., Bunclark, P., Evans, D., McMahon, R., Emerson, J. P., Stewart, M., and Beard, S.: 2004, in *Proc. SPIE 5493, Optimizing Scientific Return for Astronomy through Information Technologies*, Glasgow
- Jackman, J. A. G., Wheatley, P. J., Bayliss, D., Burleigh, M. R., Casewell, S. L., Eigm, P., Goad, M. R., Pollacco, D., Raynard, L., Watson, C. A., and West, R. G.: 2019, *MNRAS* **485**(1), L136
- Jackman, J. A. G., Wheatley, P. J., Pugh, C. E., Gänsicke, B. T., Gillen, E., Broomhall, A.-M., Armstrong, D. J., Burleigh, M. R., Chaushev, A., Eigmüller, P., Erikson, A., Goad, M. R., Grange, A., Günther, M. N., Jenkins, J. S., McCormac, J., Raynard, L., Thompson, A. P. G., Udry, S., Walker, S., Watson, C. A., and West, R. G.: 2018, *MNRAS* **477**(4), 4655
- Janesick, J. and Blouke, M.: 1987, *Sky and Telescope* p. 238
- Johnson, J. A., Apps, K., Gazak, J. Z., Crepp, J. R., Crossfield, I. J., Howard, A. W., Marcy, G. W., Morton, T. D., Chubak, C., and Isaacson, H.: 2011, *Astrophysical Journal* **730**(2), A79

- Joye, W. A. and Mandel, E.: 2003, in *Astronomical Data Analysis Software and Systems XII ASP Conference Series*, Vol. 295, pp 489–492, Astronomical Society of the Pacific
- Kalas, P., Graham, J. R., Chiang, E., Fitzgerald, M. P., Clampin, M., Kite, E. S., Stapelfeldt, K., Marois, C., and Krist, J.: 2008, *Science* **322**(5906), 1345
- Kaluzny, J., Thompson, I. B., Dotter, A., Rozyczka, M., Pych, W., Rucinski, S. M., and Burley, G. S.: 2014, *Acta Astronomica* **64**(1), 11
- Kasting, J. F., Whitmire, D. P., and Reynolds, R. T.: 1993, *Icarus* **101**(1), 108
- Khodachenko, M. L., Ribas, I., Lammer, H., Grießmeier, J.-M., Leitner, M., Selsis, F., Eiroa, C., Hanslmeier, A., Biernat, H. K., Farrugia, C. J., and Rucker, H. O.: 2007, *Astrobiology* **7**(1), 167
- Kirk, J.: 2018, *Ph.D. thesis*, University of Warwick
- Kopparapu, R. K., Ramirez, R., Kasting, J. F., Eymet, V., Robinson, T. D., Mahadevan, S., Terrien, R. C., Domagal-Goldman, S., Meadows, V., and Deshpande, R.: 2013, *The Astrophysical Journal* **765**(2), A131
- Kostov, V. B., Schlieder, J. E., Barclay, T., Brande, J., Quintana, E. V., Col, K. D., Collins, K. A., Hadden, S., Kane, S. R., Kreidberg, L., Kruse, E., Lam, C., Matthews, E., Montet, B. T., Pozuelos, F. J., Stassun, K. G., Winters, J. G., Ricker, G., Vanderspek, R., Latham, D., Seager, S., Winn, J., Jenkins, J. M., Afanasev, D., Armstrong, J. J. D., Boyd, P., Bayliss, D., Burdanov, A., Cacciapuoti, L., Carson, A., Charbonneau, D., Collins, K. I., Conti, D. M., Covone, G., Clampin, M., Delrez, L., Dressing, C., Ducrot, E., Essack, Z., Everett, M. E., Hamann, A., Hedges, C., Horch, E. P., Kielkopf, J. F., Lissauer, J. J., Mann, A. W., Narita, N., Palte, E., Quinn, D., Relles, H., Rinehart, S., Ritsko, M., and Rodriguez, J. E.: 2019, *The Astronomical Journal* **158**(1), A32
- Kotani, T., Tamura, M., Suto, H., Nishikawa, J., Sato, B., Usuda, T., Kurokawa, T., Kashiwagi, K., Nishiyama, S., Hall, D. B., Hodapp, K. W., Hashimoto, J., Morino, J.-i., Tanaka, Y., Suzuki, S., Inoue, S., Kwon, J., Oh, D., Baba, H., Narita, N., Kokubo, E., Hayano, Y., Izumiura, H., Kambe, E., Kudo, T., Kusakabe, N., Hori, Y., Omiya, M., Genda, H., Fukui, A., Fujii, Y., Guyon, O., Harakawa, H., Hayashi, M., Hidai, M., Kuzuhara, M., Machida, M., Matsuo, T., Nagata, T., Ogihara, M., Takami, H., Takato, N., Takahashi, Y. H., Tachinami, C., Terada, H., Kawahara, H., and Yamamuro, T.: 2014, in *Proc. SPIE Ground-based and Airborne Instrumentation for Astronomy V*, Vol. 9147, p. 12

- Kovács, G., Bakos, G., and Noyes, R. W.: 2005, *MNRAS* **356**(2), 557
- Kovács, G., Zucker, S., and Mazeh, T.: 2002, *Astronomy and Astrophysics* **391**, 369
- Kraus, A. L., Douglas, S. T., Mann, A. W., Agüeros, M. A., Law, N. M., Covey, K. R., Feiden, G. A., Rizzuto, A. C., Howard, A. W., Isaacson, H., Gaidos, E., Torres, G., and Bakos, G.: 2017, *The Astrophysical Journal* **845**(1), 72
- Kraus, A. L., Tucker, R. A., Thompson, M. I., Craine, E. R., and Hillenbrand, L. A.: 2011, *Astrophysical Journal* **728**(1), A48
- Kupka, F., Dubernet, M., and Collaboration, V.: 2011, *Baltic Astronomy* **20**, 503
- Kuszelewicz, J. S., North, T. S. H., Chaplin, W. J., Bieryla, A., Latham, D. W., Miglio, A., Bell, K. J., Davies, G. R., Hekker, S., Campante, T. L., Deheuvels, S., and Lund, M. N.: 2019, *MNRAS* **487**(1), 14
- Lacy, C. H., Moffett, T. J., and Evans, D. S.: 1976, *Astrophysical Journal Supplement* **30**(1), 85
- Lammer, H., Lichtenegger, H. I., Kulikov, Y. N., Grießmeier, J.-M., Terada, N., Erkaev, N. V., Biernat, H. K., Khodachenko, M. L., Ribas, I., Penz, T., and Selsis, F.: 2007, *Astrobiology* **7**(1), 185
- Lepine, S. and Gaidos, E.: 2011, *The Astronomical Journal* **142**(4), A138
- Lepine, S., Hilton, E. J., Mann, A. W., Wilde, M., Rojas-Ayala, B., Cruz, K. L., and Gaidos, E.: 2013, *The Astronomical Journal* **145**(4), A102
- Lightkurve Collaboration, Cardoso, J. V. d. M., Hedges, C., Gully-Santiago, M., Saunders, N., Cody, A. M., Barclay, T., Hall, O., Sagar, S., Turtelboom, E., Zhang, J., Tzanidakis, A., Mighell, K., Coughlin, J., Bell, K., Berta-Thompson, Z., Williams, P., Dotson, J., and Barentsen, G.: 2018, *Astrophysical Source Code Library* (**record ascl:1812.013**), 12013
- Lingam, M. and Loeb, A.: 2017, *The Astrophysical Journal* **848**(1), A41
- Lomb, N. R.: 1976, *Astrophysics and Space Science* **39**(2), 447
- Lopez-Morales, M.: 2005, *The Astrophysical Journal* **631**(2), 1120
- López-Morales, M.: 2007, *The Astrophysical Journal* **660**(1), 732

- Luger, R. and Barnes, R.: 2015, *Astrobiology* **15**(2), 119
- Lustig-Yaeger, J., Meadows, V. S., and Lincowski, A. P.: 2019, *Astronomical Journal* **158**(1), A27
- Mahadevan, S., Ramsey, L., Bender, C., Terrien, R., Jason, T., Halverson, S., Hearty, F., Nelson, M., Burton, A., Redman, S., Osterman, S., Diddams, S., Kasting, J., Endl, M., and Deshpande, R.: 2012, *Ground-based and Airborne Instrumentation for Astronomy IV. Proceedings of the SPIE* **8446**, 14
- Mancini, L., Lillo-Box, J., Southworth, J., Borsato, L., Gandolfi, D., Ciceri, S., Barrado, D., Brahm, R., and Henning, T.: 2016, *A&A* **590**(A112), 12
- Mandel, K. and Agol, E.: 2002, *The Astrophysical Journal Letters* **580**(2), L171
- Mann, A. W., Dupuy, T., Kraus, A. L., Gaidos, E., Ansdell, M., Ireland, M., Rizzuto, A. C., Hung, C.-l., Dittmann, J., Factor, S., and Feiden, G.: 2019, *The Astrophysical Journal* **871**(1), A63
- Mann, A. W., Feiden, G. A., Gaidos, E., Boyajian, T., and Braun, K. V.: 2015, *The Astrophysical Journal* **804**(1), A64
- Mann, A. W., Gaidos, E., and Ansdell, M.: 2013, *The Astrophysical Journal* **779**(2), A188
- Marois, C., Macintosh, B., Barman, T., Zuckerman, B., Song, I., Patience, J., and Lafreni, D.: 2008, *Science* **322**(5906), 1348
- Maxted, P. F. L.: 2016, *A&A* **591**(A111), 16
- Mayor, M. and Queloz, D.: 1995, *Nature* **378**(6555), 355
- McCormac, J., Pollacco, D., Skillen, I., Faedi, F., Todd, I., and Watson, C. A.: 2013, *PASP* **125**(927), 548
- McCormac, J., Skillen, I., Pollacco, D., Faedi, F., Ramsay, G., Dhillon, V. S., Todd, I., and Gonzalez, A.: 2014, *Monthly Notices of the Royal Astronomical Society* **438**(4), 3383
- Metropolis, N., Rosenbluth, A. W., Rosenbluth, M. N., Teller, A. H., and Teller, E.: 1953, *The Journal of Chemical Physics* **21**(6), 1087
- Mondrik, N., Newton, E., Charbonneau, D., and Irwin, J.: 2019, *The Astrophysical Journal* **870**(1), A10

- Morales, J. C., Ribas, I., Jordi, C., Torres, G., Gallardo, J., Guinan, E. F., Charbonneau, D., Wolf, M., Latham, D. W., Anglada-Escudé, G., Bradstreet, D. H., Everett, M. E., O'Donovan, F. T., Mandushev, G., and Mathieu, R. D.: 2009, *Astrophysical Journal* **691**(2), 1400
- Morley, C. V., Kreidberg, L., Rustamkulov, Z., Robinson, T., and Fortney, J. J.: 2017, *The Astrophysical Journal* **850**(2), 121
- Morris, M., Bobra, M. G., Agol, E., Lee, Y. J., and Hawley, S. L.: 2020, *MNRAS* **493**(4), 5489
- Morton, T. D.: 2015, *Astrophysical Source Code Library* (2015ascl.soft03010M)
- Muirhead, P. S., Dressing, C., Mann, A. W., Rojas-Ayala, B., Lepine, S., Paegert, M., De Lee, N., and Oelkers, R.: 2018, *The Astronomical Journal* **155**(4), A180
- Murphy, S. J., Lawson, W. A., Onken, C. A., Yong, D., Costa, G. S. D., Zhou, G., Mamajek, E. E., Bell, C. P. M., Bessell, M. S., and Feinstein, A. D.: 2020, *MNRAS* **491**(4), 4902
- Nefs, S. V., Birkby, J. L., Snellen, I. A. G., Hodgkin, S. T., Sipocz, B. M., Kovács, G., Mislis, D., Pinfield, D. J., and Martin, E. L.: 2013, *Monthly Notices of the Royal Astronomical Society* **431**(4), 3240
- Newton, E. R., Irwin, J., Charbonneau, D., Berta-thompson, Z. K., Dittmann, J. A., and West, A. A.: 2016, *The Astrophysical Journal* **821**(2), A93
- Newton, E. R., Mondrik, N., Irwin, J., and Winters, J. G.: 2018, *The Astronomical Journal* **156**(5), A217
- Nutzman, P. and Charbonneau, D.: 2008, *PASP* **120**(865), 317
- O'Connor, E.: 2015, *Andor iKon-L Linearity and Sensitivity Test Report*, Technical report, Andor, Oxford Instruments
- Ofir, A., Gandolfi, D., Buchhave, L., Lacy, C. H. S., Hatzes, A. P., and Fridlund, M.: 2012, *MNRAS* **423**(1), L1
- Orosz, J. A., Welsh, W. F., Carter, J. A., Brugamyer, E., Buchhave, L. A., Cochran, W. D., Endl, M., Ford, E. B., MacQueen, P., Short, D. R., Torres, G., Windmiller, G., Agol, E., Barclay, T., Caldwell, D. A., Clarke, B. D., Doyle, L. R., Fabrycky, D. C., Geary, J. C., Haghighipour, N., Holman, M. J., Ibrahim, K. A., Jenkins, J. M., Kinemuchi, K., Li, J., Lissauer, J. J., Prša, A., Ragozzine, D., Shporer, A., Still, M., and Wade, R. A.: 2012, *Astrophysical Journal* **758**(2), A87

- Parviainen, H.: 2015, *MNRAS* **450**(3), 3233
- Parviainen, H. and Aigrain, S.: 2015, *Monthly Notices of the Royal Astronomical Society* **453**(4), 3821
- Pecaut, M. J. and Mamajek, E. E.: 2013, *The Astrophysical Journal Supplement Series* **208**(1), A9
- Perruchot, S., Kohler, D., Bouchy, F., Richaud, Y., Richaud, P., Moreaux, G., Sottile, R., Hill, L., Knispel, G., Regal, X., Meunier, J., Ilovaisky, S., Mégevand, D., Blanc, P. E., Carol, C., Point, A., Laloge, A., and Brunel, J.: 2008, in *Proc. SPIE 7014, Ground-based and Airborne Instrumentation for Astronomy II*, No. 70140J, Marseille, France
- Perryman, M.: 2011, *The Exoplanet Handbook*, Cambridge University Press, Cambridge, United Kingdom, 1st edition
- Perryman, M.: 2018, *The Exoplanet Handbook*, Cambridge University Press, Cambridge, 2nd edition
- Perryman, M., Hartman, J., Bakos, G. Á., and Lindegren, L.: 2014, *ApJ* **797**(1), A14
- Pollacco, D., Skillen, I., Cameron, A., Christian, D., Irwin, J., Lister, T., Street, R., West, R., Clarkson, W., Evans, N., Fitzsimmons, A., Haswell, C., Hellier, C., Hodgkin, S., Horne, K., Jones, B., Kane, S., Keenan, F., Norton, A., Osborne, J., Ryans, R., and Wheatley, P.: 2006, *Publications of the Astronomical Society of the Pacific* **118**(848), 1407
- Pope, B. J. S., White, T. R., Farr, W. M., and Yu, J.: 2019, *The Astrophysical Journal Supplement Series* **245**(1), A8
- Pope, B. J. S., White, T. R., Huber, D., Murphy, S. J., Bedding, T. R., Caldwell, A., Sarai, A., Aigrain, S., and Barclay, T.: 2016, *MNRAS* **455**(1), L36
- Press, W. H. and Rybicki, G. B.: 1989, *ApJ* **338**, 277
- Prsa, A., Batalha, N., Slawson, R. W., Doyle, L. R., Welsh, W. F., Orosz, J. A., Seager, S., Rucker, M., Mjaseth, K., Engle, S. G., Conroy, K., Jenkins, J., Caldwell, D., Koch, D., and Borucki, W.: 2011, *The Astronomical Journal* **141**(3), A83

- Ratzloff, J. K., Corbett, H. T., Law, N. M., Barlow, B. N., Glazier, A., Howard, W. S., Fors, O., Ser, D., and Trifonov, T.: 2019, *PASP* **131**(1002), 084201
- Rauer, H., Aerts, C., Cabrera, J., and PLATO Team: 2016, *Astronomische Nachrichten* **337**(8-9), 961
- Rauer, H., Catala, C., Aerts, C., Appourchaux, T., Benz, W., Brandeker, A., Gizon, L., Pagano, I., Piotto, G., Santos, N. C., Smith, A., Udry, S., Adibekyan, V., Alibert, Y., Eiff, M. A.-v., Asplund, M., Antonello, E., Ball, W., Barnes, S., Belkacem, K., Bergemann, M., Bihain, G., Birch, A. C., Bonfils, X., Boisse, I., Bonomo, A. S., Brocato, E., Brun, S., Burleigh, M., Burston, R., Cabrera, J., Cassisi, S., Charpinet, S., Chiappini, C., Church, R. P., Cunha, M., Damasso, M., Deeg, H. J., Dreizler, S., Dreyer, C., Eggenberger, P., Ehrenreich, D., Farmer, R., Feltzing, S., Fialho, F. D. O., Figueira, P., Forveille, T., Fridlund, M., Giommi, P., Giuffrida, G., Godolt, M., Granzer, T., Grenfell, J. L., and Zwintz, K.: 2014, *Experimental Astronomy* **38**(1-2), 249
- Raynard, L., Goad, M. R., Gillen, E., Nielsen, L. D., Watson, C. A., Thompson, A. P. G., McCormac, J., Bayliss, D., Soto, M., Csizmadia, S., Chaushev, A., Burleigh, M. R., Alexander, R., Armstrong, D. J., Briegal, J. T., Cabrera, J., Casewell, S. L., Cooke, B. F., Erikson, A., Boris, T. G., Grange, A., Maximilian, N. G., Hodgkin, T., Hooton, M. J., Jenkins, J. S., Lambert, G., Loudon, T., Metrailler, L., Moyano, M., Pollacco, D., Queloz, D., Raddi, R., Rauer, H., Andrew, M., Smalley, B., Smith, A. M. S., Turner, O., Walker, R., West, R. G., and Wheatley, J.: 2018, *MNRAS* **481**(4), 4960
- Rhodes, B. C.: 2011, *Astrophysics Source Code Library* **1112.014**, 2011ascl.soft12014R
- Ribas, I.: 2003, *A&A* **398**, 239
- Ribas, I.: 2006, *Astrophysics and Space Science* **304**(1-4), 89
- Ricker, G. R., Winn, J. N., Vanderspek, R., Latham, D. W., Bakos, G. Á., Bean, J. L., Berta-Thompson, Z. K., Brown, T. M., Buchhave, L., Butler, N. R., Butler, R. P., Chaplin, W. J., Charbonneau, D., Christensen-Dalsgaard, J., Clampin, M., Deming, D., Doty, J., Lee, N. D., Dressing, C., Dunham, E. W., Endl, M., Fressin, F., Ge, J., Henning, T., Holman, M. J., Howard, A. W., Ida, S., Jenkins, J. M., Jernigan, G., Johnson, J. A., Kaltenegger, L., Kawai, N., Kjeldsen, H., Laughlin, G., Levine, A. M., Lin, D., Lissauer, J. J., Macqueen, P., Marcy, G., McCullough, P. R., Morton, T. D., Narita, N., Paegert, M., Palle, E., Pepe, F.,

- Pepper, J., Quirrenbach, A., Rinehart, S. A., Sasselov, D., Sato, B., Seager, S., Sozzetti, A., Stassun, K. G., Sullivan, P., Szentgyorgyi, A., Torres, G., Udry, S., and Villaseñor, J.: 2015, *J. Astron. Telesc. Instrum. Syst.* **1**(1), 014003
- Rimmer, P. B., Xu, J., Thompson, S. J., Gillen, E., Sutherland, J. D., and Queloz, D.: 2018, *Science Advances* **4**(8), eaar3302
- Roques, F. and Schneider, J.: 2015, *The Extrasolar Planets Encyclopaedia Catalog*
- Scalo, J., Kaltenegger, L., Segura, A., Fridlund, M., Ribas, I., Kulikov, Y. N., Grenfell, J. L., Rauer, H., Odert, P., Leitzinger, M., Selsis, F., Khodachenko, M. L., Eiroa, C., Kasting, J., and Lammer, H.: 2007, *Astrobiology* **7**(1), 85
- Scargle, J. D.: 1982, *Astrophysical Journal* **263**, 835
- Schmidt, S. J., Cruz, K. L., Bongiorno, B. J., Liebert, J., and Reid, I. N.: 2007, *Astronomical Journal* **133**(5), 2258
- Schwamb, M. E., Orosz, J. A., Carter, J. A., Welsh, W. F., Fischer, D. A., Torres, G., Howard, A. W., Crepp, J. R., Keel, W. C., Lintott, C. J., Kaib, N. A., Terrell, D., Gagliano, R., Jek, K. J., Parrish, M., Smith, A. M., Lynn, S., Simpson, R. J., Giguere, M. J., and Schawinski, K.: 2013, *Astrophysical Journal* **768**(2), A127
- Segura, A., Walkowicz, L. M., Meadows, V., Kasting, J., and Hawley, S.: 2010, *Astrobiology* **10**(7), 751
- Sestito, P. and Randich, S.: 2005, *A&A* **442**(2), 615
- Shields, A. L., Ballard, S., and Johnson, J. A.: 2016, *Physics Reports* **663**, 1
- Siverd, R. J., Beatty, T. G., Pepper, J., Eastman, J. D., Collins, K., Bieryla, A., Latham, D. W., Buchhave, L. A., Jensen, E. L., Crepp, J. R., Street, R., Stassun, K. G., Scott Gaudi, B., Berlind, P., Calkins, M. L., Depoy, D. L., Esquerdo, G. A., Fulton, B. J., Furész, G., Geary, J. C., Gould, A., Hebb, L., Kielkopf, J. F., Marshall, J. L., Pogge, R., Stanek, K. Z., Stefanik, R. P., Szentgyorgyi, A. H., Trueblood, M., Trueblood, P., Stutz, A. M., and Van Saders, J. L.: 2012, *Astrophysical Journal* **761**(2), A123
- Skrutskie, M. F., Cutri, R. M., Stiening, R., Weinberg, M. D., Schneider, S., Carpenter, J. M., Beichman, C., Capps, R., Chester, T., Elias, J., Huchra, J., Liebert, J., Lonsdale, C., Monet, D. G., Price, S., Seitzer, P., Jarrett, T., Kirkpatrick, J. D., Gizis, J. E., Howard, E., Evans, T., Fowler, J., Fullmer, L., Hurt, R., Light, R.,

- Kopan, E. L., Marsh, K. A., McCallon, H. L., Tam, R., Dyk, S. V., and Wheelock, S.: 2006, *The Astronomical Journal* **131**(2), 1163
- Sousa, S. G., Santos, N. C., Adibekyan, V., Tabernero, H. M., González Hernández, J. I., Montes, D., Smiljanic, R., Korn, A., Bergemann, M., Soubiran, C., and Mikolaitis, S.: 2014, *A&A* **561**, A21
- Southworth, J.: 2015, *EPJ Web of Conferences* **101**, 04001
- Stassun, K. G., Oelkers, R. J., Paegert, M., Torres, G., Pepper, J., Lee, N. D., Collins, K., Latham, D. W., Muirhead, P. S., and Chittidi, J.: 2019, *The Astronomical Journal* **158**(4), A138
- Stassun, K. G., Oelkers, R. J., Pepper, J., Paegert, M., DeLee, N., Torres, G., Latham, D. W., Charpinet, S., Dressing, C. D., Huber, D., Kane, S. R., Lepine, S., Mann, A., Muirhead, P. S., Rojas-Ayala, B., Silvotti, R., Fleming, S. W., Levine, A., Plavchan, P., and Group, t. T. T. S. W.: 2018, *Astronomical Journal* **156**(3), A102
- Sullivan, P. W., Winn, J. N., Berta-Thompson, Z. K., Charbonneau, D., Deming, D., Dressing, C. D., Latham, D. W., Levine, A. M., McCullough, P. R., Morton, T., Ricker, G. R., Vanderspek, R., and Woods, D.: 2015, *Astrophysical Journal* **809**(1), A77
- Segransan, D., Kervella, P., Forveille, T., and Queloz, D.: 2003, *A&A* **397**, 5
- Tamuz, O., Mazeh, T., and Zucker, S.: 2005, *Monthly Notices of the Royal Astronomical Society* **356**(4), 1466
- Telting, J. H., Avila, G., Buchhave, L., Frandsen, S., Gandolfi, D., Lindberg, B., Stempels, H. C., and Prins, S.: 2014, *Astronomische Nachrichten* **335**(1), 41
- The Astropy Collaboration, Price-Whelan, A. M., Sipcz, B. M., Günther, H. M., Lim, P. L., Crawford, S. M., Conseil, S., Shupe, D. L., Craig, M. W., Dencheva, N., Ginsburg, A., VanderPlas, J. T., Bradley, L. D., Pérez-Suárez, D., de Val-Borro, M., Aldcroft, T. L., Cruz, K. L., Robitaille, T. P., Tollerud, E. J., Ardelean, C., Babej, T., Bachetti, M., Bakanov, A. V., Bamford, S. P., Barentsen, G., Barmby, P., Baumbach, A., Berry, K. L., Biscani, F., Boquien, M., Bostroem, K. A., Bouma, L. G., Brammer, G. B., Bray, E. M., Breytenbach, H., Buddelmeijer, H., Burke, D. J., Calderone, G., Rodríguez, J. L. C., Cara, M., Cardoso, J. V. M., Cheedella, S., Copin, Y., Crichton, D., DÁvella, D., Deil, C., Depagne, É., Dietrich, J. P., Donath, A., Droettboom, M., Earl, N., Erben, T., Fabbro, S., Ferreira,

L. A., Finethy, T., Fox, R. T., Garrison, L. H., Gibbons, S. L. J., Goldstein, D. A., Gommers, R., Greco, J. P., Greenfield, P., Groener, A. M., Grollier, F., Hagen, A., Hirst, P., Homeier, D., Horton, A. J., Hosseinzadeh, G., Hu, L., Hunkeler, J. S., Ivezić, Ž., Jain, A., Jenness, T., Kanarek, G., Kendrew, S., Kern, N. S., Kerzendorf, W. E., Khvalko, A., King, J., Kirkby, D., Kulkarni, A. M., Kumar, A., Lee, A., Lenz, D., Littlefair, S. P., Ma, Z., Macleod, D. M., Mastropietro, M., McCully, C., Montagnac, S., Morris, B. M., Mueller, M., Mumford, S. J., Muna, D., Murphy, N. A., Nelson, S., Nguyen, G. H., Ninan, J. P., Nöthe, M., Ogaz, S., Oh, S., Parejko, J. K., Parley, N., Pascual, S., Patil, R., Patil, A. A., Plunkett, A. L., Prochaska, J. X., Rastogi, T., Janga, V. R., Sabater, J., Sakurikar, P., Seifert, M., Sherbert, L. E., Sherwood-Taylor, H., Shih, A. Y., Sick, J., Silbiger, M. T., Singanamalla, S., Singer, L. P., Sladen, P. H., Sooley, K. A., Sornarajah, S., Streicher, O., Teuben, P., Thomas, S. W., Tremblay, G. R., Turner, J. E. H., Terrón, V., van Kerkwijk, M. H., de la Vega, A., Watkins, L. L., Weaver, B. A., Whitmore, J. B., Woillez, J., and Zabalza, V.: 2018, *AJ* **156**(3), A123

The Astropy Collaboration, Robitaille, T. P., Tollerud, E. J., Greenfield, P., Droettboom, M., Bray, E., Aldcroft, T., Davis, M., Ginsburg, A., Price-whelan, A. M., Kerzendorf, W. E., Conley, A., Crighton, N., Barbary, K., Muna, D., Ferguson, H., Grollier, F., Parikh, M. M., Nair, P. H., Günther, H. M., Deil, C., Woillez, J., Conseil, S., Kramer, R., Turner, J. E. H., Singer, L., Fox, R., Weaver, B. A., Zabalza, V., Edwards, Z. I., Bostroem, K. A., Burke, D. J., Casey, A. R., Crawford, S. M., Dencheva, N., Ely, J., Jenness, T., Labrie, K., Lim, P. L., Pierfederici, F., Pontzen, A., Ptak, A., Refsdal, B., Servillat, M., and Streicher, O.: 2013, *A&A* **558**(A33), 9

Tilley, M. A., Segura, A., Meadows, V. S., Hawley, S., and Davenport, J.: 2019, *Astrobiology* **19**(1), 64

Torres, G.: 2013, *Astronomische Nachrichten* **334**(1-2), 4

Torres, G., Andersen, J., and Giménez, A.: 2010, *Astronomy and Astrophysics Review* **18**(1-2), 67

Torres, G., Sandberg Lacy, C. H., Feiden, G. A., Bruntt, H., and Viggo Clausen, J.: 2014, *The Astrophysical Journal* **797**(1), A31

Triaud, A. H. M. J., Hebb, L., Anderson, D. R., Cargile, P. A., Collier Cameron, A., and Gómez Maqueo Chew, Y.: 2013, *Astronomy & Astrophysics* **549**(A18), 16

- Udalski, A.: 2003, *Acta Astronomica* **53**, 291
- Vaccaro, T. R., Rudkin, M., Kawka, A., Vennes, S., Oswalt, T. D., Silver, I., Wood, M., and Smith, J. A.: 2007, *The Astrophysical Journal* **661(2)**, 1112
- Vanderspek, R., Huang, C. X., Vanderburg, A., Ricker, G. R., Latham, D. W., Seager, S., Winn, J. N., Jenkins, J. M., Burt, J., Dittmann, J., Newton, E., Quinn, S. N., Shporer, A., Charbonneau, D., Irwin, J., Ment, K., Winters, J. G., Collins, K. A., Evans, P., Gan, T., Hart, R., Jensen, E. L. N., Kielkopf, J., Mao, S., Waalkes, W., Bouchy, F., Marmier, M., Nielsen, L. D., Ottoni, G., Pepe, F., Ségransan, D., Udry, S., Henry, T., Paredes, L. A., James, H.-S., Hinojosa, R. H., Silverstein, M. L., Palte, E., Berta-Thompson, Z., Davies, M. D., Fausnaugh, M., Glidden, A. W., Pepper, J., Morgan, E. H., Rose, M., Twicken, J. D., Villaseñor, J. N. S., and Team, t. T.: 2019, *The Astrophysical Journal Letters* **871(2)**, L24
- von Boetticher, A., Triaud, A. H. M. J., Queloz, D., Gill, S., Lendl, M., Anderson, D. R., Cameron, A. C., Faedi, F., Gillon, M., Maqueo, Y. G., Hebb, L., Hellier, C., Jehin, E., Maxted, P. F. L., Martin, D. V., Pepe, F., Ségransan, D., Smalley, B., Udry, S., and West, R.: 2017, *A&A* **604(L6)**, 6
- von Boetticher, A., Triaud, A. H. M. J., Queloz, D., Gill, S., Maxted, P. F. L., Anderson, D. R., Bouchy, F., Burdanov, A., Cameron, A. C., Delrez, L., Faedi, F., Gillon, M., Gómez, Y., Chew, M., Hebb, L., Hellier, C., Lendl, M., Marmier, M., Martin, D. V., McCormac, J., Pepe, F., Ségransan, D., Smalley, B., Thompson, S., Turner, O., Udry, S., Van Grootel, V., and West, R.: 2019, *A&A* **625(A150)**, 18
- Weiss, L. M. and Marcy, G. W.: 2014, *The Astrophysical Journal Letters* **783(1)**, L6
- Welsh, W. F., Orosz, J. A., Short, D. R., Cochran, W. D., Endl, M., Brugamyer, E., Haghighipour, N., Buchhave, L. A., Doyle, L. R., Fabrycky, D. C., Hinse, T. C., Kane, S. R., Kostov, V., Mazeh, T., Mills, S. M., Müller, T. W. A., Quarles, B., Quinn, S. N., Ragozzine, D., Shporer, A., Steffen, J. H., Tal-Or, L., Torres, G., Windmiller, G., and Borucki, W. J.: 2015, *The Astrophysical Journal* **809(1)**, A26
- Wenger, M., Ochsenbein, F., Egret, D., Dubois, P., Bonnarel, F., Borde, S., Genova, F., Jasiewicz, G., Laloe, S., Lesteven, S., and Monier, R.: 2000, *A&A Supplement Series* **143**, 9

- West, R. G., Gillen, E., Bayliss, D., Matthew, R., Delrez, L., Maximilian, N. G., Hodgkin, S. T., Jackman, J. A. G., Jenkins, J. S., King, G., McCormac, J., Nielsen, L. D., Raynard, L., Smith, A. M. S., Soto, M., Wheatley, P. J., Almleaky, Y., Armstrong, D. J., Briegal, J. T., Burdanov, A., Cabrera, J., Casewell, S. L., Chaushev, A., Chazelas, B., Chote, P., Cooke, F., Csizmadia, S., Ducrot, E., Eigm, P., Foxell, E., Boris, T. G., Goad, M. R., Lambert, G., Longstaff, E. S., Loudon, T., Moyano, M., Murray, C., Pollacco, D., Queloz, D., Rauer, H., Sohy, S., Thompson, S. J., Walker, R., and Watson, C. A.: 2019, *MNRAS* **486**(4), 5094
- Wheatley, P. J., West, R. G., Goad, M. R., Jenkins, J. S., Pollacco, D. L., Queloz, D., Rauer, H., Udry, S., Watson, C. A., Chazelas, B., Eigmuller, P., Lambert, G., Genolet, L., McCormac, J., Walker, S., Armstrong, D. J., Bayliss, D., Bento, J., Bouchy, F., Burleigh, M. R., Cabrera, J., Casewell, S. L., Chaushev, A., Chote, P., Csizmadia, S., Erikson, A., Faedi, F., Foxell, E., Gansicke, B. T., Gillen, E., Grange, A., Gunther, M. N., Hodgkin, S. T., Jackman, J., Jordan, A., Loudon, T., Metrailler, L., Moyano, M., Nielsen, L. D., Osborn, H. P., Poppenhaeger, K., Raddi, R., Raynard, L., Smith, A. M. S., Soto, M., and Titz-Weider, R.: 2018, *MNRAS* **475**(4), 4476
- White, T. R., Pope, B. J. S., Antoci, V., Aerts, C., Gies, D. R., Gordon, K., Huber, D., Schaefer, G. H., Aigrain, S., Albrecht, S., Barclay, T., Barentsen, G., Beck, P. G., Bedding, T. R., Fredslund, M., Grundahl, F., Howell, S. B., Ireland, M. J., Murphy, S. J., Nielsen, M. B., Aguirre, V. S., and Tuthill, P. G.: 2017, *MNRAS* **471**(3), 2882
- Windmiller, G., Orosz, J. A., and Etzel, P. B.: 2010, *The Astrophysical Journal* **712**(2), 1003
- Winters, J. G., Henry, T. J., Jao, W.-c., Subasavage, J. P., Chatelain, J. P., Slatten, K., Riedel, A. R., Silverstein, M. L., and Payne, M. J.: 2019, *The Astronomical Journal* **157**(6), A216
- Wolfgang, A., Rogers, L. A., and Ford, E. B.: 2016, *The Astrophysical Journal* **825**(1), A19
- Wolszczan, A. and Frail, D. A.: 1992, *Nature* **355**(6356), 145
- Wunderlich, F., Godolt, M., Grenfell, J. L., Smith, A. M. S., Gebauer, S., Schreier, F., Hedelt, P., and Rauer, H.: 2019, *A&A* **624**(A49), 17
- Yashiro, S., Akiyama, S., Gopalswamy, N., and Howard, R. A.: 2006, *ApJ L* **650**(2), L143